Algebraic Screw Pairs

by

James D. Robinson

A Dissertation submitted to
the Faculty of Graduate and Postdoctoral Affairs
in partial fulfilment of
the requirements for the degree of
Doctor of Philosophy
in
Mechanical Engineering

Ottawa-Carleton Institute for
Mechanical and Aerospace Engineering

Department of Mechanical and Aerospace Engineering
Carleton University
Ottawa, Ontario, Canada
May 2012

Abstract

The algebraic screw pair, or A-pair, represents a novel class of kinematic pair that algebraically couples relative curvilinear translation with rotation about a single reference translation curve. The A-pair is a generalization of the well known helical screw pair, or H-pair, that linearly couples rotation with translation along the axis of rotation where the pitch of the screw is the linear constant of proportionality. The particular kind of A-pair examined in this thesis generates a sinusoidal coupling of relative rotation and linear translation along the axis of rotation between two adjacent links in a kinematic chain. The novelty of the A-pair requires that a full kinematic and dynamic analysis be performed prior to the implementation of the A-pair into useful kinematic chains (A-chains) and the determination of the advantages and disadvantages of A-pairs when compared to other kinematic constraints, in particular revolute pairs (R-pairs). This dissertation establishes the full kinematic and dynamic analysis of A-pairs and A-chains.

The existing position level kinematic analysis of A-chains is revised for application to general A-chains. This includes revising the application of the Denavit-Hartenburg parameter convention to general A-chains, adapting the direct kinematics to this new definition, and determining the constraint varieties of 2A-chains using kinematic mapping techniques for use in the inverse kinematics algorithm. The joint limits that result from the collisions between the legs of the A-pair are found and a novel algorithm for approximating the reachable workspace of serial manipulators is used to obtain the workspaces of 2A- and 4A-chains. The velocity level kinematics are addressed by obtaining the Jacobian matrices for nA-chains by adapting standard methods to account for the coupled A-pair motion.

The dynamic analysis provides dynamic equations of motion for A-chains. The single

A-pair is used to show that the inertial effects of the A-pair legs can often be considered negligible however, the potential energy effects of the legs have a larger effect on the dynamic model.

Though much of the material presented is applicable to general nA-chains, focus is given to 4A-chains. Such reduced-mobility chains are used because the coupled translation and rotation of the A-pair makes it impossible to have a wrist-partitioned 6A-chain, making it difficult to compare directly to existing 6R-chains. A numeric example based on the prototype 4A-chain is used to illustrate the application of the kinematic and dynamic analysis techniques developed in the dissertation.

To Jessie and Olivia, my amazing family, for their love and support.

Acknowledgments

I have many people I would like to thank for their help and support throughout my PhD studies and throughout my entire student career at Carleton. To begin with, John Hayes has taken me under his wing since my fourth year of undergrad and has guided my throughout the course of my graduate studies. He has provided much encouragement and support on and off the ice and his proficient editing skills and financial support have helped send me to many exotic conferences (in Montreal). Also, his financial support (and that of NSERC) have put the "professional" in professional student for many years. I must also acknowledge Owen Roberts who did an amazing job with the construction of the prototype 4A-chain.

I owe much thanks to the people at the Institute for Geometrie und CAD at Leopold-Franzens-Universität Innsbruck for their help and support through both my master's and PhD. Manfred Husty, Martin Pfurner, and Hans-Peter Shröcker have helped me understand the math and theory behind the kinematics and Dominic Walter has been amazingly helpful in the area of constraint varieties.

The secretaries in the MAAE office have been very helpful over the years. Nancy, Christie, Irene, and Marlene (who will be missed, go Habs go!). Also providing invaluable support in the areas of sounding boards and procrastination are my fellow gad students, including Sean, Ali, Heather, Calvin, Wes, Derek, Peter, Alanna, and many others.

Thanks to my parents, Gwen and Andy McDougall, and Don and Karen Robinson for their support over my many years in school. And also to my in-laws, Brian Simon and Amy Simon, who have welcomed me into their family, and are certain to be among the only ones who call me "Doctor" when I am done. I appreciate everything my entire family has done for me, but I must certainly acknowledge my brother Tom Robinson who has helped me

through a lot of `Maple` problems, even as he is working on his own PhD.

Last, but most importantly I want to thank my wonderful wife Jessie and our beautiful baby girl Olivia. Jessie has been so patient as I strive to become Dr. Dad, and Olivia has been the best distraction in the whole world.

Table of Contents

List of Tables

List of Figures

Chapter 1

Introduction

The algebraic screw pair, or A-pair, represents a novel class of kinematic pair that algebraically couples relative curvilinear translation with rotation about a single reference translation curve between two adjacent links in a kinematic chain. The A-pair is a generalization of the well known helical screw pair, or H-pair, that linearly couples rotation with translation along the axis of rotation where the pitch of the screw is the linear constant of proportionality. The particular A-pair investigated in this thesis, introduced in [1] and shown in Figure 1.1, generates a sinusoidal coupling of relative rotation and linear translation along the axis of rotation. It is based on a specific configuration of parallel manipulator called the Griffis-Duffy platform (GDP). The GDP is a special configuration of the six legged, six degree-of-freedom (DOF) Gough-Stewart platform (GSP) that, in most configurations, is subject to self-motions regardless of the lengths of the actuated legs. Self motions are instances where a manipulator possesses at least one DOF that is not controllable by the actuators of the manipulator. It turns out that most configurations of the GDP are subject to self-motions throughout their entire workspace, meaning that the moving platform can move relative to the fixed base without actuator input. In the case of the specific configuration of the GDP used to construct the A-pair the self-motion couples rotation about an axis with translation along that axis. The relationship between the rotation and translation is sinusoidal.

In [1] it is proposed that the A-pair be used in serial kinematic chains as a substitute for traditional revolute pairs, or R-pairs. This dissertation presents the kinematics and

Figure 1.1: The A-pair, based on a specific configuration of the GDP.

dynamics of A-chains (chains constructed using A-pairs as joints), laying the foundation for the future study of A-pairs and A-chains. While the investigation into the advantages and disadvantages of A-pairs relative to R-pairs is still an open topic the work presented here is required for further investigations of A-pairs and A-chains.

The objective of this dissertation is to establish the methods and techniques for performing the kinematic and dynamic analysis of A-pairs and A-chains. Most of the methods presented are applicable to general A-chains with n joints, nA-chains, however emphasis has been placed on A-chains with four joints, 4A-chains, corresponding to a prototype 4A-chain that has been designed and constructed, though not actuated. Although it is possible to design a 6A-chain, it is not possible for it to be wrist-partitioned. This is because wrist-partitioned chains require the last three axes to intersect in a point. The coupling of translation and rotation means that even if the last three axes intersect in one specific configuration, as one of the joints is actuated at least one of the axes will no longer intersect the others making it difficult to make useful comparisons to existing 6R-chains used in industry. Hence, work has focused on the reduced mobility 4A-chain. Moreover, there is also interest in reduced-mobility four DOF manipulators since that is all that is required in

many industrial applications, such as pick-and-place operations [2, 3].

1.1 Organization of this Dissertation

The first portion of this dissertation, Chapter 2, presents an overview of the background material required to understand the original work presented in Chapter 3. Contained within Chapter 2 are reviews of the relevant literature associated with the various topics.

The background material begins in Section 2.1 with an examination of how displacements are represented, first with conventional representations in Euclidean space then moving towards the less standard concepts involved in the kinematic mapping of displacements to higher order spaces. A discussion of the basics of serial manipulators is presented in Section 2.2, focusing on the direct and inverse kinematics of serial manipulators and methods for representing the reachable workspace of kinematic chains. The concept of constraint varieties, a method for representing the displacements achievable by a manipulator, is in Section 2.3 and a recently developed method for obtaining the constraint variety of short serial chains is discussed in Section 2.3.1. The constraint variety concept is integral to the material in Section 2.4 where an algorithm for the inverse kinematics of serial 6R-manipulators is presented. The algebraic screw pair is described in Section 2.5 along with a summary of existing research into the kinematics of A-pairs and A-chains. The focus on serial manipulator kinematics concludes in Section 2.6 with the velocity level kinematics and a description of how to obtain the Jacobian matrix for serial chains. Section 2.7 describes two methods for formulating the dynamic equations of motion of serial manipulators, the Lagrange formulation and the Newton-Euler formulation. The remainder of the background chapter shifts from a discussion of kinematic chains to other tools that are required to support the material presented in Chapter 3. Section 2.8 discusses the use of Plücker coordinates to describe lines in space, Section 2.9 discusses cylinder collision detection, and trigonometric identities and notation are discussed in Section 2.11.

The novel material of this dissertation is presented in Chapter 3. Section 3.1 describes revisions to generalize the existing work on the direct and inverse kinematics of A-chains.

The rotation limits of A-pairs are examined in Section 3.2 and the proposed actuation method is described in Section 3.3. Before continuing with the Study of A-chains, Section 3.4 presents a novel algorithm for quickly approximating the reachable workspace of serial manipulators, this algorithm is then applied to A-chains in Section 3.5. The method for deriving the Jacobian matrix of A-chains is covered in Section 3.6 and the dynamics of A-pairs and A-chains is discussed in Section 3.7, first using the analysis of a single A-pair to determine the impact of the A-pair legs on the dynamics and then applying the results to obtain the dynamic equations of motion of a 4A-chain. The original material concludes in Section 3.8 with a kinematic and dynamic analysis of the prototype 4A-chain.

1.2 Statement of Originality and Contributions

To the best of the knowledge of the author the following contributions presented in this dissertation stem from original ideas and results.

1. The generalisation of the A-chain Denavit-Hartenburg parameters, the determination of the geometric constant ρ for A-pairs, and the associated revisions to direct dynamics equations of nA-chains.

2. The revision of the derivation of the set of equations that describe the constraint varieties of 2A-chains.

3. The application of the revised 2A-chain constraint varieties to the inverse kinematics algorithm for 4A-chains.

4. The determination of the range of motion available to A-pairs.

5. A novel algorithm for approximating the reachable workspace of serial manipulators that greatly reduces the computation time compared to existing algorithms.

6. The derivation of the Jacobian matrices of A-chains for use in the velocity level kinematics and static force analysis.

7. The dynamic analysis of single A-pairs using both the Lagrange and Newton-Euler formulations of the dynamic equations of motion and the determination of the impact of the mass effects of the legs of the A-pair on the dynamics.

8. The derivation of the dynamic equations of motion of nA-chains, with focus on 4A-chains.

9. A numeric analysis of the kinematics and dynamics of a prototype 4A-chain.

The major original contributions of this dissertation lie in the full kinematic and dynamic analysis of the A-pair and A-chains. The A-pair is a novel kinematic pair and thus it is important that the general kinematics and dynamics be fully understood before further work can be conducted. Existing work on A-pairs provides some insight into the kinematics of A-chains, however that work is based on assumptions that proved to be false in general. The original work presented in this dissertation will be the basis for future study into the design, simulation, and control of A-chains, as well as the comparison of A-chains with similar R-chains.

In addition to the study of A-pairs and A-chains a new algorithm for the approximation of the reachable workspace of serial kinematic chains is presented. This is a novel method for producing a representation of the reachable workspace that can be plotted in three dimensions. The new algorithm is significantly faster when compared to the run-time of existing algorithms.

Chapter 2

Background Theory and Literature Review

Prior to a discussion of the original material presented in this dissertation, it is important to review the background concepts and theory. This chapter begins with a discussion of the representation of displacements in space; an introduction to manipulators that defines the nomenclature and introduces the concepts behind the analysis of manipulator kinematics and dynamics; an introduction to A-pairs; an overview of other necessary concepts including Plücker coordinates and cylinder collision checking; and finally an overview of required trigonometric identities.

2.1 Representation of Displacements

This section introduces the tools and concepts required to characterise displacements, including the representation of points in three-dimensional space with homogeneous coordinates, the matrix representation of transformations and displacements in Euclidean space, and the representation of rotations and displacements using quaternions and dual quaternions, respectively. Using these representations, the concept of the kinematic mapping of displacements is introduced.

2.1.1 Homogeneous Coordinates

Homogeneous coordinates are used in projective geometry to represent points in the projective space, similar to how Cartesian coordinates are used to represent points in Euclidean

space [4–6]. Homogeneous coordinates are additionally useful for representing rigid body displacements in Euclidean space as linear coordinate transformation matrices (see Section 2.1.2).

A Cartesian coordinate system with origin O and orthogonal axes x, y, z is established in Euclidean space, E_3. A point S in this space, and the ray passing through O and S are described by the Cartesian coordinates (x, y, z). If another distinct point Q is selected on this ray, away from the origin, it can be represented by $(\mu x, \mu y, \mu z)$, as illustrated in Figure 2.1. With this representation if $\mu \to \infty$, then Q becomes the seemingly meaningless

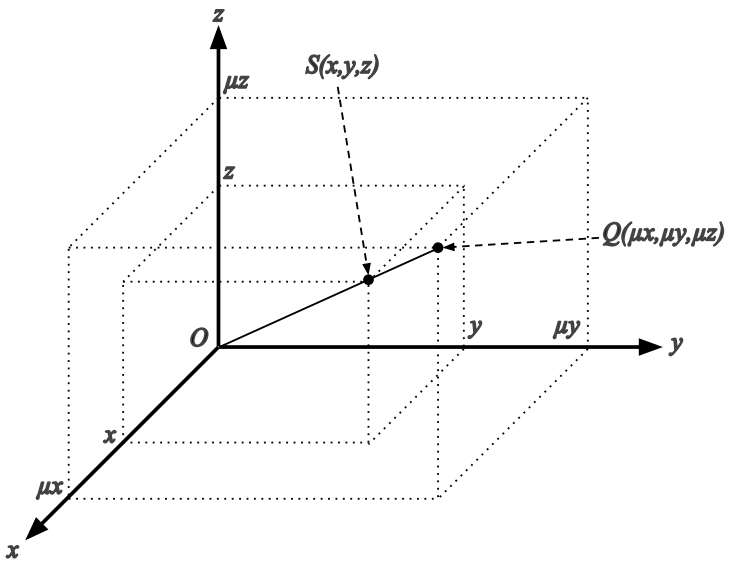

Figure 2.1: Cartesian coordinates in E_3.

triple (∞, ∞, ∞). If homogenous coordinates are introduced, some meaning can be brought to the point at infinity. A homogenizing coordinate is introduced such that

$$x = \frac{x_1}{x_0}, \quad y = \frac{x_2}{x_0}, \quad z = \frac{x_3}{x_0} \ , \tag{2.1}$$

where $x_0 \neq 0$. The homogenous coordinates of S are now written as the ratios $(x_0 : x_1 : x_2 : x_3)$. Note that the European convention has been used here, that is the homogenizing coordinate x_0 is the first element of the coordinate group, as opposed to the North American notation that uses $(x_1 : x_2 : x_3 : x_4)$, where x_4 is the homogenizing coordinate. The

European convention is used throughout this dissertation because of the following: assigning x_0 as the homogenizing coordinate means that points in any n dimensional projective space will have the homogenizing coordinate in the first position. An example of use of the European convention can be found in [7], and an example of the North American convention is given in [8].

In this representation if $x_0 = 1$, then the original Cartesian coordinates of S are recovered. If two proportional sets of homogenous coordinates are given, i.e. $(x_0 : x_1 : x_2 : x_3)$ and $(\lambda x_0 : \lambda x_1 : \lambda x_2 : \lambda x_3)$, where $\lambda \neq 0$, they represent the same point in space. The case where $x_0 \to 0$ is analogous to $\mu \to \infty$ in Cartesian coordinates, the difference now is that $(0 : x_1 : x_2 : x_3)$ describes the point at infinity on the line OS, removing some of the ambiguity of the Cartesian representation of a point at infinity, (∞, ∞, ∞). Cartesian coordinates are used to describe E_3 space, which is unbounded, so the point (∞, ∞, ∞) has no physical meaning. When E_3 space is bounded by the plane at infinity a projective space is created which is infinite but still bounded. When the homogenizing term is zero, *i.e.* $x_0 = 0$, the direction on which the point lies is identified (by x_1, x_2 and x_3), and all lines parallel to this direction intersect at the point $(0 : x_1 : x_2 : x_3)$, the point at infinity for this class of lines.

2.1.2 Displacements in Euclidean Space, E_3

When looking at relative displacements in E_3 one must consider two bodies with coordinate reference frames affixed to them. Craig [9] defines a reference frame as a set of four vectors providing position and orientation information. One vector describes the position of the origin of the reference frame relative to some coordinate system and the other three vectors are mutually orthogonal unit vectors along the principle X, Y and Z axes of the frame. The frame is a description of one coordinate system relative to another. This being said, consider reference frame Σ affixed to one of the bodies, which is called the base and will remain relatively fixed for the purposes of this discussion. Reference frame Σ' is affixed to the second body which moves relative to Σ.

Using Cartesian coordinates, a point $\mathbf{p}'$, given by a 3×1 position vector in Σ' can be

transformed to a point $\mathbf{p}$, represented by a 3×1 position vector in Σ:

$$\mathbf{p} = \mathbf{A}\mathbf{p}' + \mathbf{d}, \tag{2.2}$$

where $\mathbf{d}$ represents the 3×1 position vector of the origin of Σ' with respect to Σ, and $\mathbf{A}$ is a 3×3 orthogonal rotation matrix describing the orientation of Σ' relative to Σ. There are many ways to represent the orientation of a frame and the method used in this dissertation will be discussed in the following sections.

Utilizing homogenous coordinates it is possible to use one single matrix to produce the same results as Equation 2.2, thereby making it a linear transformation [10]. If $\mathbf{p}$ and $\mathbf{p}'$ are now represented by homogenous coordinates, the equation becomes

$$\mathbf{p} = \mathbf{T}\mathbf{p}'. \tag{2.3}$$

The coordinate transformation matrix, $\mathbf{T}$, takes the form

$$\mathbf{T} = \begin{bmatrix} 1 & 0 & 0 & 0 \\ d_1 & a_{11} & a_{12} & a_{13} \\ d_2 & a_{21} & a_{22} & a_{31} \\ d_3 & a_{31} & a_{32} & a_{33} \end{bmatrix}, \tag{2.4}$$

where d_i, $i = 1, \ldots, 3$ are the elements of position vector $\mathbf{d}$ and a_{jk}, $j, k = 1, \ldots, 3$ are the elements of the rotation matrix $\mathbf{A}$. This homogeneous transformation matrix represents the group of all displacements in E_3, called $SE(3)$.

One possible parametrization of the rotations is given using Euler angles [11]. This method uses three rotations about the moving coordinate axes to define the rotation [12,13]. Another parametrization of rotations in E_3 utilizes quaternions, which provide a computational singularity-free representation of these rotations. In order to understand this an overview of quaternions and how they are used to represent rotations in E_3 is required and is provided in Section 2.1.4, but first the concept of groups should be introduced.

2.1.3 Groups

A group, $G(\mathcal{G}, *)$, is a set $\mathcal{G}$ of elements that are all related by a binary operator $*$ [14]. The operator can be viewed as a way to combine the elements contained in $\mathcal{G}$. If the elements in $\mathcal{G}$ and the binary operator $*$ possess the following properties, they form a group, $G(\mathcal{G}, *)$.

- if $a, b \in G$, then $a * b \in G$;
- if $a, b, c \in G$, then $a * (b * c) = (a * b) * c$;
- the identity I of G under $*$, exists such that $a * I = I * a = a$ for $a \in G$; and
- for all $a \in G$, the inverse of a under $*$, $a^{-1} \in G$, exists such that $a * a^{-1} = a^{-1} * a = I$.

2.1.4 Quaternions and Representation of Rotations in E_3

Introduced by W.R. Hamilton in 1847 [15], quaternions were originally intended to describe the relative position of two vectors in three-dimensional space. They are essentially the three-dimensional equivalent to complex numbers in the plane [16].

A quaternion is represented by an ordered quadruple of real numbers, such as $P = (p_0, p_1, p_2, p_3)$, where p_i, $i \in 0 \ldots, 3$, are all contained in $\mathbb{R}$, the set of all real numbers. The set of all such quadruples is called $\mathbb{H}$. The p_0 element of P is called the scalar component and the remaining three elements form the vector component, $\mathbf{p} = (p_1, p_2, p_3)$. A quaternion is called vectorial if the scalar component is equal to zero.

To illustrate the definitions of quaternion operations, let $P = (p_0, p_1, p_2, p_3)$ and $Q = (q_0, q_1, q_2, q_3)$ be two quaternions. Addition and subtraction are component wise, while multiplication is defined by

$$\begin{aligned} P * Q = \quad & (p_0 q_0 - p_1 q_1 - p_2 q_2 - p_3 q_3,\ p_0 q_1 + p_1 q_0 + p_2 q_3 - p_3 q_2, \\ & p_0 q_2 - p_1 q_3 + p_2 q_0 + p_3 q_1,\ p_0 q_3 + p_1 q_2 - p_2 q_1 + p_3 q_0)\,. \end{aligned} \tag{2.5}$$

An alternative representation of a quaternion is

$$P = p_0 \mathbf{1} + p_1 \mathbf{i} + p_2 \mathbf{j} + p_3 \mathbf{k} = p_0 + \mathbf{p},$$

where $\mathbf{1} = (1,0,0,0)$, $\mathbf{i} = (0,1,0,0)$, $\mathbf{j} = (0,0,1,0)$, and $\mathbf{k} = (0,0,0,1)$ are the basis quaternions. It is important to note that $\mathbf{i}, \mathbf{j}$, and $\mathbf{k}$ are defined in quaternion algebra where the fundamental special products are $\mathbf{i}^2 = \mathbf{j}^2 = \mathbf{k}^2 = \mathbf{ijk} = -1$, $\mathbf{ij} = \mathbf{k} = -\mathbf{ji}$, $\mathbf{jk} = \mathbf{i} = -\mathbf{kj}$, and $\mathbf{ki} = \mathbf{j} = -\mathbf{ik}$. Defining the conjugate of a quaternion, which is analogous to the conjugate of a complex number, as

$$\widetilde{P} = p_0\mathbf{1} - p_1\mathbf{i} - p_2\mathbf{j} - p_3\mathbf{k}$$

leads to the norm being defined as

$$\|P\| = \sqrt{P * \widetilde{P}} = \sqrt{p_0^2 + p_1^2 + p_2^2 + p_3^2},$$

and the inverse defined as

$$P^{-1} = \frac{\widetilde{P}}{\|P\|^2}.$$

When $\|P\| = 1$, the quaternion is said to be normalized and $P^{-1} = \widetilde{P}$.

With an understanding of the basic quaternion operations it is possible to understand how they are used to describe rotations. Euler used what amounts to normalized quaternions to define the rotation of vector $\mathbf{q}$ in E_3 about an axis with direction given by $\mathbf{p}$ as

$$Ad\,P(\mathbf{q}) = P * \mathbf{q} * \widetilde{P} = P * \mathbf{q} * P^{-1}, \tag{2.6}$$

where $Ad\,P(\mathbf{q})$ is defined as the quaternion rotation operator, P is a normalized quaternion and $\mathbf{q}$ is a vectorial quaternion. P may be represented by $P = \cos(\frac{\theta}{2}) + \mathbf{p}\sin(\frac{\theta}{2})$ and describes a rotation of $\mathbf{q}$ about $\mathbf{p}$ by angle θ.

The orthogonal rotation matrix representing the group of rotations in E_3, $SO(3)$, can now be obtained by rotating the basis vectors $\mathbf{i}, \mathbf{j}$ and $\mathbf{k}$ about the axis described by the normalized quaternion $X = x_0\mathbf{1} + x_1\mathbf{i} + x_2\mathbf{j} + x_3\mathbf{k}$. First looking at the rotation of each axis

the following is obtained:

$$\begin{aligned} X * \mathbf{i} * \widetilde{X} &= (x_0\mathbf{1} + x_1\mathbf{i} + x_2\mathbf{j} + x_3\mathbf{k})\mathbf{i}(x_0\mathbf{1} - x_1\mathbf{i} - x_2\mathbf{j} - x_3\mathbf{k}) \\ &= (x_0\mathbf{i} - x_1\mathbf{1} - x_2\mathbf{k} + x_3\mathbf{j})(x_0\mathbf{1} - x_1\mathbf{i} - x_2\mathbf{j} - x_3\mathbf{k}) \\ &= (x_0^2 + x_1^2 - x_2^2 - x_3^2)\mathbf{i} + 2(x_1x_2 + x_0x_3)\mathbf{j} + 2(x_1x_3 - x_0x_2)\mathbf{k}, \\ X * \mathbf{j} * \widetilde{X} &= 2(x_1x_2 - x_0x_3)\mathbf{i} + (x_0^2 - x_1^2 + x_2^2 - x_3^2)\mathbf{j} + 2(x_2x_3 + x_0x_1)\mathbf{k}, \\ X * \mathbf{k} * \widetilde{X} &= 2(x_1x_3 + x_0x_2)\mathbf{i} + 2(x_2x_3 - x_0x_1)\mathbf{j} + (x_0^2 - x_1^2 - x_2^2 + x_3^2)\mathbf{k}. \end{aligned} \tag{2.7}$$

The coefficients of the resulting quaternions in Equation (2.7) can now be assembled into a matrix that represents SO(3). This matrix is

$$Ad\,X = \begin{bmatrix} x_0^2 + x_1^2 - x_2^2 - x_3^2 & 2(x_1x_2 - x_0x_3) & 2(x_1x_3 + x_0x_2) \\ 2(x_1x_2 + x_0x_3) & x_0^2 - x_1^2 + x_2^2 - x_3^2 & 2(x_2x_3 - x_0x_1) \\ 2(x_1x_3 - x_0x_2) & 2(x_2x_3 + x_0x_1) & x_0^2 - x_1^2 - x_2^2 + x_3^2 \end{bmatrix}, \tag{2.8}$$

where the parameters $x_i, i \in \{0, \ldots, 3\}$ are known as Euler-Rodrigues parameters [12,17–19]. A method for obtaining the Euler-Rodrigues parameters is shown in Section 2.1.6, but first a parametrization of SE(3) is required. The concept of dual quaternions can be used to do this.

2.1.5 Dual Quaternions and Representing Displacements in E_3

As shown by Pfurner [7] and Bottema and Roth [12] $SE(3)$, the set of all displacements in E_3, can be represented in a way that is free from parametrization singularities by using dual quaternions, also known as biquaternions, or octonions [12]. In this section the necessary characteristics of dual quaternions are defined and then used to show the parametrization of general displacements in E_3.

The dual quaternion is created by substituting dual numbers for the coefficients of a quaternion. A dual number is written as $a_i = x_i + \varepsilon y_i$, where $\varepsilon^2 = 0$. At this time it is useful to look at the algebra of dual numbers as described by Bottema and Roth [12]. The dual numbers posses the following characteristics, for a_1 and a_2 both dual numbers:

- $0\varepsilon = \varepsilon 0 = 0$;
- $a\varepsilon = \varepsilon a$;
- $a_1 + a_2 = (x_1 + \varepsilon y_1) + (x_2 + \varepsilon y_2) = x_1 + x_2 + \varepsilon(y_1 + y_2)$;
- $a_1 a_2 = (x_1 + \varepsilon y_1)(x_2 + \varepsilon y_2) = x_1 x_2 + \varepsilon(x_1 y_2 + x_2 y_1)$; and
- if $x_1 + \varepsilon y_1 = x_2 + \varepsilon y_2$, then $x_1 = x_2$ and $y_1 = y_2$.

Division of dual numbers is not always possible because the product of two dual numbers may be zero even if neither dual number is equal to zero. This is because of the fact that ε was defined such that $\varepsilon^2 = 0$, therefore $(\varepsilon y_1)(\varepsilon y_2) = 0$ for any y_1 and y_2.

Substituting a dual number into a quaternion as previously defined gives

$$\begin{aligned} P &= (x_0 + \varepsilon y_0)\mathbf{1} + (x_1 + \varepsilon y_1)\mathbf{i} + (x_2 + \varepsilon y_2)\mathbf{j}(x_3 + \varepsilon y_3)\mathbf{k} \\ &= a + \mathbf{p}, \end{aligned}$$

where $a = x_0 + \varepsilon y_0$ and $\mathbf{p} = \mathbf{p_1} + \varepsilon \mathbf{p_2}$ with $\mathbf{p_1} = (x_1, x_2, x_3)$ and $\mathbf{p_2} = (y_1, y_2, y_3)$. All elements of a dual quaternion are dual numbers.

The product of dual quaternions $P = a + \mathbf{p}$ and $Q = b + \mathbf{q}$ is

$$P * Q = ab - \mathbf{pq} + a\mathbf{p} + b\mathbf{q} + \mathbf{p} \times \mathbf{q},$$

where $\mathbf{p} \times \mathbf{q}$ is the cross product of vectors $\mathbf{p}$ and $\mathbf{q}$. Dual quaternions can be conjugated in two different ways,

$$\widetilde{P} = x_0 + \varepsilon y_0 - \mathbf{p_1} - \varepsilon \mathbf{p_2}$$

and

$$P_\varepsilon = x_0 - \varepsilon y_0 + \mathbf{p_1} - \varepsilon \mathbf{p_2}.$$

The norm of the dual quaternion is defined as

$$\|P\| = \sqrt{P * \widetilde{P}}$$

where the product under the root is

$$\begin{aligned} P * \widetilde{P} &= a^2 + \mathbf{pp} \\ &= x_0^2 + 2\varepsilon x_0 y_0 + \mathbf{p_1 p_1} + 2\varepsilon \mathbf{p_1 p_2} \\ &= x_0^2 + \mathbf{p_1 p_1} + 2\varepsilon(x_0 y_0 + \mathbf{p_1 p_2}) \\ &= x_0^2 + x_1^2 + x_2^2 + x_3^2 + \varepsilon(x_0 y_0 + x_1 y_1 + x_2 y_2 + x_3 y_3). \end{aligned}$$

As with quaternions, the condition for a dual quaternion to be called normalized is $\|P\| = 1$, which means $x_0^2 + x_1^2 + x_2^2 + x_3^2 = 1$ and $x_0 y_0 + x_1 y_1 + x_2 y_2 + x_3 y_3 = 0$.

When X and Y are defined such that $X = (x_0, x_1, x_2, x_3), Y = (y_0, y_1, y_2, y_3) \in \mathbb{H}$, then it can be said that $P = X + \varepsilon Y$. If $\mathbb{V}$ is defined as the set of all dual quaternions of the form $1 + \varepsilon\mathbf{r}$ with $\mathbf{r}$ a vector of $\mathbb{R}^3$, then the mapping from $\mathbb{V}$ to $\mathbb{H}$ is

$$\begin{aligned} Ad_e\, P(\mathbf{r}) &= P_\varepsilon \mathbf{r} \widetilde{P} \\ &= (X - \varepsilon Y)(1 + \varepsilon\mathbf{r})(\widetilde{X} + \varepsilon\widetilde{Y}) \\ &= 1 + \varepsilon(X\mathbf{r}\widetilde{X} + X\widetilde{Y} - Y\widetilde{X}). \end{aligned} \tag{2.9}$$

Pfurner [7] shows that Ad_e is a mapping of the set of normalized dual quaternions, $\mathbb{U}_d$, into the group $SE(3)$. $\mathbb{U}_d$ is a group with the inverse element being the conjugate quaternion. The $X\mathbf{r}\widetilde{X}$ term is the quaternion description of a rotation about the origin and the $X\widetilde{Y} - Y\widetilde{X}$ term represents the translational part of a displacement in E_3. Expanding the translational component yields

$$\begin{aligned} X\widetilde{Y} - Y\widetilde{X} = {} & 2(-x_0 y_1 + x_1 y_0 - x_2 y_3 + x_3 y_2)\mathbf{i} + 2(-x_0 y_2 + x_1 y_3 + x_2 y_0 - x_3 y_1)\mathbf{j} \\ & + 2(-x_0 y_3 - x_1 y_2 + x_2 y_1 + x_3 y_0)\mathbf{k}. \end{aligned} \tag{2.10}$$

Utilizing homogenous coordinates and Equation (2.8), the matrix representation of displacements in $SE(3)$ is

$$\mathbf{A} = \begin{bmatrix} 1 & 0 & 0 & 0 \\ l & x_0^2 + x_1^2 - x_2^2 - x_3^2 & 2(x_1x_2 - x_0x_3) & 2(x_1x_3 + x_0x_2) \\ m & 2(x_1x_2 + x_0x_3) & x_0^2 - x_1^2 + x_2^2 - x_3^2 & 2(x_2x_3 - x_0x_1) \\ n & 2(x_1x_3 - x_0x_2) & 2(x_2x_3 + x_0x_1) & x_0^2 - x_1^2 - x_2^2 + x_3^2 \end{bmatrix},$$

where

$$\begin{aligned} l &= 2(-x_0y_1 + x_1y_0 - x_2y_3 + x_3y_2), \\ m &= 2(-x_0y_2 + x_1y_3 + x_2y_0 - x_3y_1), \\ n &= 2(-x_0y_3 - x_1y_2 + x_2y_1 + x_3y_0). \end{aligned}$$

To obtain the matrix representation of the displacements of $SE(3)$, the normalizing condition may be removed and left as $x_0^2 + x_1^2 + x_2^2 + x_3^2 \neq 0$ and $\mathbf{A}$ becomes

$$\mathbf{A} = \frac{1}{\Delta} \begin{bmatrix} x_0^2 + x_1^2 + x_2^2 + x_3^2 & 0 & 0 & 0 \\ l & x_0^2 + x_1^2 - x_2^2 - x_3^2 & 2(x_1x_2 - x_0x_3) & 2(x_1x_3 + x_0x_2) \\ m & 2(x_1x_2 + x_0x_3) & x_0^2 - x_1^2 + x_2^2 - x_3^2 & 2(x_2x_3 - x_0x_1) \\ n & 2(x_1x_3 - x_0x_2) & 2(x_2x_3 + x_0x_1) & x_0^2 - x_1^2 - x_2^2 + x_3^2 \end{bmatrix}, \quad (2.11)$$

where $\Delta = x_0^2 + x_1^2 + x_2^2 + x_3^2$. The $x_i, y_i, i \in \{0, \ldots, 3\}$ are called the Study parameters, or soma coordinates [20]. Using the algebra of dual quaternions means that the mapping Ad_e is 2 to 1. This leads to the fact that there are two dual quaternions, P and $-P$, describing every displacement in E_3. As noted by Brunnthaler [14], the terms $X\widetilde{Y} - Y\widetilde{X}$ and $X\mathbf{r}\widetilde{X}$ are vector quaternions which are equal to their negative quaternions. The issue of the 2 to 1 mapping is resolved by looking at the eight terms of the dual quaternions as the homogenous coordinates of a point in seven-dimensional projective space, P^7, called the kinematic image space.

2.1.6 Kinematic Mapping

The representation of E_3 displacements as points in P^7 utilizes the Study parameters $(x_0, x_1, x_2, x_3, y_0, y_1, y_2, y_3)$, a normalized dual quaternion which must satisfy the condition

$$x_0y_0 + x_1y_1 + x_2y_2 + x_3y_3 = 0. \tag{2.12}$$

This includes the trivial case $x_0 = x_1 = x_2 = x_3 = 0$, called the exceptional generator, which does not represent a displacement in E_3 because all of the Euler parameters representing the rotation about the origin would be zero, a situation having no physical meaning. Equation (2.12) with the exceptional generator removed is called the Study quadric [12], represented by S_6^2, and can be viewed as a hyperboloid in P^7. Any displacement in E_3 maps to a single unique point on S_6^2. The mapping of displacements from $SE(3)$ to S_6^2 is called kinematic mapping [12]. The displacements in E_3 are represented one to one in P^7.

Kinematic mapping is used in this dissertation to represent the displacements obtainable by a mechanism as a set of related points in the kinematic image space. This is the concept of constraint varieties which is presented in detail in Section 2.3, but for this section it is important to understand that there is a need to map the group of displacements in E_3, represented by the matrix $\mathbf{T}$ in Equation (2.3), to the points lying on S_6^2. A method for obtaining the Study parameters for a displacement represented by $\mathbf{T}$ is therefore required.

2.1.7 Study Parameters

Two methods of obtaining the Study parameters are presented here. The first is the most commonly used method employing skew symmetric matrices and the second is the method developed by Study [20]. Study's method is used in this dissertation as its use is very straightforward and overcomes a major shortcoming of the skew symmetric matrices method. The skew symmetric matrix method is shown for completeness and its use produces equivalent results to Study's method.

The theorem of Cayley [21] states that any orthogonal matrix $\mathbf{A}$ may be decomposed such that

$$\mathbf{A} = (\mathbf{I} - \mathbf{S})^{-1}(\mathbf{I} + \mathbf{S})$$

where $\mathbf{I}$ is the 3×3 identity matrix and $\mathbf{S}$ is a skew symmetric matrix of the form

$$\mathbf{S} = \begin{bmatrix} 0 & -b_3 & b_2 \\ b_3 & 0 & -b_1 \\ -b_2 & b_1 & 0 \end{bmatrix}.$$

For an orthogonal matrix $\mathbf{A}$ with eigenvalues not equal to -1, $\mathbf{S}$ can be computed with $\mathbf{S} = (\mathbf{A} - \mathbf{I})(\mathbf{A} + \mathbf{I})^{-1}$. The entries of $\mathbf{S}$ describe the rotation in E_3 of angle ϕ about the axis represented by the vector (b_1, b_2, b_3), where $\tan(\frac{\phi}{2}) = \sqrt{b_1^2 + b_2^2 + b_3^2}$. When the $b_i, i = 1, 2, 3$ terms are made homogenous such that $b_i = \frac{x_i}{x_0}$ they become the Euler-Rodrigues parameters. From Craig [9] it is shown that the Euler-Rodrigues parameters are given by:

$$\begin{aligned} x_0 &= \cos\tfrac{\phi}{2}, \\ x_1 &= b_1 \sin\tfrac{\phi}{2}, \\ x_2 &= b_2 \sin\tfrac{\phi}{2}, \\ x_3 &= b_3 \sin\tfrac{\phi}{2}. \end{aligned} \tag{2.13}$$

The property $x_0^2 + x_1^2 + x_2^2 + x_3^2 \neq 0$ must always hold.

In the event that the rotation angle ϕ approaches any multiple of π this method no longer holds because an eigenvalue of $\mathbf{A}$ is -1 and $\tan(\frac{\phi}{2})$ goes to infinity. In such situations, an alternative method is required to obtain the Euler-Rodrigues parameters, such as using limits when ϕ approaches a singularity.

The Study method for obtaining the Euler-Rodrigues parameters is very straightforward.

The ratios

$$\begin{aligned} x_0 : x_1 : x_2 : x_3 &= 1 + a_{11} + a_{22} + a_{33} : a_{32} - a_{23} : a_{13} - a_{31} : a_{21} - a_{12} \\ &= a_{32} - a_{23} : 1 + a_{11} - a_{22} - a_{33} : a_{12} + a_{21} : a_{31} + a_{13} \\ &= a_{13} - a_{31} : a_{12} + a_{21} : 1 - a_{11} + a_{22} - a_{33} : a_{23} + a_{32} \\ &= a_{21} - a_{12} : a_{31} + a_{13} : a_{23} + a_{32} : 1 - a_{11} - a_{22} + a_{33}. \end{aligned} \tag{2.14}$$

are found by the 3×3 lower-right sub-matrix of $\mathbf{T}$ in Equation (2.3) and 3×3 lower-right sub-matrix in Equation (2.11). The derivation of these ratios is shown by Pfurner in [7]. In general the four ratios of Equation (2.14) will yield the same results, but in special cases, such as when ϕ is a multiple of π, one or more, but not all of the ratios may be $0 : 0 : 0 : 0$. In such a case one of the solutions with non-zero terms is selected, thus the Euler-Rodrigues parameters can always be found directly from $\mathbf{T}$.

The remaining Study parameters, y_0, y_1, y_2, y_3, can now be found from the set of equations that includes the l, m, n terms of $\mathbf{A}$ in Equation (2.11) set equal to the corresponding terms of $\mathbf{T}$ in Equation (2.3) and the Study quadric of Equation (2.12). Solving this set for the remaining Study parameters gives

$$\begin{aligned} y_0 &= \tfrac{1}{2}(d_1 x_1 + d_2 x_2 + d_3 x_3), \\ y_1 &= \tfrac{1}{2}(-d_1 x_0 + d_3 x_2 - d_2 x_3), \\ y_2 &= \tfrac{1}{2}(-d_2 x_0 - d_3 x_1 + d_1 x_3), \\ y_3 &= \tfrac{1}{2}(-d_3 x_0 + d_2 x_1 - d_1 x_2), \end{aligned} \tag{2.15}$$

where d_1, d_2 and d_3 are defined in Equation (2.3).

2.1.8 Effect of Transformations in E_3 on Points in P^7

In this dissertation it is necessary to understand the effect of a coordinate transformation in E_3 on the Study parameters in P^7. That is, if the Study parameters of a displacement

are known for a specific coordinate system and that system changes, what is the effect on the Study parameters? The two important transformations are those in the base reference frame, which results in a change of the fixed coordinate system of a manipulator, and those in the moving reference frame, which results in a change of the end effector, or EE, coordinate system. Both types of transformation has a different influence on the Study parameters in P^7 and must be examined separately.

In both cases the following two matrices are used. The first, $\mathbf{A}$, describes Σ_{EE} relative to Σ_0 and is built by substituting the Study parameters $\mathbf{a} = (a_0, a_1, a_2, a_3, a_4, a_5, a_6, a_7)^T$ for $(x_0, x_1, x_2, x_3, y_0, y_1, y_2, y_3)^T$ in Equation (2.11). Similarly, the coordinate transformation is described by matrix $\mathbf{T}$ which is built by substituting $\mathbf{t} = (t_0, t_1, t_2, t_3, t_4, t_5, t_6, t_7)^T$ for $(x_0, x_1, x_2, x_3, y_0, y_1, y_2, y_3)^T$. The matrix $\mathbf{A}$ can be thought of as describing the EE pose of a manipulator with respect to Σ_0, and $\mathbf{a}$ contains the Study parameters of $\mathbf{A}$. The matrix $\mathbf{T}$ represents some form of change in the kinematic architecture of a kinematic chain, such as moving the entire manipulator relative to the fixed coordinate system or changing the architecture of the links and altering the parameters that define the manipulator (Section (2.2.2)), *i.e.* actuating the joints of the manipulator. Moving the whole manipulator to a new position represents a transformation in the base frame, while actuating the joints of the manipulator results in a transformation in the moving frame. The elements of $\mathbf{t}$ are the Study parameters of $\mathbf{T}$.

Transformation in the Base Frame

A transformation in the base frame is described by the matrix product $\mathbf{TA}$. After the matrix multiplication the Study parameters are found using Study's method as presented

in Section 2.1.6. The resulting Study parameters are

$$\mathbf{t}_b = \Delta \begin{pmatrix} a_0t_0 - a_1t_1 - a_2t_2 - a_3t_3 \\ a_0t_1 + a_1t_0 + a_3t_2 - a_2t_3 \\ a_0t_2 + a_2t_0 + a_1t_3 - a_3t_1 \\ a_0t_3 + a_3t_0 + a_2t_1 - a_1t_2 \\ a_0t_4 - a_1t_5 - a_2t_6 - a_3t_7 + a_4t_0 - a_5t_1 - a_6t_2 - a_7t_3 \\ a_0t_5 + a_1t_4 - a_2t_7 + a_3t_6 + a_4t_1 + a_5t_0 - a_6t_3 + a_7t_2 \\ a_0t_6 + a_1t_7 + a_2t_4 - a_3t_5 + a_4t_2 + a_5t_3 + a_6t_0 - a_7t_1 \\ a_0t_7 - a_1t_6 + a_2t_5 + a_3t_4 + a_4t_3 - a_5t_2 + a_6t_1 + a_7t_0 \end{pmatrix}, \tag{2.16}$$

where

$$\Delta = \frac{a_0t_0 - a_1t_1 - a_2t_2 - a_3t_3}{(a_0^2 + a_1^2 + a_2^2 + a_3^2)(t_0^2 + t_1^2 + t_2^2 + t_3^2)}.$$

The Δ term may be ignored because homogeneous coordinates are being used. The subscript b indicates that the transformation is in the base frame.

Equation (2.16) can be written as $\mathbf{T}_b\mathbf{a}$, where

$$\mathbf{T}_b = \begin{bmatrix} t_0 & -t_1 & -t_2 & -t_3 & 0 & 0 & 0 & 0 \\ t_1 & t_0 & -t_3 & -t_2 & 0 & 0 & 0 & 0 \\ t_2 & t_3 & t_0 & -t_1 & 0 & 0 & 0 & 0 \\ t_3 & -t_2 & t_1 & t_0 & 0 & 0 & 0 & 0 \\ t_4 & -t_5 & -t_6 & -t_7 & t_0 & -t_1 & -t_2 & -t_3 \\ t_5 & t_4 & -t_7 & t_6 & t_1 & t_0 & -t_3 & t_2 \\ t_6 & t_7 & t_4 & -t_5 & t_2 & t_3 & t_0 & -t_1 \\ t_7 & -t_6 & t_5 & t_4 & t_3 & -t_2 & t_1 & t_0 \end{bmatrix}. \tag{2.17}$$

With this representation, the effect of a transformation in the base frame on the Study parameters in P^7 can be found using the Study parameters of the transformation matrix.

Transformations in the Moving Frame

The same procedure as for the transformation in the base frame is used in the case of a transformation in the moving frame, however the transformation is now described by the matrix product **AT**. A similar matrix to $\mathbf{T}_b$ is developed called $\mathbf{T}_m$, where the subscript m indicates that the transformation takes place in the moving frame, such that the transformed Study parameters are given by $\mathbf{T}_m\mathbf{a}$, where

$$\mathbf{T}_m = \begin{bmatrix} t_0 & -t_1 & -t_2 & -t_3 & 0 & 0 & 0 & 0 \\ t_1 & t_0 & t_3 & -t_2 & 0 & 0 & 0 & 0 \\ t_2 & -t_3 & t_0 & t_1 & 0 & 0 & 0 & 0 \\ t_3 & t_2 & -t_1 & t_0 & 0 & 0 & 0 & 0 \\ t_4 & -t_5 & -t_6 & -t_7 & t_0 & -t_1 & -t_2 & -t_3 \\ t_5 & t_4 & t_7 & -t_6 & t_1 & t_0 & t_3 & -t_2 \\ t_6 & -t_7 & t_4 & t_5 & t_2 & -t_3 & t_0 & t_1 \\ t_7 & t_6 & -t_5 & t_4 & t_3 & t_2 & -t_1 & t_0 \end{bmatrix}. \tag{2.18}$$

In [7], Pfurner shows and proves many useful properties of the $\mathbf{T}_b$ and $\mathbf{T}_m$ matrices. The most important results include the fact that under a transformation in E_3 the quadric S_6^2 and the exceptional generator remain unchanged and the inverse of $\mathbf{T}_b$ or $\mathbf{T}_m$ can be found by substituting $(t_0, -t_1, -t_2, -t_3, t_4, -t_5, -t_6, -t_7)$ for $(t_0, t_1, t_2, t_3, t_4, t_5, t_6, t_7)$ which results in no change for t_0 and t_4.

To describe the matrix $\mathbf{T}_b$ or $\mathbf{T}_m$ for a displacement described by a 4×4 matrix, for example $\mathbf{M}_i$, the form $\mathbf{T}_b(\mathbf{M}_i)$ is used, meaning the $\mathbf{T}_b$ matrix is populated by the Study parameters associated with the matrix $\mathbf{M}_i$.

2.2 Manipulator Basics

This section introduces some of the basic topics in the study of robotic manipulators that are germane to this dissertation. Addressed are some of the various classes of manipulators, a standard method for describing kinematic chains (Denavit-Hartenburg Parameters), the

direct and inverse kinematics of serial manipulators, and the workspaces of serial manipulators.

2.2.1 Classes of Manipulators

There are three main classes of manipulators: serial, parallel, and hybrid. While much of this dissertation focuses on serial manipulators it is useful to understand some of the characteristics of the different arrangements.

A *serial manipulator* can be described as an open chain where each link is connected to exactly two others, with the exception of the EE which is connected to only one other link. It is common for the links to be connected using revolute joints (R-pairs) or prismatic joints (P-pairs), though other joint types also exist [9,22]. A serial manipulator consisting of links connected by n R-pairs is referred to as an nR-manipulator. Similar naming conventions can be used for the other joint types, or a combination of different types. The most well known serial manipulators are industrial robot arms such as that shown in Figure 2.2. Because

Figure 2.2: Example of a serial manipulator from KUKA Robotics [23].

serial manipulators have only one connection to the base or ground, in general they can reach a large number of positions and orientations when compared to their parallel counterpart, depending on the joint and link geometry. This single connection to the base can also be

a disadvantage because the manipulator essentially becomes a cantilever beam, meaning stiffness is lower than if there were more connections with the base. As will be discussed later in this dissertation, obtaining the direct kinematic equations for serial manipulators has a well known and simple solution, but the inverse kinematics problem is not as trivial.

A *parallel manipulator* is characterized by having two or more serial manipulators working simultaneously on the EE. The serial chains work together to influence the motion of the EE. There exist many configurations of parallel manipulator, however a common example is the Gough-Stewart Platform, GSP. In this configuration six legs connect the fixed base to the moving EE platform, and the position and orientation of the moving platform is controlled by independently actuating the joints in each of the legs. Parallel manipulators are covered in detail by Merlet [24]. The multiple legs connecting the moving EE platform to the fixed base means that the parallel manipulator is inherently more stiff than a serial chain since the EE is no longer at the end of a cantilevered arm as is discussed by Carbone and Ceccarelli [25]. The additional legs also have a negative aspect, they lead to self-collisions where the legs interfere with each other and the rest of the manipulator structure meaning there is a restricted reachable workspace and often no dextrous workspace at all. Figure 2.3 shows a flight simulator from CAE. The motion platform for the simulator is a Gough-Stewart platform. The inverse kinematics of a parallel manipulator provides a

Figure 2.3: Example of a parallel manipulator from CAE [26].

simple unique solution for the leg lengths for every desired EE pose. On the other hand, the direct kinematics for a general GSP were an unsolved problem until a solution was provided by Husty [27].

Hybrid manipulators are typically characterised by combining parallel and serial manipulators or concatenating parallel manipulators such that the *moving* platform of one parallel manipulator becomes the *fixed* base of the next, creating a serial chain of parallel manipulators. The intent of hybrid manipulators is to take advantage of the high stiffness of parallel manipulators and the typically larger workspace of serial manipulators. Examples of hybrid manipulators are given in [25, 28–31] Figure 2.4 shows a sketch of a redundant hybrid manipulator from the Shenyang Institute for Automation [30]. Each new configura-

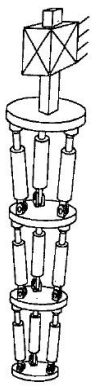

Figure 2.4: Sketch of a redundant hybrid manipulator from the Shenyang Institute for Automation [30].

tion of hybrid manipulator has a different kinematics and control scheme. The kinematics must be re-evaluated for each new architecture.

2.2.2 Denavit-Hartenburg Parameters

Denavit-Hartenburg parameters [32], or DH-parameters, are commonly used when working with serial manipulators to provide an unambiguous mathematical description of the kinematic chain. Many distinct forms have evolved since their introduction in 1954, but the particular form used in this dissertation is from [22]. The procedure described here is intended for labeling an nR-chain but for a more detailed description of DH-parameters

the interested reader is referred to Denavit and Hartenberg [32], Craig [9], Shigley and Uicker [33], or most introductory textbooks on robotics.

The procedure for assigning the DH-parameters begins by numbering each link in the serial kinematic chain, with the base being Link 0, Link 1 being the next link, and so on up to Link n. Next, each joint axis in the chain and the common normal between each axis are established. The axes are numbered sequentially from 1 to n, starting with the joint between the base (Link 0) and Link 1. Each link is assigned one reference frame and the assignment of this reference frame depends on the two axes at the ends of the link. For the purposes of this description, each Link i, $i = 1, \ldots, n$, describes a rigid link that lies on the common normal between Axis i and Axis $i + 1$ irrespective of the actual shape of the physical link in the manipulator. The special cases of intersecting or parallel axes will be addressed as needed.

Assignment of Link Reference Frames

Frame i is denoted Σ_i. The origin of Σ_i is established where Link i intersects Axis i. The Z_i-axis of Σ_i points along Axis i, the direction is arbitrary but, with experience, is selected to ease future calculations. The X_i-axis points along the common normal towards the origin of Σ_{i+1}. If the axes i and $i + 1$ intersect, the axis X_i is parallel to the normal of the intersecting axes, again the direction is selected to ease future calculations. The Y_i-axis is assigned to complete the right-handed coordinate system. For parallel axes the location of the frame origin along the joint axis is arbitrary, however it is often selected to make as many parameters as possible be equal to zero. These procedures work well for intermediate links, however the base and EE frames, Σ_0 and Σ_n respectively, are often selected to ease calculations by providing for as many DH-parameters to be zero as possible.

Assignment of DH-Parameters

Once the link frames have been established the DH-parameters can be determined. The four DH-parameters are defined as follows:

Link length a_i, the directed distance from Axis $i-1$ to i along X_i;

Link twist α_i, the directed angle from Axis $i-1$ to i about X_i;

Joint offset d_i, the directed distance from the origin of Σ_{i-1} to the intersection of Axis $i-1$ and X_i along Z_{i-1}; and

Joint angle θ_i, the directed angle from X_{i-1} to X_i about Z_{i-1}.

Figure 2.5 shows a typical link with reference frames and the DH-parameters identified.

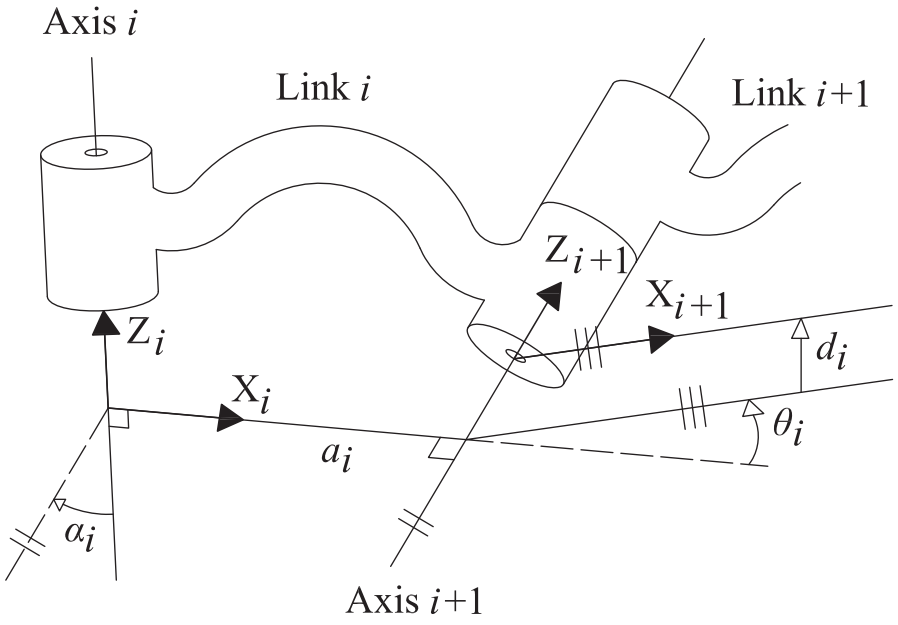

Figure 2.5: Link with reference frames and DH-parameters.

In a chain with n revolute joints, an nR-chain, the values θ_i, $i = 1 \ldots n$ are variable as the links rotate about the joint, and thus called the joint variables, while the remaining three parameters are fixed and are called the link and joint parameters. For a prismatic pair, a P-pair, the d_i parameter becomes the joint variable.

The DH-parameters are not unique since the assignment of the reference frames possesses some ambiguity and thus a given kinematic chain may have any number of different sets of

DH-parameters, however the DH-parameters are unambiguous and if provided with a set of DH-parameters one could reconstruct the kinematic geometry of the manipulator.

2.2.3 Direct Kinematics of Serial Manipulators

The process of obtaining the *direct kinematics* of a serial kinematic chain refers to the determination the set of equations that provides the EE pose (position and orientation of the EE reference frame) for a given complete set of joint variables. For this dissertation, as is often the case in literature, the direct kinematic equations are presented in matrix form and the resulting 4×4 homogeneous matrix is the transformation matrix, ${}^0\mathbf{T}_{EE}$, the coordinates of points from the base reference frame Σ_0 to the EE reference frame Σ_{EE} (which may or may not be coincident with Σ_n) and the elements of ${}^0\mathbf{T}_{EE}$ are functions of the joint variables, *i.e.* θ_i, $i = 1 \ldots n$ for an nR-chain. Algorithms for obtaining the matrix representations of the direct kinematic equations are well known and are covered in most introductory robotics text books. The method used in this dissertation is based on that used by Pfurner [7] and Husty, *et al.* [34, 35].

The transformation matrix ${}^0\mathbf{T}_n$ is obtained by

$$ {}^0\mathbf{T}_n = \mathbf{M}_1\mathbf{G}_1 \ldots \mathbf{M}_i\mathbf{G}_i \ldots \mathbf{M}_n\mathbf{G}_n, \tag{2.19} $$

where

$$ \mathbf{G}_i = \begin{bmatrix} 1 & 0 & 0 & 0 \\ a_i & 1 & 0 & 0 \\ 0 & 0 & \cos(\alpha_i) & -\sin(\alpha_i) \\ d_i & 0 & \sin(\alpha_i) & \cos(\alpha_i) \end{bmatrix}, \tag{2.20} $$

and

$$ \mathbf{M}_i = \begin{bmatrix} 1 & 0 & 0 & 0 \\ 0 & \cos(\theta_i) & -\sin(\theta_i) & 0 \\ 0 & \sin(\theta_i) & \cos(\theta_i) & 0 \\ 0 & 0 & 0 & 1 \end{bmatrix}. \tag{2.21} $$

The $\mathbf{G}_i$ matrices contain the DH-parameters of each link that remain constant as the joints are actuated (the link and joint parameters) and the $\mathbf{M}_i$ matrices contain the DH-parameters that vary with the joint actuation (the joint variables). Additional transformations may be required if Σ_{EE} is not coincident with Σ_n and/or Σ_0 is not coincident with the global reference frame.

2.2.4 Inverse Kinematics of Serial Manipulators

The converse to the direct kinematics problem is the *inverse kinematics* problem, which involves finding the set(s) of joint variables that place the EE of a manipulator in a desired pose. The existence of a solution to this problem is dependent on the desired pose lying within the workspace of the manipulator (Section 2.2.5). Depending on the configuration of the manipulator, it is possible that more than one set of joint variables achieves the desired EE pose. The complete solution to the inverse kinematic problem provides all possible sets of joint variables that place the EE of a manipulator in a desired pose. Historically there are many methods for solving this problem utilizing different techniques including both numerical and algebraic methods. Many of the methods focus on a specific type of serial manipulator, such as R-chains with intersecting joint axes.

Of particular interest are 6R-manipulators because of their relative simplicity while maintaining, in general (but not always), 6DOF and a large reachable workspace. Such manipulators are commonly used for industrial applications and have therefore been the focus of study for many researchers. Some examples of applying inverse kinematics methods to industrial 6R-manipulators include Chen and Parker [36] who use a numerical approach to the inverse kinematics to aid in the calibration of a PUMA 560 industrial 6R robotic manipulator; Lloyd and Hayward [37] use symbolic algebra to set up solutions for special configurations of 6R industrial robots; Manseur and Doty [38] present algorithms to improve the efficiency of the solution to the inverse kinematics problem for industrial applications of 6R-manipulators; Pashkevich [39] implements an algorithm for the inverse kinematics of industrial manipulators with offset wrists; and Chapelle and Bidaud [40] use analytical methods on kinematic models of PUMA 560 and GMF Arc Mate industrial

6R-manipulators.

Overview of Some Methods of Solving the Inverse Kinematics Problem

The inverse kinematics problem is well known and because of the usefulness of 6R-manipulators in industry there has been extensive research in this area. It is not feasible to explore all of the methods and publications that exist, but it is important to look at some major milestones and well known techniques. Using the results of the direct kinematics as presented in Section 2.2.3, evaluating Equation (2.19) yields 12 equations in six unknown joint variables. Many of the methods aim to reduce the number of equations or determine the exact number of solutions. This section gives an overview of major milestones in solving the inverse kinematics problem. A detailed history may be found in [7].

In 1968 Pieper [41] explored 6DOF manipulators, focusing on those with three consecutive intersecting axes. His methods apply to many manipulators with R- and P-pairs and is often applied to many existing industrial robots which, because of the intersecting axes limitation, leads to many being wrist-partitioned. The method for applying Pieper's method to 6R-manipulators is provided in [9].

Roth *et al.* [42] in 1973 showed that there were at most 32 solutions to the problem. Duffy and Crane [43] in 1980 provided a method for obtaining a polynomial of degree 32, though some of the roots did not provide solutions to the inverse kinematics problem. In 1985 Tsai and Morgen [44] used homotopy continuation methods to solve the problem and obtained 16 solutions for a variety of manipulators, leading to the hypothesis that this was the maximum number of real solutions. The following year Primrose [45] proved the 16 solution hypothesis to be correct using projective geometry. Papers by Lee and Liang in 1987 [46] and 1988 [47] extended the work by Duffy to obtain a polynomial of degree 16 in the tangent of the half-angle of one of the joint variables.

In 1990 a paper by Raghavan and Roth [48] introduced an algorithm for a complete solution to the inverse kinematics problem for 6R-manipulators. Elimination methods are used on a set of nonlinear equations to obtain a polynomial of degree 16 which can be solved and then each solution back-substituted to obtain the 16 sets of joint angles. This

algorithm is the basis for the work of many other researchers. One example is Manocha and Canny [49] in 1992 where the efficiency of the Raghavan-Roth algorithm is improved using symbolic preprocessing and Eigenvalues. Another Eigenvalue technique was developed in 1993 by Kohli and Osvatic [50] who use the Eigenvalues of a 16×16 matrix that represent the equations that are linear in one variable; a similar algorithm was introduced in the same year by Ghazvini [51] in which he used the fact that the equations of Raghavan and Roth are linear in the tangent of the half angle of the third joint variable to set up a generalized Eigenproblem.

The algorithms based on the method of Raghavan and Roth are the most well known though many other authors have provided their input on the inverse kinematics problem. In 2006 a new algorithm for the inverse kinematics of 6R-manipulators that utilizes the kinematic mapping of displacements and the constraint varieties of serial chains was presented by Pfurner in [7, 34, 35, 52, 53]. This new algorithm is the basis for the method of solving the inverse kinematics problem used in this dissertation. The kinematic mapping technique for the inverse kinematics of general 6R-chains is discussed in Section 2.4.

2.2.5 Manipulator Workspace Analysis

In its simplest form, the *workspace* of a manipulator is the volume of space that can be reached by a reference point on the EE of a manipulator [9]. The definition of a workspace can be further refined and most references focus on two definitions in particular, the reachable and dextrous workspaces. The *reachable workspace* is the volume of space in which the EE can be positioned in at least one orientation and the *dextrous workspace* is the volume of space in which the EE can be positioned in all orientations, if such a space exists for a particular manipulator.

Theoretically the reachable workspace is obtained by identifying the position of the origin of the EE reference frame for every combination of the n joint variables, though doing so directly is impractical and comparing the resulting workspaces of different manipulators is difficult.

The dextrous workspace, if it exists for a particular manipulator, is a subspace of the

reachable workspace. At each point in the dextrous workspace the manipulator can be arbitrarily oriented (*i.e.* in three-dimensional Euclidean space the EE can be oriented at any combination of roll, pitch and yaw angles). An example of a device with a dexterous workspace that is as large as its reachable workspace is the Atlas motion platform [54]. A manipulator with less than six DOF cannot obtain general poses in three-dimensional Euclidean space [9]. Manipulators may posses a dextrous workspace based on the types of kinematic pairs used and their configuration, however due to realistic limitations to the motion such as joint limits (most revolute joints cannot rotate a full 360°) or self-collisions (components of the manipulator collide with one another) the dextrous workspace is much smaller than suggested theoretically.

While the reachable and dextrous workspaces are the most common in literature Castelli, Ottaviano and Ceccarelli [55] have compiled a list of additional workspaces that may be considered. The list is based on types of workspaces defined by Lee and Yang [56] and Merlet [24]. In addition to the reachable and dexterous workspaces they list:

total orientation workspace the EE positions that can be reached by a manipulator with a specified range of orientations;

orientation workspace the orientations that can be achieved when the manipulator EE is in a particular position; and

constant orientation workspace the EE positions that can be reached with one specified orientation.

These additional workspace classifications are not addressed further in this dissertation, but are presented because they may be used for future work. The solvability of the inverse kinematics problem is dependent on the desired EE position lying in the reachable workspace of the manipulator and the desired orientation being in the orientation workspace at that point.

The type of workspace most relevant to this dissertation is the reachable workspace. The reachable workspace is defined by Choset [57] as the set of points in the ambient space

around the manipulator that can be reached by a specific point or EE of a kinematic chain. In literature the analysis of the reachable workspace of a manipulator is approached using either numeric or algebraic techniques with the former being much more abundant and the later being either focused on very specific manipulators (usually short R-chains) or addressed in a general manner very similar to techniques used to find the direct kinematics of a manipulator. The numeric analysis appears to begin with Roth in 1975 [58] where he examines the relationship between the kinematic geometry of a manipulator and its performance. Kumar and Waldron in 1980 [59] and 1981 [60] present a numeric algorithm for tracing the boundary surfaces of a mechanism's workspace.

In 1983 Yang and Lee published two companion articles [56, 61] that discuss methods for obtaining and evaluating the workspace of a manipulator. The first paper, [61], suggests a method for analytically determining the workspace of a manipulator which, as presented in the paper, is essentially the same as obtaining the direct kinematic equations. The paper then continues by discussing how to find holes and voids in the reachable workspace of R-chains by starting at the joint closest to the EE, looking at the workspace and then moving to the next joint and examining how the cross-section of the first workspace interacts with the joint axis to determine if any holes or voids are created. The process is then repeated by examining progressively larger workspace cross-sections with each successive joint until the base is reached. This technique can be used for R-chains but is not general enough to be easily applied to other kinematic pairs, such as those explored in this dissertation. The companion paper, [56], presents an algorithm for finding the workspace boundaries, uses the cross-section of the workspace to determine the volume of the workspace and proposes performance indices for manipulators. The algorithm for the boundary determination steps through all achievable joint angle combinations to find a convenient cross-section of the workspace and utilizes the axial symmetry when rotating an R-pair to determine the reachable workspace boundaries and its volume. The proposed performance indices, the volume index (VI), relates the volume of the manipulator workspace to the total length of the manipulator. Similar geometric techniques are employed in [62–65] to determine the dextrous workspace of parallel manipulators, utilizing the axial symmetry of R-pairs to

transform the workspace of shorter chains.

In 1983 Tsai and Soni [66] recognized that as the number of joints in an R-chain increases it becomes increasingly impractical to describe the boundaries of the workspace by explicit equations. The authors instead describe how to find the contour of the workspace on an arbitrary plane and suggest using multiple planes to gain an understanding of the workspace as a whole. In 1986 Kumar and Patel [67] addressed issues with graphically representing and manipulating the workspace of a manipulator on a computer display. The technique involves representing the workspace as a series of points or pixels. A similar technique is employed by Castelli, Ottaviano and Ceccarelli in 2008 [55] that divides the ambient space around a manipulator into pixels and steps through the available joint angles (similar to [56], but not limited to a cross-section) to determine which pixels can be reached by the manipulator. The algorithm of Castelli *et al.* is summarized in Section 2.2.5 as similar concepts are used in the original workspace algorithm presented in this dissertation.

Other investigators, such as Ceccarelli in 1989 [68] and 1996 [69], have taken an algebraic approach to the determination of the reachable workspace of a manipulator, however these papers focus on R-chains. These techniques utilize the axial symmetry of the workspaces of R-chains to facilitate the derivation of an analytic description of the workspace. These techniques cannot be easily adapted to chains constructed using other kinematic pairs as the same axial symmetry does not necessarily exist in such manipulators.

Castelli's Algorithm for Obtaining the Reachable Workspace

Castelli *et al.* [55] have presented an algorithm for obtaining the reachable workspace of a manipulator. The algorithm involves discretizing the ambient space around a manipulator into three-dimensional elements called pixels and incrementing each joint angle in sequence by a small amount to determine which pixels are reached by the EE. The following outlines the algorithm step-by-step.

1. Determine the extreme values in each of the X, Y, and Z axes that can be reached by the EE of the manipulator.

2. Select the desired resolution in each axis (the dimensions of each pixel), ΔX, ΔY, and ΔZ.

3. Define two three-dimensional arrays, $\mathbf{P}_{ijk}$ and $\mathbf{D}_{ijk}$, that each represent the discretized ambient space, that is each of the elements in the arrays represents one pixel of the ambient space. The $\mathbf{P}_{ijk}$ array is a binary array whose elements are set equal to one if the EE of the manipulator can be placed within that pixel and zero if it cannot. The $\mathbf{D}_{ijk}$ array counts the number of times a particular pixel is reached by the EE as each joint of the manipulator is incremented. The elements of both arrays are initially set to zero.

4. Starting with a predetermined set of joint variables, sequentially step each joint variable by a small amount and complete the following steps for every possible combination of joint variables. The step size must be determined for each manipulator based on its design parameters and the ambient space pixel size (based on the required accuracy and time/computing power constraints).

    4.1 Determine, using the direct kinematics, the position of the EE in the ambient space.

    4.2 Determine which pixel the EE is in (*i.e.* determine the values of i, j, k in the subscript of $\mathbf{P}_{ijk}$ and $\mathbf{D}_{ijk}$).

    4.3 Set the element of $\mathbf{P}_{ijk}$ corresponding to the reached pixel equal to one, if it is not already equal to one, to indicate that the pixel corresponding to that matrix element has been reached.

    4.4 Increment the element of $\mathbf{D}_{ijk}$ corresponding to the reached pixel by one to count the number of times that pixel is reached.

The discretization of the ambient space and the determination of reached pixels are important to the original workspace work presented in this dissertation.

2.3 Constraint Varieties

Constraint varieties are used in this dissertation to describe the displacements, represented by points in P^7, that a mechanism bound by mechanical constraints can achieve. The EE of a mechanism is constrained to move within its reachable workspace and in the kinematic image space the displacement from the base frame to any unique EE pose is represented by a point. If, as shown in Section 2.1.6, every point on S_6^2 excluding the exceptional generator maps to a displacement, then the set of displacements of a constrained mechanism is a subset of all points on S_6^2. Then, as noted by Hayes *et al.* [8], because a continuous motion is a continuous set of displacements, a constrained motion will map to a continuous set of points on S_6^2 in P^7. Depending on the nature of the mechanical constraints the set of points in P^7 obtainable by a mechanism may be represented by a line, surface or higher dimensional algebraic variety.

A definition of varieties is useful at this time, but first the nomenclature for polynomials must be defined. The set of all polynomials in n variables is denoted by $k[x_1, \ldots, x_n]$, such that k is any field (for example real numbers, $\mathbb{R}$, natural numbers, $\mathbb{N}$, or complex numbers, $\mathbb{C}$) and a polynomial is a finite sum of terms having the form $ax_1^{\beta_1} \cdots x_n^{\beta_n}$ with $\beta_i \in \mathbb{N}, i = 1, \ldots, n$ and $a \in k$. For a finite set of polynomials $\{f_1, f_2, \ldots, f_s\} \in k[x_1, \ldots, x_n]$, the set of all solutions to the system $f_1 = 0, f_2 = 0, \ldots, f_s = 0$ is called the variety defined by $\{f_1, f_2, \ldots, f_s\}$, and is represented by $V(f_1, f_2, \ldots, f_s)$. This leads to the term constraint variety. In this dissertation constraint varieties will be given as the intersection of a set of polynomials and the intersections occur at the point or set of points in P^7 where all polynomials in the set are identical to zero. That is, the variety defined by the set of polynomials that result from the mechanical constraints.

The number of polynomials in the set depends on the number of constraints. In P^7 any point is represented by seven homogeneous parameters as shown in Sections 2.1.4 and 2.1.6 meaning that seven parameters must be defined to define a displacement. If a single constraint is provided, defined by a joint variable, a variable joint angle for an example, with the remaining joint parameters defined constants, then the constraint variety is defined by

six polynomials (S_6^2 and five others.) In some cases, such is in Hayes *et al.* [8], Brunnthaler [14] or Pfurner [7] the constraint varieties may be defined by the intersection of some geometric entity with S_6^2 but for the purposes of this thesis the constraint variety is given as the intersection of a set of polynomials.

A constraint variety may be visualized as a surface in the kinematic mapping image space. The points of the surface represent all possible displacements of the end effector reference frame given the constraints imposed by the kinematic chain. For example, for a planar 2R chain the constraint variety is a hyperboloid of one sheet in a three-dimensional subspace of the kinematic mapping image space, as illustrated in Figure 2.6 [8].

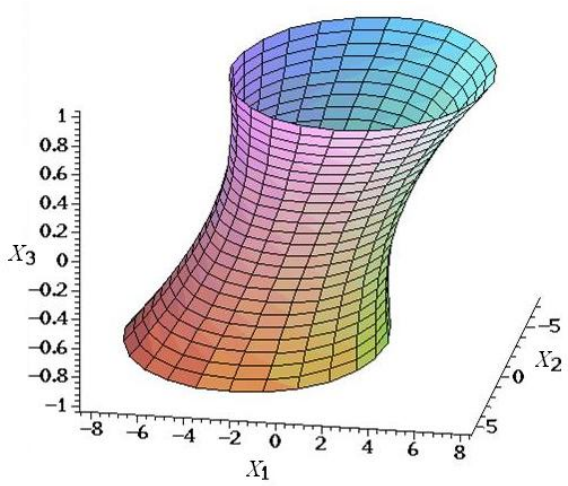

Figure 2.6: Projection of the constraint of an arbitrary planar 2R-chain to a three-dimensional subspace of the kinematic mapping image space [8].

2.3.1 A New Method for Obtaining Constraint Varieties of Serial Chains

Obtaining the constraint variety of serial kinematic chains is a critical element of Pfurner's inverse kinematics algorithm for 6R-chains (Section 2.4). The adaptation of Pfurner's algorithm to A-chains [1, 70] requires the determination of the constraint variety of A-chains, and more specifically 2A-chains. The derivation of the canonical 2A-chain constraint variety in the work presented in [1] proved to be very challenging using elimination methods

and with the updates to the DH-parameters of A-chains to be presented in this dissertation it is required that the constraint varieties be re-evaluated. Since the publication of the original A-chain inverse kinematics algorithm [1] a new approach to obtaining a useful representation of the constraint variety has been developed by Walter and Husty [71]. This section describes the new method, called the implicitization algorithm, which is applied to 2A-chains in Section 3.1.4. Applications of the implicitization algorithm for obtaining the constraint varieties of various manipulators are presented in [72–75].

The Algorithm for the Implicitization of Kinematic Constraint Equations

The purpose of the implicitization algorithm is to take the parametric representation of the constraint variety in the Study space (the Study parameters are represented by functions of the n joint variables) and convert them to implicit polynomials in terms of the Study parameters.

The algorithm, taken from [71], requires the parametric representation of the constraint variety in the kinematic image space. This is obtained by finding the matrix form of the direct kinematic equations using Equation (2.19) and obtaining the Study parameters via Equations (2.14) and (2.15). The result is the eight Study parameters being represented by parametric equations of the form

$$\begin{aligned} x_0 &= f_0(t_1, \ldots, t_n) \\ x_1 &= f_1(t_1, \ldots, t_n) \\ &\vdots \\ y_3 &= f_7(t_1, \ldots, t_n), \end{aligned} \tag{2.22}$$

where the t_i terms are the joint variables. The Study parameters are homogeneous and therefore any non-zero factors common to all of the equations can be eliminated to simplify the equations as much as possible.

It is noted in Section 2.3 that for most serial manipulators the number of implicit equations, m, required to define the variety $\mathcal{V} \in P^7$ which contains the Study parameters of

all displacements achievable by the manipulator is $m = 6 - n$ and one of those equations is always the Study quadric, S_6^2, given by Equation (2.12). The intent of this algorithm is to find the remaining $m-1$ independent implicit equations whose intersection with S_6^2 defines the constraint variety. These equations are homogeneous polynomials in terms of the Study parameters $x_0, x_1, x_2, x_3, y_0, y_1, y_2, y_3$. Each equation is equal to zero for all values of the joint parameters t_i.

To find these polynomials Walter and Husty propose using an initial guess, or *ansatz*, of a homogeneous polynomial of degree n in terms of the Study parameters, starting with a linear polynomial ($n = 1$) and increasing the degree as necessary until $m-1$ independent equations are obtained. A general linear polynomial takes the form

$$f = C_1x_0 + C_2x_1 + C_3x_2 + C_4x_3 + C_5y_0 + C_6y_1 + C_7y_2 + C_8y_3 = 0, \tag{2.23}$$

where the coefficients C_i are currently unknown. For the linear polynomial *ansatz* there are eight unknown coefficients while for polynomials of higher degree n there are $n + 7$ choose n, *i.e.* $\binom{n+7}{n}$, unknown coefficients. Substitution of the parametric representation of the constraint variety, Equation (2.22), into Equation (2.23) yields a polynomial $f(t_1, \ldots, t_n)$ in terms of the joint variables, t_i, with the coefficients C_i. Collecting and extracting the coefficients of the powerproducts of the t_i terms yields a set of linear equations in terms of the unknown C_i which must all equal zero to satisfy $f(t_1, \ldots, t_n) = 0$. Depending on the design of the chain there may be more equations than unknowns, suggesting that there is no solution, however some of the equations may be dependant. All independent solutions to the system are part of the variety $\mathcal{V}$ whose intersection defines the constraint variety. If no solution other than the trivial solution (the null vector) can be found for the system then the degree of the *ansatz* polynomial is increased to $n = 2$ and the determination of the coefficients is repeated for the 36 coefficients of the general quadratic polynomial. It should be noted that the Study quadric should be one of the solutions obtained at this stage. If the procedure thus far has failed to produced m independent equations (including S_6^2) the degree of the *ansatz* polynomial is increased and the procedure for obtaining the coefficients

is repeated until all of the equations are found. As each new polynomial is obtained it is important to verify that it is independent of the previously obtained polynomials, including S_6^2. To do this Walter and Husty suggest reducing each new polynomial with respect to a Gröbner basis [76–78] generated from all previously obtained polynomials.

The intersection of the m polynomials obtained by the algorithm is the implicit representation of the constraint variety for the given kinematic chain. It is noted by Walter and Husty that this algorithm, in some cases, may produce a constraint variety that is larger than that obtained by the actual kinematic chain, though the true constraint variety is always contained within the resulting implicit representation.

2.4 The Inverse Kinematics of General 6R-Chains Using Kinematic Mapping

The method of solving the inverse kinematics problem for 6R-manipulators using kinematic mapping was first introduced by Husty, Pfurner and Schröcker [34] and was further generalized by Pfurner [7]. This section provides an overview of these techniques focusing on those that are relevant to the work presented in this dissertation. The adaptation and application of this inverse kinematics algorithm for A-chains is introduced in Section 2.5.6 and further developed in Chapter 3.

Consider a prescribed EE target pose, Σ_{target}, for a known 6R-manipulator. It is desired to obtain all sets of joint parameters required to make the EE frame, Σ_{EE}, coincident with Σ_{target}. This is illustrated for a general 6R-manipulator in Figure 2.7. The manipulator is theoretically "split" into two 3R-chains which will be called the left and right chains. The split is made where the third link meets the fourth joint. The left chain maintains the original base frame Σ_0, called Σ_{0L} when referring to the left chain, and the new EE frame of the left chain, Σ_L, is affixed at the break in the original chain. The left chain contains Joints 1, 2 and 3 from the original 6R-chain. The new "base" of the right chain, Σ_{0R}, is coincident with Σ_{EE} in the target pose and the EE of the right chain, Σ_R is coincident with Σ_L before the chain is broken. That is, when Σ_L and Σ_R are coincident, the original

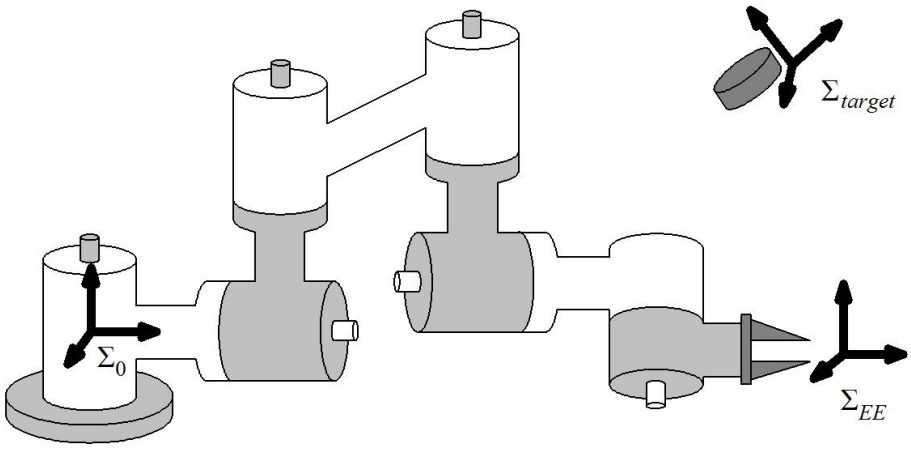

Figure 2.7: Illustration of inverse kinematics problem for a general 6R-manipulator.

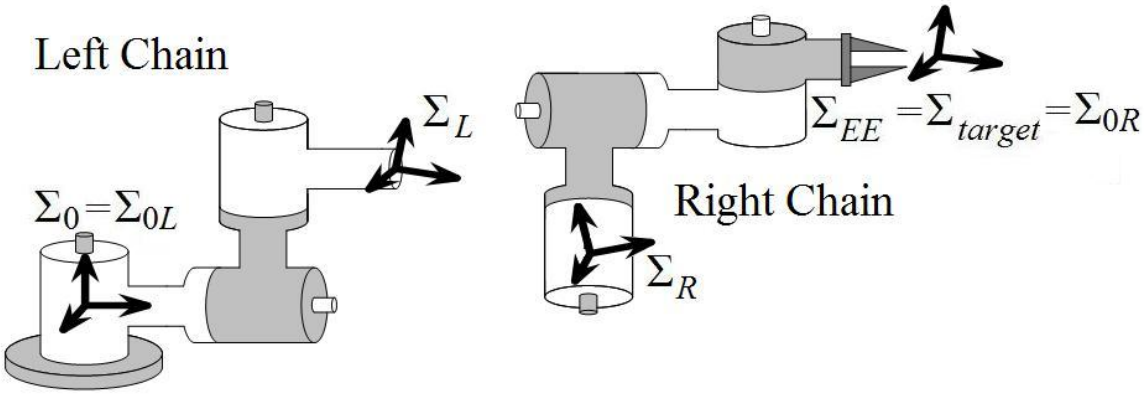

Figure 2.8: Illustration of left and right 3R-chains with reference frames.

6R-chain is obtained. The right chain contains Joints 4, 5 and 6 from the original 6R-chain. From Σ_{0R} to Σ_R the order of the joints is Joint 6, 5, then 4. Figure 2.8 illustrates the split into the two 3R-chains and placement of reference frames for the left and right chains.

The direct kinematic equations for the left and right chains are found using Equation (2.19). The constraint variety is then determined for each chain, providing the set of all points in P^7 that represent the manifold of all possible displacements from the base frame to the EE frame achievable by the 3R-manipulator. If the target EE pose is within the workspace of the 6R-manipulator then the constraint varieties of the left and right chains will intersect in at least one real point in P^7. The set of all intersection points provides all

the real sets of joint angles that keep Σ_L and Σ_R, as well as Σ_{EE} and Σ_{target} coincident and the 6R-chain unbroken.

Theoretically this technique should apply to all six-jointed manipulators, but requires the determination of the constraint varieties for each of the left and right chains, which varies for different combinations of joint types. In [7] Pfurner provided the derivation of the constraint varieties for 3R-chains and uses them to describe an algorithm to obtain the inverse kinematic solution to general 6R-manipulators.

Pfurner shows that the constraint variety of the 3R-chain is a well known geometric entity called a Segre manifold, which consists of four hyperplanes in the kinematic image space. This observation allows for simplification of the inverse kinematics algorithm for 6R-manipulators, but has no application to this dissertation and will not be discussed further, except to say that the intersection of the Segre manifolds for the left and right chains with S_6^2 results in 16 intersection points. Some of these intersection points may be real, representing physically-obtainable solutions to the inverse kinematics problem (ignoring joint limits and self-collisions); and some may be complex conjugate, which have no physical meaning but still mathematically result in Σ_L and Σ_R being coincident. But, there are at most 16 real intersection points, which correspond to the fact that there are at most 16 solutions to the inverse kinematics problem (see Section 2.2.4). More information about Segre manifolds and the intersection of these special constraint varieties to solve the inverse kinematics problem for general 6R-chains is to be found in [7].

2.5 The Algebraic Screw Pair

The concept of the Algebraic Screw pair, or A-pair, was introduced in [1] to take advantage of the undesirable, yet well-defined self-motions of a special six-legged parallel manipulator called the Griffis-Duffy Platform (GDP). This section describes GDPs in general, emphasizing the characteristics and the special configuration that is relevant to this dissertation. The self-motion phenomenon associated with the relevant configuration is then discussed,

leading to how the GDP is used as a kinematic pair in a serial kinematic chain. The kinematic chain constructed using the special configuration of GDP is called an A-pair and kinematic chains constructed using serially-connected A-pairs are called A-chains. This section concludes with an introduction to the kinematics of A-chains based on the work presented in [1].

2.5.1 Overview of Griffis-Duffy Platforms

The GDP is a special configuration of the six-legged Gough-Stewart platform patented by Griffis and Duffy in 1993 [79]. The GDP is characterized by a planar fixed base and planar moving platform each connected by six legs with six specially placed spherical joint anchor points on each of the moving and relatively fixed platforms. The anchor points lie on the perimeter of a triangle on each platform. Six of the anchor points are located one on each of the vertices of the two triangles and the remaining six anchor points are located one on each edge of the triangles such that each leg has one anchor point on the fixed base and one anchor point on the moving platform.

The patent by Griffis and Duffy proposes controlling the pose of the platform by actively changing the length of each leg using linear actuators. As is shown in the next section, controlling the leg lengths may not provide for full control of the EE pose for all GDPs because many sets of anchor point locations lead to the phenomenon of self-motion, which means there can be motion between the fixed and moving platforms that is not controllable even when the leg lengths are held fixed. It is these constant leg length self-motions which are exploited by A-pairs.

There are many different GDP architecture configurations that satisfy the definition of a GDP. One additional common condition, though not necessary, is that each edge connection be on the midpoints of the line segments between vertices of the triangle. With this condition there are still many possible configurations, but two important groups are vertex-to-vertex and midline-to-vertex. In the vertex-to-vertex configuration, shown in Figure 2.9, a leg with a vertex anchor point on the base has a vertex anchor point on the platform, with the order of the leg end points around the perimeters of the triangles being the same on both the fixed

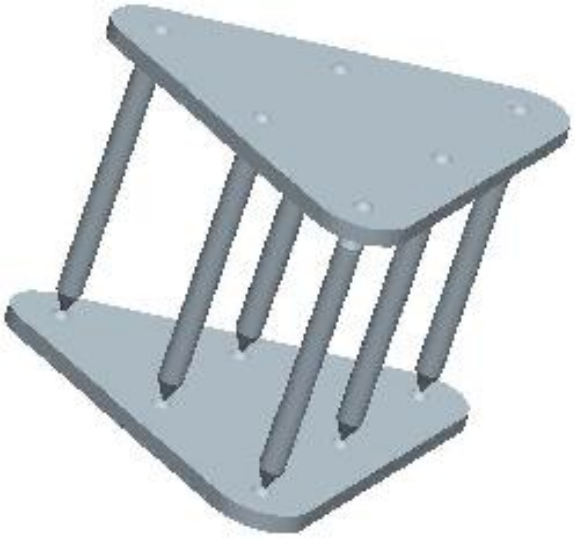

Figure 2.9: Example of the vertex-to-vertex configuration of GDP.

base and moving platform. The midline anchor points are between the same legs on both the fixed base and moving platform. The midline-to-vertex configuration, shown in Figure 2.10, connects a vertex anchor point on the fixed base with a midline anchor point on the moving platform and vice versa, maintaining the same order of legs around the perimeter

Figure 2.10: Example of the midline-to-vertex configuration of GDP.

of the fixed base and moving platform.

It is the midline-to-vertex configuration that is used to create the A-pair, with the added conditions that the fixed base and moving platform anchor points form congruent equilateral triangles. This configuration is used because the self-motions of the platform are simple and the moving platform remains parallel to the fixed base throughout the self-motions when the legs are of equal length.

2.5.2 Self-motions of GDPs

In [80], Husty and Karger examine self-motions of GDPs. The term self-motion refers to the ability of the EE of a mechanism to move without actuator input. In the GDP this means that the moving platform can move relative to the fixed base without changing the leg lengths. Husty and Karger's procedure for obtaining the self-motions of a GDP is summarized here. Discussions on the self-motions of all Gough-Stewart platforms are provided in [81, 82].

Husty shows in [27] that a set of seven quadratic equations governs the direct kinematics for all Gough-Stewart platforms. One of the equations is S_6^2, Equation (2.12), and the remaining six are of the form

$$\begin{aligned} h_i = \; & R_i(x_0^2+x_1^2+x_2^2+x_3^2)+4(y_0^2+y_1^2+y_2^2+y_3^2)-2x_0^2(Aa+Bb+Cc)+ \\ & 2x_1^2(-Aa+Bb+Cc)+2x_2^2(Aa-Bb-Cc)+2x_3^2(Aa+Bb+Cc)+ \\ & 2x_3^2(Aa+bb-Cc)+4(x_0x_1(Bc-Cb)+x_0x_2(Ca-Ac)+x_0x_3(Ab-Ba)- \\ & x_1x_2(Ab+Ba)-x_1x_3(Ac+Ca)-x_2x_3(Bc+Cb)+(x_0y_1-y_0x_1)(A-a)+ \\ & (x_0y_2-y_0x_2)(B-b)+(x_0y_3-y_0x_3)(C-c)+(x_1y_2-y_1x_2)(C-c)- \\ & (x_1y_3-y_1x_3)(B-b)+(x_2y_3-y_2x_3)(A-a))=0, \end{aligned} \tag{2.24}$$

with $i = 1, \ldots, 6$. The terms (a, b, c) are the coordinates of the anchor point for leg i moving with the moving platform of the manipulator in a reference frame fixed to the moving platform, (A, B, C) are the coordinates of the corresponding anchor point for leg i on the fixed base of the manipulator in a reference frame affixed to the fixed base, and

$R_i = A^2 + B^2 + C^2 + a^2 + b^2 + c^2 + r_i^2$, with r_i, $i = 1, \ldots, 6$ being the joint parameter or length of leg i. The variables x_j and y_j, $j \in \{0, \ldots 3\}$ are the Study parameters. It is convenient to assign the base and platform reference frames such that the equations are as simple as possible, which can be done without loss in generality.

For general Gough-Stewart type manipulators the solution to the set of seven quadratic equations is a set of discrete points on S_6^2. There are however platform configurations including, as Husty and Karger show, many GDP configurations where the solution variety is a curve or surface on S_6^2, meaning that the platform can move independent of the joint parameters, which are assigned fixed values for a particular pose.

In [80] Husty and Karger use the midline-to-vertex configuration with the coordinates given in Table 2.1. The coordinate systems are shown in Figure 2.11, wherein the variables

Table 2.1: Coordinates of anchor points for special midline-to-vertex configuration.

	A	B	C		a	b	c
P_1	$-p$	0	0	p_1	$\frac{q}{2}$	$\frac{q\sqrt{3}}{2}$	0
P_2	0	0	0	p_2	0	$q\sqrt{3}$	0
P_3	p	0	0	p_3	$-\frac{q}{2}$	$\frac{q\sqrt{3}}{2}$	0
P_4	$\frac{p}{2}$	$\frac{p\sqrt{3}}{2}$	0	p_4	$-q$	0	0
P_5	0	$p\sqrt{3}$	0	p_5	0	0	0
P_6	$-\frac{p}{2}$	$\frac{p\sqrt{3}}{2}$	0	p_6	q	0	0

p and q are defined. With these coordinates, the six constraint equations $h_i, i = 1, \ldots, 6$ can be constructed by substituting the values from Table 2.1 into Equation (2.24) for each leg. The seventh constraint equation is the Study quadric S_6^2. A set of five difference equations, $U_i, i = 1, \ldots, 5$, that are linear in the terms y_0, y_1, y_2 and y_3 is constructed where $U_1 = h_1 - h_3$, $U_2 = h_2 - h_5$, $U_3 = h_4 - h_6$, $U_4 = h_1 - h_2$ and $U_5 = h_1 - h_4$. The motion of interest is where all leg anchor points on the platform move on a spherical path. This is called Borel-Bricard motion and is discussed by Bottema and Roth [12]. Such motions lead to the situation where $x_1 = x_2 = 0$. Three of the difference equations are used to construct a system that can be solved for four of the y_i terms. The remaining Study parameters can, without loss in generality, be set such that $x_0 = \cos(\theta)$ and $x_3 = \sin(\theta)$ to yield the

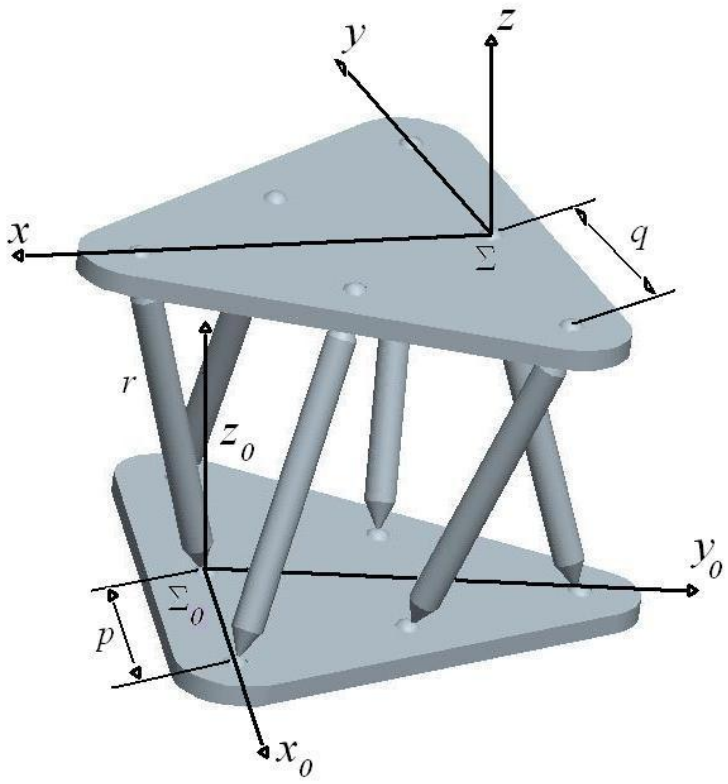

Figure 2.11: Midline-to-vertex GDP with coordinate systems and variables defined.

transformation matrix

$$\mathbf{Q} = \begin{bmatrix} 1 & 0 & 0 & 0 \\ \frac{2}{3}\rho\sqrt{3}\sin(\theta)\cos(\theta) & \cos(2\theta) & -\sin(2\theta) & 0 \\ \frac{2}{3}\rho\sqrt{3}\sin^2(\theta) & \sin(2\theta) & \cos(2\theta) & 0 \\ \rho\cos(\theta) & 0 & 0 & 1 \end{bmatrix}, \tag{2.25}$$

where ρ is a function of the leg length r, and θ is the rotation of the moving platform frame relative to the fixed base frame about an axis perpendicular to both triangles. The transformation from the platform coordinate system with position vectors $\mathbf{x}$ to the base coordinate system with position vectors $\mathbf{x}_0$ is given by

$$\mathbf{x}_0 = \mathbf{Q}\mathbf{x}. \tag{2.26}$$

Of interest in this dissertation is the change in distance between the base and platform. From **Q** it can be shown by a linear translation that a point at the geometric centre of the platform triangle moves on a line perpendicular to the plane of the platform, where the motion is characterized by

$$\mathbf{Q} = \begin{bmatrix} 1 & 0 & 0 & 0 \\ 0 & \cos(2\theta) & -\sin(2\theta) & 0 \\ 0 & \sin(2\theta) & \cos(2\theta) & 0 \\ \rho\cos(\theta) & 0 & 0 & 1 \end{bmatrix}. \tag{2.27}$$

When $\theta = 0$ the distance between the base and platform is ρ.

An alternative zero position, that differs from the one presented by Husty and Karger, is the theoretical position where the fixed base and moving platform are coincident. In this position the rotation angle between the fixed base and moving platform is zero ($\theta = 0$). This position is not obtainable in reality as it requires that the rigid fixed base and moving platform of the GDP pass through one another, but it is conceptually useful for analysis. The variable θ refers to the rotation angle about the shared Z-axis of the frame affixed to the moving platform relative to the frame affixed after the new zero position is established. After shifting the zero position of the platform and repositioning the moving platform coordinate system such that it is coincident with the fixed base coordinate system in the new zero position, which can be done without loss in generality, the motion of the point at the geometric centre of the platform triangle is now given by

$$\mathbf{Q} = \begin{bmatrix} 1 & 0 & 0 & 0 \\ 0 & \cos(\theta) & -\sin(\theta) & 0 \\ 0 & \sin(\theta) & \cos(\theta) & 0 \\ \rho\sin\left(\frac{\theta}{2}\right) & 0 & 0 & 1 \end{bmatrix} \tag{2.28}$$

and the distance, d, between the fixed base and moving platform is sinusoidal, given by the

equation

$$d = \rho \sin\left(\frac{\theta}{2}\right), \tag{2.29}$$

where ρ is a function of the GDP geometry and its value is obtained in Section 3.1.

It is this well-defined one DOF self-motion that is utilized to construct the A-pair. Equation (2.29) describes the coupled translation and rotation that is utilized by the A-pair and requires an adaptation of serial manipulator kinematic and dynamic analysis.

2.5.3 The Griffis-Duffy Platform as a Kinematic Pair

The A-pair is based on the midline-to-vertex configuration of the GDP with congruent, equilateral base and platform triangles and all six legs being the same fixed length such that the path of any point on the platform undergoing a self-motion is the same as that described in Section 2.5.2. The fixed-length legs of the GDPs are passive such that the only relative motion between each fixed base and moving platform is due to the self-motion phenomenon. To simplify the computations the added constraint that the leg lengths, l, are equal to the height, h, of the congruent fixed base and moving platform triangles is used. Figure 2.12 shows the dimensions of the fixed base and moving platform triangles. The constraint $l = h$ is applied so that the entire range of self motions can be obtained without disassembling and reassembling the joint (if self-collisions of the legs, fixed base and moving

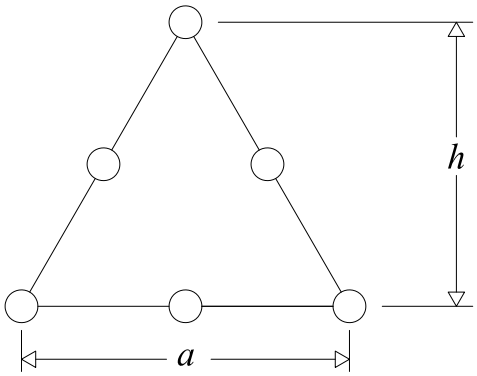

Figure 2.12: Illustration of the fixed base and moving platform triangle height, h, and side length, a.

platform are ignored). In the early analysis of A-pairs (such as [1, 83]) self-collisions were ignored, that is it was assumed that the individual solid bodies that make up the fixed base, moving platform and legs of the A-pair can pass through each other and occupy the same points in space at the same instant.

For the described configuration it is shown in Section 2.5.2 that self-motions result in a coupling of rotation and translation of the platform. The displacement of the platform along the joint axis mutually perpendicular to the fixed base and moving platform, d, is related to the rotation angle about the joint axis, θ, by the Equation (2.29). When replacing an R-pair in a chain with the special configuration of GDP the rotation axis of the joint is unchanged. The base of the GDP connects to one link, Link $i-1$, and the platform connects to the other link, Link i, such that if Link $i-1$ is fixed Link i will rotate and translate relative to Link $i-1$. The base link, or ground link, is called Link 0 (corresponding to $i=0$). The joint axis is the line mutually perpendicular to the fixed base and moving platform and that passes through the geometric centres of the fixed base and moving platform triangles.

The coupling of rotation and translation leads to a kinematic pair which is referred to as an A-pair [1]. In a traditional screw pair (or helical pair, H-pair) the relationship between the rotation and translation is linear, while in the case of the A-pair this relationship is an algebraic equation (after utilizing the tangent of the half-angle substitution to eliminate trigonometric functions). Replacing the R-pair joints of the 6R-manipulator with A-pair joints makes it a 6A-manipulator. There exist many possible A-pair configurations but for the purposes of this dissertation the term A-pair refers to the special configuration of GDP described previously.

When an R-pair in a serial chain is actuated the pose of the EE frame is displaced relative to the base frame by a rotation about the actuated joint's axis. For an A-pair the motion is different, the joint axis and magnitude of the rotation is unchanged, but there is now a translation parallel to the joint axis that is a sinusoidal function of the joint angle. The addition of coupled rotation and translation necessitates an examination of the kinematic and dynamic properties of serial chains constructed using A-pairs.

2.5.4 Preliminary Assignment of DH-Parameters to A-Chains

The coupling of translation and rotation in the A-pair requires some modifications to the descriptions of the DH-parameters introduced in Section 2.2.2. The assignment of DH-parameters to A-chains is initially addressed in [1] however, though not incorrect, the DH-parameters assigned in that work have proven to be insufficient to unambiguously describe the kinematic chain. This section shows how the A-chain DH-parameters are addressed in [1] and Section 3.1 provides the revisions to the assignment of DH-parameters that address the ambiguities and are original to this dissertation.

The assignment of reference frames and basic DH-parameters for nA-chains are similar to those for nR-chains presented in Section 2.2.2. The method begins with the same initial steps: each joint axis is determined and reference frames are affixed to each link based on the interactions of the adjacent joint axes.

The definitions of most of the DH-parameters remains unchanged from Section 2.2.2, such as the link length, a_i, link twist, α_i and joint angle, θ_i. In the A-chain the joint offset, d_i, is now variable, but coupled to θ_i. The d_i term is separated into two parts, one fixed and one variable. The variable component is known and is equal to $\rho \sin\left(\frac{\theta_i}{2}\right)$. The fixed component depends on the architecture of the manipulator and has the same definition as in Section 2.2.2 when Joint i is in the zero position. Figure 2.13 shows the application of the DH-parameters to a link connecting two A-pair joints.

This description, taken from [1], proves to be incomplete because of the coupling of translation and rotation. To provide for a completely unambiguous description it is necessary to clearly identify a certain position of the coupled translation and rotation, *i.e.* the home position. This additional parameter for A-pairs is part of the new work introduced in Section 3.1.

2.5.5 The Direct Kinematics of A-Chains

The method for obtaining the direct kinematic equations for nA-chains is very similar to the method presented in Section 2.2.3 for serial chains (the material presented in Section 2.2.3

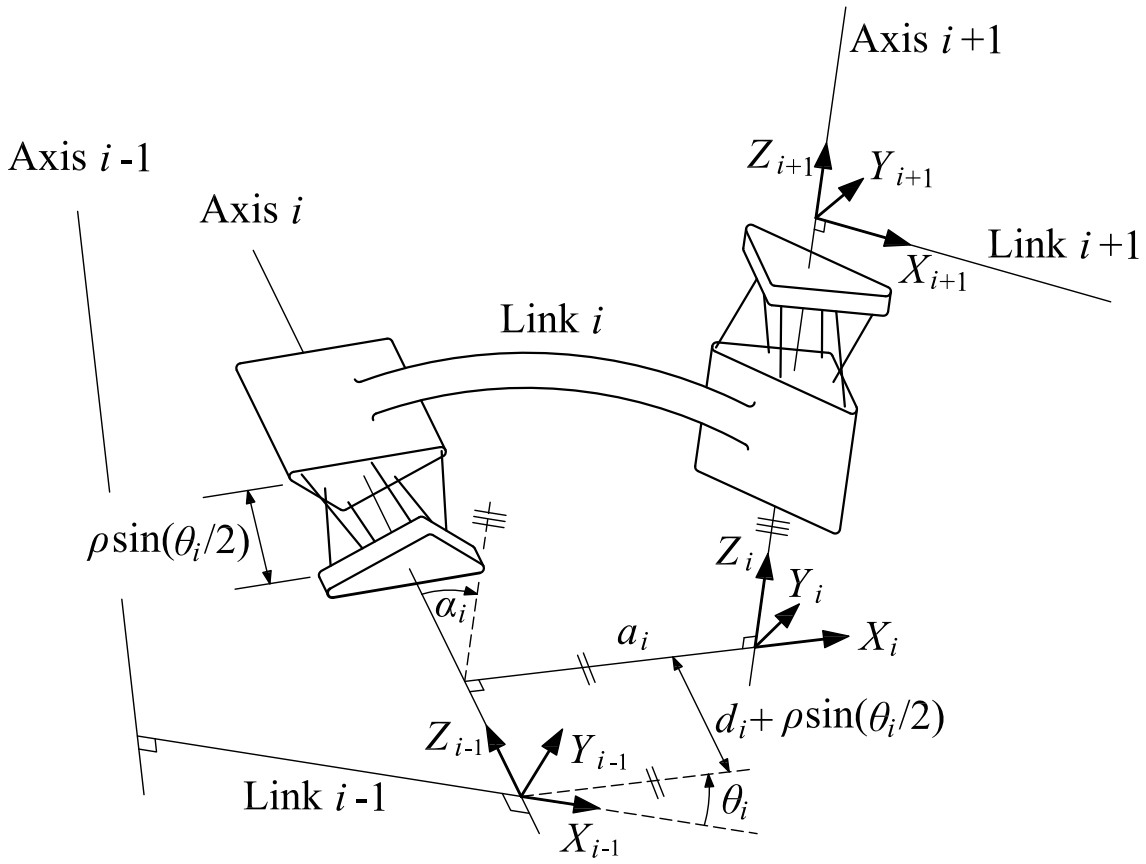

Figure 2.13: The DH-parameters applied to a link in an A-chain.

is intended for R-chains and/or P-chains). The direct kinematics of A-chains is introduced in [1] using the non-general A-chain DH-parameters of Section 2.5.4 and the assumption that the geometric constant in Equation (2.29) is equal to unity, $\rho = 1$. This assumption is shown to not be general in Section 3.1.2, regardless, the basic theory presented in [1] is correct and is revisited in this section to highlight the new work presented in Section 3.1.

The matrix form of the nA-chain direct kinematic equations is found by Equation (2.19) with updated $\mathbf{M}_i$ and $\mathbf{G}_i$ matrices, $i = 1 \ldots n$. The $\mathbf{G}_i$ matrix remains unchanged, though the definition of the d_i term is altered according to the discussion in Section 2.5.4. The matrix $\mathbf{M}_i$ is altered to account for the translation that is coupled with the joint rotation

and becomes

$$\mathbf{M}_i = \begin{bmatrix} 1 & 0 & 0 & 0 \\ 0 & \cos(\theta_i) & -\sin(\theta_i) & 0 \\ 0 & \sin(\theta_i) & \cos(\theta_i) & 0 \\ \rho\sin(\frac{\theta_i}{2}) & 0 & 0 & 1 \end{bmatrix}. \tag{2.30}$$

The $(4,1)$ element of $\mathbf{M}_i$ ($\rho\sin(\frac{\theta_i}{2})$) accounts for the translation of the reference frame along a line parallel to Axis i as Joint i rotates.

In [1] the matrix $\mathbf{M}_i$ is rewritten as

$$\mathbf{M}_{\mathrm{IK}_i} = \begin{bmatrix} 1 & 0 & 0 & 0 \\ 0 & \cos(2\phi_i) & -\sin(2\phi_i) & 0 \\ 0 & \sin(2\phi_i) & \cos(2\phi_i) & 0 \\ \rho\sin(\phi_i) & 0 & 0 & 1 \end{bmatrix}, \tag{2.31}$$

where $\phi_i = \frac{\theta}{2}$ is used to remove fractions. This is done to simplify the inverse kinematics algorithm but is less intuitive. In this dissertation the $\mathbf{M}_i$ matrix of Equation (2.30) is used for most of the analysis, while the $\mathbf{M}_{\mathrm{IK}_i}$ matrix of Equation (2.31) is used only for the inverse kinematics algorithm.

The $\mathbf{G}_i$ and $\mathbf{M}_i$ matrices have been assembled such that the $\mathbf{G}_i$ matrices contain the link and joint parameters that remain constant at all times and the $\mathbf{M}_i$ matrices contain the joint variables that change as the joint is actuated. It quickly becomes impractical to show the substitution of the new $\mathbf{M}_i$ and $\mathbf{G}_i$ matrices into Equation (2.19) as n increases for a completely general manipulator, but an examination of the structure of the matrices reveals the effect of introducing the coupled rotation and translation. Recalling that in the general transformation matrix $\mathbf{T}$ of Equation (2.4) the first column represents the position vector of the origin of the frame Σ' relative to Σ and the lower right 3×3 sub matrix represents the orientation of Σ' relative to Σ, the effect of the new joint can be seen. The $\sin(\theta_i/2)$ term, representing the translation part of the coupled joint motion, appears only in the first column of $\mathbf{M}_i$ and the first row of both $\mathbf{M}_i$ and $\mathbf{G}_i$ is always $\begin{bmatrix} 1 & 0 & 0 & 0 \end{bmatrix}$.

It can therefore be seen that any term in the first column will, after matrix multiplication, remain only in the first column of the product matrix. This means that if the R-pairs of an nR-manipulator are replaced with A-pairs and the home positions of all joints are identical the orientation of the EE reference frame for any set of joint variables would be unchanged while only the position in space would be different.

In a chain with mixed joint types, such as a combination of R-, P- and A-pairs, the appropriate $\mathbf{M}_i$ and $\mathbf{G}_i$ matrices are used for the different joints in the chain and substituted into Equation (2.19).

2.5.6 The Inverse Kinematics of A-chains

The inverse kinematics of A-chains was the main focus in [1]. That work examined the inverse kinematics problem as it relates to general 4A- and 6A-chains utilizing a modified method similar to that found in [7]. The method for solving the inverse kinematics problem for 4A-chains is complete (while it turns out that the constraint varieties obtained were not completely general, the foundation of the theory is sound) and has been generalised in [84]. The inverse kinematics problem for 6A-chains, as presented in [1], is presented in theory, but in practice numeric examples are incomplete because the number of terms in the polynomials representing the constraint varieties was prohibitively large such that it proved to be difficult to determine the intersections of the polynomials.

This section summarises the basic theory behind the inverse kinematics algorithm of 4A-chains as presented in [1]. Within the description of the algorithm reference is made to the constraint varieties of 2A-chains and the sets of five polynomials, whose intersection represents the constraint variety of a 2A-chain. At this time it is assumed that the polynomials used to represent the constraint varieties are known, even though their derivation has yet to be shown. The constraint varieties obtained in [1] were based on assumptions that have proven to be invalid and therefore are not provided here. The update to the constraint varieties of A-chains is presented in Section 3.1.4 and the inverse kinematics of 4A-chains is revisited in Section 3.8.

The Inverse Kinematics Algorithm for 4A-Chains

For a known 4A-manipulator the inverse kinematics problem involves obtaining all sets of four joint variables that put the EE in a target pose, Σ_{target}, described by matrix $\mathbf{EE}_T$, relative to the base frame. Real solutions exist only if the target pose is within the workspace of the manipulator. The inverse kinematics algorithm for 4A-chains is based on the 6R-chain inverse kinematics algorithm [7] that is summarised in Section 2.4.

The 4A-chain is theoretically broken at the end of the second link where it connects to the third joint. When the 4A-chain is unbroken Σ_L and Σ_R are coincident with reference frame Σ_2. This means Σ_L and Σ_R are affixed to the 'fixed' base of the GDP making up the third A-pair in the chain, when the 'fixed' base of Joint i is considered to be the part of the joint fixed to Link $i-1$. Figure 2.14 shows where the theoretical break is made in the 4A-chain to produce the base and EE 2A-chains.

The base 2A-chain contains Joint 1, Link 1, Joint 2, and Link 2 of the original 4A-chain.

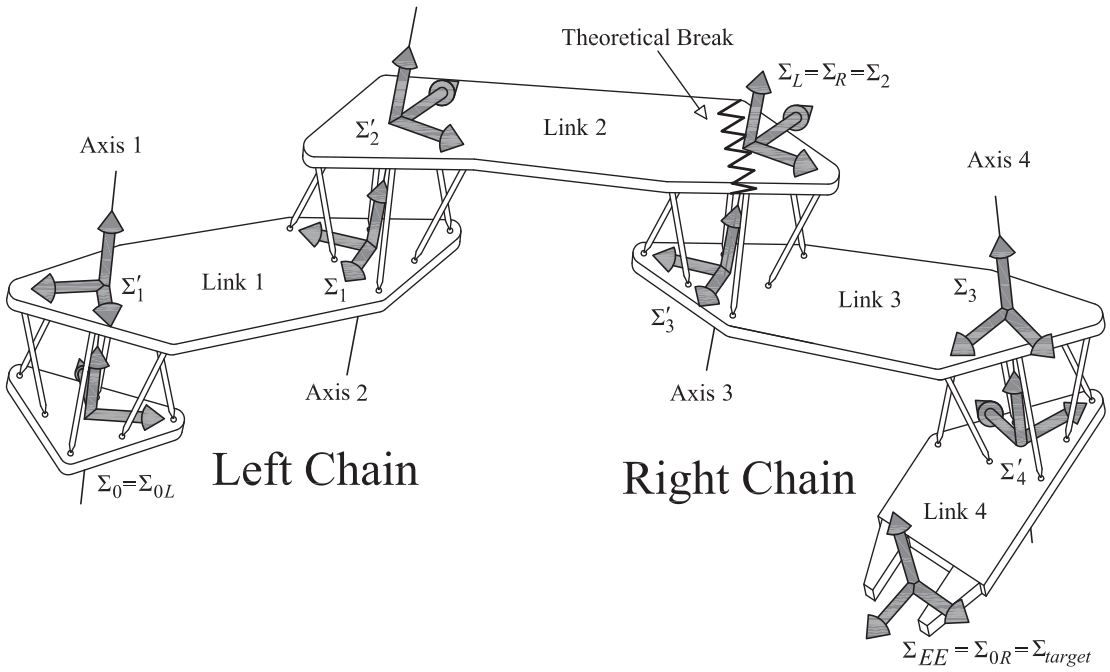

Figure 2.14: 4A-manipulator showing the theoretical break between the base and EE 2A-chains. In the figure the base 2A-chain is labelled as the Left Chain and the EE 2A-chain is labelled as the Right Chain, based on their respective positions in the figure.

The base reference frame of the base 2A-chain, Σ_{0L}, remains the same as the base reference frame of the original 4A-chain, represented by frame Σ_0. The EE 2A-chain contains Joint 3, Link 3, Joint 4, and Link 4 of the original 4A-chain. The base reference frame of the EE 2A-chain, Σ_{0R} is established as the 4A-manipulator EE in the target pose. Frame Σ_{0R} is known and fixed relative to Σ_0. The order of the joints in the EE 2A-chain is Joint 4 then Joint 3 of the original chain.

With the two 2A-chains defined it is now possible to obtain the constraint varieties of the base and EE 2A-chains by utilizing the constraint varieties of the 2A-chains (again, assume that the five polynomial equations, in terms of the eight Study parameters, whose intersection represents the constraint variety of the 2A-chains are known). The assumption that the base of the original 4R-chain was selected such that as many DH-parameters as possible are zero has been made, meaning that the base reference frame of the manipulator is coincident with the universal reference frame. If this is not the case additional transformations in the base reference frame are required. The procedure for this change is similar to that of the EE 2A-chain, and is not shown here to simplify the equations.

The constraint variety for the canonical 2A-chain includes only Joint 1, Link 1, and Joint 2, but Σ_L is located at the end of Link 2 in the left chain, meaning the effect of the second link must be added to the constraint variety. The addition of Link 2 and Σ_L is illustrated in Figure 2.15. Link 2 is represented by substitution of the link parameters into Equation (2.20) which, after tangent of the half-angle substitution (Section 2.11.1) is

$$\mathbf{G}_2 = \begin{bmatrix} 1 & 0 & 0 & 0 \\ a_2 & 1 & 0 & 0 \\ 0 & 0 & \dfrac{1-al_2^2}{1+al_2^2} & -\dfrac{2al_2^2}{1+al_2^2} \\ d_2 & 0 & \dfrac{2al_2^2}{1+al_2^2} & \dfrac{1-al_2^2}{1+al_2^2} \end{bmatrix}.$$

After obtaining the Study parameters of matrix $\mathbf{G}_2$ using Equations (2.14) and (2.15) and substituting them into $\mathbf{T}_m$ of Equation (2.18) the transformed equations of the now

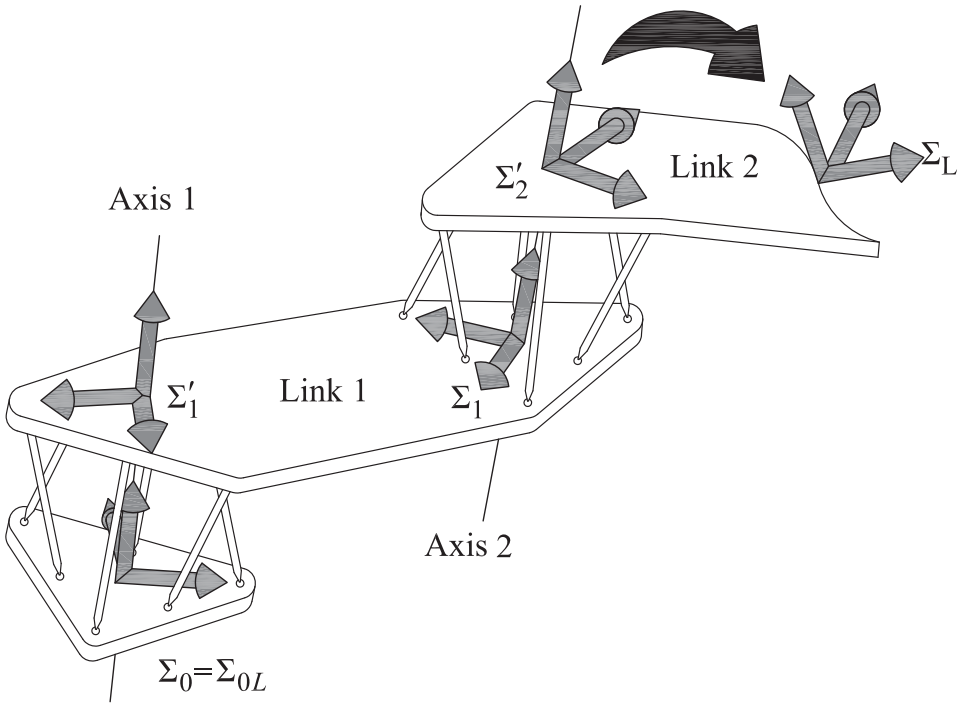

Figure 2.15: 2A-pair showing the addition of the second link to the base 2A-chain with Σ_L.

non-canonical constraint variety are found by substituting the new Study parameters, represented by vector $\mathbf{x}'$, for the existing Study parameters of the constraint variety polynomials, $\mathbf{x}$, where $\mathbf{x}'$ is found by

$$\mathbf{x}' = \mathbf{T}_m(\mathbf{G}_2)\mathbf{x}. \tag{2.32}$$

The intersection of the resulting set of equations, which includes the invariant S_6^2, is the constraint variety for the base 2A-chain.

The procedure for obtaining the equations that represent the constraint variety of the EE 2A-chain starts by substituting $-a_3$ and $-al_3$ for a_1 and al_1 respectively into the set of equations in the canonical constraint variety equations. The negative DH-parameters are introduced to account for the difference between the definition of the DH-parameters in the canonical 2A-chain and the 4A-chain.

Unlike the base 2A-chain, it is not possible to assume the base coincides with the base used in the canonical chain and this must be accounted for. To do this, the position of

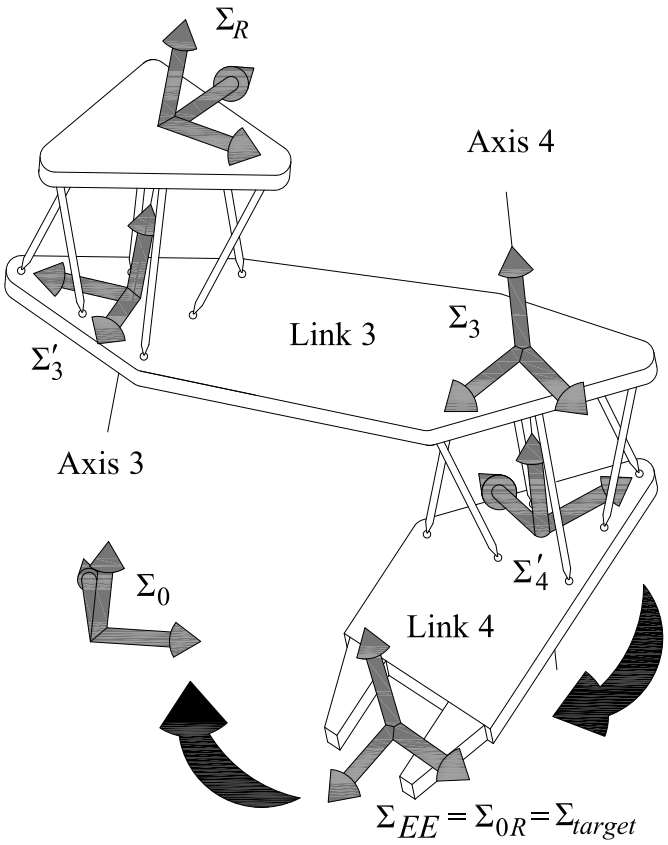

Figure 2.16: 2A-pair illustrating the addition of the fourth link to the canonical 2A-chain in order to obtain the EE 2A-chain with Σ_R and the target frame Σ_{EE} relative to the base frame Σ_0.

the target EE pose relative to the original base reference frame is accounted for using the target pose matrix $\mathbf{EE}_T$ and the fact that the base of the EE 2A-chain is not at the base of the first A-pair, but at the end of the the last link, defined by the matrix $\mathbf{G}_4$. Figure 2.16 shows the addition of the fourth link to the canonical 2A-chain and the position of the EE 2A-chain in space relative to the base frame. To get from the original base to the base of the canonical form of the EE 2A-chain the matrix $\mathbf{A}$ is used such that

$$\mathbf{A} = \mathbf{EE}_T \mathbf{G}_4^{-1}. \tag{2.33}$$

The inverse of $\mathbf{G}_4$ is used because the link is approached in the opposite direction to how it is defined for the direct kinematics. The Study parameters of the matrix $\mathbf{A}$ are obtained and substituted into the matrix $\mathbf{T}_b$ of Equation (2.17). Notice that this time the transformation occurs in the base frame. The transformed equations of the constraint variety are obtained by substituting the Study parameters $\mathbf{x}'$ for $\mathbf{x}$ in the polynomials of the canonical 2A-chain constraint variety, where $\mathbf{x}'$ is now found by

$$\mathbf{x}' = \mathbf{T}_b(\mathbf{A})\mathbf{x}. \tag{2.34}$$

The EE 2A-chain is not yet fully accounted for because the offset of the third link must be included. In Section 2.2.2 d_3 is described as the directed distance along axis Z_3 and the shift of reference frame is in the opposite direction to which d_3 was defined, therefore a translation of $-d_3$ is required. This translation is given by the transformation matrix

$$\mathbf{G}_3' = \begin{bmatrix} 1 & 0 & 0 & 0 \\ 0 & 1 & 0 & 0 \\ 0 & 0 & 1 & 0 \\ -d_3 & 0 & 0 & 1 \end{bmatrix}. \tag{2.35}$$

This translation is accounted for by again substituting $\mathbf{x}'$ for $\mathbf{x}$ in the set of equations of the previous step where $\mathbf{x}'$ is given by Equation (2.32) with $\mathbf{G}_3'$ substituted for $\mathbf{G}_2$. The resulting set of equations is the representation of the constraint variety of the EE 2A-chain. This set again contains the unmodified S_6^2 and four additional equations. The intersection of the five polynomials (one of which is always the Study quadric) is the constraint variety for the EE 2A-chain.

The constraint variety of each of the base and EE 2A-chains is described by the intersection of five equations. In both cases one of those equations is the Study quadric, S_6^2. Therefore it can be seen that the intersection of the base and EE 2A-chain constraint varieties is the intersection of a set of eight equations with S_6^2. The unknowns in the set of nine equations are the eight homogenous Study parameters, of which one unknown

can be used to normalize the others leading to $x_0 = 1$, since the exceptional generator $x_0 = x_1 = x_2 = x_3 = 0$ is excluded (see Section 2.1.6). This yields an over determined set of nine equations in eight unknowns. In general there are no solutions to an over determined system, but due to the method of obtaining this set of equations there is at least one real solution for a target pose that is within the 4A-manipulator workspace.

The procedure for finding the solution(s) to the intersection problem requires examining the structure of the equations and eliminating variables in the most logical way, starting with linear terms and working towards a univariate polynomial using seven of the nine equations. The zeros of this polynomial are obtained and back-substituted to obtain a set of variables that can be tested in the remaining two equations. Those sets of Study parameters that satisfy all equations describe instances where Σ_L and Σ_R are coincident and the 4A-manipulator is a continuous kinematic chain with the EE in the target pose.

The set(s) of Study parameters obtained from the intersection of the base and EE 2A-chain constraint varieties describe the pose of the coincident reference frames Σ_L and Σ_R relative to Σ_0. In order to obtain the four joint angles of the 4A-manipulator the inverse kinematic problem for the two 2A-chains must be solved. For the base 2A-chain this can be done as follows. Obtaining the Study parameters of Σ_L in general, by finding the Study parameters of the transformation matrix

$$\mathbf{EE}_L = \mathbf{M}_1\mathbf{G}_1\mathbf{M}_2\mathbf{G}_2, \tag{2.36}$$

provides eight functions in terms of the two joint variables u_1 and u_2, and can be normalized by dividing each equation by one of the others. It is useful to divide by the equation corresponding to the Study parameter that was used for normalization during the intersection of the constraint manifolds. The equations are now set equal to the set of Study parameters obtained in the previous step for the base 2A-chain, resulting in a set of seven equations in two unknowns. Once again, in general there is no solution to this over determined system, but due to the nature of the problem at least one real solution exists if a real solution was obtained when intersecting the constraint varieties. Solving two of the equations provides

many solutions which are tested in the remaining five equations. The set(s) of joint variables that satisfy all seven equations are the solution. It is believed that like 2R-chains [34] there is in general only one solution.

The EE 2A-chain provides the joint variables u_3 and u_4. The method of the base 2A-chain can be applied after some initial pre-processing. Using the matrix of Equation (2.11) the 4×4 transformation matrix $\mathbf{T}_{EE_R}$ describing Σ_R relative to Σ_0 can be constructed using the Study parameters found in the solution to the intersection problem. Σ_{EE} relative to Σ_R is given by

$$\mathbf{EE}_{\mathrm{T-relative}} = \mathbf{T}_{EE_R}^{-1}\mathbf{EE}_T, \tag{2.37}$$

where $\mathbf{EE}_{\mathrm{T-relative}}$ is the matrix describing the pose of Σ_{EE} relative to Σ_R. The transformation from Σ_R to Σ_{EE} given by

$$\mathbf{T}_R = \mathbf{M}_3\mathbf{G}_3\mathbf{M}_4\mathbf{G}_4 \tag{2.38}$$

is a function of u_3 and u_4. Obtaining the Study parameters of $\mathbf{EE}_{\mathrm{T-relative}}$ and the $\mathbf{T}_R$ and normalizing produces a set of seven equations and two unknowns that can be solved in a similar manner to base 2A-chain yielding the joint variables u_3 and u_4.

With the joint variables $u_i, i \in \{1, \ldots, 4\}$ obtained for every intersection point between the base and EE 2A-chain constraint varieties, the solution to the inverse kinematic problem has been found.

2.6 Obtaining the Jacobian Matrix of a Serial Manipulator

The *Jacobian Matrix*, or simply the *Jacobian*, of a serial manipulator is a matrix that maps joint rates (rate at which each joint is actuated, often called the joint velocity) to the linear and angular velocities of the manipulator's EE. The method for obtaining the Jacobian matrix used in this dissertation is based on Siciliano *et al.* [22] and Sciavicco and Siciliano [85]. The Jacobian matrix is covered in most introductory robotics texts

including [9, 57, 86].

When working in three-dimensional Euclidean space, the Jacobian is a $6 \times n$ matrix, where n is the number of joints in the chain, that relates the joint rates with the linear and angular velocity of the EE by

$$\boldsymbol{v}_e = \begin{bmatrix} \dot{\mathbf{p}}_e \\ \boldsymbol{\omega}_e \end{bmatrix} = \mathbf{J}(\mathbf{q})\dot{\mathbf{q}}, \tag{2.39}$$

where $\dot{\mathbf{p}}_e$ is the 3×1 EE linear velocity vector, $\boldsymbol{\omega}_e$ is the 3×1 EE angular velocity vector, the Jacobian, $\mathbf{J}$, is a function of the joint variables which are represented by the $n \times 1$ vector $\mathbf{q}$, and $\dot{\mathbf{q}}$ is the $n \times 1$ vector of joint rates. The $\dot{\mathbf{p}}_e$ and $\boldsymbol{\omega}_e$ components of the EE motion can be examined separately using

$$\dot{\mathbf{p}}_e = \mathbf{J}_P(\mathbf{q})\dot{\mathbf{q}}, \tag{2.40}$$

and

$$\boldsymbol{\omega}_e = \mathbf{J}_O(\mathbf{q})\dot{\mathbf{q}}, \tag{2.41}$$

where $\mathbf{J}_P$ and $\mathbf{J}_O$ are the $3 \times n$ matrices that relate the contributions of the joint rates to the EE linear velocity and angular velocity, respectively.

The Jacobian is obtained by examining the contribution of each individual joint to the linear and angular velocities of the EE. The total linear velocity of the EE is written as

$$\dot{\mathbf{p}}_e = \sum_{i=1}^{n} \frac{\partial \mathbf{p}_e}{\partial q_i}\dot{q}_i = \sum_{i=1}^{n} \boldsymbol{\jmath}_{P_i}\dot{q}_i, \tag{2.42}$$

where $\boldsymbol{\jmath}_{P_i}$ is the 3×1 vector mapping the rate of actuation of Joint i to its contribution to the linear velocity of the EE when all other joints are held fixed. The linear velocity contribution can come from two aspects of the joint motion: rotation and translation. For a prismatic joint the translation component of the motion of Joint i is along the joint axis z_{i-1} and actuated at a rate $\dot{d}_i$. The influence on the EE motion is then $\dot{\mathbf{p}}_e = \dot{d}_i z_{i-1} = \boldsymbol{\jmath}_{P_i}\dot{q}_i$ and therefore

$$\boldsymbol{\jmath}_{P_i} = z_{i-1}. \tag{2.43}$$

For a revolute joint the joint is actuated at a rate $\dot{\theta}_i$ about the axis z_{i-1}. The position of the EE with respect to the joint is given by $\mathbf{p}_e - \mathbf{p}_{i-1}$, where $\mathbf{p}_e$ is the position vector of the EE (a function of the n joint variables) and $\mathbf{p}_{i-1}$ is the position vector of the origin of Σ_{i-1}. The linear velocity of the EE is $\dot{\mathbf{p}}_e = \dot{\theta}_i z_{i-1} \times (\mathbf{p}_e - \mathbf{p}_{i-1}) = \boldsymbol{\jmath}_{P_i} \dot{q}_i$ and therefore

$$\boldsymbol{\jmath}_{P_i} = z_{i-1} \times (\mathbf{p}_e - \mathbf{p}_{i-1}). \tag{2.44}$$

For a kinematic pair that couples translation and rotation, such as the A-pair, the linear velocity of the EE is a combination of the results for a prismatic and a revolute joint and depends on how the joint variable is defined and the relationship between the translation and rotation.

The total angular velocity of the EE is written as

$$\boldsymbol{\omega}_e = \boldsymbol{\omega}_n = \sum_{i=1}^{n} \boldsymbol{\omega}_{i-1,i} = \sum_{i=1}^{n} \boldsymbol{\jmath}_{O_i} \dot{q}_i, \tag{2.45}$$

where $\boldsymbol{\omega}_{i-1,i}$ is the angular velocity of Link i with respect to Link $i-1$. For a prismatic joint there is no angular velocity of Link i with respect to Link $i-1$ so $\boldsymbol{\omega}_e = \boldsymbol{\jmath}_{O_i} \dot{q}_i = 0$ and therefore

$$\boldsymbol{\jmath}_{O_i} = \mathbf{0}. \tag{2.46}$$

For a revolute joint the angular velocity of the EE is $\boldsymbol{\omega}_e = \boldsymbol{\jmath}_{O_i} \dot{q}_i = \dot{\theta}_i z_{i-1}$ and therefore

$$\boldsymbol{\jmath}_{O_i} = z_{i-1}. \tag{2.47}$$

The full Jacobian that maps the joint rates to the EE velocities by Equation (2.39) is assembled using the vectors $\boldsymbol{\jmath}_{P_i}$ and $\boldsymbol{\jmath}_{O_i}$as

$$\mathbf{J} = \begin{bmatrix} \boldsymbol{\jmath}_{P_1} & & \boldsymbol{\jmath}_{P_n} \\ & \cdots & \\ \boldsymbol{\jmath}_{O_1} & & \boldsymbol{\jmath}_{O_n} \end{bmatrix}. \tag{2.48}$$

The Jacobian as assembled in Equation (3.54) is with respect to the base reference frame. Siciliano, *et al.* [22] show that finding the Jacobian with respect to another frame, u, requires knowing only the relative rotation matrix $\mathbf{R}^u$ from the base to frame u and using

$$\mathbf{J}^u = \begin{bmatrix} \mathbf{R}^u & \mathbf{0} \\ \mathbf{0} & \mathbf{R}^u \end{bmatrix} \mathbf{J}. \tag{2.49}$$

2.7 Dynamics of Serial Manipulators

Obtaining the dynamic equations of motion of a serial manipulator is required for the simulation of the manipulator, the development of control algorithms, and the sizing of actuation devices. Once the dynamic equations have been obtained one can explore the *direct dynamics* problem, determining how the manipulator EE will move when given joint torques are applied, which is useful for simulation of existing or conceptual dynamic systems. The *inverse dynamics* problem involves determining what joint torques are required to move the EE in a desired trajectory, useful for motor sizing and controller design.

There are two standard methods for obtaining the dynamic equations of motion: energy methods such as the Lagrange formulation and force balance methods such as the Newton-Euler formulation. Because the two approaches use independent physical relationships to derive the equations of motion, they can be used as concurrent methods: one can be used to verify the other. Section 2.7.1 describes how the Lagrange formulation is used to obtain the dynamic equations and Section 2.7.2 describes the Newton-Euler formulation. The Lagrange formulation as presented here is based on [22] and [85].

2.7.1 Lagrange Formulation of the Dynamic Equations of Motion

The Lagrange formulation of the dynamic equations utilizes generalized coordinates, q_i, $i = 1, \ldots, n$, to describe the pose of an n DOF manipulator independent of the reference frames. The Lagrangian of the system is defined as

$$\mathcal{L} = \mathcal{T} - \mathcal{U}, \tag{2.50}$$

where $\mathcal{T}$ is the total kinetic energy of the system and $\mathcal{U}$ is the total potential energy of the system. The Lagrangian equations can be written in a compact form as

$$\frac{d}{dt}\left(\frac{\partial \mathcal{L}}{\partial \dot{\mathbf{q}}}\right)^T - \left(\frac{\partial \mathcal{L}}{\partial \mathbf{q}}\right)^T = \boldsymbol{\xi}, \tag{2.51}$$

where $\mathbf{q}$ is a vector of the joint variables and $\boldsymbol{\xi}$ is a vector of the non conservative generalized forces such as the joint actuator torques, joint friction torques and joint torques induced by forces and moments applied to the EE.

In order to use the Lagrangian equations one must first determine the total kinetic and potential energy of the system. A full derivation of the energy terms is available in [22] and [85].

Kinetic Energy

The total kinetic energy in the serial chain is given by

$$\mathcal{T} = \sum_{i=1}^{n} (\mathcal{T}_{l_i} + \mathcal{T}_{m_i}), \tag{2.52}$$

where $\mathcal{T}_{l_i}$ is the kinetic energy of Link i and $\mathcal{T}_{m_i}$ is the kinetic energy of the motor driving Joint i.

The kinetic energy of Link i is given by

$$\mathcal{T}_{l_i} = \frac{1}{2} m_{l_i} \dot{\mathbf{p}}_{l_i}^T \dot{\mathbf{p}}_{l_i} + \frac{1}{2} \boldsymbol{\omega}_i^T \mathbf{R}_i \mathbf{I}_{l_i}^i \mathbf{R}_i^T \boldsymbol{\omega}_i, \tag{2.53}$$

where m_{l_i} is the mass of Link i, $\dot{\mathbf{p}}_{l_i}$ is the linear velocity of the link's centre of mass ($\mathbf{p}_{l_i}$ is the position of the centre of mass), $\boldsymbol{\omega}_i$ is the angular velocity of the link, $\mathbf{R}_i$ is the rotation matrix from the reference frame for Link i to the base frame, and $\mathbf{I}_{l_i}^i$ is the link's moment of inertia tensor with respect to the Link i reference frame. The linear and angular velocities can be written as

$$\dot{\mathbf{p}}_{l_i} = \mathbf{J}_P^{(l_i)} \dot{\mathbf{q}}, \tag{2.54}$$

$$\boldsymbol{\omega}_i = \mathbf{J}_O^{(l_i)} \dot{\mathbf{q}}, \tag{2.55}$$

where the components of the Jacobian matrix, $\mathbf{J}_P^{(l_i)}$ and $\mathbf{J}_O^{(l_i)}$, are assembled by accounting for only the joint motion between the link of interest and the base, *i.e.*

$$\mathbf{J}_P^{(l_i)} = \begin{bmatrix} \boldsymbol{\jmath}_{P_1}^{(l_i)} & \cdots & \boldsymbol{\jmath}_{P_i}^{(l_i)} & 0 & \cdots & 0 \end{bmatrix}, \tag{2.56}$$

$$\mathbf{J}_O^{(l_i)} = \begin{bmatrix} \boldsymbol{\jmath}_{O_1}^{(l_i)} & \cdots & \boldsymbol{\jmath}_{O_i}^{(l_i)} & 0 & \cdots & 0 \end{bmatrix}. \tag{2.57}$$

The columns of the Jacobian matrices depend on if the joint is prismatic:

$$\boldsymbol{\jmath}_{P_j}^{(l_i)} = z_{j-1}, \qquad \boldsymbol{\jmath}_{O_j}^{(l_i)} = 0, \tag{2.58}$$

or revolute:

$$\boldsymbol{\jmath}_{P_j}^{(l_i)} = z_{j-1} \times (\mathbf{p}_{l_i} - \mathbf{p}_{j-1}), \qquad \boldsymbol{\jmath}_{O_j}^{(l_i)} = z_{j-1}. \tag{2.59}$$

The kinetic energy of Link i is now written as

$$\mathcal{T}_{l_i} = \frac{1}{2} m_{l_i} \dot{\mathbf{q}}^T \mathbf{J}_P^{(l_i)T} \mathbf{J}_P^{(l_i)} \dot{\mathbf{q}} + \frac{1}{2} \dot{\mathbf{q}}^T \mathbf{J}_O^{(l_i)T} \mathbf{R}_i \mathbf{I}_{link_i}^i \mathbf{R}_i^T \mathbf{J}_O^{(l_i)} \dot{\mathbf{q}}, \tag{2.60}$$

The contribution of the motor on Joint i is determined separately. The fixed part of the motor is included with the link on which it is mounted, but the rotor kinetic energy must be accounted for separate to that of the joint. The contribution of the gears to the kinetic energy are included with the motors. The kinetic energy of Rotor i is

$$\mathcal{T}_{m_i} = \frac{1}{2} m_{m_i} \dot{\mathbf{p}}_{m_i}^T \dot{\mathbf{p}}_{m_i} + \frac{1}{2} \boldsymbol{\omega}_{m_i}^T \mathbf{I}_{m_i} \boldsymbol{\omega}_{m_i}, \tag{2.61}$$

where m_{m_i} is the mass of the rotor, $\dot{\mathbf{p}}_{m_i}$ is the linear velocity of the rotor's centre of mass ($\mathbf{p}_{m_i}$ is the position of the centre of mass), $\boldsymbol{\omega}_{m_i}$ is the angular velocity of the rotor, and $\mathbf{I}_{m_i}$ is the rotor's moment of inertia tensor about its centre of mass. To put the equation in

terms of the joint variables the linear and angular velocities can be written as

$$\dot{\mathbf{p}}_{m_i} = \mathbf{J}_P^{(m_i)} \dot{\mathbf{q}}, \tag{2.62}$$

$$\boldsymbol{\omega}_{m_i} = \mathbf{J}_O^{(m_i)} \dot{\mathbf{q}}. \tag{2.63}$$

The Jacobian matrices are constructed as

$$\mathbf{J}_P^{(m_i)} = \begin{bmatrix} \boldsymbol{\jmath}_{P_1}^{(m_i)} & \cdots & \boldsymbol{\jmath}_{P_{i-1}}^{(m_i)} & 0 & \cdots & 0 \end{bmatrix}, \tag{2.64}$$

$$\mathbf{J}_O^{(m_i)} = \begin{bmatrix} \boldsymbol{\jmath}_{O_1}^{(m_i)} & \cdots & \boldsymbol{\jmath}_{O_{i-1}}^{(m_i)} & \boldsymbol{\jmath}_{O_i}^{(m_i)} & 0 & \cdots & 0 \end{bmatrix}. \tag{2.65}$$

The columns of $\mathbf{J}_P^{(m_i)}$ are computed for a prismatic joint as $\boldsymbol{\jmath}_{P_j}^{(m_i)} = z_{j-1}$ and for a revolute joint as $\boldsymbol{\jmath}_{P_j}^{(m_i)} = z_{j-1} \times (\mathbf{p}_{m_i} - \mathbf{p}_{j-1})$. The columns of $\mathbf{J}_O^{(m_i)}$ are computed as $\boldsymbol{\jmath}_{O_j}^{(m_i)} = \boldsymbol{\jmath}_{O_j}^{(l_i)}$ for $j = 1, \ldots, i-1$ and $\boldsymbol{\jmath}_{O_j}^{(m_i)} = k_{r_i} z_{m_i}$ for $j = i$, where k_{r_i} is the gear reduction ratio and z_{m_i} is the unit vector along the rotor axis. The motor contribution to the kinetic energy is written as

$$\mathcal{T}_{m_i} = \frac{1}{2} m_{m_i} \dot{\mathbf{q}}^T \mathbf{J}_P^{(m_i)T} \mathbf{J}_P^{(m_i)} \dot{\mathbf{q}} + \frac{1}{2} \dot{\mathbf{q}}^T \mathbf{J}_O^{(m_i)T} \mathbf{R}_{m_i} \mathbf{I}_{m_i}^{m_i} \mathbf{R}_{m_i}^T \mathbf{J}_O^{(m_i)} \dot{\mathbf{q}}. \tag{2.66}$$

The total kinetic energy of the manipulator is written as

$$\mathcal{T} = \frac{1}{2} \dot{\mathbf{q}}^T \mathbf{B}(\mathbf{q}) \dot{\mathbf{q}}, \tag{2.67}$$

where

$$\begin{aligned} \mathbf{B}(\mathbf{q}) \quad = \sum_{i=1}^{n} \quad & \Big(m_{l_i} \mathbf{J}_P^{(l_i)T} \mathbf{J}_P^{(l_i)} + \mathbf{J}_O^{(l_i)T} \mathbf{R}_i \mathbf{I}_{l_i}^{i} \mathbf{R}_i^T \mathbf{J}_O^{(l_i)} \\ & + m_{m_i} \mathbf{J}_P^{(m_i)T} \mathbf{J}_P^{(m_i)} + \mathbf{J}_O^{(m_i)T} \mathbf{R}_{m_i} \mathbf{I}_{m_i}^{m_i} \mathbf{R}_{m_i}^T \mathbf{J}_O^{(m_i)} \Big) \end{aligned} \tag{2.68}$$

is the $n \times n$ inertial matrix.

Potential Energy

The total potential energy of the system is written as

$$\mathcal{U} = -\sum_{i=1}^{n} \left(m_{l_i} \mathbf{g}_0^T \mathbf{p}_{l_i} + m_{m_i} \mathbf{g}_0^T \mathbf{p}_{m_i} \right), \tag{2.69}$$

where $\mathbf{g}_0$ is the gravity acceleration vector in the base frame ($\mathbf{g}_0 = \begin{bmatrix} 0 & 0 & -g \end{bmatrix}^T$) and g is the acceleration due to gravity. If flexibility of the links in the chain is being considered, the potential energy due to elastic deformation must also be considered. Link flexibility and any other potential energy effects are not considered in this dissertation.

Equations of Motion

Using the results obtained for the kinetic and potential energy the Lagrangian equations can be written as

$$\mathbf{B}(\mathbf{q})\ddot{\mathbf{q}} + \mathbf{n}(\mathbf{q}, \dot{\mathbf{q}}) = \boldsymbol{\xi}, \tag{2.70}$$

where

$$\mathbf{n}(\mathbf{q}, \dot{\mathbf{q}}) = \dot{\mathbf{B}}(\mathbf{q})\dot{\mathbf{q}} - \frac{1}{2} \left(\frac{\partial}{\partial \mathbf{q}} (\dot{\mathbf{q}}^T \mathbf{B}(\mathbf{q}) \dot{\mathbf{q}}) \right)^T + \left(\frac{\partial \mathcal{U}(\mathbf{q})}{\partial \mathbf{q}} \right)^T.$$

The joint space dynamic model can be written as

$$\mathbf{B}(\mathbf{q})\ddot{\mathbf{q}} + \mathbf{C}(\mathbf{q}, \dot{\mathbf{q}})\dot{\mathbf{q}} + \mathbf{F}_v \dot{\mathbf{q}} + \mathbf{F}_s \mathrm{sgn}(\dot{\mathbf{q}}) + \mathbf{g}(\mathbf{q}) = \boldsymbol{\tau} - \mathbf{J}^T(\mathbf{q}) \mathbf{h}_e, \tag{2.71}$$

where $\mathbf{h}_e$ is the vector of forces and moments exerted by the EE on its surrounding environment ($\mathbf{J}^T(\mathbf{q})\mathbf{h}_e$ gives the portion of the actuator torques used to exert that force), $\mathbf{F}_s$ is the $n \times n$ diagonal matrix representing the static friction coefficients ($\mathbf{F}_s \mathrm{sgn}(\dot{\mathbf{q}})$ is a simplified model of the static friction forces and depends on the direction of the joint velocities), $\mathbf{F}_v$ is the $n \times n$ diagonal matrix representing the viscous friction coefficients, $\mathbf{g}(\mathbf{q})$ is the final

term of the equation for $\mathbf{n}(\mathbf{q}, \dot{\mathbf{q}})$ where

$$g_i(\boldsymbol{\theta}) = \frac{\partial \mathcal{U}}{\partial \theta_i} = -\sum_{j=1}^{n} \left(m_{l_j} \mathbf{g}_0^T \boldsymbol{\jmath}_{P_i}^{(l_j)}(\boldsymbol{\theta}) \right), \tag{2.72}$$

and the elements of the $n \times n$ matrix $\mathbf{C}(\mathbf{q}, \dot{\mathbf{q}})$ are found by

$$c_{ij} = \sum_{k=1}^{n} c_{ijk} \dot{q}_k, \tag{2.73}$$

where

$$c_{ijk} = \frac{1}{2} \left(\frac{\partial b_{ij}}{\partial q_k} + \frac{\partial b_{ik}}{\partial q_j} + \frac{\partial b_{jk}}{\partial q_i} \right), \tag{2.74}$$

where c_{ijk} are the Christoffel symbols of the first type [22] and $\mathbf{C}(\mathbf{q}, \dot{\mathbf{q}})$ contains the Coriolis and centrifugal terms [22].

2.7.2 Newton-Euler Formulation of the Dynamic Equations of Motion

The Newton-Euler formulation involves the analysis of the forces acting on each link in the kinematic chain. The dynamic equations are obtained by balancing the forces on each link. The theory presented here is based on that in [9, 22].

The following lists several variable definitions important to the Newton-Euler formulation. Each Link i has a centre of mass C_i and the following parameters:

- m_i, the mass of Link i plus any motor and transmission affixed to Link i;
- $\mathbf{I}_i$, the inertial tensor of Link i;
- $\mathbf{r}_{i-1,C_i}$, the vector from origin of Frame $i-1$ to C_i;
- $\mathbf{r}_{i,C_i}$, the vector from origin of Frame i to C_i;
- $\mathbf{r}_{i-1,i}$, the vector from origin of Frame $i-1$ to the origin of Frame i; and
- I_{m_i}, the moment of inertia of the rotor in the motor driving Link i.

For each link the following velocities and accelerations are defined:

- $\dot{\mathbf{p}}_{C_i}$, the linear velocity of C_i;
- $\dot{\mathbf{p}}_i$, the linear velocity of the origin of Frame i;
- $\boldsymbol{\omega}_i$, the angular velocity of Link i;
- $\ddot{\mathbf{p}}_{C_i}$, the linear acceleration of C_i;
- $\ddot{\mathbf{p}}_i$, the linear acceleration of the origin of Frame i;
- $\dot{\boldsymbol{\omega}}_i$, the angular acceleration of Link i;
- $\mathbf{g}_0$, the gravity vector;
- $\boldsymbol{\omega}_{m_i}$, the angular velocity of the rotor in the motor driving Link i; and
- $\dot{\boldsymbol{\omega}}_{m_i}$, the angular acceleration of the rotor in the motor driving Link i.

The forces and moments acting between each link are:

- $\boldsymbol{f}_i$, the force exerted by Link $i-1$ on Link i;
- $-\boldsymbol{f}_{i+1}$, the force exerted by Link $i+1$ on Link i;
- $\boldsymbol{\mu}_i$, the moment exerted by Link $i-1$ on Link i with respect to the origin of Frame $i-1$; and
- $-\boldsymbol{\mu}_{i+1}$, the moment exerted by Link $i+1$ on Link i with respect to the origin of Frame i.

At this point all vectors are given with respect to the base frame.

The basis of the Newton-Euler formulation is a balance of forces and moments on each link in the chain and thus the Newton equation for the translation of the centre of mass ($F = ma$) is

$$\boldsymbol{f}_i - \boldsymbol{f}_{i+1} + m_i \mathbf{g}_0 = m_i \dot{\mathbf{p}}_{C_i}, \tag{2.75}$$

and the Euler equation for rotation about the centre of mass ($M = I\dot{\omega}$) is

$$\boldsymbol{\mu}_i + \boldsymbol{f}_i \times \mathbf{r}_{i-1,C_i} - \boldsymbol{\mu}_{i+1} - \boldsymbol{f}_{i+1} \times \mathbf{r}_{i,C_i} = \frac{d}{dt}\left(\mathbf{I}_i \boldsymbol{\omega}_i + k_{r,i+1} \dot{q}_{i+1} I_{m_{i+1}} \mathbf{z}_{m_{i+1}}\right), \tag{2.76}$$

where $k_{r,i}$ is the gear ratio of the transmission driving Link i and $\mathbf{z}_{m_i}$ is the unit vector along the rotor axis. The first term in the righthand side of Equation (2.76) can be written as

$$\frac{d}{dt}\left(\mathbf{I}_i\boldsymbol{\omega}_i\right) = \mathbf{I}_i\dot{\boldsymbol{\omega}}_i + \boldsymbol{\omega}_i \times \left(\mathbf{I}_i\boldsymbol{\omega}_i\right), \tag{2.77}$$

and the second term as

$$\frac{d}{dt}\left(k_{r,i+1}\dot{q}_{i+1}I_{m_{i+1}}z_{m_{i+1}}\right) = k_{r,i+1}\ddot{q}_{i+1}I_{m_{i+1}}z_{m_{i+1}} + k_{r,i+1}\dot{q}_{i+1}I_{m_{i+1}}\boldsymbol{\omega}_i \times \mathbf{z}_{m_{i+1}}. \tag{2.78}$$

The Newton-Euler formulation is a recursive algorithm that works by first performing a forward recursion to propagate the velocities and accelerations from the base towards the EE and a backwards recursion that propagates the forces and moments from the EE towards the base. Once the velocities, accelerations, forces and moments are known for each link in the chain the Newton and Euler equations are used to obtain the dynamic equations of motion. It is more efficient to work with all vectors in the current frame on Link i and therefore the following equations are adjusted accordingly.

With known initial conditions $\boldsymbol{\omega}_0^0$, $\ddot{\mathbf{p}}_0^0 - \mathbf{g}_0$ and $\dot{\boldsymbol{\omega}}_0^0$ defined the following velocities and accelerations can be determined starting with Link 1 and working towards Link n.

$$\boldsymbol{\omega}_i^i = \begin{cases} \mathbf{R}_i^{i-1T}\boldsymbol{\omega}_{i-1}^{i-1} & \text{for a prismatic joint} \\ \mathbf{R}_i^{i-1T}(\boldsymbol{\omega}_{i-1}^{i-1} + \dot{\theta}_i\mathbf{z}_0) & \text{for a revolute joint,} \end{cases} \tag{2.79}$$

$$\dot{\boldsymbol{\omega}}_i^i = \begin{cases} \mathbf{R}_i^{i-1T}\dot{\boldsymbol{\omega}}_{i-1}^{i-1} & \text{for a prismatic joint} \\ \mathbf{R}_i^{i-1T}(\dot{\boldsymbol{\omega}}_{i-1}^{i-1} + \ddot{\theta}_i\mathbf{z}_0 + \dot{\theta}_i\boldsymbol{\omega}_{i-1}^{i-1} \times \mathbf{z}_0) & \text{for a revolute joint,} \end{cases} \tag{2.80}$$

$$\ddot{\mathbf{p}}_i^i = \begin{cases} \mathbf{R}_i^{i-1T}\left(\ddot{\mathbf{p}}_{i-1}^{i-1} + \ddot{d}_i\mathbf{z}_0\right) + 2\dot{d}\boldsymbol{\omega}_i^i \times \mathbf{R}_i^{i-1T}\mathbf{z}_0 & \\ \quad +\dot{\boldsymbol{\omega}}_{i-1}^{i-1} \times \mathbf{r}_{i-1,i}^i + \boldsymbol{\omega}_i^i \times \left(\boldsymbol{\omega}_i^i \times \mathbf{r}_{i-1,i}^i\right) & \text{for a prismatic joint} \\ \mathbf{R}_i^{i-1T}\ddot{p}_{i-1}^{i-1} + \dot{\boldsymbol{\omega}}_i^i \times \mathbf{r}_{i-1,i}^i & \text{for a revolute joint,} \\ \quad +\boldsymbol{\omega}_i^i \times \left(\boldsymbol{\omega}_i^i \times \mathbf{r}_{i-1,i}^i\right) & \end{cases} \tag{2.81}$$

$$\ddot{\mathbf{p}}_{C_i}^i = \ddot{\mathbf{p}}_i^i + \dot{\boldsymbol{\omega}}_i^i \times \mathbf{r}_{i,C_i}^i + \left(\boldsymbol{\omega}_i^i \times \mathbf{r}_{i,C_i}^i\right), \tag{2.82}$$

and

$$\dot{\boldsymbol{\omega}}_{m_i}^{i-1} = \dot{\boldsymbol{\omega}}_{i-1}^{i-1} + k_{ri}\ddot{q}_i \mathbf{z}_{m_i}^{i-1} + k_{ri}\dot{q}_i \boldsymbol{\omega}_{i-1}^{i-1} \times \mathbf{z}_{m_i}^{i-1}. \tag{2.83}$$

When the above velocity and acceleration terms are obtained for all of the links the forward recursion is complete.

The backward recursion begins with any external forces, $\boldsymbol{f}_{n+1}^{n+1}$, or moments $\boldsymbol{\mu}_{n+1}^{n+1}$ applied at the end effector and obtains the following equations starting with Link n and working towards Link 1:

$$\boldsymbol{f}_i^i = \mathbf{R}_{i+1}^1 \boldsymbol{f}_{i+1}^{i+1} + m_i \ddot{\mathbf{p}}_{C_i}^i, \tag{2.84}$$

and

$$\begin{aligned} \boldsymbol{\mu}_i^i = & -\boldsymbol{f}_i^i \times \left(\mathbf{r}_{i-1,i}^i + \mathbf{r}_{i,C_i}^i \right) + \mathbf{R}_{i+1}^1 \boldsymbol{\mu}_{i+1}^{i+1} + \mathbf{R}_{i+1}^1 \boldsymbol{f}_{i+1}^{i+1} \times \mathbf{r}_{i,C_i}^i + \mathbf{I}_i^i \dot{\boldsymbol{\omega}}_i^i + \boldsymbol{\omega}_i^i \times \left(\mathbf{I}_i^i \boldsymbol{\omega}_i^i \right) \\ & + k_{r,i+1} \ddot{q}_{i+1} I_{m_{i+1}} \mathbf{z}_{m_{i+1}}^i + k_{r,i+1} \dot{q}_{i+1} I_{m_{i+1}} \boldsymbol{\omega}_i^i \times \mathbf{z}_{m_{i+1}}^i. \end{aligned} \tag{2.85}$$

From this forward and backward recursion algorithm the generalized forces at each joint can be computed and thus the torque at each joint can be determined by

$$\tau_i = \begin{cases} \boldsymbol{f}_i^{iT} \mathbf{R}_i^{i-1T} \mathbf{z}_0 + k_{ri} I_{m_i} \dot{\boldsymbol{\omega}}_{m_i}^{i-1T} \mathbf{z}_{m_i}^{i-1} + F_{vi} \dot{d}_i + F_{si} \mathrm{sgn}(\dot{d}_i) & \text{for a prismatic joint} \\ \boldsymbol{\mu}_i^{iT} \mathbf{R}_i^{i-1T} \mathbf{z}_0 + k_{ri} I_{m_i} \dot{\boldsymbol{\omega}}_{m_i}^{i-1T} \mathbf{z}_{m_i}^{i-1} + F_{vi} \dot{\theta}_i + F_{si} \mathrm{sgn}(\dot{\theta}_i) & \text{for a revolute joint,} \end{cases} \tag{2.86}$$

where F_{vi} and F_{si} are the coefficients of viscous and Coulomb friction, respectively.

The results of Equation (2.86) provide a solution to the inverse dynamics problem directly (the torques required for a desired motion at any given time) and by rearranging the equations can provide the solution to the direct dynamics problem (finding the joint accelerations for an applied torque). The Newton-Euler formulation is an alternative method to the Lagrange formulation for obtaining the equations of motion of a mechanical system. Both methods produce the same results and the choice of method depends on the application. The Newton-Euler formulation is much more efficient (up to 100 times for a six jointed serial chain [9]), however the Lagrange formulation is considered by some to be easier to comprehend, compact and better suited to the inclusion of more complex effects such as

link deformation [22].

2.8 Plücker Line Coordinates

Plücker line coordinates are used to unambiguously describe a line in E_3, and are used in this dissertation to describe the centrelines of the legs of the A-pair. Lines in space can be represented by the linear connection between two points in space, or by the intersection of two planes. The coordinates used in this dissertation are obtained by connecting two points and are called *Plücker line coordinates* (or simply *Plücker coordinates*). The coordinates obtained by intersecting two planes are called *Axial Coordinates*. There is only a representational difference between the two different sets of coordinates describing the same line and only Plücker coordinates are discussed here. The derivation and use of Plücker coordinates are provided in [10, 87–90].

Two distinct, non-coincident points represented by homogeneous coordinates, X=(x_0:x_1:x_2:x_3) and Y=(y_0:y_1:y_2:y_3), lie on a line in E_3. Assembling the coordinates of X and Y into a 2×4 matrix and taking the Grassmannian sub-determinants [89] yields the homogeneous Plücker coordinates, p_{ik}, of the line:

$$p_{ik} = \begin{vmatrix} x_i & x_k \\ y_i & y_k \end{vmatrix} \qquad i,k \in \{0,\ldots,3\}, i \neq k. \tag{2.87}$$

Because $p_{ik} = -p_{ki}$ only six of the possible twelve Grassmanians are independent. The following six are commonly used and are assembled into the *Plücker array*:

$$(p_{01} : p_{02} : p_{03} : p_{23} : p_{31} : p_{12}). \tag{2.88}$$

The coordinates are homogeneous and thus it is necessary that

$$(p_{01} : p_{02} : p_{03} : p_{23} : p_{31} : p_{12}) \neq (0 : 0 : 0 : 0 : 0 : 0).$$

Additionally it is shown in [10, 90] that the Plücker coordinates must also satisfy the condition

$$\Omega(p) : p_{01}p_{23} + p_{02}p_{31} + p_{03}p_{12} = 0. \tag{2.89}$$

$\Omega(p)$ is called the *Plücker condition* or *Plücker identity*. In a homogeneous five-dimensional projective space $\Omega(p)$ represents a four-dimensional quadric hyper-surface called the *Plücker quadric*, $\mathcal{P}_4^2$. Distinct points on $\mathcal{P}_4^2$ represent distinct lines on E_3.

2.8.1 Intersection of Lines

Two lines are each represented by two distinct, non coincident points. The first line, p, by points $X = (x_0 : x_1 : x_2 : x_3)$ and $Y = (y_0 : y_1 : y_2 : y_3)$ and the second line, q, by $S = (s_0 : s_1 : s_2 : s_3)$ and $T = (t_0 : t_1 : t_2 : t_3)$. Lines p and q intersect or are parallel (intersect at a point at infinity) iff X, Y, S, T are coplanar. This case occurs if, and only if

$$D := \begin{vmatrix} x_0 & x_1 & x_2 & x_3 \\ y_0 & y_1 & y_2 & y_3 \\ s_0 & s_1 & s_2 & s_3 \\ t_0 & t_1 & t_2 & t_3 \end{vmatrix} = 0.$$

The determinant, D, can be obtained by the Laplacian Expansion Theorem [6] to produce the equation

$$\Omega(p, q) := D := p_{01}q_{23} + p_{02}q_{31} + p_{03}q_{12} + p_{23}q_{01} + p_{31}q_{02} + p_{12}q_{03} = 0. \tag{2.90}$$

2.8.2 Normalized Plücker Coordinates

Every line can be represented uniquely using *normalized Plücker coordinates*. The normalized form describes a line by a pair of vectors $p = (\mathbf{p}, \overline{\mathbf{p}})$ with $\mathbf{p}^2 = 1$ and $\mathbf{p}\overline{\mathbf{p}} = 0$. The Plücker coordinates are normalized using

$$\mathbf{p} = \frac{1}{\sqrt{p_{01}^2 + p_{02}^2 + p_{03}^2}}(p_{01} : p_{02} : p_{03}), \tag{2.91}$$

and

$$\overline{\mathbf{p}} = \frac{1}{\sqrt{p_{01}^2 + p_{02}^2 + p_{03}^2}}(p_{23} : p_{31} : p_{12}). \tag{2.92}$$

Physically $\mathbf{p}$ can be viewed as the unit direction vector giving the direction of the line and $\overline{\mathbf{p}}$ is the normal vector of the plane spanned by $\mathbf{p}$ and the origin of the reference frame. $\overline{\mathbf{p}}$ is often referred to as the moment of the line about the origin and can be written as $\overline{\mathbf{p}} = \mathbf{r} \times \mathbf{p}$, where $\mathbf{r}$ is the vector normal to the line from the origin to a point on the line.

2.8.3 Distance Between Lines

In this dissertation it is of interest that the perpendicular (shortest) distance between two spatial lines be obtained using Plücker coordinates. This knowledge can be applied to detecting leg collisions in individual A-pairs.

In [90] Pernkopf shows that

$$\Omega(p, q) = -M(p, q) = -d \sin \varphi, \tag{2.93}$$

where $M(p, q)$ is the moment of the two lines, d is the perpendicular distance between p and q and φ is the angle between p and q. The absolute value of $\Omega(p, q)$ becomes

$$|\Omega(p, q)| = |d||\sin \varphi|,$$

which can be rearranged to

$$|d| = \frac{|\Omega(p, q)|}{|\sin \varphi|}. \tag{2.94}$$

Using the normalized Plücker coordinates it can be stated that

$$\mathbf{p} \times \mathbf{q} = |\mathbf{p}||\mathbf{q}|\hat{\mathbf{n}} \sin \varphi, \tag{2.95}$$

where $\hat{\mathbf{n}}$ is a unit vector perpendicular to both $\mathbf{p}$ and $\mathbf{q}$. The normalization means that

$|\mathbf{p}| = |\mathbf{q}| = |\hat{\mathbf{n}}| = 1$ and therefore

$$|\mathbf{p} \times \mathbf{q}| = |\sin\varphi|. \tag{2.96}$$

Substitution of Equation (2.96) into the denominator of Equation (2.94) reveals that when using Plücker coordinates the magnitude of the perpendicular distance between the two lines p and q, d_{pq}, is found by

$$d_{pq} = \frac{|\Omega(p,q)|}{|\mathbf{p} \times \mathbf{q}|}. \tag{2.97}$$

The denominator of Equation (2.97) will be zero if the lines p and q are parallel. This is because the lines theoretically intersect at a point at infinity and therefore the numerator is also zero meaning that the lines intersect and the distance between them is equal to zero. Alternative methods are required to obtain the distance between parallel lines, however there is no such need for the work presented in this dissertation.

Zsombor-Murray [91] provides additional insight on connecting skew lines using Plücker coordinates.

2.9 Collision of Cylinders

Ketchel and Larochelle [92–94] have developed an algorithm for determining the interference of cylindrical rigid bodies in space. The algorithm is outlined here with emphasis placed on the aspects relevant to the work presented in this dissertation. The interested reader is referred to the publications by Ketchel and Larochelle for more thorough coverage. The original purpose of the algorithm is to approximate the links of a serial manipulator as cylinders and determine if self collisions might occur.

The algorithm for determining where two cylinders collide is broken into two main parts: infinite cylinder testing and finite cylinder testing. The infinite cylinder testing assumes cylinders of a given radius are infinite in length and is used to quickly rule out collisions. If infinite cylinder testing yields no collision then testing is complete and no collision is possible, however if the initial test suggests a collision might be possible then finite cylinder

testing is required to determine if in fact the cylinders interfere with each other.

2.9.1 Infinite Cylinder Testing

The method used by Ketchel and Larochelle for obtaining the distance between skew lines varies from the method used in this report, however it is the value that is important, not the method.

For two distinct non-parallel lines in space the perpendicular distance between the lines is provided by Equation (2.97). If these lines, called S_1 and S_2 are viewed as the centrelines of two infinite cylinders of radius r_1 and r_2 respectively it can be concluded that if $d(S_1, S_2) > r_1 + r_2$ then no collision is possible because any finite cylinders that are derived from these two infinite cylinders will never interfere and the testing is complete.

If $d(S_1, S_2) \leq r_1 + r_2$ then somewhere along the length of the infinite cylinders a collision has occurred. In such cases finite cylinder testing is required to determine if the interference occurs within the length of the finite cylinder segments of interest.

2.9.2 Finite Cylinder Testing

In reality the cylinders being tested will be finite cylinder segments whose axes lie on the infinite lines S_1 and S_2. If infinite cylinder testing suggests that a collision may have occurred then the finite cylinder testing is required. This test requires determining where the common normal of S_1 and S_2 intersects the infinite lines and where these intersections are relative to the finite cylinder segments.

If the cylinders are parallel and the perpendicular distance between S_1 and S_2 is less than the sum of the radii, then the cylinders interfere if any plane to which both axes are normal ever intersects both cylinders. If no such plane exists then no interference occurs.

If the axes are skew lines then the closest points on each line must be found before continuing. Consider two finite cylinders with axes represented by lines S_1 and S_2 called Cylinders 1 and 2 respectively. Each cylinder is represented by a starting point where the axis intersects the cylinder end and a vector along the axis towards the other end of the cylinder segment. For Cylinder 1 the start point is labeled c with position vector $\mathbf{c}$ and

the vector along the axis towards the other end of the cylinder is **s**. Similarly the point e and position vector **d** describe the start point of Cylinder 2 and direction vector **w** gives the direction of the cylinder. The magnitudes |**s**| and|**w**| are equal to the lengths of their respective cylinders. Points f and g are established where S_1 and S_2 intersect the the other ends of there respective finite cylinders. This configuration is illustrated in Figure 2.17.

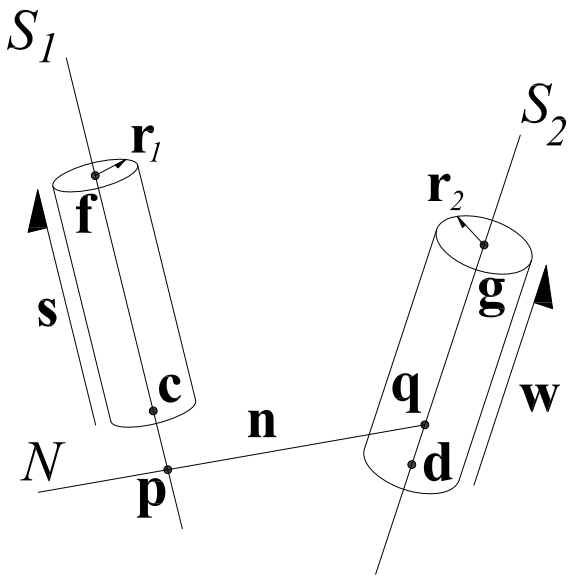

Figure 2.17: Representation of cylinders used for collision detection.

The common normal lies on Line N which intersects S_1 and S_2 in the two points p_n and q_n respectively. The position vectors describing these points are $\mathbf{p}_n$ and $\mathbf{q}_n$ and can be described by the parametric equations

$$\begin{aligned} \mathbf{p}_n &= \mathbf{c} + t_1\mathbf{s}, \\ \mathbf{q}_n &= \mathbf{d} + t_2\mathbf{w}, \end{aligned} \tag{2.98}$$

where

$$\begin{aligned} t_1 &= \frac{((\mathbf{d}-\mathbf{c})\times\mathbf{w})\cdot\mathbf{n}}{\mathbf{n}\cdot\mathbf{n}}, \\ t_2 &= \frac{((\mathbf{d}-\mathbf{c})\times\mathbf{s})\cdot\mathbf{n}}{\mathbf{n}\cdot\mathbf{n}}, \\ \mathbf{n} &= \mathbf{s}\times\mathbf{w}. \end{aligned}$$

The values of t_1 and t_2 can be used to determine the nature of the intersection of the

common normal with the cylinder axes. For Cylinder 1 there are three possible scenarios:

- $t_1 \leq 0$: p_n is located at the start of the finite cylinder segment or further outside of the cylinder (not between c and f, and closer to c),
- $0 < t_1 < 1$: p_n is located within the finite cylinder segment (between c and f), and
- $t_1 \geq 0$: p_n is located at the end of the finite cylinder segment or further outside of the cylinder (not between c and f, and closer to f).

The results are the same for Cylinder 2 if t_2 replaces t_1 and q_n replaces p_n.

With the positions of p_n and q_n known relative to their respective finite cylinder segments there are three possible situations that each require a different test to determine if the cylinders interfere. The three types of testing are:

- On-On testing: both p_n and q_n lie on their respective axis within the limits of their finite cylinder segment,
- On-Off testing: one of p_n or q_n lies within its cylinder segment while the other does not, or
- Off-Off testing both p_n and q_n lie outside of the respective cylinder segments.

In their papers Ketchel and Larochelle thoroughly describe each type of testing. In this dissertation only the On-On testing is required and therefore it is the only type of finite cylinder testing discussed in this section. The interested reader is referred to [92–94] for further details on the other types of finite cylinder testing.

Having already covered infinite cylinder testing the On-On test is in fact already completed. The infinite test has already provided the distance between the two points p_n and q_n and because these points are located within their respective cylinder segments cylinder interference will occur if $d_{S_1S_2} \leq r_1 + r_2$, the same criteria as was used in infinite cylinder testing.

2.10 Simple Feedback Control Scheme

A simple control scheme to make a manipulator follow a given joint trajectory is provided by Craig [9]. The dynamic equations of motion of a manipulator (with n joints) have the form

$$\boldsymbol{\tau} = \mathbf{B}(\dot{\boldsymbol{\theta}})\ddot{\boldsymbol{\theta}} + \mathbf{C}(\boldsymbol{\theta}, \dot{\boldsymbol{\theta}})\dot{\boldsymbol{\theta}} + \mathbf{G}(\boldsymbol{\theta}). \tag{2.99}$$

The system model is nonlinear but can be linearized using the partitioned control scheme [9] to give the $n \times 1$ vector of joint torques as

$$\boldsymbol{\tau} = \boldsymbol{\alpha}\boldsymbol{\tau}' + \boldsymbol{\beta}, \tag{2.100}$$

where $\boldsymbol{\alpha} = \mathbf{B}(\dot{\boldsymbol{\theta}})$ contains the inertial terms and $\boldsymbol{\beta} = \mathbf{C}(\boldsymbol{\theta}, \dot{\boldsymbol{\theta}}) + \mathbf{G}(\boldsymbol{\theta})$. The error between the desired and actual joint position at any given time is $\mathbf{E} = \boldsymbol{\theta}_d - \boldsymbol{\theta}$ and the error between the desired and actual joint velocities is $\dot{\mathbf{E}} = \dot{\boldsymbol{\theta}}_d - \dot{\boldsymbol{\theta}}$. The control law for trajectory-following is

$$\boldsymbol{\tau}' = \ddot{\boldsymbol{\theta}}_d + \mathbf{K}_v\dot{\mathbf{E}} + \mathbf{K}_p\mathbf{E}, \tag{2.101}$$

where $\mathbf{K}_v$ and $\mathbf{K}_p$ are diagonal matrices containing the control gains and the system is now characterized by the error equation

$$\ddot{\mathbf{E}} + \mathbf{K}_v\dot{\mathbf{E}} + \mathbf{K}_p\mathbf{E} = 0. \tag{2.102}$$

The control gains can be manipulated to obtained desired characteristics such as minimized oscillations or settling time. Figure 2.18 shows the block diagram for the simple trajectory-following controller. This generic controller can be applied to a manipulator with any number of joints, including A-chains.

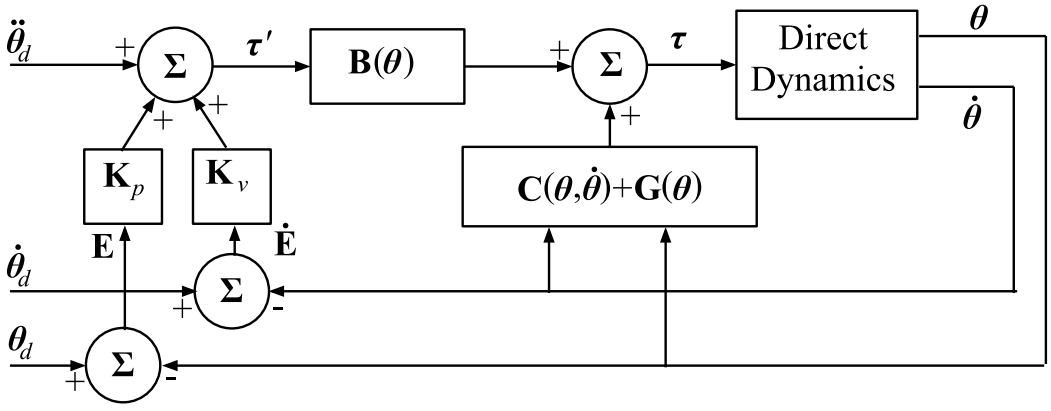

Figure 2.18: Block diagram of the generic trajectory-following controller.

2.11 Trigonometric Identities and Notation

This section presents the essential trigonometric identities and notation conventions that are used in this dissertation.

2.11.1 Tangent of the Half-angle Substitution

Analysis of mechanical systems that possess design or motion parameters described by angles involves equations containing trigonometric functions. Computer algebra systems are generally more efficient with algebraic equations than ones containing trigonometric functions, therefore a method of converting the trigonometric functions to algebraic terms is desired. The process of tangent of the half-angle substitution is commonly used to accomplish this.

Tangent of the half-angle substitution is based on the trigonometric identities

$$\sin(\phi) = \frac{2\tan(\frac{\phi}{2})}{1+\tan^2(\frac{\phi}{2})},$$

and

$$\cos(\phi) = \frac{1-\tan^2(\frac{\phi}{2})}{1+\tan^2(\frac{\phi}{2})},$$

where $\phi \neq (2k+1)\pi$ and $k \in \{0, 1, \ldots\}$. Substitution of a new variable

$$u = \tan(\frac{\phi}{2}) \tag{2.103}$$

into the identities provides the following identities

$$\sin(\phi) = \frac{2u}{1+u^2}, \tag{2.104}$$

and

$$\cos(\phi) = \frac{1-u^2}{1+u^2}. \tag{2.105}$$

As noted by Pfurner [7] these identities define a mapping of the points of a unit circle parameterized by ϕ to the set of real numbers. The inverse mapping is given by

$$\phi = 2\arctan(u). \tag{2.106}$$

From these mappings it can be seen that when $u = 0$ then $\phi = 0$, when $u = 1$ then $\phi = \frac{\pi}{2}$ and as u goes to infinity ϕ approaches π.

The tangent of the half-angle substitution technique is utilized throughout this dissertation to convert trigonometric functions to rational algebraic functions, a form more suitable for analysis with algebraic software.

2.11.2 Simplified Trigonometric Notation

When possible, trigonometric functions will be written in standard forms, however when space does not permit the use of standard notation the following simplified trigonometric notation is used

$$\begin{aligned} \sin(\theta_{v_i}) &= s_i, \\ \cos(\theta_{v_i}) &= c_i, \\ \sin\left(\frac{\theta_{v_i}}{2}\right) &= s\frac{\theta_i}{2}, \\ \sin\left(\frac{\theta_{v_i}}{2}\right) &= c\frac{\theta_i}{2}, \end{aligned} \tag{2.107}$$

as are the following trigonometric identities

$$\begin{aligned}
\cos\left(\theta_{v_1}+\theta_{v_1}\right) &= c_{1+2} &= c_1c_2 - s_1s_2,\\
\sin\left(\theta_{v_1}+\theta_{v_1}\right) &= s_{1+2} &= c_1s_2 + s_1c_2,\\
\cos\left(\theta_{v_1}-\theta_{v_1}\right) &= c_{1-2} &= c_1c_2 + s_1s_2,\\
\sin\left(\theta_{v_1}-\theta_{v_1}\right) &= s_{1-2} &= s_1c_2 - c_1s_2.
\end{aligned} \tag{2.108}$$

Chapter 3

Analysis of A-Pairs

This chapter presents the original work of this dissertation that details the contributions outlined in Section 1.2. The work presented characterises the kinematics and dynamics of serial kinematic chains constructed using A-pairs and significantly advances the work presented in [1], where A-pairs were introduced.

The position level kinematics of A-chains are revised to account for a more general definition of the A-chain DH-parameters. This includes an examination of the direct kinematics with revised parameters, and the determination of the constraint variety using the new algorithm of Section 2.3.1 to be used in the inverse kinematics algorithm for 4A-chains. The limits of the A-pair motion are addressed which leads into the introduction of the prototype 4A-chain and a discussion of the actuation method employed on that manipulator. The reachable workspace of A-chains are obtained using a novel algorithm for approximating the reachable workspace of serial chains. Obtaining the Jacobian matrices of A-chains leads into the velocity level kinematics as well as the dynamic analysis. The chapter concludes with a numeric example based on the prototype 4A-chain.

3.1 Revising the A-Chain Position Level Kinematics

The direct kinematics of nA-chains and the inverse kinematics of 4A- and 6A-chains, as presented in [1], were based on assumptions that do not represent truly general A-pairs and A-chains. This section revisits the position level kinematics of A-chains (Section 2.5).

3.1.1 A-Chain DH-Parameters Revision

When working with kinematic pairs that have a limited range of motion or, as is also the case with A-pairs, where there is a coupling of two or more DH-parameters it is necessary to identify the direction of the home position (or some other reference position) of the joint with respect to the preceding link in the kinematic chain. The A-pair has both a limited range of motion due to self-collisions between the legs (see Section 3.2) and couples the joint angle with the joint offset, so it is important to know which way the A-pair is attached to the preceding link.

In [61] Yang and Lee introduce a new joint parameter called the location angle, β_i, to identify the centre of the range of motion for a limited revolute joint. It is not necessary to introduce an entirely new joint parameter, but by breaking the joint angle, θ_i, into two components, one fixed and one variable (similar to the joint offset of the A-pair which has a fixed component and a variable component that is coupled to the rotation angle) the direction of the home position with respect to the preceding link can be identified. The fixed component of the joint angle, θ_{f_i}, is the angle between adjacent links measured about the axis of Joint i when the A-pair is in the home position as defined in Section 2.5.2 and the variable component of the joint angle, θ_{v_i}, is measured relative to the home position. That is, if $\theta_{v_i} = 0$ the joint would be in the home position (recall that this is a theoretical position that is mechanically inaccessible due to self-collisions). The full joint angle as defined in Section 2.2.2 is

$$\theta_i = \theta_{f_i} + \theta_{v_i}. \tag{3.1}$$

With this new definition the separation of the fixed base and moving platform of the A-pair is a function of θ_{v_i} and independent of θ_{f_i}. The equation for the separation, denoted d in Equation (2.29), becomes:

$$d = \rho \sin\left(\frac{\theta_{v_i}}{2}\right). \tag{3.2}$$

This partitioning of the fixed and variable components of θ_i, along with the DH-parameters of Section 2.5.4 provide for an unambiguous geometric representation of

A-chains.

3.1.2 Determining the Geometric Constant

In [1] it was assumed that the value of the geometric constant, ρ, in Equations (2.29) and (3.2) could be set equal to unity without loss in generality. It turns out that this assumption is not valid in general and the value of ρ must be determined by the geometry of the A-pair.

In Section 2.5.3 when describing the specific configuration of the Griffis-Duffy platform that is used to construct the A-pair it is stated that the leg lengths are equal to the height of the congruent equilateral anchor point triangles that represent the fixed base and moving platform of the A-pair. This means that the leg lengths, l, are a function of the size of the A-pair which is given as the length of one of the sides of the triangle, a, and that relationship is

$$l = \frac{a\sqrt{3}}{2}. \tag{3.3}$$

The geometric constant ρ represents the maximum distance between the fixed base and moving platform of the A-pair. The value of ρ is determined by examining the geometry of the A-pair when $\sin(\theta/2) = 1$, *i.e.* when $\theta = 180^\circ$. In this position, a profile of which is shown in Figure 3.1, Equation (3.2) becomes $d(180^\circ) = \rho \sin(180^\circ/2) = \rho$. Knowing the anchor point positions (provided in Section 3.2.1) and the length of the legs in terms of the dimensions of the A-pair, Equation (3.3), the value ρ is

$$\rho = d(180^\circ) = \frac{a\sqrt{6}}{3}. \tag{3.4}$$

Equation (3.4) negates the need to assume a value for the geometric constant. It is required that the correct value of ρ be introduced to all equations and algorithms presented in [1] where it was assumed that $\rho = 1$.

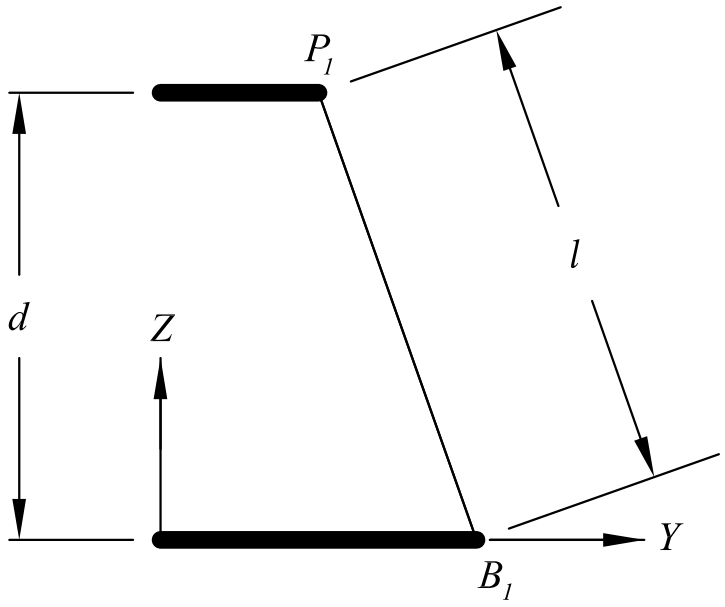

Figure 3.1: Profile view of Leg 1 when $\theta = 180°$, illustrating the measurement d.

3.1.3 A-Chain Direct Kinematics Revision

The method for obtaining the matrix form of the direct kinematic equations of nA-chains is presented in Section 2.5.5, however some slight modifications to the $\mathbf{M}_i$ matrices are required based on the new results presented in Sections 3.1.1 and 3.1.2.

The geometric constant, ρ, is determined in Section 3.1.2 in terms of the length of the sides of the anchor point triangles, a, by Equation (3.4) and can also be written in terms of the leg length, l, using a combination of Equations (3.4) and (3.3). In this section only ρ is used to maintain simplicity in the equations.

The matrix form of the direct kinematic equations for an nA-chain is found by Equation (2.19) where the $\mathbf{G}_i$ matrices are found by Equation (2.20) and the $\mathbf{M}_i$ matrices are

now written based on the work presented in Section 3.1.1 as

$$\mathbf{M_i} = \begin{bmatrix} 1 & 0 & 0 & 0 \\ 0 & \cos(\theta_{f_i} + \theta_{v_i}) & -\sin(\theta_{f_i} + \theta_{v_i}) & 0 \\ 0 & \sin(\theta_{f_i} + \theta_{v_i}) & \cos(\theta_{f_i} + \theta_{v_i}) & 0 \\ \rho \sin(\frac{\theta_{v_i}}{2}) & 0 & 0 & 1 \end{bmatrix}. \tag{3.5}$$

The value of θ_{f_i} is fixed by definition and in many cases trigonometric identities can be used to simplify the resulting matrices, for example if $\theta_{f_i} = 0°$ the $\mathbf{M}_i$ matrix returns to that of Equation (2.30) or if $\theta_{f_i} = 90°$ then, using angle sum trigonometric identities, $\cos(\theta_{f_i} + \theta_{v_i}) = -\sin(\theta_{v_i})$ and $\sin(\theta_{f_i} + \theta_{v_i}) = \cos(\theta_{v_i})$.

3.1.4 Constraint Varieties of A-Chains

Obtaining the constraint varieties of 2A-chains is a critical component of the 4A-chain inverse kinematics algorithm. In [1] the constraint varieties of the 2A-chains were found using resultant elimination, however this was prior to the revision of the A-chain DH-parameters. In this section the implicitization algorithm by Walter and Husty (see Section 2.3.1) is used to obtain the constraint varieties of the 2A-chains required for the inverse kinematics algorithm.

It turns out that defining the joint twist (α_i) parameters and the fixed component of the joint angles (θ_{f_i}) greatly simplifies the problem of obtaining the constraint varieties that are otherwise impractical to express in general terms. In Section 3.8 a specific numeric example analyzes the kinematics and dynamics of a prototype 4A-chain. In this section the α_i and θ_{f_i} values of that chain are used to illustrate the method for obtaining the constraint varieties of the two 2A-chains required for the inverse kinematics analysis. The joint twist values used in this section are

$$\begin{aligned} \alpha_1 &= 90°, \\ \alpha_2 &= 180°, \\ \alpha_3 &= -90°, \\ \alpha_4 &= 0°, \end{aligned} \tag{3.6}$$

and the fixed components of the joint angles are

$$\begin{aligned} \theta_{f_1} &= 0^\circ, \\ \theta_{f_2} &= -90^\circ, \\ \theta_{f_3} &= 90^\circ, \\ \theta_{f_4} &= 0^\circ. \end{aligned} \tag{3.7}$$

The two 2A-chains required for the inverse kinematics analysis are the base (left) 2A-chain that contains Joints and Links 1 and 2, and the EE (right) 2A-chain that contains Joints and Links 3 and 4. The method for obtaining the two chains is similar though there are some differences in the required preprocessing.

Constraint Variety of the Base 2A-Chain

Obtaining the constraint variety using the implicitization algorithm requires the matrix form of the direct kinematic equations. Substitution of the θ_{f_i} values of Equation (3.7) into Equation (3.5) yields

$$\begin{aligned} \mathbf{M}_1 &= \begin{bmatrix} 1 & 0 & 0 & 0 \\ 0 & \cos(\theta_{v_1}) & -\sin(\theta_{v_1}) & 0 \\ 0 & \sin(\theta_{v_1}) & \cos(\theta_{v_1}) & 0 \\ \rho \sin\left(\frac{\theta_{v_1}}{2}\right) & 0 & 0 & 1 \end{bmatrix}, \\ \mathbf{M}_2 &= \begin{bmatrix} 1 & 0 & 0 & 0 \\ 0 & \sin(\theta_{v_2}) & \cos(\theta_{v_2}) & 0 \\ 0 & -\cos(\theta_{v_2}) & \sin(\theta_{v_2}) & 0 \\ \rho \sin\left(\frac{\theta_{v_2}}{2}\right) & 0 & 0 & 1 \end{bmatrix}. \end{aligned} \tag{3.8}$$

Fractions are removed by substituting $\theta_{v_i} = 2\phi_i$ and the use of trigonometric identities results in

$$\begin{aligned}
\mathbf{M}_1 &= \begin{bmatrix} 1 & 0 & 0 & 0 \\ 0 & \cos^2(\phi_1) - \sin^2(\phi_1) & -2\sin(\phi_1)\cos(\phi_1) & 0 \\ 0 & 2\sin(\phi_1)\cos(\phi_1) & \cos^2(\phi_1) - \sin^2(\phi_1) & 0 \\ \rho\sin(\phi_1) & 0 & 0 & 1 \end{bmatrix}, \\
\mathbf{M}_2 &= \begin{bmatrix} 1 & 0 & 0 & 0 \\ 0 & 2\sin(\phi_2)\cos(\phi_2) & \cos^2(\phi_2) - \sin^2(\phi_2) & 0 \\ 0 & -\cos^2(\phi_2) - \sin^2(\phi_2) & 2\sin(\phi_2)\cos(\phi_2) & 0 \\ \rho\sin(\phi_2) & 0 & 0 & 1 \end{bmatrix}.
\end{aligned} \tag{3.9}$$

Tangent of the half-angle substitution (Section 2.11.1) yields

$$\begin{aligned}
\mathbf{M}_1 &= \begin{bmatrix} 1 & 0 & 0 & 0 \\ 0 & \frac{1-6\,{u_1}^2+{u_1}^4}{\left(1+{u_1}^2\right)^2} & 4\,\frac{u_1\left(-1+{u_1}^2\right)}{\left(1+{u_1}^2\right)^2} & 0 \\ 0 & -4\,\frac{u_1\left(-1+{u_1}^2\right)}{\left(1+{u_1}^2\right)^2} & \frac{1-6\,{u_1}^2+{u_1}^4}{\left(1+{u_1}^2\right)^2} & 0 \\ 2\,\frac{\rho\,u_1}{1+{u_1}^2} & 0 & 0 & 1 \end{bmatrix}, \\
\mathbf{M}_2 &= \begin{bmatrix} 1 & 0 & 0 & 0 \\ 0 & -4\,\frac{u_2\left(-1+{u_2}^2\right)}{\left(1+{u_2}^2\right)^2} & \frac{1-6\,{u_2}^2+{u_2}^4}{\left(1+{u_2}^2\right)^2} & 0 \\ 0 & -\frac{1-6\,{u_2}^2+{u_2}^4}{\left(1+{u_2}^2\right)^2} & -4\,\frac{u_2\left(-1+{u_2}^2\right)}{\left(1+{u_2}^2\right)^2} & 0 \\ 2\,\frac{\rho\,u_2}{1+{u_2}^2} & 0 & 0 & 1 \end{bmatrix},
\end{aligned} \tag{3.10}$$

where $u_i = \tan\left(\frac{\phi_i}{2}\right)$. The $\mathbf{G}_i$ matrices are assembled by substituting the α_i values of Equation (3.6) into Equation (2.20).

The matrix form of the direct kinematics equations is given by Equation (2.19) with $n = 2$. The resulting transformation matrix ${}^0\mathbf{T}_2$ describes the position of the EE of the base 2A-chain (Σ_2) with respect to the base frame as a function of the joint variables

u_1 and u_2. The Study parameters of ${}^0\mathbf{T}_2$ are found using Equations (2.14) and (2.15) resulting in parametric equations for the eight Study parameters in terms of u_1 and u_2. The implicitization algorithm of Section 2.3.1 is then used to obtain the implicit equations that represent the constraint variety of the 2A-chain.

The linear *ansatz* produces only the trivial solution, thus the constraint variety does not include any linear equations. Increasing to the second order *ansatz* yields four nontrivial solutions. Recall that in P^7 the number of polynomials required to define the constraint variety is seven minus the number of constraints (there are two constraints, u_1 and u_2, in this case). Therefore five polynomials are required to define the constraint variety of the 2A-chain, thus one more independent polynomial is required in addition to the four quadratic polynomials. Using a cubic *ansatz* 40 solutions are found, though most solutions prove to be not independent of the first four quadratic polynomials. Walter and Husty [71] state that any of the remaining cubic polynomials may be used without any losses, though the intersection of the five resulting polynomials may contain extra information.

The five polynomials that intersect to form the constraint variety of the base 2A-chain are:

$$
\begin{aligned}
&1: x_0y_0 + x_1y_1 + x_2y_2 + x_3y_3 = 0,\\
&2: {x_0}^2 - {x_1}^2 - {x_2}^2 + {x_3}^2 = 0,\\
&3: {x_1}^2a_1 + {x_2}^2a_1 - x_0x_1a_2 + 2\,x_0y_0 - x_2x_3a_2 + 2\,x_3y_3 = 0,\\
&4: -x_2y_1d_1 - x_0y_3d_2 - \tfrac{1}{4}\,x_0x_1\rho^2 - \tfrac{1}{4}\,x_1x_3\rho^2 + x_1y_2d_1 + x_1y_2d_2 - x_0x_2d_1a_2\\
&\quad + x_1x_3d_1a_2 - x_2y_3a_2 + x_3y_2a_2 - x_3y_0d_1 + x_0y_1a_2 - x_1y_0a_2 + x_3y_0d_2\\
&\quad + \tfrac{1}{4}\,x_0x_2\rho^2 - x_2y_1d_2 + \tfrac{1}{4}\,x_2x_3\rho^2 + x_0y_3d_1 + {y_3}^2 + {y_1}^2 + {y_2}^2 + {y_0}^2 - \tfrac{1}{2}\,{x_2}^2\rho^2\\
&\quad - \tfrac{1}{2}\,{x_2}^2{a_1}^2 - \tfrac{1}{2}\,{x_1}^2\rho^2 - \tfrac{1}{2}\,{x_1}^2{a_1}^2 + \tfrac{1}{2}\,{x_2}^2{d_2}^2 + \tfrac{1}{2}\,{x_1}^2{d_1}^2 + \tfrac{1}{2}\,{x_2}^2{d_1}^2\\
&\quad + \tfrac{1}{2}\,{x_1}^2{d_2}^2 + \tfrac{1}{2}\,{x_1}^2{a_2}^2 + \tfrac{1}{2}\,{x_2}^2{a_2}^2 = 0,\\
&5: 2\,x_0x_3y_0 - x_2{x_3}^2a_2 - 2\,{x_0}^2y_3 + {x_2}^2x_3a_1 + 2\,{x_2}^2y_3 - x_0x_1x_3a_2 + 2\,{x_1}^2y_3\\
&\quad + {x_1}^2x_3a_1 = 0.
\end{aligned}
\tag{3.11}
$$

The set of polynomials includes the Study quadric and the constraint variety of the base

2A-chain is the intersection of the other four polynomials with S_6^2.

Constraint Variety of the EE 2A-Chain

The implicit form of the EE 2A-chain constraint variety is obtained using the same algorithm as the previous section with some modifications to how the direct kinematics equations are obtained. The $\mathbf{M}_i$ and $\mathbf{G}_i$ matrices are obtained by substituting the Joint 3 and 4 parameters of Equations (3.7) and (3.6) into Equations (3.5) and (2.20), respectively. The $\mathbf{M}_i$ matrices are

$$\begin{aligned}
\mathbf{M}_3 &= \begin{bmatrix} 1 & 0 & 0 & 0 \\ 0 & -\sin(\theta_{v_3}) & -\cos(\theta_{v_3}) & 0 \\ 0 & \cos(\theta_{v_3}) & -\sin(\theta_{v_3}) & 0 \\ \rho \sin\left(\frac{\theta_{v_3}}{2}\right) & 0 & 0 & 1 \end{bmatrix}, \\
\mathbf{M}_4 &= \begin{bmatrix} 1 & 0 & 0 & 0 \\ 0 & \cos(\theta_{v_4}) & -\sin(\theta_{v_4}) & 0 \\ 0 & \sin(\theta_{v_4}) & \cos(\theta_{v_4}) & 0 \\ \rho \sin\left(\frac{\theta_{v_4}}{2}\right) & 0 & 0 & 1 \end{bmatrix},
\end{aligned} \tag{3.12}$$

and after substitution of $\theta_{v_i} = 2\phi_i$ and tangent of the half-angle substitution the $\mathbf{M}_i$ matrices become

$$\begin{aligned}
\mathbf{M}_3 &= \begin{bmatrix} 1 & 0 & 0 & 0 \\ 0 & 4\,\frac{u_3\left(-1+{u_3}^2\right)}{\left(1+{u_3}^2\right)^2} & -\frac{1-6\,{u_3}^2+{u_3}^4}{\left(1+{u_3}^2\right)^2} & 0 \\ 0 & \frac{1-6\,{u_3}^2+{u_3}^4}{\left(1+{u_3}^2\right)^2} & 4\,\frac{u_3\left(-1+{u_3}^2\right)}{\left(1+{u_3}^2\right)^2} & 0 \\ 2\,\frac{\rho\,u_3}{1+{u_3}^2} & 0 & 0 & 1 \end{bmatrix}, \\
\mathbf{M}_4 &= \begin{bmatrix} 1 & 0 & 0 & 0 \\ 0 & \frac{1-6\,{u_4}^2+{u_4}^4}{\left(1+{u_4}^2\right)^2} & 4\,\frac{u_4\left(-1+{u_4}^2\right)}{\left(1+{u_4}^2\right)^2} & 0 \\ 0 & -4\,\frac{u_4\left(-1+{u_4}^2\right)}{\left(1+{u_4}^2\right)^2} & \frac{1-6\,{u_4}^2+{u_4}^4}{\left(1+{u_4}^2\right)^2} & 0 \\ 2\,\frac{\rho\,u_4}{1+{u_4}^2} & 0 & 0 & 1 \end{bmatrix}.
\end{aligned} \tag{3.13}$$

The transformation matrix describing Σ_4 (also Σ_{EE}) with respect to Σ_2, ${}^2\mathbf{T}_4$, is obtained by

$$ {}^2\mathbf{T}_4 = \mathbf{M}_3\mathbf{G}_3\mathbf{M}_4\mathbf{G}_4. \tag{3.14} $$

Recalling the inverse kinematics algorithm of Sections 2.4 and 2.5.6 the EE of the 4A-chain is placed in the target pose and $\Sigma_4 = \Sigma_{EE} = \Sigma_{target}$. When obtaining the constraint variety of the EE 2A-chain the base reference frame becomes $\Sigma_{0R} = \Sigma_{target}$ and the EE reference frame is $\Sigma_2 = \Sigma_R$. Thus the transformation matrix describing Σ_R or Σ_2 with respect to Σ_{0R} or Σ_4, ${}^4\mathbf{T}_2$, is required. The required matrix is obtained by

$$ {}^4\mathbf{T}_2 = {}^2\mathbf{T}_4^{-1}. \tag{3.15} $$

Using ${}^4\mathbf{T}_2$ the polynomials representing the constraint variety of the EE 2A-chain are derived using the same methods that were used for the base 2A-chain. The implicitization algorithm resulted in four quadratic polynomials (including S_6^2) and one cubic polynomial. The five polynomials that intersect to provide the constraint variety of the EE 2A-chain are:

$$
\begin{aligned}
&1 : x_0y_0 + x_1y_1 + x_2y_2 + x_3y_3 = 0,\\
&2 : {x_0}^2 - {x_1}^2 - {x_2}^2 + {x_3}^2 = 0,\\
&3 : -a_3{x_1}^2 - {x_2}^2a_3 + a_4x_2x_3 + 2\,x_1y_1 + 2\,x_2y_2 - a_4x_0x_1 = 0,\\
&4 : -x_0x_1\rho^2 - x_1x_3\rho^2 + 4\,a_4d_3x_0x_2 + 4\,a_4d_3x_1x_3 - 4\,a_4x_0y_1 - 2\,{a_3}^2{x_1}^2 - 2\,{a_3}^2{x_2}^2\\
&\quad +2\,{a_4}^2{x_2}^2 + 2\,{a_4}^2{x_1}^2 + 2\,{d_3}^2{x_1}^2 + 2\,{d_4}^2{x_2}^2 + 2\,{d_4}^2{x_1}^2 + 2\,{d_3}^2{x_2}^2 - 4\,d_3x_0y_3\\
&\quad -4\,d_3x_2y_1 + 4\,d_3x_1y_2 - 4\,d_4x_1y_2 + 4\,d_4x_2y_1 + 4\,d_3x_3y_0 + 4\,a_4x_3y_2 - 4\,d_4x_0y_3\\
&\quad -4\,a_4x_2y_3 + 4\,a_4x_1y_0 + 4\,d_4x_3y_0 + x_0x_2\rho^2 - x_2x_3\rho^2 + 4\,{y_3}^2 + 4\,{y_1}^2 + 4\,{y_2}^2\\
&\quad +4\,{y_0}^2 - 2\,{x_2}^2\rho^2 - 2\,{x_1}^2\rho^2 = 0,\\
&5 : 2\,{x_2}^2y_3 - x_2{x_3}^2a_4 + x_0x_1x_3a_4 + 2\,x_0x_3y_0 + {x_2}^2x_3a_3 + {x_1}^2x_3a_3 + 2\,{x_1}^2y_3\\
&\quad -2\,{x_0}^2y_3 = 0.
\end{aligned}
\tag{3.16}
$$

These polynomials represent the constraint variety of the 2A-chain with respect to Σ_4.

The constraint variety of the 2A-chain with respect to Σ_0 when $\Sigma_4 = \Sigma_{target}$ is found by transforming the polynomials of Equation 3.16 in the base frame using the method described in Section 2.1.8. The implementation of this transformation is shown in the numeric example of Section 3.8.

The algorithm for solving the inverse kinematics of the 4A-chain is unchanged from that present in Section 2.5.6 aside from the use of the new 2A-chain constraint varieties. The implementation of the inverse kinematics algorithm with the new constraint varieties is left to Section 3.8 as part of the full kinematic and dynamic analysis of the prototype 4A-chain.

3.2 A-Pair Joint Limits

The self-motions of the A-pair are discussed in Sections 2.5 and Section 3.1.3 without consideration of self-collisions between the structural elements within the A-pair. When considering a single A-pair the moving platform and the six individual legs move relative to one another and relative to the fixed base. Since the self-motions of the A-pair possess only one DOF the relative positions of the fixed base, moving platform and the six individual legs are a function of the joint angle, θ_i. Determining at what values of θ_i self-collisions occur allows for a determination of the joint limits for the A-pairs in an A-chain. This section focuses on the self-collisions of a single A-pair and does not consider the limitations by collisions of the structural elements of the links of longer A-chains.

The remainder of this section assumes that the fixed base and moving platform are designed such that they will not collide over the regular range of motion of the single A-pair and the spherical joints that anchor the legs to the fixed base and moving platform are designed to provide for free motion of the legs over the range of motion of the A-pair. The results of this section can be used to ensure such requirements are met, but in order to proceed it must be assumed that these conditions are satisfied.

The limits to the self-motions are dictated by the interactions of the A-pair legs. Each leg can be represented as a line connecting the leg's anchor point on the fixed base to the leg's anchor point on the moving platform. This section describes how the lines representing

the legs are obtained and examines the interaction of the lines as the A-pair moves through its self-motions.

3.2.1 Leg Anchor Point Trajectory

In Section 2.5.2 and Section 3.1 the self-motions of the A-pair are described by Equations (2.29) and (3.2), respectively, which provide the distance between the fixed base and moving platform anchor point planes as a function of θ. In order to track the leg anchor points it is necessary to describe the position of each anchor point on the moving platform in a fixed reference frame as a function of θ (because only a single A-pair is being examined θ is used instead of θ_{v_i} because the orientation of the A-pair is irrelevant).

The fixed base and moving platform each have six leg anchor points oriented in a triangle. The Legs connecting the anchor points are labelled from 1 to 6 and the anchor point for Leg i on the fixed base is called B_i and on the moving platform P_i. Figure 3.2 shows the

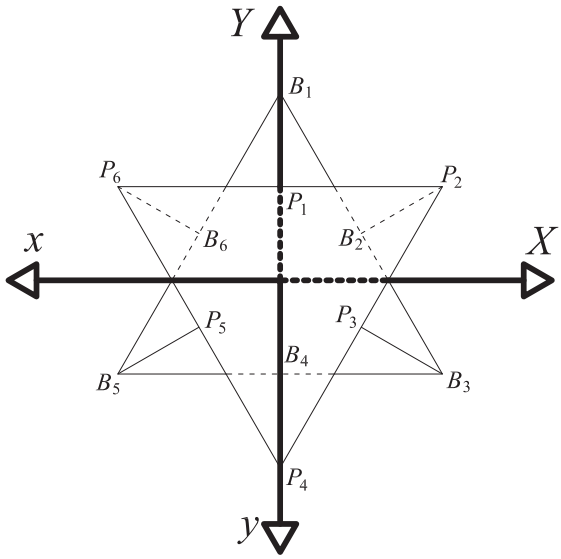

Figure 3.2: Positions of the leg anchor points on fixed base and moving platform of the A-pair at $\theta = 180°$.

position of the leg anchor points with the A-pair in the $\theta = 180°$ position. The reference frame attached to the fixed base with the origin at the geometric centre of the fixed base

triangle contains the X-, Y-, and Z-axes and the reference frame attached to the moving platform with the origin at the geometric centre of the moving platform triangle contains the x-, y-, and z-axes. The Z- and z-axes are co-linear, both pass through the geometric centres of both triangles and point in the same direction. As the moving platform rotates about the z-axis the path of every point on the moving platform projects onto a circle on the X, Y-plane of the fixed base reference frame. If points are represented in the fixed base reference frame by (X, Y, Z) and points in the moving platform reference frame by (x, y, z) then the projection of a point on the moving platform onto the X, Y-plane of the fixed base reference frame is given by

$$\begin{bmatrix} X \\ Y \end{bmatrix} = \begin{bmatrix} \cos(\theta) & -\sin(\theta) \\ \sin(\theta) & \cos(\theta) \end{bmatrix} \begin{bmatrix} x \\ y \end{bmatrix}, \tag{3.17}$$

and the paths of a point on the moving platform during the self-motions of the A-pair are parameterized as

$$\begin{aligned} X &= x\cos(\theta) - y\sin(\theta), \\ Y &= x\sin(\theta) + y\cos(\theta), \\ Z &= \rho\sin\left(\tfrac{\theta}{2}\right). \end{aligned} \tag{3.18}$$

The (X, Y) coordinates of the fixed base anchor points are:

$$\begin{aligned} B_1 &: (0, \frac{a\sqrt{3}}{3}), & B_2 &: (\frac{a}{4}, \frac{a\sqrt{3}}{12}), \\ B_3 &: (\frac{a}{2}, -\frac{a\sqrt{3}}{6}), & B_4 &: (0, -\frac{a\sqrt{3}}{6}), \\ B_5 &: (-\frac{a}{2}, -\frac{a\sqrt{3}}{6}), & B_6 &: (-\frac{a}{4}, -\frac{a\sqrt{3}}{12}), \end{aligned} \tag{3.19}$$

where a is the length of one edge of the congruent fixed base or moving platform triangles (see Figure 2.12). The (x, y) coordinates of the moving platform anchor points are:

$$\begin{aligned} P_1 &: (0, -\frac{a\sqrt{3}}{6}), & P_2 &: (-\frac{a}{2}, -\frac{a\sqrt{3}}{6}), \\ P_3 &: (-\frac{a}{4}, \frac{a\sqrt{3}}{12}), & P_4 &: (0, \frac{a\sqrt{3}}{6}), \\ P_5 &: (\frac{a}{4}, \frac{a\sqrt{3}}{12}), & P_6 &: (\frac{a}{2}, -\frac{a\sqrt{3}}{6}). \end{aligned} \tag{3.20}$$

For the examination of A-pair self-collisions the value of the variable a is invariant and can be set to unity without loss in generality. All A-pairs that satisfy the requirement of the leg lengths equal the height of the anchor point triangles will have the same physical joint limits due to self-collisions if the radius of the legs is ignored, regardless of the value of a. The value of ρ depends on the A-pair size and from Equation (3.4) for the case $a = 1$, $\rho = 0.816$. From Equation (3.3) the length of the legs that satisfy the constraints of the A-pair is $l_{(legs)} = 0.866$.

Knowing the coordinates of the leg anchor points on the moving platform in the moving platform reference frame, their coordinates in the fixed base reference frame as a function of θ are obtained by Equation (3.18), providing the paths of the leg anchor points throughout the self-motions. The positions of the fixed base anchor points do not change relative to the fixed base reference frame. With the leg anchor points on the fixed base and moving platform defined in the same frame the lines representing the legs can be determined as functions of θ. The distance between the lines is a measure of where the legs will interfere with one another.

3.2.2 Leg Interference During Self-Motions

The examination of leg interference uses Plücker coordinates (discussed in Section 2.8) to represent the centreline of each leg and cylinder collision detection (Section 2.9) is used to determine at what values of θ the legs interfere with one another.

Determination and Analysis of Leg Centrelines

The determination of the leg centrelines uses the coordinates of the anchor points on both the fixed base and moving platform which were obtained in Section 3.2.1. The anchor points on the fixed base do not change in the fixed base reference frame while the position of the moving platform anchor points move in the fixed base reference frame according to Equation (3.18) as θ varies. Using the homogeneous coordinates of the two anchor points for each leg, the Plücker coordinates that represent the centerline of each leg are obtained by Equation (2.87). As θ varies, so do the Plücker coordinates of each centreline.

As an example, the Plücker coordinates of the centerline of Leg 1 are computed using the base anchor point B_1 from Equation (3.19) and the platform anchor point P_1 from Equation (3.20) which are transformed to the base reference frame by Equation (3.18). The anchor point B_1 in the base reference frame is represented by the homogeneous point coordinates $(1, 0, \frac{a\sqrt{3}}{3}, 0)$ and P_1 in the base reference frame by $(1, \frac{a\sqrt{3}}{6}\sin\theta, -\frac{a\sqrt{3}}{6}\cos\theta, \rho\sin\frac{\theta}{2})$. Using Equation (2.88) the Plücker coordinates of the line connecting the two points are represented by the array

$$p_1 = \left(\frac{a\sqrt{3}}{6}\sin\theta : -\frac{a\sqrt{3}}{6}(2 + cos\theta) : \rho\sin\frac{\theta}{2} : \frac{a\rho\sqrt{3}}{3}\sin\frac{\theta}{2} : 0 : -\frac{a^2}{6}\sin\theta \right). \tag{3.21}$$

From the observation of physical and computer A-pair models it is revealed that, aside from the theoretical – and physically unobtainable – home position where all of the legs lie on the same plane simultaneously, the leg interference will only occur between adjacent legs. That is, if the legs are numbered according to Figure 3.2, Leg 1 will interfere only with Leg 2 or Leg 6. To determine where this interference occurs using Plücker coordinates it is required to determine when two legs are coplanar. To do this one must compute $\Omega(p, q)$ using Equation (2.90), where p is the Leg 1 centreline and q either the Leg 2 centerline or the Leg 6 centreline ($\Omega(1, 2)$ and $\Omega(1, 6)$, respectively). The other combinations of adjacent legs yield identical results because of symmetry around the A-pair.

Figure 3.3 is a plot of $\Omega(1, 2)$ and $\Omega(1, 6)$ as θ is varied from 0° to 720°, one complete cycle of the A-pair. When $\Omega(p, q)$ is equal to zero the anchor points of the two corresponding legs are coplanar, meaning that the legs either intersect or are parallel. Clearly, if the intersection is finite the leg centrelines cross one another. If the intersection occurs in the plane at infinity the leg centrelines are parallel. It is only necessary to look at half of the cycle (0° to 360°) because the intersections repeat in the second half of the cycle.

From Figure 3.3 it is seen that $\Omega(1, 2) = 0$ at $\theta = 0^\circ$, $\theta = 120^\circ$, $\theta = 300^\circ$, and $\theta = 360^\circ$. At $\theta = 0^\circ$ and $\theta = 360^\circ$ the A-pair is in the home position and all legs are coplanar, this position is mechanically unaccessible because it requires that the fixed base and moving platform be coincident. A computer model of the A-pair has been used to check the other

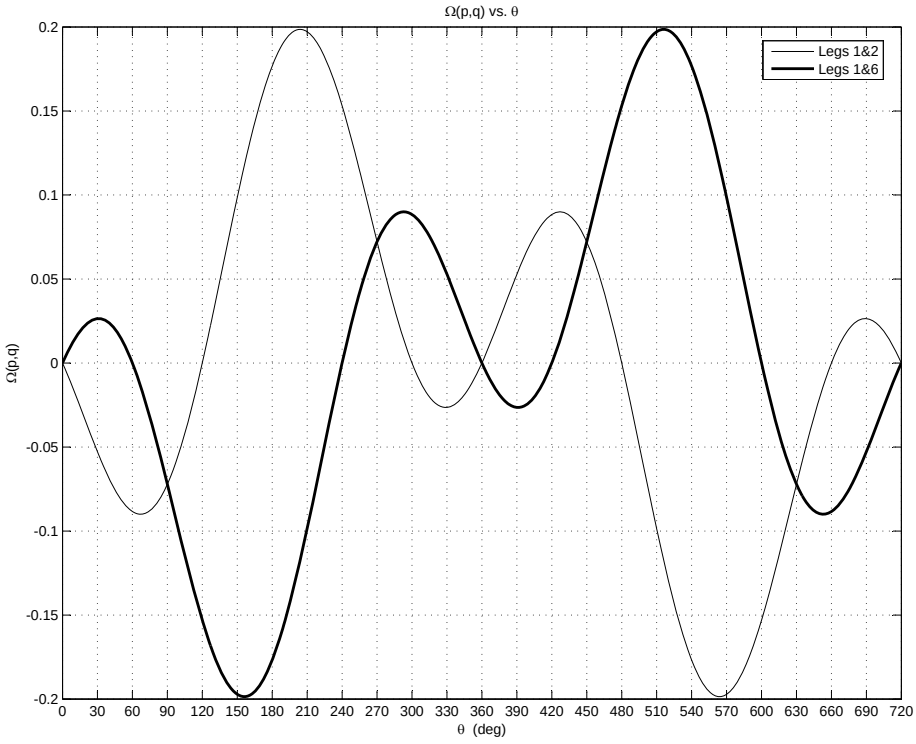

Figure 3.3: Plot of $\Omega(p, q)$ vs. θ for Legs 1&2 and Legs 1&6.

two instances of coplanar anchor points. At $\theta = 120°$ Leg 1 and Leg 2 are parallel and therefore do not interfere with each other, however at $\theta = 300°$ Leg 1 and Leg 2 intersect in one finite point. Similarly, $\Omega(1, 6) = 0$ at four instances over the half cycle. At $\theta = 0°$ and $\theta = 360°$ the A-pair is in the home position, at $\theta = 60°$ Leg 1 and Leg 6 intersect in one finite point and at $\theta = 240°$ Leg 1 and Leg 6 are parallel.

With information regarding the interference of adjacent legs it is now possible to determine the limits to the self-motions of an A-pair. Starting from the home position ($\theta = 0°$), where all of the legs are coplanar, there is no leg interference until $\theta = 60°$ where Leg 1 and Leg 6 intersect, then there is free motion until Leg 1 and Leg 2 intersect at $\theta = 300°$, and there is no more interference until $\theta = 360°$. The same intervals exist from $\theta = 360°$ to $\theta = 720°$. The region of interest to a practical A-pair is over the range $60° < \theta < 300°$. This

is the range that includes the fully extended A-pair ($\theta = 180°$) and provides for the largest range of motion without leg interference. There are 240° of motion available ($180° \pm 120°$). Over this range of motion the legs, fixed base, and moving platform do not interfere with one another.

This preliminary analysis is based on the centrelines of the legs, providing an ideal range of motion. In reality the legs are cylindrical, reducing the range of the self-motions. Knowing the absolute limits of the motion provides a starting point for the analysis of cylindrical legs.

Self-Motion Limits Due to Collisions of Cylindrical Legs

When considering the legs of the A-pair as cylinders with the leg centerlines as the axis the range of rotation available to the joint is reduced because the cylinder edges collide before the centrelines intersect. To determine the joint limits due to leg interference Plücker coordinates (Section 2.8) and cylinder collision testing (Section 2.9) are used.

The method for obtaining Plücker coordinates of the leg centerlines is presented in the previous section and the distance between lines is provided by Equation (2.97). As θ varies from 0° to 720° the distance between the centrelines of Leg 1 and Leg 2, d_{12}, as well as the distance between the centrelines of Leg 1 and Leg 6, d_{16}, are plotted versus θ in Figure 3.4. This plot corresponds with the results of the previous section in that the distance between lines is zero at the same values of θ where it was determined that the leg centrelines are coplanar, and hence intersect. The discontinuities in the plots (for example at $\theta = 120°$ and $\theta = 240°$) are situations where the legs are parallel and the four anchor points are coplanar. When two lines are parallel the denominator of Equation (2.97) vanishes.

The legs are represented as finite cylinders around the leg centerlines and the procedures of finite cylinder collision testing (Section 2.9) are used to determine the interaction between the adjacent legs. To determine the type of finite cylinder required the values of t_1 and t_2 (Section 2.9.2) for each pair of adjacent legs are obtained over the entire range of self-motions. Figure 3.5 shows the value of t_1 and t_2 versus θ for the cylinders representing Legs 1 & 2 and Legs 1 & 6. The plot shows that over the entire cycle of the A-pair self-motions

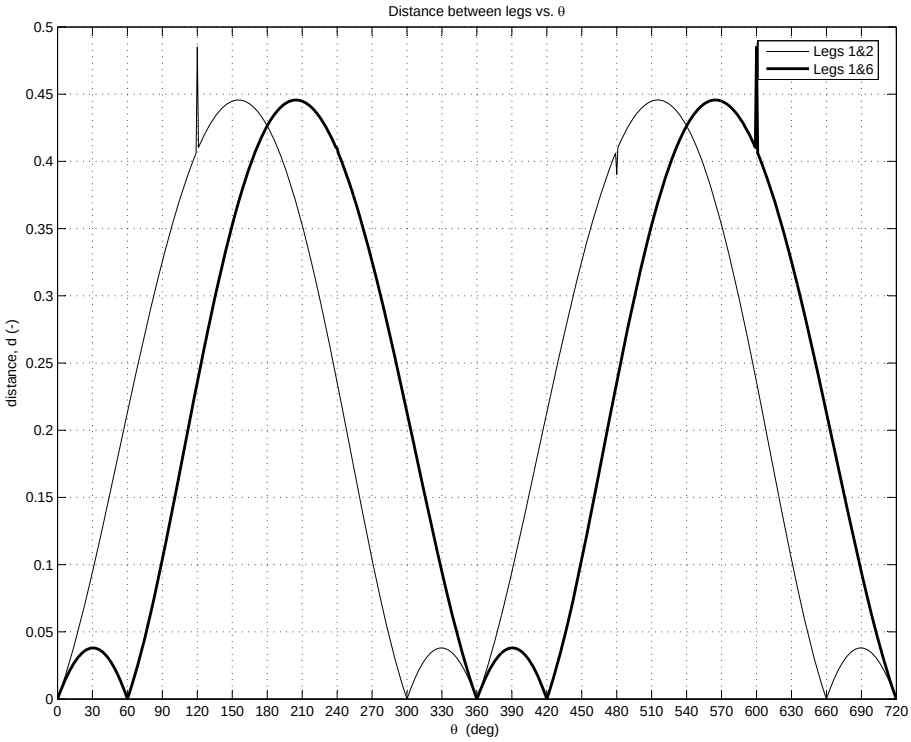

Figure 3.4: Plot of d vs. θ for Legs 1&2 and Legs 1&6.

both t_1 and t_2 remain within the range $0 < t_i < 1$, $i = 1, 2$ meaning that the intersection of the common normal with the centreline of the legs is always within the finite cylinder segment. Therefore the on-on form of finite cylinder testing is used, meaning the results presented in Figure 3.4 still apply.

For cylindrical legs with radius r the legs will interfere when the distance between the leg centrelines is $2r$ or less. From Figure 3.4 the range of θ available for legs of various r can be obtained by finding $2r$ along the distance axis and finding the corresponding values of θ where the leg interference occurs. For a typical A-pair where the absolute limits ($r = 0$) are $60^\circ < \theta < 300^\circ$, one must determine the lower rotation limit using the curve showing the distance between the centrelines of Leg 1 and Leg 6 and the upper rotation limit using the curve showing the distance between the centrelines of Leg 1 and Leg 2. Figure 3.6

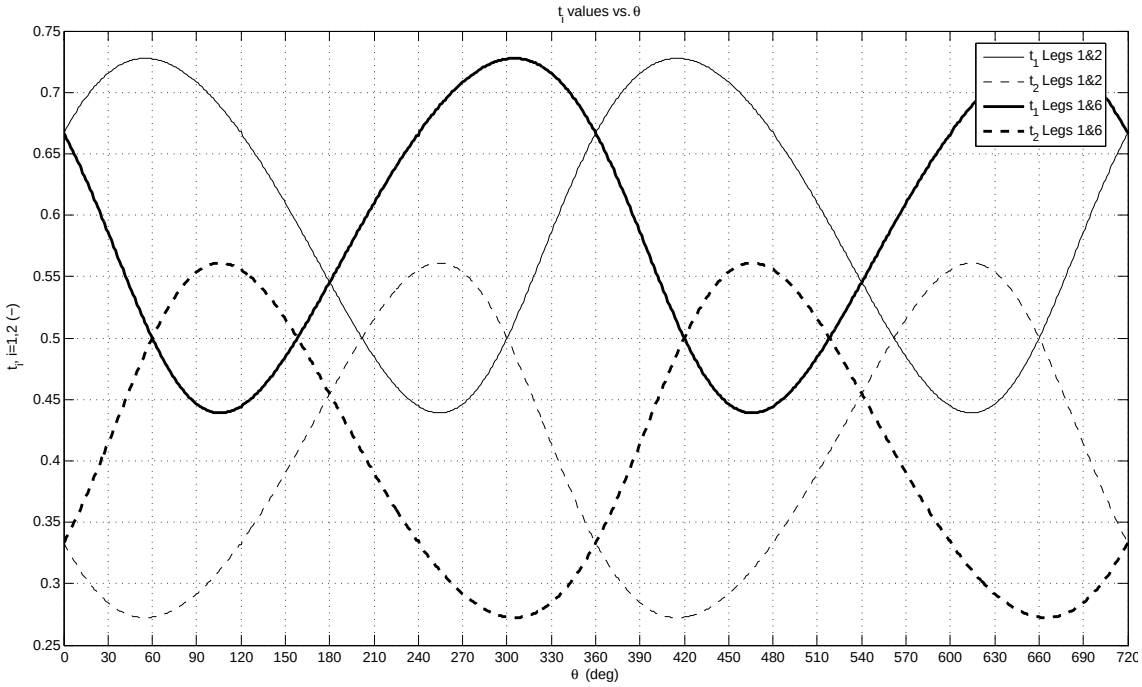

Figure 3.5: Plot of t_i, $i = 1, 2$ vs. θ for Legs 1 & 2 and Legs 1 & 6.

shows the range of θ available for legs of various radius (r), assuming that all legs have the same radius. The range is centred about $\theta = 180°$, *e.g.* a θ range of $200°$ means that $80° < \theta < 280°$.

3.3 Prototype 4A-Chain and Actuation

A prototype 4A-chain has been constructed to demonstrate the motion of A-pairs and A-chains. The joint orientations and link dimensions of the prototype 4A-chain are based on the relative locations of the first four joints and link dimensions of the Thermo CRS A465 robotic manipulator [95]. The prototype 4A-chain is shown in Figure 3.7 and the Thermo CRS A465 manipulator is shown in shown in Figure 3.8. In Appendix A an assembly drawing of the full prototype 4A-chain is shown in Figure A.1 and a more detailed assembly

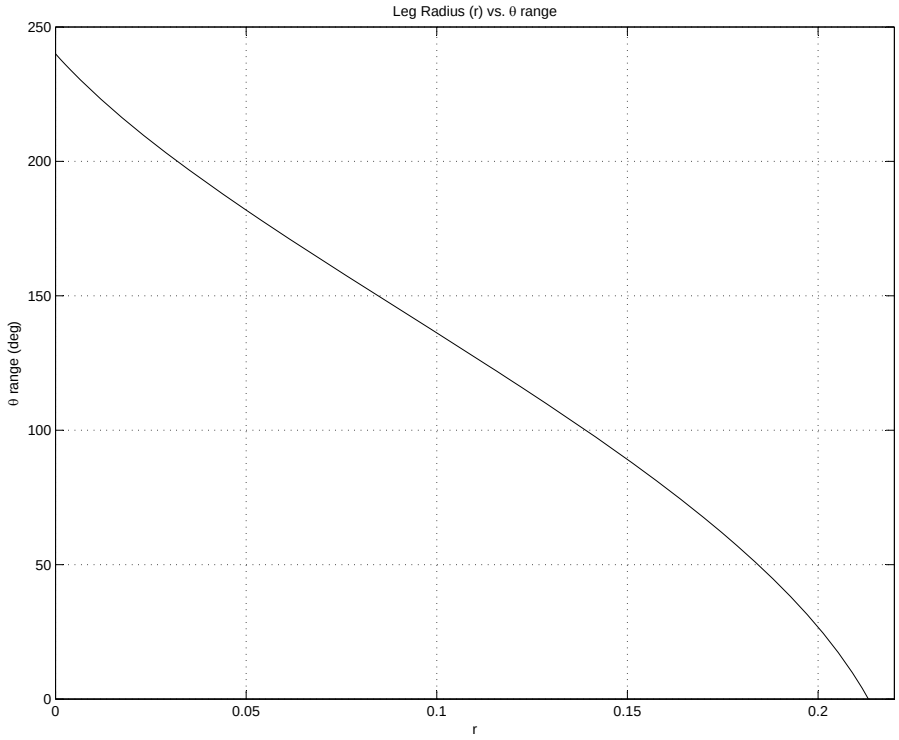

Figure 3.6: Plot of r vs. θ range from the Pücker method. The values of r correspond to the ratio of the leg radii to the length of one of the sides of the fixed base triangle, a.

drawing of the A-pair that make up the joints of the prototype is shown in Figure A.2. Figure A.3 shows the bill of materials. At the time of writing the motors and transmissions for the prototype manipulator have not been selected, though the actuation system has been designed conceptually.

The actuation system for the prototype 4A-chain consists of a central spline affixed to the moving platform that is constrained by three spur gears affixed to the base, all possessing identical pitch diameters. One of the spur gears on the fixed base is actively driven by a motor and transmission. The rotation of the driven spur gear rotates the central spline which rotates the moving platform. This arrangement allows the spline to translate along its axis of rotation as it is driven. The remaining two spur gears on the fixed base are passive and are present only to support the spur gear. This configuration is shown in

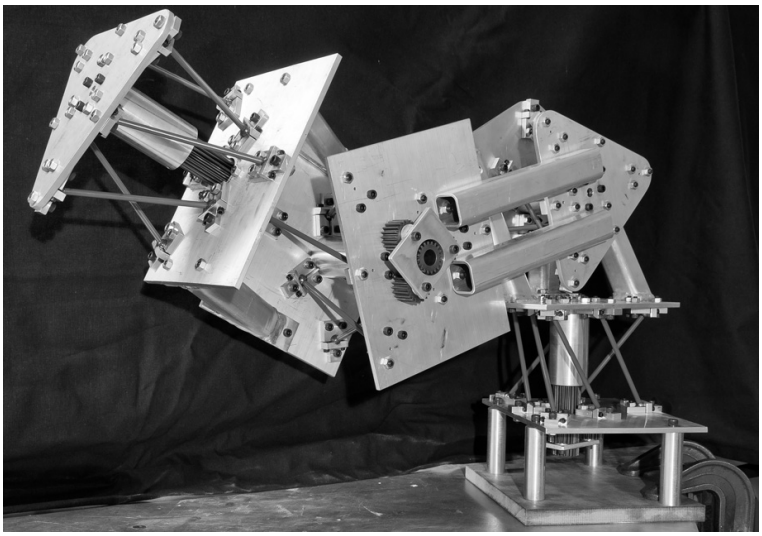

Figure 3.7: The prototype 4A-chain.

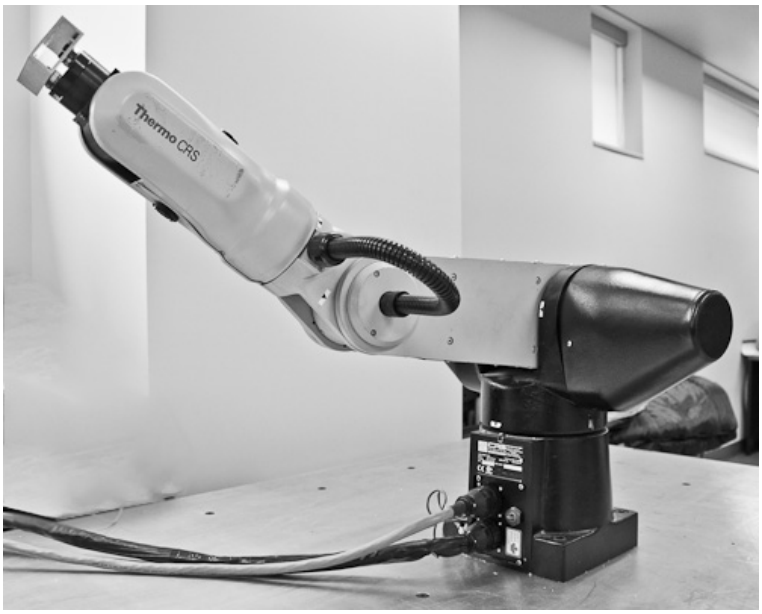

Figure 3.8: The Thermo CRS A465 robotic manipulator.

Figure 3.9. One major benefit of this actuation configuration is that the rotation of the moving platform is controlled directly and the entire A-pair range of motion is covered without any singularities. The motor and transmission for each joint are carried on the fixed base of each respective joint.

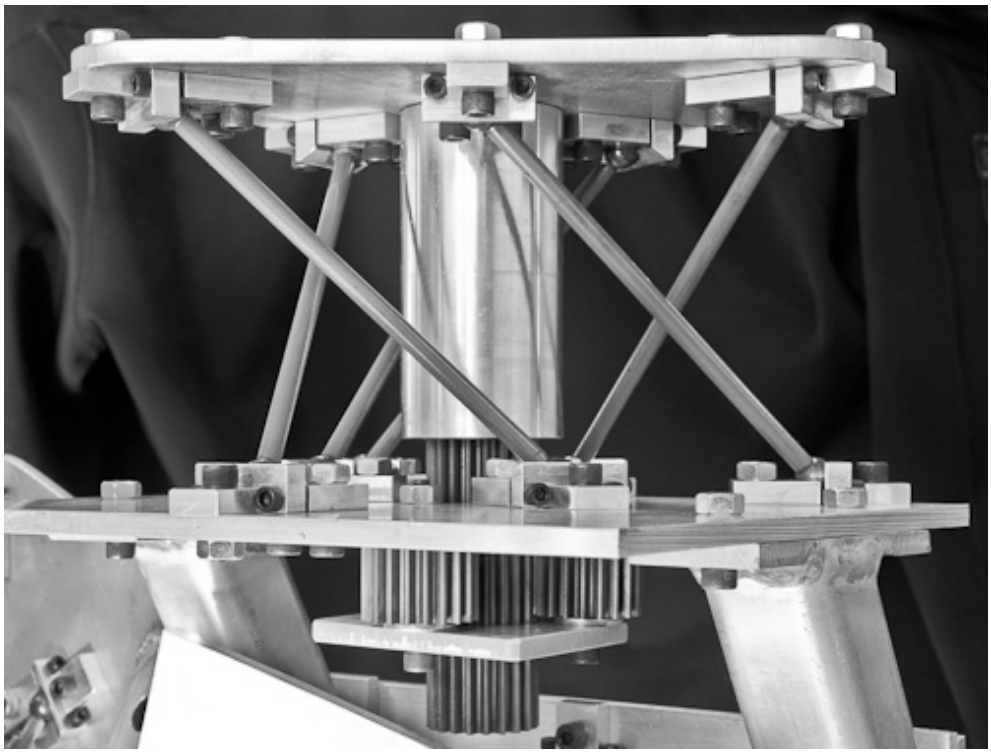

Figure 3.9: The actuation system for the prototype 4A-chain. Motors and transmissions are not shown.

3.4 A New Algorithm for Approximating the Reachable Workspace of a Serial Chain

In Section 2.2.5 an algorithm for obtaining the reachable workspace of serial and parallel manipulators by Castelli, *et al.* [55] was presented. In Castelli's algorithm many of the joints are swept multiple times and as the number of joints in the chain is increased, the time to determine the full workspace becomes prohibitively long. This is especially true if small joint step sizes are used. This section proposes a new algorithm for obtaining an approximate graphical representation of the reachable workspace of a serial kinematic chain that greatly reduces the computation time when compared to Castelli's algorithm. The implementation of the new algorithm using MATLAB is described, and the results are compared with Castelli's algorithm with regards to computation time and the resulting representations of the reachable workspace.

3.4.1 Obtaining the Reachable Workspace

The new algorithm for obtaining the reachable workspace uses parts of the algorithm of Castelli, *et al.* [55] for representing the reachable workspace of a manipulator as well as elements of the analytical method of Yang and Lee [56]. Like Castelli's algorithm the ambient space around the manipulator is discretized into three-dimensional rectangular prism elements called pixels. Each pixel is given a binary value: one if it can be reached by the manipulator's EE and zero if it cannot. Yang and Lee's work with revolute jointed manipulators works by first actuating only the joint closest to the EE and obtaining the workspace (a circle or circle segment for revolute joints). The second joint from the EE is then actuated and the entire workspace is rotated about the joint axis (the swept circle segment becomes a part of the surface of a torus). This process is repeated for each consecutive joint until the base is reached.

The new algorithm combines elements of the two methods to create a new three-dimensional binary array that represents the serial manipulator's reachable workspace and can be displayed using a three-dimensional scatter plot on a computer display. The following outlines the algorithm, whereas the detailed logic and mathematics behind each step are discussed in Section 3.4.2.

1. Determine the extreme values in each of the X-, Y-, and Z-axes that can be reached by the EE of the manipulator.

2. Select the desired resolution for each axis (the dimensions of each pixel), ΔX, ΔY, and ΔZ.

3. Define two three-dimensional arrays, $\mathbf{P}_{ijk}$ and $\mathbf{D}_{ijk}$, that each represent the discretized ambient space, where each of the elements in the array represents one pixel of the ambient space. The $\mathbf{P}_{ijk}$ array is a binary array whose elements are set equal to one if the EE of the manipulator can be placed within that pixel and zero if it cannot. The $\mathbf{D}_{ijk}$ array counts the number of times a particular pixel is reached by the EE as each joint of the manipulator is incremented ($\mathbf{D}_{ijk}$ is not necessary for the algorithm but is

used to provide additional information, it may be omitted to save time and memory if desired). The elements of both matrices are initially set to zero.

4. Define the joint and link parameters and define the maximum and minimum values of each joint variable.

5. Assemble the matrices for obtaining the direct kinematic equations (based on the equations found in Section 2.2.3).

   5.1 Assemble the $\mathbf{G}_m$, $m = 1 \ldots n$, matrices. These remain constant at all times.

   5.2 Assemble the $\mathbf{M}_m$, $m = 1 \ldots n$, matrices for the minimum value of each joint variable. Though the $\mathbf{M}_m$ matrices do not remain constant as the joints are actuated the matrix with the minimum joint variable is used several times throughout the algorithm.

6. Obtain the initial position of the EE with all joint variables at their minimum value.

   6.1 Determine, using the direct kinematics, the position of the EE in the ambient space (*i.e.* evaluate $\mathbf{T} = \mathbf{M}_1\mathbf{G}_1 \ldots \mathbf{M}_n\mathbf{G}_n$).

   6.2 Determine which pixel the EE is in (*i.e.* determine the element values of i, j, k in the $\mathbf{P}_{ijk}$ and $\mathbf{D}_{ijk}$ arrays).

   6.3 Set the elements of $\mathbf{P}_{ijk}$ and $\mathbf{D}_{ijk}$ corresponding to the reached pixel equal to one to indicate that the pixel corresponding to that array element has been reached.

7. Begin the process of transforming the workspaces one joint at a time, starting with the joint closest to the EE and working towards the base. The following steps are completed for each joint.

   7.1 Find the non-zero pixels in $\mathbf{P}_{ijk}$ and determine the (x, y, z) position of a specified point[1] within those pixels with respect to the global coordinate system.

   7.2 Determine the (x, y, z) position of the specified point within each non-zero pixel with respect to the joint being actuated.

[1] See Section 3.4.3 for a discussion of which point to use to represent the pixel.

7.3 Step through the range of motion for the joint from the minimum to the maximum joint variable values with the predetermined step size. At each step determine how the specified point within the non-zero pixels are transformed by the actuation of the joint (from the joint minimum to the current step). Determine which pixel the transformed point now lies in and update the $\mathbf{P}_{ijk}$ and $\mathbf{D}_{ijk}$ arrays accordingly.

When all joints have been stepped through the non-zero elements of the final $\mathbf{P}_{ijk}$ array represent an approximation of the reachable workspace of the manipulator. The elements of $\mathbf{D}_{ijk}$ contain a count of the number of times a pixel is reached by the EE. This can be used to optimize the step and size and pixel resolution and also to give a measure of the dexterity of the manipulator at a given point.

3.4.2 MATLAB Implementation

In order to compare the results of the new algorithm with Castelli's algorithm, it must be coded. This section describes how the new algorithm is implemented using MATLAB while providing some additional insight into how the steps of the algorithm (from Section 3.4.1) are put into practice. The decision to use MATLAB to implement the algorithm is based on the high level functions available for handling matrices and multidimensional arrays, particularly when determining which elements of a binary three-dimensional array are non-zero.

The geometry of the manipulator is defined using DH-parameters as per Section 2.2.2. The $\mathbf{G}_m$ matrices, $m = 1, \ldots, n$, are constructed using the DH-parameters and remain constant throughout the entire procedure. Also defined are the variables for the ambient space surrounding the manipulator such as the maximum and minimum values in the X, Y and Z directions (X_{max}, X_{min}, *etc.*); and the resolution of the pixels in each direction: ΔX, ΔY and ΔZ. The step size (the amount that the joint variable values are incremented between each iteration) is also selected and is based on the size of the pixels and the geometry of the manipulator. At this time trial and error is used to determine the best

value of the step size, however a better method for determining the pixel and step sizes may exist, perhaps based on the pixel dimensions and link lengths.

The array representations of the workspace, $\mathbf{P}_{ijk}$ and $\mathbf{D}_{ijk}$, are constructed based on the designated size and resolution of the ambient workspace. The elements of the two arrays are all set to zero to indicate that the corresponding pixels have not yet been reached by the EE of the manipulator.

With the manipulator geometry defined and the ambient space discretized it is now possible to start with the main algorithm. The first step is to find the initial position of the manipulator. To do this the $\mathbf{M}_m$ matrices are found for each Joint variable $m = 1, \ldots, n$ at its minimum value. The transformation matrix from the base coordinate system to the EE coordinate system, $\mathbf{T}$, for this initial position is found by the direct kinematics algorithm of Section 2.2.3 as

$$\mathbf{T} = \mathbf{M}_1\mathbf{G}_1 \ldots \mathbf{M}_m\mathbf{G}_m \ldots \mathbf{M}_n\mathbf{G}_n, \tag{3.22}$$

where n is the number of joints in the chain. The (X, Y, Z) position of the origin of the EE coordinate system is obtained from the first column of $\mathbf{T}$ (the second, third and fourth elements of that vector respectively) and adjusted such that the position $(0, 0, 0)$ is in the centre of the ambient space. The pixel coordinates corresponding to the EE position are obtained by

$$i = \text{floor}\left(\tfrac{X-\Delta X}{\Delta X}\right), \quad j = \text{floor}\left(\tfrac{Y-\Delta Y}{\Delta Y}\right), \quad k = \text{floor}\left(\tfrac{Z-\Delta Z}{\Delta Z}\right), \tag{3.23}$$

where the floor() operator returns the nearest integer that is less than or equal to the value inside the brackets (rounded towards negative infinity). These pixel coordinates correspond to an element in the discretized ambient space arrays $\mathbf{P}_{ijk}$ and $\mathbf{D}_{ijk}$ and the arrays are updated accordingly ($\mathbf{P}_{ijk}(i, j, k)$ is set equal to one to indicate that the pixel has been reached at least once and $\mathbf{D}_{ijk}(i, j, k)$ is incremented by one to count the number of times the pixel has been reached).

Each joint is then swept through once, starting with the joint closest to the EE (usually

Joint n) and then moving towards the base (Joint 1). The following describes the procedure for each joint sweep specifically designed for use with R-pairs and A-pairs, however it could be modified for any joint type.

Before the joint is stepped the previous workspace is determined with respect to the joint being actuated. In MATLAB the non-zero pixels from the 3D array $\mathbf{P}_{ijk}$ are found using the command `find`. The expression `[r,c]=find(P)` provides two vectors that identify the i, j and k index of each non-zero pixel. Each element of `r` represents the i index of the pixel in the array, the j index of each pixel is the remainder after dividing the elements of `c` by the maximum value of j in the $\mathbf{P}_{ijk}$ array (*i.e.* `rem(c,Psize(2))`, where `Psize = size(P)`), and the k index of the pixel is the nearest integer above (rounded towards positive infinity) the resultant of `c` divided by the maximum value of j in the $\mathbf{P}_{ijk}$ array (*i.e.* `ceil(c/Psize(2))`). Each pixel must now be represented by a point. The selection of which point within the pixel to use depends on how the resulting workspace representation is being used. Section 3.4.3 discusses this issue further, but for the description of the MATLAB code the centre point of the pixel is used. The centre point of each non-zero pixel (represented by (i, j, k) values) are converted to (x, y, z) coordinates (with respect to the global coordinates system with the origin at the centre of the three-dimensional ambient space array) by

$$\begin{aligned} x &= i\Delta X - \frac{X_{max} - X_{min}}{2} - \frac{\Delta X}{2}, \\ y &= j\Delta Y - \frac{Y_{max} - Y_{min}}{2} - \frac{\Delta Y}{2}, \\ z &= k\Delta Z - \frac{Z_{max} - Z_{min}}{2} - \frac{\Delta Z}{2}, \end{aligned} \tag{3.24}$$

and each centre point is represented by homogeneous coordinates by $\mathbf{x} = \begin{bmatrix} 1 & x & y & z \end{bmatrix}^T$. The transformation from the base frame to the frame at the end of Joint m is

$$\mathbf{T} = \mathbf{M}_1\mathbf{G}_1 \ldots \mathbf{M}_m. \tag{3.25}$$

Each centre point is then found with respect to the frame affixed to Joint m by $\mathbf{x}_{rel} = \mathbf{T}^{-1}\mathbf{x}$, where $\mathbf{x}_{rel}$ is the position vector of centre point of the pixel with respect to the joint being

actuated.

With the centre point of each non-zero pixel defined with respect to the joint being actuated the joint can be incremented by the step size from the minimum towards the maximum value. At each step the previous workspace (from the actuation of Joint $m+1$, or the initial position if $m = n$), defined by the centre point of each activated pixel, is transformed and added to the new workspace. Only the workspace of the previous joints are transformed, not the workspace of the previous steps of the current active joint.

Each centre point, $\mathbf{x}_{rel}$, is transformed by

$$\mathbf{x}'_{rel} = \mathbf{M}_{m,rel}\mathbf{x}_{rel}, \tag{3.26}$$

where $\mathbf{x}'_{rel}$ is the transformed centre point with respect to the joint being actuated and

$$\mathbf{M}_{m,rel} = \begin{bmatrix} 1 & 0 & 0 & 0 \\ 0 & \cos(\theta_{step} - \theta_{min}) & -\sin(\theta_{step} - \theta_{min}) & 0 \\ 0 & \sin(\theta_{step} - \theta_{min}) & \cos(\theta_{step} - \theta_{min}) & 0 \\ \rho\sin\left(\frac{\theta_{step}}{2}\right) - \rho\sin\left(\frac{\theta_{min}}{2}\right) & 0 & 0 & 1 \end{bmatrix}.$$

The variable θ_{step} is the value of the joint angle for the current step in the joint sweep and θ_{min} is the minimum joint angle for the joint being swept. The matrix $\mathbf{M}_{m,rel}$ describes the transformation from the minimum joint variable to the joint variable at the current step in the joint sweep. Note that $\mathbf{M}_{m,rel}$ is set up for A-pair joints, for R-pairs the geometric constant, ρ, is set to zero. For serial chains constructed using different types of kinematic pairs $\mathbf{M}_{m,rel}$ must be modified accordingly to account for each joint type.

The new point, $\mathbf{x}'_{rel}$, is defined relative to the active joint and its position relative to the base frame is $\mathbf{x}' = \mathbf{T}\mathbf{x}'_{rel}$. The x, y, and z components of the new point and Equation (3.23) are used to determine the pixel coordinates (i, j, k) and the arrays $\mathbf{P}_{ijk}$ and $\mathbf{D}_{ijk}$ are updated accordingly.

When the process of obtaining and transforming the previous workspace has been completed for each joint from Joint n to Joint 1, the final $\mathbf{P}_{ijk}$ array is the binary representation

of the reachable workspace.

3.4.3 Method Comparison and Discussion

This section compares the two algorithms both conceptually and based on the time required to execute for manipulators of varying lengths, the actual workspaces that the different algorithms produce and discusses the characteristics of the results from the new algorithm.

Comparing the Methods Conceptually

To determine if a pixel is reached by the EE, Castelli steps through all possible combinations of joint values obtainable by a manipulator one at a time. A simple example illustrates the sweep through all possible joint combinations. Imagine a three-jointed serial manipulator with Joint 1 being the joint closest to the base and Joint 3 closest to to the EE. Each joint is to be swept through its range of motion by looking at ten discrete values of the joint variable (ten joint variable steps is used as an example, in a real application a finer step-size may be desired). Joints 1 and 2 are held fixed in their first position and Joint 3 is swept through all ten variable values, the position of the EE is determined using the direct kinematic equations for the manipulator and the binary values of the pixels reached by the EE are set to one. Joint 2 is then stepped to its second joint variable value and Joint 3 sweeps through its range again. This is repeated until Joint 2 completely sweeps through all ten variable values, then Joint 1 is stepped to its next value and the sweeps of Joints 2 and 3 start again. By this method Joint 1 is stepped 10 times, Joint 2 is stepped $10 \times 10 = 100$ times and Joint 3 is stepped $100 \times 10 = 1000$ times. That means that direct kinematic equations of the entire three-jointed chain are computed 1000 times.

The new algorithm involves stepping through each joint once, starting with the joint closest to the EE. This means that Joint 3's value is changed 10 times, Joint 2's value is changed 10 times and Joint 1's value is changed 10 times, for a total of $10 + 10 + 10 = 30$ manipulator configurations. The complexity of the calculations at each step is greater for the new method as compared to simply evaluating the direct kinematics as with Castelli's method, however the large reduction in the number of times the calculations need to be

processed can result in large time savings depending on factors such as joint step size and the resolution of the discretized ambient space.

Algorithm Run Time Comparison

Both Castelli's and the new algorithms for obtaining the reachable workspaces of serial chains were programmed using MATLAB. The `tic` and `toc` functions were used to determine the time required to run the algorithms (excluding the plotting time and the time required to save the variables to disc, but including the definition of variables). The times vary slightly from run to run but usually remain within the same order of magnitude. All runs were completed on a computer with 2.00 GB of RAM and an Intel Core2 T5300 CPU with two 1.73 GHZ cores. The time results are provided in Table 3.1. From the table it

Table 3.1: Run time comparison of the old and new algorithms for obtaining the reachable workspace of a serial manipulator.

Chain	Castelli's Algorithm	New Algorithm
1R	0.02 sec.	0.3 sec.
2R	2.3 sec.	0.7 sec.
3R	1.45×10^3 sec. $\approx$ 24 min.	2.3 sec.

can be seen that for 1R-chains the new algorithm is outperformed by Castelli's algorithm, however as more joints are added the new algorithm executes much faster than its predecessor. At just three joints the new algorithm outperforms Castelli's algorithm by taking just 2.3 seconds compared to over 24 minutes. The reachable workspace of a four-jointed chain can be obtained in about 12.8 seconds with the new algorithm and would be many orders of magnitude longer using Castelli's algorithm. For all of the test cases run for this comparison the joint step size was 0.5°, the joints were swept 240° (to correspond to the maximum range of an A-pair), the pixel dimensions (ΔX, ΔY and ΔZ) were all 0.5 units and the dimensions of the ambient space varied depending on the manipulator dimensions, but were constant between the different algorithms.

The algorithms also differ in how they react to changes in the step size or the discretization of the ambient space. Castelli's algorithm is greatly affected by the joint step size because if the step size is doubled (say from 0.5° to 1°) each sweep will take half as long, so the time savings are dependant on the number of joints. With the new algorithm the doubling of the step size essentially means halving the time (there is an almost linear relationship). As for changing the resolution (pixel size), Castelli's algorithm is unaffected with regards to run time because the same number of computations are required, however the new algorithm is greatly affected because it changes the number of calculations that are required at each step. A test where the dimensions of the cubic pixel were reduced from 0.5 to 0.1 units for the 3R-chain took 42.4 seconds or if the dimension was increased to 1 unit it took 1.2 seconds to approximate the workspace (compared to 2.3 seconds for a pixel dimension of 0.5 units).

Algorithm Output Comparison

The output of the two algorithms is not identical and the following compares the reachable workspace estimates from the two algorithms and discusses the reasons for the discrepancy and potential methods for reducing or accounting for it. It is important to recognize that both algorithms only produce an approximation of the workspace because of the discretization of the ambient space. The EE may pass through only a small piece of the corner of a pixel yet the entire pixel is activated.

The reachable workspace of the 3R-chain with the DH-parameters defined in Table 3.2. is shown in Figure 3.10 where the reachable workspaces obtained by both algorithms are compared. It is difficult to gather much information from the plot other than recognizing

Table 3.2: DH-parameters of a 3R-chain.

i	a_i	d_i	α_i
1	5	8	180°
2	2	8	90°
3	2	8	0°

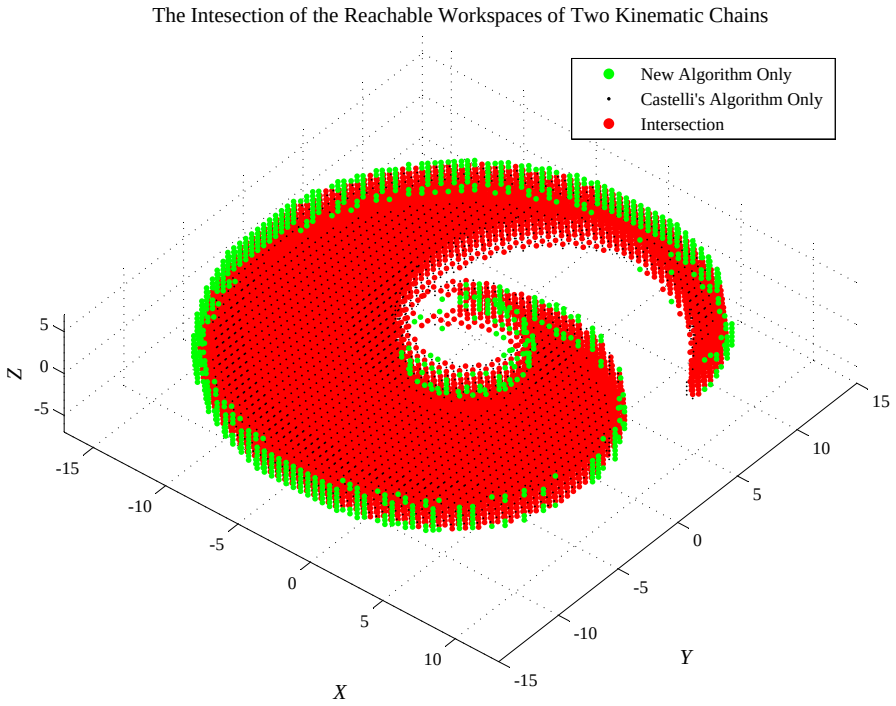

Figure 3.10: Comparison plot of the reachable workspaces of a 3R-chain obtained with the new algorithm and Castelli's algorithm.

that the shapes are very similar and that the patches of pixels that do not coincide are only a single pixel away from overlapping. The new algorithm reaches 14897 pixels, Castelli's algorithm reaches 16157 pixels and they share 13977 (86%) of those pixels.

Pixel Size

The dimensions of the pixels used to discretize the ambient space around the manipulator has a large effect on both the computation time and accuracy of the new algorithm. When the pixel size is decreased, more pixels are reached during the sweeping of a joint. This means that during each subsequent joint sweep more computations are required because more non-zero pixels exist. The selection of the pixel size comes down to a balance between time, computing power and desired accuracy.

With regards to accuracy, because we are representing the entire pixel as a point at the centre of that pixel, the larger the pixel the less the final result will represent the true

workspace of the manipulator. This is because the EE may only clip a small part of a certain pixel yet in later joint sweeps that pixel is represented by a point at its centre. For a pixel with all dimensions of 0.5 units that could be as much as 0.433 units, the distance from one corner of the pixel to its centre. This means the resulting representation of the workspace may be larger than the actual workspace. The opposite may be true if the EE passes through a large part of the pixel and by representing the pixel by a point at the centre the resulting workspace may be smaller than the actual workspace. The overall impact of the selected pixel size depends on the size of the manipulator relative to the pixel size.

Pixel Representation as a Point

The topic of accuracy vs. pixel size raises another question with regards to how the pixel is represented as a point. Perhaps it is not best to represent the pixel as its centre point but as maybe the corner or point closest to the global origin or maybe furthest away. This may depend on the objective of the analysis.

From a design point of view, if it is desirable for the manipulator to be guaranteed to reach a certain volume of space it may be advisable to use the coordinates of the corner of the pixel nearest to the origin, that way the resulting workspace would be smaller than that of the actual manipulator and coverage of the desired workspace would be ensured. Alternatively if the manipulator is to be used in a confined space and it needs to be certain that the reachable workspace fit in that confined space it may be desirable to use a point at the corner of the pixel furthest from the origin such that the resulting representation of the workspace is larger than that actually obtainable by the manipulator.

3.5 The Reachable Workspace of A-Chains

The coupled translation and rotation of A-pairs means that as each joint in an nA-chain is actuated the manipulator EE will translate parallel to the axis of rotation of the joint as a function of the rotation angle. The translation component of the coupled motion is not present in chains constructed using R-pairs and thus it is necessary to examine the effect

of the coupled motion on the workspace of the A-chain and compare it to that of similar R-chains.

There are infinitely many configurations of manipulators that can be constructed with different numbers of joints and different sets of DH-parameters making it difficult to simply compare R-chains with A-chains. To gain an initial understanding of how the reachable workspaces of R-chains and A-chains compare this section begins with an examination of short chains comprising one and two joints before examining specific configurations of similar 4R- and 4A-chains.

For this section all joints will be limited to the range $60^\circ \leq \theta_i \leq 300^\circ$ in order to correspond to the absolute maximum range of an A-pair. Self-collisions between the links of the manipulator are ignored. In order to show the characteristics of the A-chain workspace a very large A-pair relative to the size of the links has been used (the length of one of the sides of the triangles, a, has been set to 10). In reality the joint would likely be much smaller than the links and the shape of the workspace would not be as exaggerated. This is important to remember since at first glance the R- and A-chain workspaces bear little resemblance to one another.

3.5.1 The Reachable Workspaces of Single-Joints

Examining the workspace of chains with only one joint appears trivial but it is important to understand how each joint in the chain works in order to fully understand and predict how a chain of multiple joints might move in space.

Figure 3.11 compares the reachable workspaces of a 1R-chain and a 1A-chain. The 1R-chain has the DH-parameters (the units are irrelevant): $a_1 = 10$, $\alpha_1 = 0^\circ$, and $d_1 = 6$, and the DH-parameters of the 1A-chain are: $a_1 = 10$, $\alpha_1 = 0^\circ$, $d_1 = 0$ and the fixed component of the joint angle is $\theta_{f1} = 0^\circ$. The difference in the joint offset (d_1) between the two manipulators is set so the workspaces of the manipulators will overlap.

The workspace of the 1R-chain is a planar semi-circle while the workspace of the 1A-chain is a semi-circle when projected onto the X-Y plane, but the Z value varies according to $Z = \rho \sin(\theta_v/2)$. Near the beginning and end of the range of rotation the 1A-chain

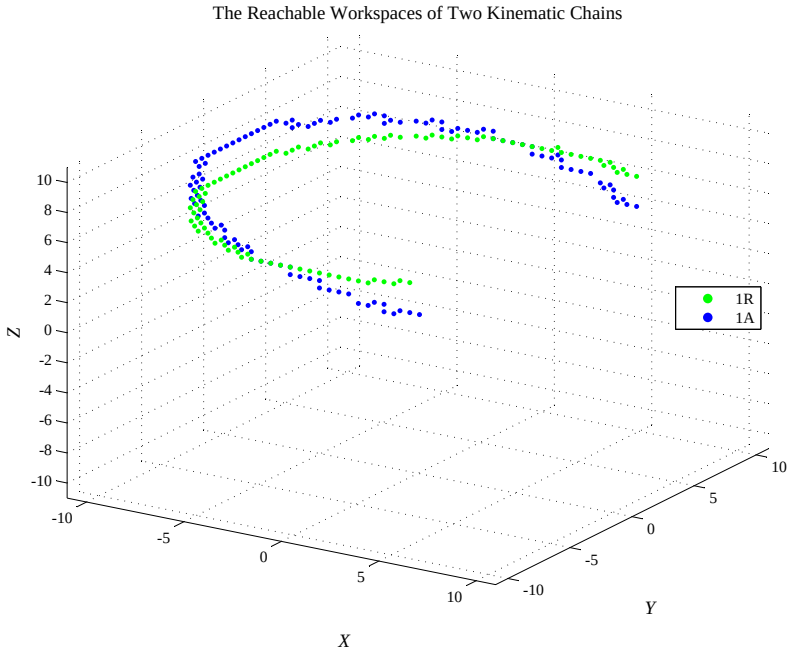

Figure 3.11: Plots of the reachable workspaces of a 1R-chain and a 1A-chain.

workspace is below the 1R-chain while near the middle of the range of rotation it is above. In Figure 3.11 it appears that the workspaces share three points in common around each intersection (they share six pixels), but this is a result of the discretization of the ambient space and in fact the reachable workspaces intersect in two points, one at each crossing. The orientation of the EE of both manipulators is the same for identical joint angles but aside from the two intersection points the EE position is different.

3.5.2 The Reachable Workspaces of 2-Joint Chains

Comparing two-jointed chains becomes increasingly difficult because there are many more configuration possibilities. Three cases are examined: two parallel joint axes (the workspace of the 2R-chain is planar); two skew perpendicular axes; and two intersecting perpendicular axes.

Parallel Axes

When a 2R-chain has parallel joint axes (and links with non-zero lengths) the reachable workspace lies on a plane. The shape of the planar workspace depends on the link lengths and available range of motion of each joint, however the reachable workspace will typically be an annulus segment whose thickness depends on the length of the second link and the range of rotation of the second joint.

The DH-parameters of the 2R- and 2A-chains that are compared are listed in Table 3.3. Joint offsets (d_i) of six units were used for the 2R-chain in order to remain consistent with

Table 3.3: DH-Parameters of the two chains with two parallel axes.

Chain/Link i	a_i	α_i	d_i	θ_{fi}	θ Range
2R-Chain					
1	10	180°	6	N/A	$60° \leq \theta_1 \leq 300°$
2	5	0°	6	N/A	$-120° \leq \theta_2 \leq 120°$
2A-Chain					
1	10	180°	0	0°	$60° \leq \theta_1 \leq 300°$
2	5	0°	0	180°	$60° \leq \theta_2 \leq 300°$

the 1R-chain from the previous section. The link twist of 180° was used so that the plane of the 2R-chain reachable workspace is on the X-Y plane at $Z = 0$. The reachable workspace of the 2R-chain with parallel axes is illustrated in Figure 3.12 (a).

The workspace of the 2R-chain is to be compared to a dimensionally similar 2A-chain. Because of the coupled translation and rotation the reachable workspace of the 2A-chain is not planar, but a more complex shape, see Figure 3.12 (b). To gain better understanding of the shape features, several cross-sections of the workspace are examined in Figure 3.13.

The cross-sections show that the 2A-chain workspace does not contain any large planar segments like the 2R-chain, suggesting that the reachable workspaces of the two types of chains have little in common.

Using the pixel representation of the ambient space around the manipulator it is possible to determine which pixels are reached by both types of manipulators, this gives some insight into the intersection of the two workspaces. It must be noted that because of the

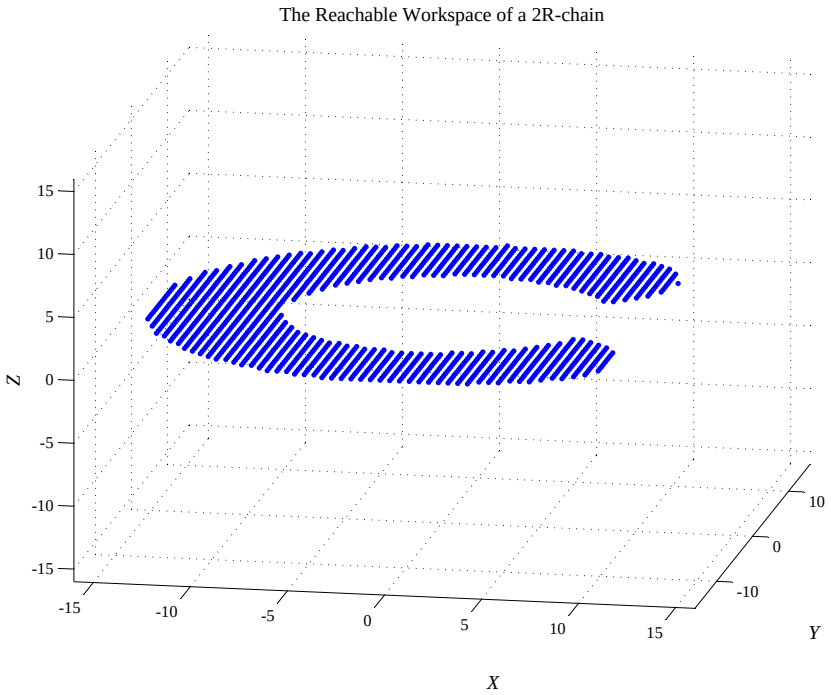

(a)

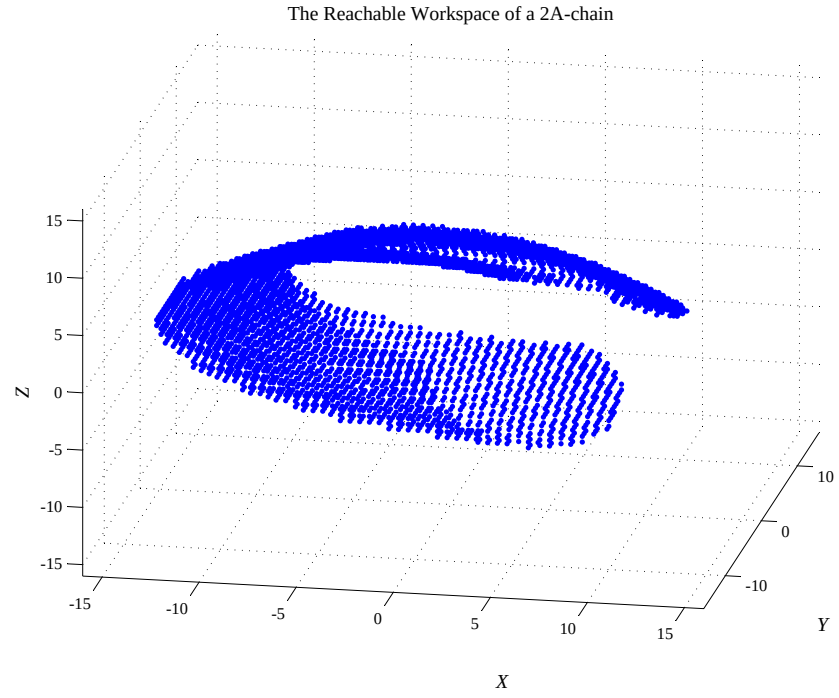

(b)

Figure 3.12: Plots of the reachable workspace of (a) a 2R-chain with parallel axes and (b) a 2A-chain with parallel axes.

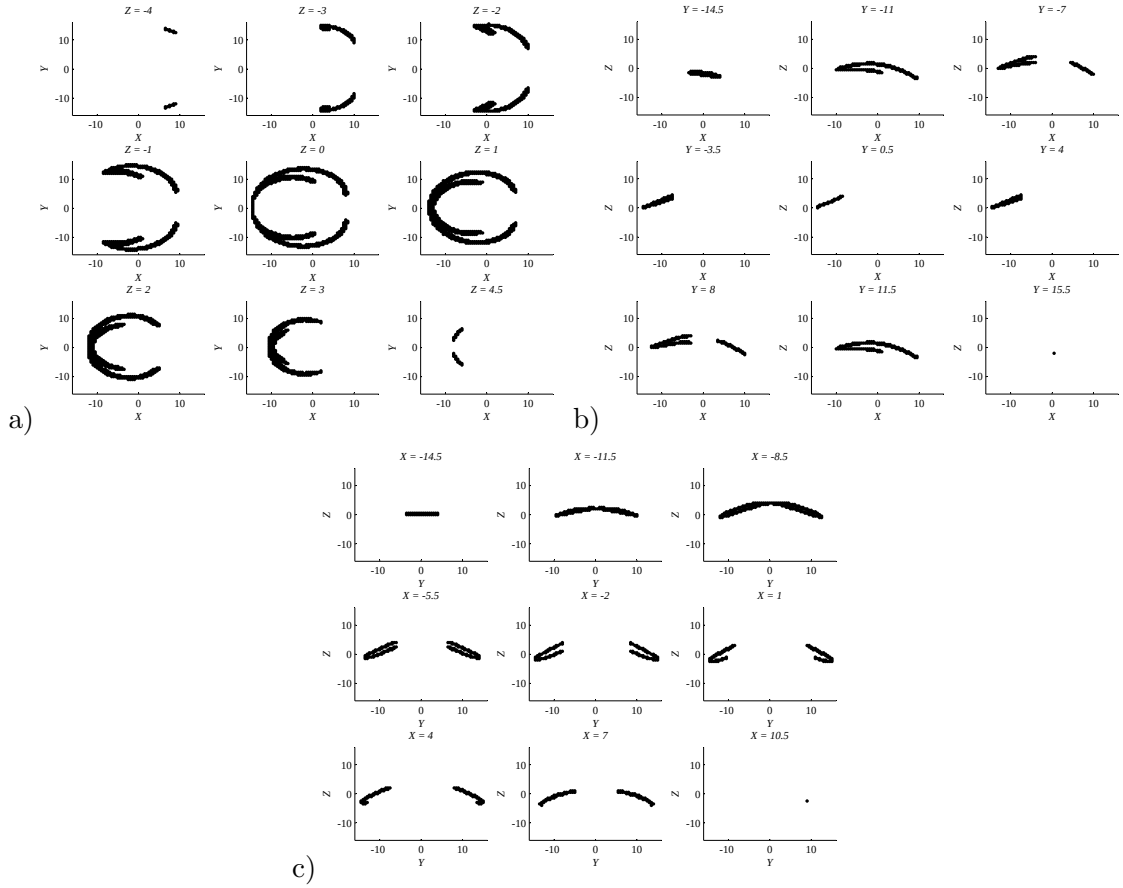

Figure 3.13: Cross sections of the reachable workspace of a 2A-chain with parallel axes along a) the Z-axis, b) the Y-axis and c) the X-axis.

discretization of the ambient space the same pixel may be activated, but in reality the same exact point in space has not been reached. Figure 3.14 shows the intersection of the workspaces. The intersection appears to be segments of a plane, but in reality it is likely curves on the plane. This is similar to the point intersection in Figure 3.11 appearing as three pixels because of the coarse discretization of the ambient space.

Non-Intersecting Perpendicular Axes

When the axes of the 2R-chain are perpendicular, but not intersecting, the reachable workspace differs from that of the two parallel axes configuration in that its reachable workspace is no longer planar. The DH-parameters of the two 2R- and 2A-chains with non-intersecting perpendicular axes are listed in Table 3.4. For the 2R-chain joint offsets of

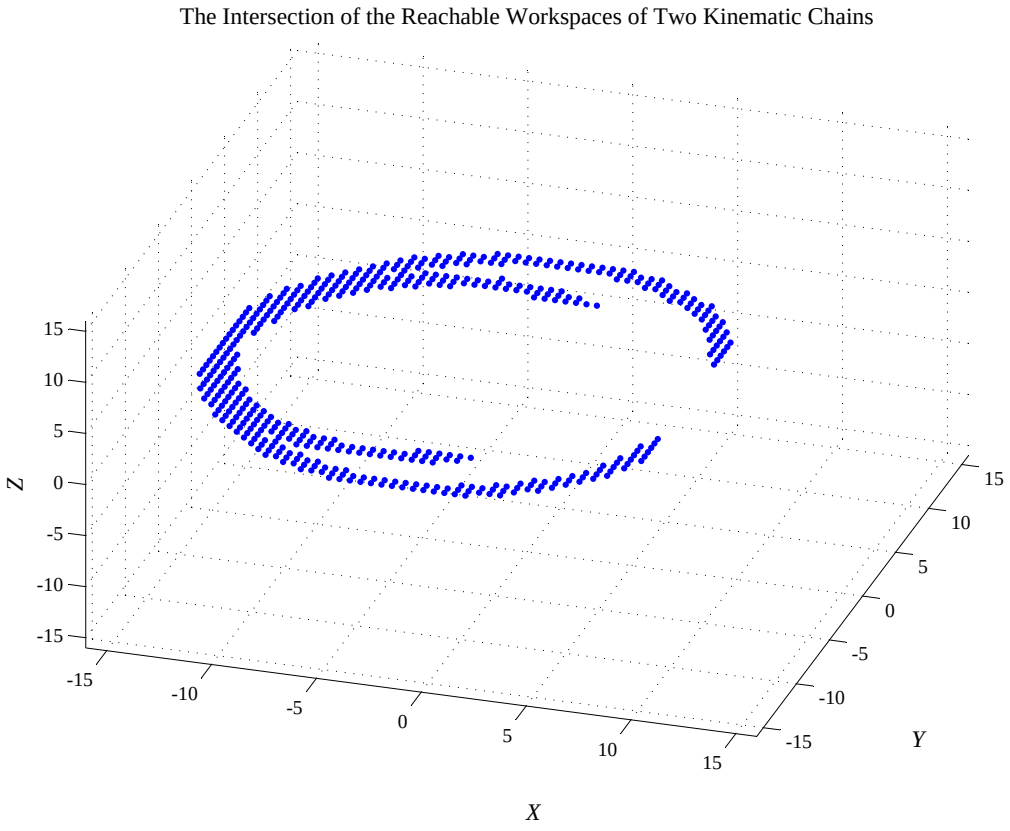

Figure 3.14: Plot of the intersection of the 2R-chain and 2A-chain reachable workspaces for 2-jointed chains with parallel axes.

Table 3.4: DH-Parameters of the two chains with two non-intersecting perpendicular axes.

Chain/Link i	a_i	α_i	d_i	θ_{fi}	θ Range
2R-Chain					
1	10	90°	8	N/A	$60° \leq \theta_1 \leq 300°$
2	5	0°	8	N/A	$-120° \leq \theta_2 \leq 120°$
2A-Chain					
1	10	90°	0	0°	$60° \leq \theta_1 \leq 300°$
2	5	0°	0	180°	$60° \leq \theta_2 \leq 300°$

$d_i = 8$ were used to put the two workspaces in the same region of the ambient space. The pixel resolution for the discretization of the ambient space is 0.5 units.

The reachable workspace of the 2R-chain is the toroidal section with a plane of symmetry parallel to the X-Y plane at $Z = 8$, seen in in Figure 3.15 (a). At first glance the reachable

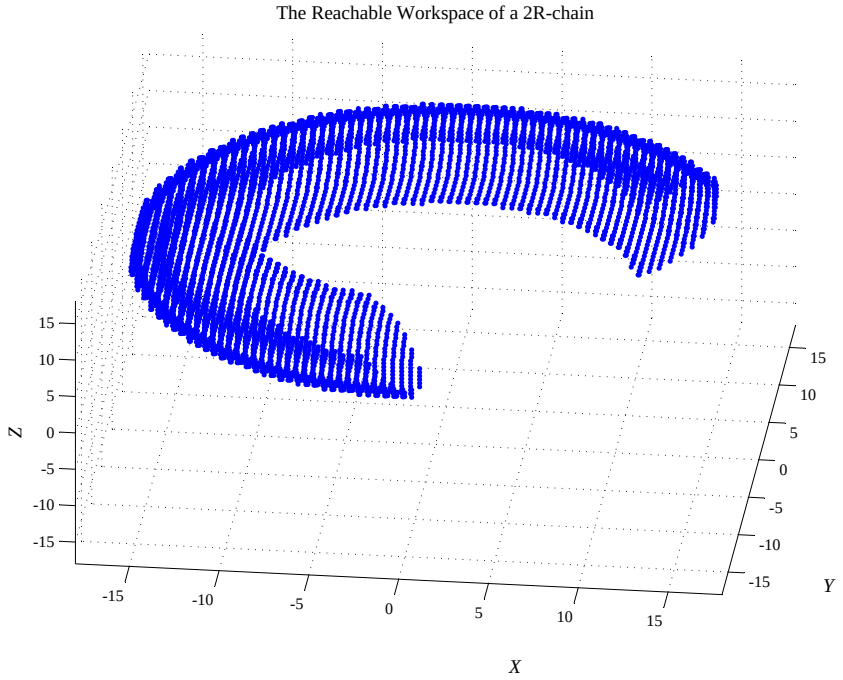

(a)

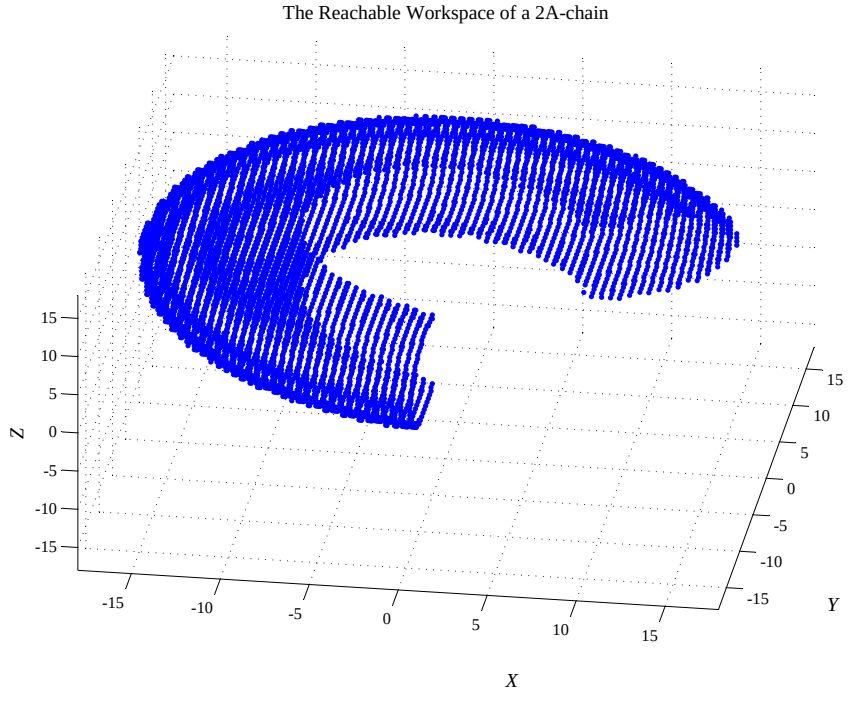

(b)

Figure 3.15: Plots of the reachable workspace of (a) a 2R-chain and (b) a 2R-chain, both with non-intersecting perpendicular axes.

workspace of the geometrically similar 2A-chain, shown in Figure 3.15 (b), appears to be similar to that of the 2R-chain, but the 2A-chain workspace has no plane of symmetry, as can be seen in the cross-sections of the workspace in Figure 3.16. An estimate of the intersection

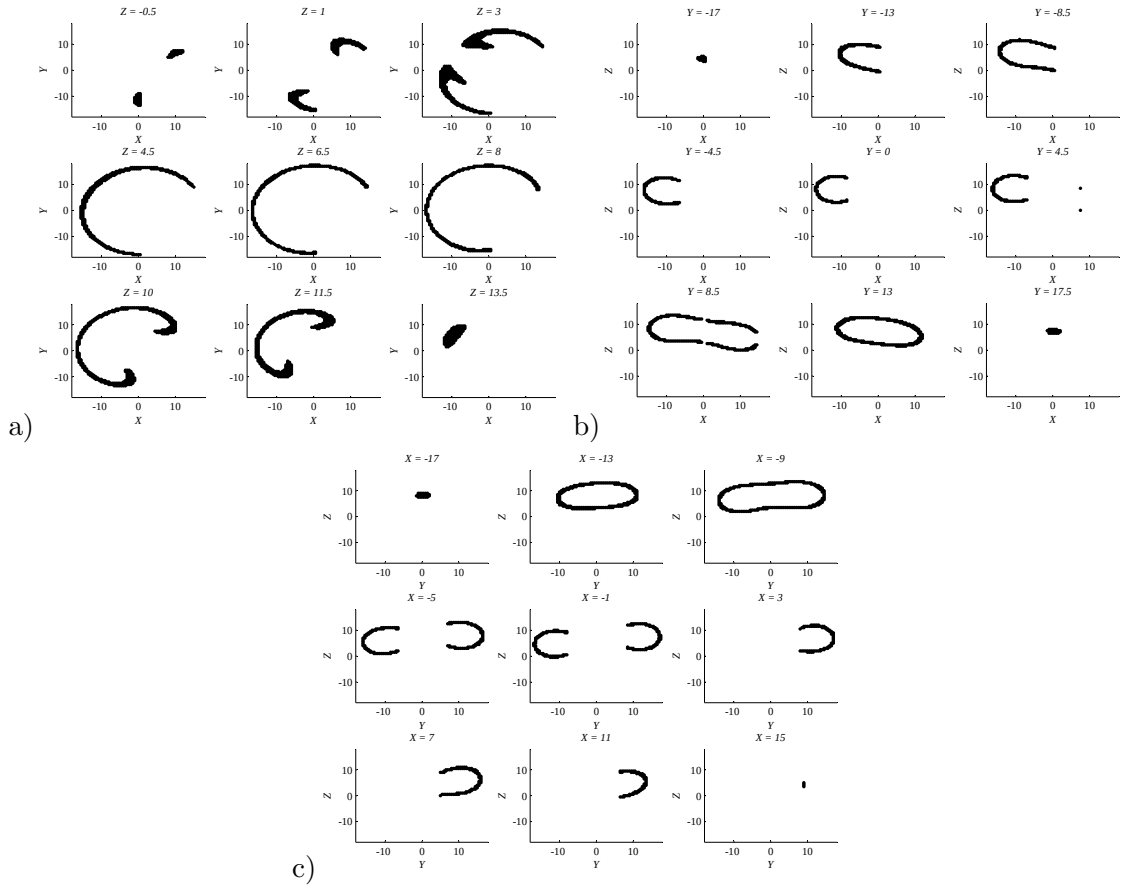

Figure 3.16: Cross sections of the reachable workspace of a 2A-chain with non-intersecting perpendicular axes along a) the Z-axis, b) the Y-axis and c) the X-axis.

of the reachable workspaces of the two manipulators can be obtained by determining which pixels in the ambient space are reached by both the 2R- and 2A-chain. Figure 3.17 reveals the intersection of the two workspaces and the scatter plot of the common pixels shows that the two workspaces intersect in a planar semi-circle. Some of the additional pixels that the two workspaces have in common are artifacts of the coarseness of the pixel's resolution. This shows that the 2A-chain can only reach a somewhat small number of the same points as a 2R-chain. Regardless, the study so far has not involved any quantitative comparisons (*i.e.* workspace area, *etc.*) between chain types. Such discussion is left until Section 3.5.3

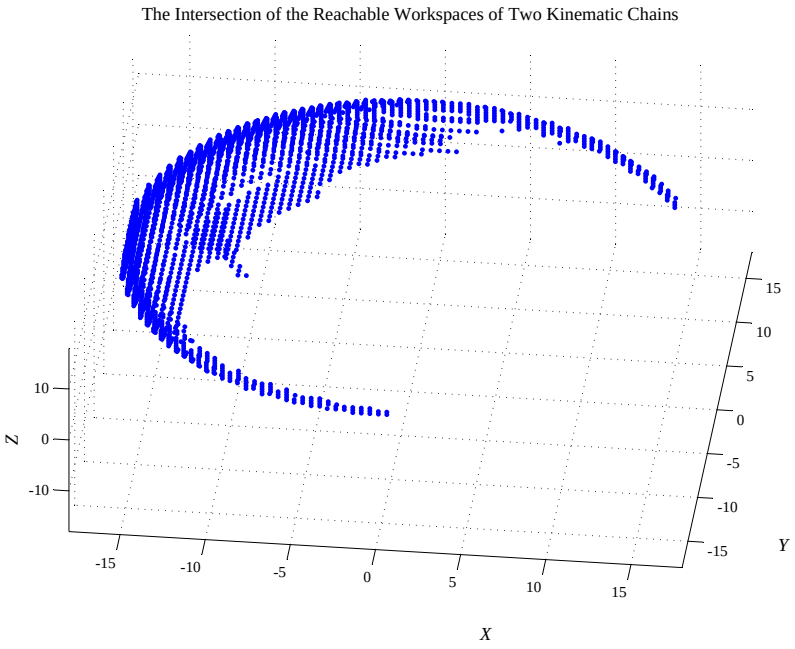

Figure 3.17: Plot of the intersection of the 2R-chain and 2A-chain reachable workspaces for 2-jointed chains with non-intersecting perpendicular axes.

where the reachable workspaces of four-jointed chains are examined.

Intersecting Perpendicular Axes

The pixel representation of the reachable workspace of a 2R-chain with perpendicular intersecting axes is a band of pixels that lies on a cylinder about the axis of the first joint. The DH-parameters of the 2R- and 2A-chains are provided in Table 3.5. The joint offset of the second joint, $d_2 = 18$, was selected to account for the length of the first link (different

Table 3.5: DH-Parameters of the two chains with two intersecting perpendicular axes.

Chain/Link i	a_i	α_i	d_i	θ_{fi}	θ Range
2R-Chain					
1	0	$-90°$	8	N/A	$60° \leq \theta_1 \leq 300°$
2	5	$0°$	18	N/A	$-120° \leq \theta_2 \leq 120°$
2A-Chain					
1	0	$90°$	0	$0°$	$60° \leq \theta_1 \leq 300°$
2	5	$0°$	10	$180°$	$60° \leq \theta_2 \leq 300°$

from a_1 for intersecting joint axes) that is 10 units long and also to account for the inherent joint offset of A-pairs, which is approximately 8 units.

Figure 3.18 (a) shows the reachable workspace of a 2R-chain with intersecting perpendicular axes. The workspace is characterised as a semi-circular band with width a_2 and radius d_2 (the length of the first link plus the joint offset of the second joint). The workspace has a plane of symmetry that is offset from the X-Y plane by the joint offset of the first joint, d_1. The reachable workspace of the geometrically similar 2A-chain (shown in Figure 3.18 (b)) appears to be more toroidal than the workspace of the 2R-chain of this configuration, however the 2A-chain workspace has no plane of symmetry and again the centerline of the torus-like surface is the curve for the 1A-chain shown in Figure 3.11. The torus-like structure is due to the fact that as the second joint rotates it also translates towards or away from the Z-axis of the base reference frame (an axis passing through the middle of the void of the torus-like surface). Cross sections of the workspace are shown in Figure 3.19.

The intersection of the two workspaces is provided in Figure 3.20. The intersection appears to be a portion of the band that is the workspace of the 2R-chain though it is expected that intersection is actually a planar semi-circle.

3.5.3 Four Jointed Chains

The reachable workspace of 4A-chains, or A-chains of any length, can also be computed using the algorithm in Section 3.4.1. When considering 4A-chains the number of possible configurations is unlimited, making it difficult to generalize the resulting reachable workspace and compare it to architecturally similar 4R-chains. The reachable workspaces of R-chains and A-chains with similar DH-parameters will never be identical due to the coupled translation and rotation that is present in A-chains and absent in R-chains. The amount of the deviation of the A-chain workspace from the R-chain workspace depends on the size of the A-pairs used as joints in the A-chain (the value of the geometric constant ρ).

The ability to recreate the reachable workspace of an R-chain is one measure of the A-chain workspace. One must also examine characteristics such as the volume of the

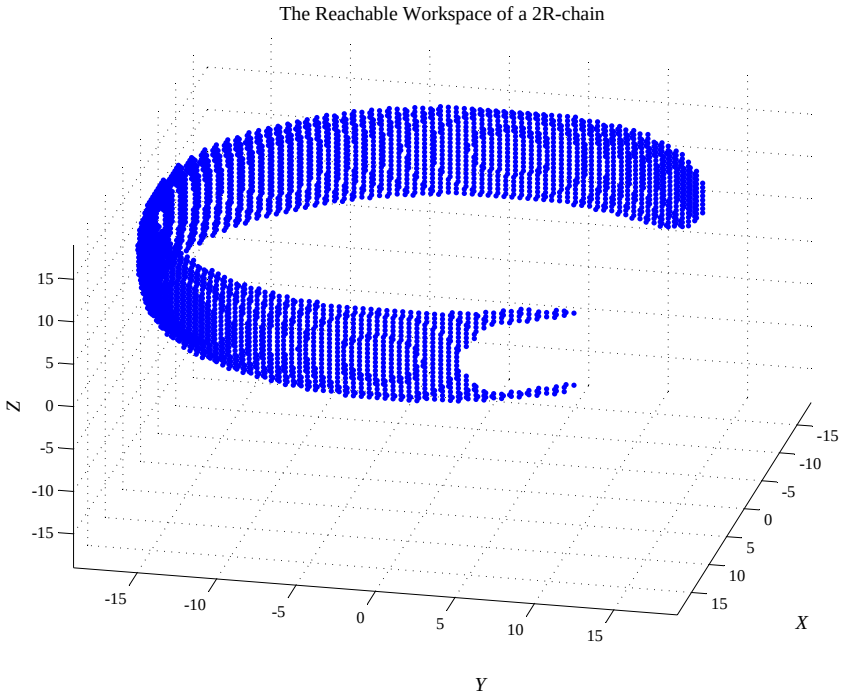

(a)

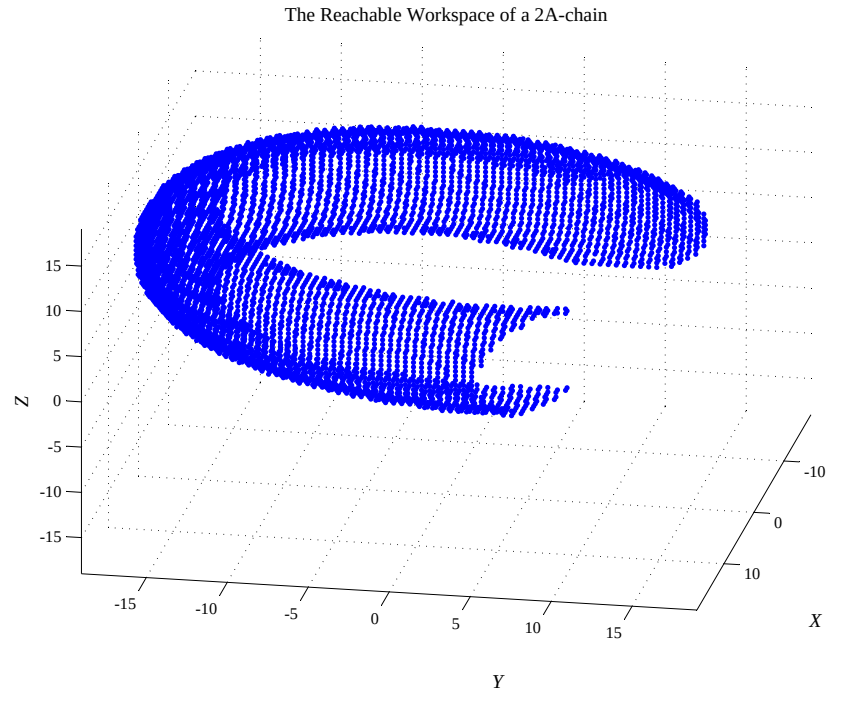

(b)

Figure 3.18: Plots of the reachable workspace of (a) a 2R-chain and (b) a 2A-chain, both with intersecting perpendicular axes.

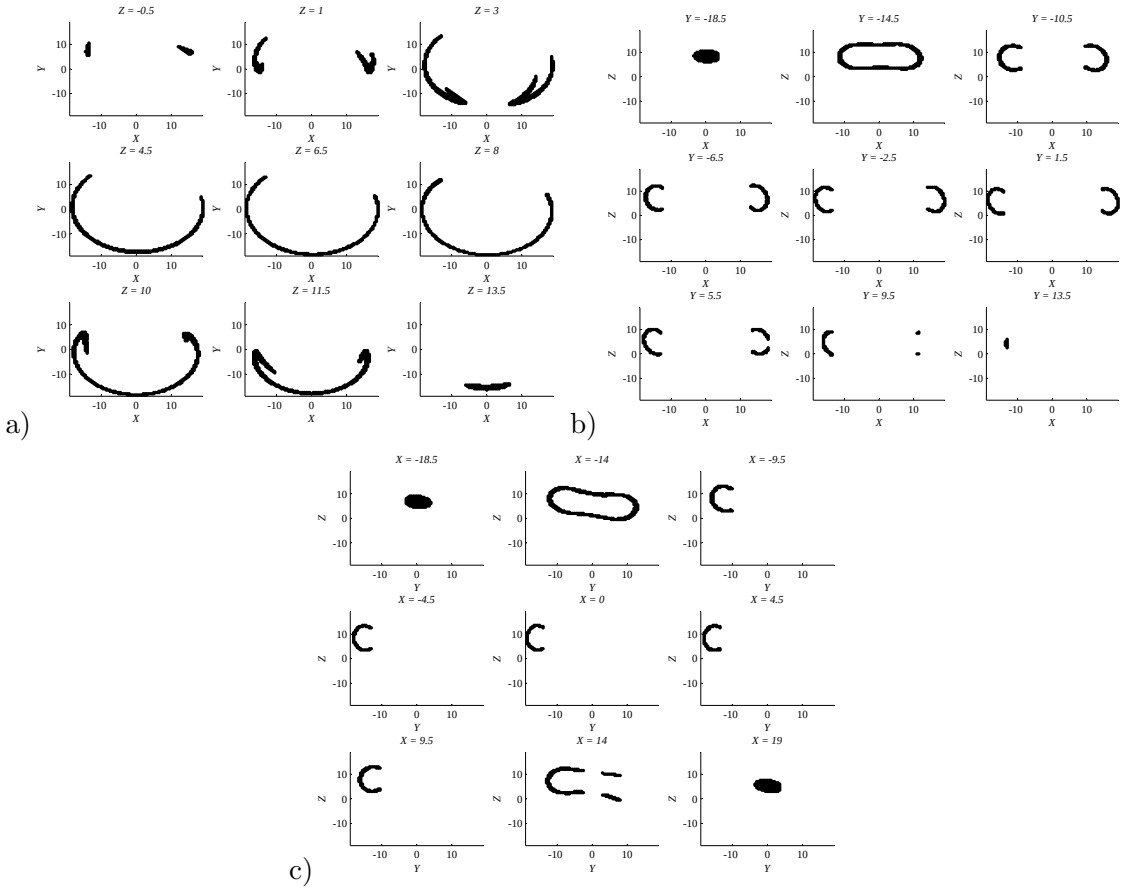

Figure 3.19: Cross sections of the reachable workspace of a 2A-chain with intersecting perpendicular axes along a) the Z-axis, b) the Y-axis and c) the X-axis.

workspace, the volume index (Section 2.2.5), and the ability of the manipulator to perform a desired task. The first two of these characteristics allow for a direct comparison of the results for similar R-chains and A-chains, while the later, the ability to perform a given task, is not easily compared. In fact, when one selects or designs a serial manipulator to perform a certain task it may result in different DH-parameters for the A-chain and R-chain that can perform that task, making it difficult to compare the chains in a meaningful way.

The inability to generalize the reachable workspaces of four-jointed chains due to the large number of possible different configurations means that this section does not focus on quantitative analysis. Such an examination is left to the comprehensive numeric example of Section 3.8 which examines the workspace, kinematics, and dynamics of a specific 4A-chain.

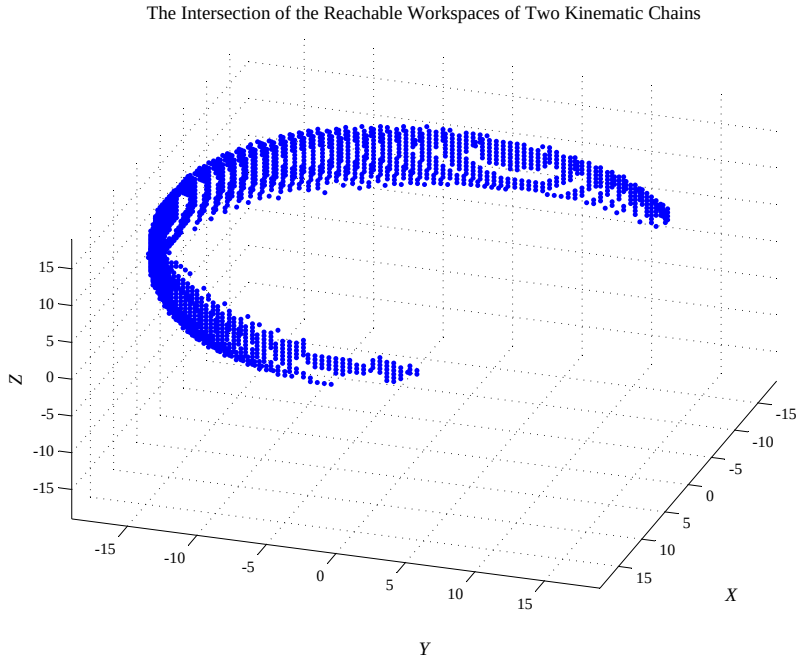

Figure 3.20: Plot of the intersection of the 2R-chain and 2A-chain reachable workspaces for 2-jointed chains with intersecting perpendicular axes.

3.6 Determination of the A-Chain Jacobian Matrix

Moving towards a velocity, force and dynamic level analysis of A-pairs and A-chains requires the determination of the Jacobian matrix. The background theory for obtaining the Jacobian matrices of manipulators containing R-pairs and P-pairs was presented in Section 2.6. This section shows the adaptation of the standard methods to account for the coupled translation and rotation of the A-pair. A single A-pair is examined first to show the effect of the coupled motion and a 4A-chain is then examined to illustrate how the Jacobian matrix is obtained for longer serial A-chains.

3.6.1 Jacobian Matrix for a Single A-Pair

Utilizing the techniques of Section 2.6 the Jacobian matrix of a single A-pair is found by examining the rotation and translation components of the coupled motion separately.

The state of the joint is represented by the joint variable θ_1, which directly represents the rotation component of the joint and the translation component of the joint motion is a function of the joint variable by Equation (2.29). The Jacobian is examined in two parts, first the linear velocity component and then the angular velocity component.

The linear velocity of the EE as induced by the motion of the joint has two components: one component due to the rotation of the joint (perpendicular to the axis of rotation, similar to a revolute joint) and one component due to the translation which is coupled to the rotation by

$$p_{e_z} = d_1 + \rho \sin\left(\frac{\theta_1}{2}\right), \tag{3.27}$$

where p_{e_z} is the $\mathbf{z}_0$-component of the EE position, and d_i is the DH-parameter describing the joint offset of Joint i. There is only one variable in the joint vector, $q_1 = \theta_1$, and similarly $\dot{q}_1 = \dot{\theta}_1$. The Jacobian describing the influence of the rotation of the joint on the linear velocity of the EE, $\boldsymbol{\jmath}_{P_1 r}$, is found as if it were a revolute joint using Equation (2.44):

$$\begin{aligned}
\boldsymbol{\jmath}_{P_1 r} &= {}^0\mathbf{z}_0 \times ({}^0\mathbf{p}_e - {}^0\mathbf{p}_0) \\
&= \begin{bmatrix} 0 \\ 0 \\ 1 \end{bmatrix} \times \begin{bmatrix} -a_1 \cos\theta_1 - 0 \\ -a_1 \sin\theta_1 - 0 \\ 0 \end{bmatrix} \\
&= \begin{bmatrix} a_1 \sin\theta_1 \\ -a_1 \cos\theta_1 \\ 0 \end{bmatrix},
\end{aligned} \tag{3.28}$$

where a_1 is the DH-parameter for the link length of a link affixed to the moving platform of the single A-pair. The translation component of the Jacobian is found by taking the time derivative of p_{e_z} to get

$$\begin{aligned} \dot{q}_1 \boldsymbol{\jmath}_{P_1 t} &= \frac{d}{dt} \begin{bmatrix} 0 \\ 0 \\ d_1 + \rho \sin\left(\frac{\theta_1}{2}\right) \end{bmatrix} \\ &= \begin{bmatrix} 0 \\ 0 \\ \frac{\dot{\theta}_1}{2} \rho \cos\left(\frac{\theta_1}{2}\right) \end{bmatrix}, \end{aligned} \tag{3.29}$$

therefore $\boldsymbol{\jmath}_{P_1 t} = \begin{bmatrix} 0 & 0 & \frac{\rho}{2}\cos\left(\frac{\theta_1}{2}\right) \end{bmatrix}^T$. The two components are added together to get the mapping from the joint rate $\dot{q}_1$ to the EE linear velocity:

$$\boldsymbol{\jmath}_{P_1} = \boldsymbol{\jmath}_{P_1 r} + \boldsymbol{\jmath}_{P_1 t} = \begin{bmatrix} a_1 \sin\theta_1 \\ -a_1 \cos\theta_1 \\ \frac{\rho}{2}\cos\left(\frac{\theta_1}{2}\right) \end{bmatrix}, \tag{3.30}$$

and ${}^0\dot{\mathbf{p}}_e = \mathbf{J}_{P_1}(\mathbf{q})\dot{q}_1$.

The translation that is coupled with the rotation of the A-pair does not have an effect on the orientation of the EE, thus the contribution of the A-pair actuation rate to the angular velocity of the EE is the same as that of a revolute joint, so from Equation (2.47)

$$\begin{aligned} \boldsymbol{\jmath}_{O_1} &= {}^0\mathbf{z}_0 \\ &= \begin{bmatrix} 0 \\ 0 \\ 1 \end{bmatrix}, \end{aligned} \tag{3.31}$$

and ${}^0\boldsymbol{\omega}_e = \mathbf{J}_{O_1}(\mathbf{q})\dot{q}_1$.

Combining the two components yields the full Jacobian:

$$\mathbf{J} = \begin{bmatrix} \boldsymbol{\jmath}_{P_1} \\ \boldsymbol{\jmath}_{O_1} \end{bmatrix} = \begin{bmatrix} a_1 \sin\theta_1 \\ -a_1 \cos\theta_1 \\ \frac{\rho}{2}\cos\left(\frac{\theta_1}{2}\right) \\ 0 \\ 0 \\ 1 \end{bmatrix}. \tag{3.32}$$

In order to examine the singularities it is useful to examine a single A-pair where the EE is located at the geometric centre of the moving platform (the EE frame is coincident with a base frame located at the geometric centre of the fixed base when the A-pair is in the theoretical home position). In such a case, the origin of the EE lies on the joint axis ($a_1 = 0$) and

$$\mathbf{J} = \begin{bmatrix} 0 \\ 0 \\ \frac{\rho}{2}\cos\left(\frac{\theta_1}{2}\right) \\ 0 \\ 0 \\ 1 \end{bmatrix}. \tag{3.33}$$

This result for the Jacobian matrix makes sense conceptually when the EE origin is on the joint axis because as the joint angle is changed the EE acquires a linear velocity component along the $\mathbf{z}_0$-axis only (from the first three elements of $\mathbf{J}$) and the angular velocity (the last three elements of $\mathbf{J}$) indicate a one-to-one relationship between the joint rate and the EE angular velocity, the same as a revolute joint. In fact, when $\rho = 0$ the Jacobian of a single R-pair is recovered.

Singularity Analysis of the Single A-Pair Jacobian Matrix

The Jacobian matrix for the single A-pair is always rank deficient, which is expected because motion in an arbitrary direction will never be possible with just a single A-pair. If one considers only the two coupled DOF of the single A-pair with the EE origin on the joint axis (motion along the joint axis and rotation about the same axis) a more useful analysis can be performed.

The mapping to EE angular velocity from the joint rate is one-to-one and independent of the joint state. This implies that, if joint limits are ignored, the angular velocity of the EE can always be controlled one-to-one. However, the mapping of the joint rates to the EE linear velocity is dependant on the joint state and cannot be continuously controlled. When $\cos\left(\frac{\theta_1}{2}\right)$ goes to zero (*i.e.* when θ_1 approaches 180°) the joint approaches a singular position. At the singularity the linear velocity of the EE can only be controlled in one direction (at 180° only a velocity in the negative z_0-direction can be achieved). This is also evident if the Jacobian is rearranged to solve for the joint rate required to achieve a certain velocity, v_1, along the z_0-axis:

$$\dot{\theta}_1 = \frac{2v_1}{\rho \cos\left(\frac{\theta_1}{2}\right)}. \tag{3.34}$$

As θ_1 approaches 180°, $\dot{\theta}_1$ approaches infinity.

3.6.2 Jacobian Matrix for a 4A-Chain

Obtaining the Jacobian matrix for a general 4A-chain is tedious and the resulting matrices are too large to manage in a reasonable way so such a derivation is not presented symbolically in this dissertation. The method for obtaining the 4A-chain Jacobian is instead illustrated with a more specific manipulator with the DH-parameters listed in table Table 3.6. These DH-parameters are based on those of the prototype manipulator.

The position vector of the base frame origin is $\mathbf{p}_0 = \mathbf{0}$. The position of the EE, $\mathbf{p}_e$,

Table 3.6: DH-Parameters of a 4A-chain.

Link i	a_i	α_i	d_i	θ_{fi}
1	0	$90°$	d_1	$0°$
2	a_2	$180°$	$-\rho$	$-90°$
3	0	$-90°$	$-\rho$	$90°$
4	0	$0°$	d_4	$0°$

is found by obtaining the matrix form of the direct kinematics equations as described in Sections 2.2.3, 2.5.5 and 3.1.3. The pose of the EE reference frame, Σ_4, is represented by the matrix

$$ {}^0\mathbf{T}_4 = \begin{bmatrix} 1 & 0 & 0 & 0 \\ p_{e_x} & -c_1c_{2-3}c_4 + s_1s_4 & c_1c_{2-3}s_4 + s_1c_4 & -c_1s_{2-3} \\ p_{e_y} & -s_1c_{2-3}c_4 - c_1s_4 & s_1c_{2-3}s_4 - c_1c_4 & -s_1s_{2-3} \\ p_{e_z} & -s_{2-3}c_4 & s_{2-3}s_4 & c_{2-3} \end{bmatrix}, \tag{3.35} $$

where

$$ {}^0\mathbf{p}_e = \begin{bmatrix} p_{e_x} \\ p_{e_y} \\ p_{e_z} \end{bmatrix} = \begin{bmatrix} s_1\rho\, s\frac{\theta_2}{2} + c_1s_2a_2 - s_1\rho\, s\frac{\theta_3}{2} - c_1s_{2-3}\rho\, s\frac{\theta_4}{2} - c_1s_{2-3}d_4 \\ -c_1\rho\, s\frac{\theta_2}{2} + s_1s_2a_2 + c_1\rho\, s\frac{\theta_3}{2} - s_1s_{2-3}\rho\, s\frac{\theta_4}{2} - s_1s_{2-3}d_4 \\ \rho\, s\frac{\theta_1}{2} + d_1 - c_2a_2 + \rho\, c_{2-3}s\frac{\theta_4}{2} + d_4c_{2-3} \end{bmatrix} \tag{3.36} $$

is the position vector of the EE origin expressed in the base frame. The c_1, s_1, *etc.* terms are defined in Section 2.11.2. In addition to the EE pose, the transformation matrices describing the pose of each intermediate reference frame ($\Sigma_i, i = 1, 2, 3$) are needed. The pose of Σ_1 is given by

$$ {}^0\mathbf{T}_1 = \begin{bmatrix} 1 & 0 & 0 & 0 \\ p_{1_x} & c_1 & 0 & s_1 \\ p_{1_y} & s_1 & 0 & -c_1 \\ p_{1_z} & 0 & 1 & 0 \end{bmatrix}, \tag{3.37} $$

where

$$ {}^0\mathbf{p}_1 = \begin{bmatrix} p_{1_x} \\ p_{1_y} \\ p_{1_z} \end{bmatrix} = \begin{bmatrix} 0 \\ 0 \\ \rho\, s\frac{\theta_1}{2} + d_1 \end{bmatrix}, \tag{3.38} $$

is the position vector of the origin of Σ_1 expressed in the base frame; the pose of Σ_2 by

$$ {}^0\mathbf{T}_2 = \begin{bmatrix} 1 & 0 & 0 & 0 \\ p_{2_x} & c_1 s_2 & -c_1 c_2 & -s_1 \\ p_{2_y} & s_1 s_2 & -s_1 c_2 & c_1 \\ p_{2_z} & -c_2 & -s_2 & 0 \end{bmatrix}, \tag{3.39} $$

where

$$ {}^0\mathbf{p}_2 = \begin{bmatrix} p_{2_x} \\ p_{2_y} \\ p_{2_z} \end{bmatrix} = \begin{bmatrix} \rho\, s_1 s\frac{\theta_2}{2} + a_2\, c_1 s_2 - \rho\, s_1 \\ -\rho\, c_1 s\frac{\theta_2}{2} + a_2\, s_1 s_2 + \rho\, c_1 \\ \rho\, s\frac{\theta_1}{2} + d_1 - a_2\, c_2 \end{bmatrix}, \tag{3.40} $$

is the position vector of the origin of Σ_2 expressed in the base frame; and the pose of Σ_3 by

$$ {}^0\mathbf{T}_3 = \begin{bmatrix} 1 & 0 & 0 & 0 \\ p_{3_x} & -c_1 c_{2-3} & s_1 & -c_1 s_{2-3} \\ p_{3_y} & -s_1 c_{2-3} & -c_1 & -s_1 s_{2-3} \\ p_{3_z} & -s_{2-3} & 0 & c_{2-3} \end{bmatrix}, \tag{3.41} $$

where

$$ {}^0\mathbf{p}_3 = \begin{bmatrix} p_{3_x} \\ p_{3_y} \\ p_{3_z} \end{bmatrix} = \begin{bmatrix} \rho\, s_1 s\frac{\theta_2}{2} + a_2\, c_1 s_2 - \rho\, s_1 s\frac{\theta_3}{2} \\ -\rho\, c_1 s\frac{\theta_2}{2} + a_2\, s_1 s_2 + \rho\, c_1 s\frac{\theta_3}{2} \\ \rho\, s\frac{\theta_1}{2} + d_1 - a_2\, c_2 \end{bmatrix}, \tag{3.42} $$

is the position vector of the origin of Σ_3 expressed in the base frame.

The joint axes, taken from the respective transformation matrices, are

$$ {}^0\hat{\mathbf{z}}_0 = \begin{bmatrix} 0 \\ 0 \\ 1 \end{bmatrix}, \quad {}^0\hat{\mathbf{z}}_1 = \begin{bmatrix} s_1 \\ -c_1 \\ 0 \end{bmatrix}, \quad {}^0\hat{\mathbf{z}}_2 = \begin{bmatrix} -s_1 \\ c_1 \\ 0 \end{bmatrix}, \quad {}^0\hat{\mathbf{z}}_3 = \begin{bmatrix} -c_1 s_{2-3} \\ -s_1 s_{2-3} \\ c_{2-3} \end{bmatrix}. \tag{3.43} $$

The vector mapping the rate of actuation of Joint 1 to the linear velocity of the EE due to the rotation of Joint 1 is obtained using Equation (2.44) with $i = 1$ to get

$$ \begin{aligned} \boldsymbol{\jmath}_{P_{1,r}} &= {}^0\mathbf{z}_0 \times ({}^0\mathbf{p}_e - {}^0\mathbf{p}_0) \\ &= \begin{bmatrix} \rho\, c_1 s\frac{\theta_2}{2} - a_2\, s_1 s_2 - \rho\, c_1 s\frac{\theta_3}{2} + \rho\, s_1 s_{2-3} s\frac{\theta_4}{2} + d_4\, s_1 s_{2-3} \\ \rho\, s_1 s\frac{\theta_2}{2} + a_2\, c_1 s_2 - \rho\, s_1 s\frac{\theta_3}{2} - \rho\, c_1 s_{2-3} s\frac{\theta_4}{2} - d_4\, c_1 s_{2-3} \\ 0 \end{bmatrix}. \end{aligned} \tag{3.44} $$

The vector mapping the rate of actuation of Joint 1 to the linear velocity of the EE due to the translation of Joint 1 is obtained by the same method as Section 3.6.1:

$$ \boldsymbol{\jmath}_{P_{1,t}} = \begin{bmatrix} 0 \\ 0 \\ \frac{\rho}{2}\, c\frac{\theta_1}{2} \end{bmatrix}. \tag{3.45} $$

The total linear velocity Jacobian component for Joint 1 is the sum of Equations (3.44) and (3.45) with $i = 1$, giving

$$ \boldsymbol{\jmath}_{P_1} = \begin{bmatrix} \rho\, c_1 s\frac{\theta_2}{2} - a_2\, s_1 s_2 - \rho\, c_1 s\frac{\theta_3}{2} + \rho\, s_1 s_{2-3} s\frac{\theta_4}{2} + d_4\, s_1 s_{2-3} \\ \rho\, s_1 s\frac{\theta_2}{2} + a_2\, c_1 s_2 - \rho\, s_1 s\frac{\theta_3}{2} - \rho\, c_1 s_{2-3} s\frac{\theta_4}{2} - d_4\, c_1 s_{2-3} \\ \frac{\rho}{2}\, c\frac{\theta_1}{2} \end{bmatrix}. \tag{3.46} $$

Because only the rotational component of the joint motion impacts the orientation of the EE, the angular velocity component of the Jacobian is found by Equation (2.47) for $i = 1$

giving

$$\boldsymbol{\jmath}_{O_1} = \begin{bmatrix} 0 \\ 0 \\ 1 \end{bmatrix}. \tag{3.47}$$

Similarly for Joint 2

$$\boldsymbol{\jmath}_{P_2} = \begin{bmatrix} a_2\, s_1 c_2 - \rho\, s_1 c_{2-3} s\frac{\theta_4}{2} - d_4\, s_1 c_{2-3} - \frac{\rho}{2}\, c_1 c\frac{\theta_2}{2} \\ a_2\, s_1 c_2 - \rho\, s_1 c_{2-3} s\frac{\theta_4}{2} - d_4\, s_1 c_{2-3} - \frac{\rho}{2}\, c_1 c\frac{\theta_2}{2} \\ a_2 s_2 - \rho s_{2-3} s\frac{\theta_4}{2} - d_4 s_{2-3} \end{bmatrix}, \tag{3.48}$$

and

$$\boldsymbol{\jmath}_{O_2} = \begin{bmatrix} s_1 \\ -c_1 \\ 0 \end{bmatrix}. \tag{3.49}$$

For Joint 3

$$\boldsymbol{\jmath}_{P_3} = \begin{bmatrix} \rho\, c_1 c_{2-3} s\frac{\theta_4}{2} + d_4\, c_1 c_{2-3} - \frac{\rho}{2}\, c\frac{\theta_3}{2} s_1 \\ \rho\, s_1 c_{2-3} s\frac{\theta_4}{2} + d_4\, s_1 c_{2-3} + \frac{\rho}{2}\, c\frac{\theta_3}{2} c_1 \\ \rho s_{2-3} s\frac{\theta_4}{2} + d_4 s_{2-3} \end{bmatrix}, \tag{3.50}$$

and

$$\boldsymbol{\jmath}_{O_3} = \begin{bmatrix} -s_1 \\ c_1 \\ 0 \end{bmatrix}. \tag{3.51}$$

For Joint 4

$$\boldsymbol{\jmath}_{P_4} = \begin{bmatrix} -\frac{\rho}{2}\, c\frac{\theta_4}{2} c_1 s_{2-3} \\ -\frac{\rho}{2}\, c\frac{\theta_4}{2} s_1 s_{2-3} \\ \frac{\rho}{2}\, c\frac{\theta_4}{2} c_{2-3} \end{bmatrix}, \tag{3.52}$$

and

$$\boldsymbol{\jmath}_{O_4} = \begin{bmatrix} -c_1 s_{2-3} \\ -s_1 s_{2-3} \\ c_{2-3} \end{bmatrix}. \tag{3.53}$$

The full 6×4 Jacobian is assembled as

$$\mathbf{J} = \begin{bmatrix} \boldsymbol{\jmath}_{P_1} & \boldsymbol{\jmath}_{P_2} & \boldsymbol{\jmath}_{P_3} & \boldsymbol{\jmath}_{P_4} \\ \boldsymbol{\jmath}_{O_1} & \boldsymbol{\jmath}_{O_2} & \boldsymbol{\jmath}_{O_3} & \boldsymbol{\jmath}_{O_4} \end{bmatrix}, \tag{3.54}$$

however the elements are too large to express in component form.

Preliminary Singularity Analysis of a 4A-Chain

A full examination of the singularities has yet to be conducted but a simple example of a singular configuration is easily found. With only four joint variables it is no surprise that there will be certain directions in which the EE cannot be moved at a given time, but in certain situations the capabilities are further diminished. When $\theta_{v_1} = \theta_{v_2} = \theta_{v_3} = \theta_{v_4} = 180^\circ$ the Jacobian matrix becomes

$$\mathbf{J} = \begin{bmatrix} 0 & a_2 + \rho + d_4 & -\rho - d_4 & 0 \\ 0 & 0 & 0 & 0 \\ 0 & 0 & 0 & 0 \\ 0 & 0 & 0 & 0 \\ 0 & 1 & -1 & 0 \\ 1 & 0 & 0 & 1 \end{bmatrix} \tag{3.55}$$

In this configuration instantaneous linear velocities along the $\mathbf{y}_0$- and $\mathbf{z}_0$-axes and angular velocity about the $\mathbf{x}_0$-axis are not achievable.

This is just one example of a singular configuration and further investigation into singularities is required. The singularities of the prototype 4A-manipulator should be compared to a similar 4R-chain (*i.e.* the first four joints of the A645 Thermo CRS).

3.7 Dynamic Analysis

In chains constructed using R-pairs forces that act parallel to the axis of rotation of a revolute joint (either external or from the kinematic and potential energy of the links) have

no effect on the joint torque, and conversely actuation of that revolute joint cannot impart forces parallel to the joint axis. When A-pairs are used as joints this is no longer true. The coupling of rotation and translation means that forces along the joint axis translate into joint torques and the application of torque at an A-pair joint will produce a force parallel to the joint axis, in addition to a force perpendicular to the joint axis as would be obtained by a revolute joint. This is evident from the analysis of the single A-pair Jacobian in Section 3.6.1 and also influences the dynamics of a manipulator constructed using A-pairs.

The dynamic analysis of serial chains constructed using R- and P-pairs was discussed in Section 2.7 and two methods for formulating the dynamic equations of motion were explored: the Lagrange formulation (Section 2.7.1) which is an energy based method; and the Newton-Euler formulation (Section 2.7.2) a recursive algorithm based on the balancing of the forces and moments acting on each link. In this work the Lagrange formulation is used to derive the dynamic equations of motion of A-chains, while the Newton-Euler formulation is used to verify the results. In this dissertation the Lagrange formulation is favored because it is straightforward, makes elegant use of the Jacobian matrices which have already been derived, and the energy method allows for the simple inclusion of the leg effects on the manipulator dynamics.

3.7.1 Dynamics of a Single A-Pair Using the Lagrange Formulation Ignoring Leg Effects

Examining the dynamics of a single A-pair before looking at longer A-chains allows for a better understanding of the effects of the coupled motion of each joint. By initially ignoring the mass properties of the legs a basis for comparing different dynamic models of the leg effects is obtained and initial comparisons with R-pairs can be made. When the inertial properties of the legs are assumed negligible the mass of the legs may be ignored completely or included as a lumped parameter model of the moving platform. A reference coordinate system is affixed to the fixed base, Σ_0, and moving platform, Σ_1. The Σ_0 origin is located at the geometric centre of the fixed base triangle, the $\hat{z}_0-$axis points along the A-pair axis of rotation towards the moving platform and the $\hat{x}_0-$ and $\hat{y}_0-$axes are arbitrarily assigned in

the plane of the fixed base anchor point triangle. Coordinate system Σ_1 is established such that Σ_0 and Σ_1 are coincident when the A-pair is in the home position and Σ_1 moves with the moving platform as the A-pair is actuated. Figure 3.21 shows the single A-pair with the coordinate systems affixed on the joint axis. For this analysis the CG of the moving link is

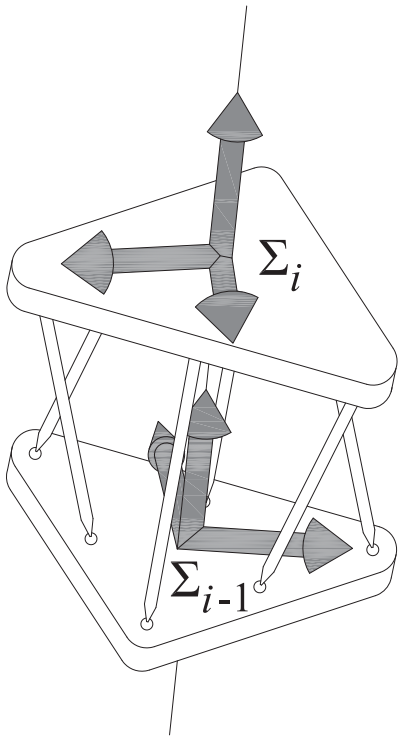

Figure 3.21: The coordinate systems affixed to the A-pair. For the single A-pair $i = 1$.

considered to be located at the origin of Σ_1 in order to simplify the leg effect analysis later. In longer A-chains (Section 3.7.4) the CG position will be more representative of the actual link properties. The Lagrange formulation as presented in Section 2.7.1 with $n = 1$ is used to obtain the dynamic equations of motion. At this time the contributions of any motors, transmissions and friction to the dynamic equations of motion have been ignored.

When working with a single A-pair it is possible to assume, without loss in generality, that the fixed component of the joint variable is $\theta_f = 0$ and therefore $\theta_v = \theta$. Recalling

Section 2.7.1 when $n = 1$ the linear component of the link Jacobian is

$$\mathbf{J}_P^{(link)} = \frac{\partial \mathbf{p}_{link}}{\partial \theta} = \begin{bmatrix} 0 \\ 0 \\ \frac{\rho}{2}\cos\left(\frac{\theta}{2}\right) \end{bmatrix}, \tag{3.56}$$

and the angular component of the link Jacobian is

$$\mathbf{J}_O^{(link)} = \begin{bmatrix} 0 \\ 0 \\ 1 \end{bmatrix}. \tag{3.57}$$

In this example the vector and matrix quantities are really just scalars because $n = 1$, however in the general case they are not, so they are still represented here as vectors and matrices. The 1×1 $\mathbf{B}(\theta)$ inertial matrix is found using Equation (2.68) as

$$\mathbf{B}(\theta) = m_{link}\mathbf{J}_P^{(link)T}\mathbf{J}_P^{(link)} + \mathbf{J}_O^{(link)T}\mathbf{R}_1\mathbf{I}_{link}^1\mathbf{R}_1^T\mathbf{J}_O^{(link)} = \frac{\rho^2 m_{link}}{4}\cos^2\left(\frac{\theta}{2}\right) + I_{zz}, \tag{3.58}$$

where m_{link} is the mass of the moving platform (not including the mass of the legs), and I_{zz} is the mass moment of inertia of the moving platform about the z_1-axis. Using the trigonometric identity

$$\cos^2\left(\frac{\theta}{2}\right) = \frac{1 + \cos(\theta)}{2}, \tag{3.59}$$

the 1×1 inertial matrix becomes

$$\mathbf{B}(\theta) = \frac{\rho^2 m_{link}}{8}(1 + \cos(\theta)) + I_{zz}. \tag{3.60}$$

Using Equation (2.74) the 1×1 matrix containing the Coriolis and centrifugal terms is

$$\mathbf{C}(\theta, \dot{\theta}) = \frac{1}{2}\left(\frac{\partial \mathbf{B}(\theta)}{\partial \theta}\right)\dot{\theta} = -\frac{\rho^2 m_{link}}{16}\sin(\theta)\,\dot{\theta}. \tag{3.61}$$

The gravitational (potential energy) term is obtained from Equation (2.72) as

$$g_i(\boldsymbol{\theta}) = -m_{link}\mathbf{g}_0^T\mathbf{J}_P^{link} = \frac{\rho m_{link} g}{2}\cos\left(\frac{\theta}{2}\right). \tag{3.62}$$

Assembling the dynamic equations in the joint space using Equation (2.71) gives

$$\tau_1 = \left(\frac{\rho^2 m_{link}}{8}\left(1+\cos\left(\theta\right)\right) + I_{zz}\right)\ddot{\theta} - \frac{\rho^2 m_{link}}{16}\sin\left(\theta\right)\dot{\theta}^2 + \frac{\rho m_{link} g}{2}\cos\left(\frac{\theta}{2}\right). \tag{3.63}$$

Equation (3.63) provides the solution to the inverse dynamics problem which allows for the determination of the joint torque profile required to follow a specified trajectory ($\theta(t)$, $\dot{\theta}(t)$ and $\ddot{\theta}(t)$ profiles), ignoring friction and external forces. If the torque and joint state are specified Equation (3.63) can be rearranged to solve for the resulting acceleration, $\ddot{\theta}$, yielding the solution to the direct dynamics problem.

3.7.2 Verification of the Single A-Pair Dynamics Using the Newton-Euler Formulation

In this dissertation the Newton-Euler formulation is used to verify the single A-pair dynamic equations of motion obtained using the Lagrange formulation in Section 3.7.1. The application of the Newton-Euler formulation to the single A-pair uses the theory presented in Section 2.7.2. This analysis assumes that the origin of the EE coordinate system lies on the joint axis, as does the CG of the moving platform. As was done in Section 3.7.1, the inertial properties of the legs are ignored in this initial analysis.

The velocities and accelerations of the base link are defined as follows. The base link is stationary, thus its angular velocity is $\boldsymbol{\omega}_0^0 = \begin{bmatrix} 0 & 0 & 0 \end{bmatrix}^T$, and its angular acceleration is $\dot{\boldsymbol{\omega}}_0^0 = \begin{bmatrix} 0 & 0 & 0 \end{bmatrix}^T$. The linear acceleration of the base frame, minus the gravity vector, is $\mathbf{0}$, thus $\ddot{\mathbf{p}}_0^0 = \mathbf{g} = \begin{bmatrix} 0 & 0 & g_0 \end{bmatrix}^T$. These vectors are then used as the initial terms in the forward recursion of the Newton-Euler formulation.

The forward recursion is used to determine the velocities and accelerations of the first (and only) link, Link $i = 1$. The angular velocity and acceleration of the moving platform

are found using Equation (2.79) and Equation (2.80) and the results are of course

$$\boldsymbol{\omega}_1^1 = \begin{bmatrix} 0 \\ 0 \\ \dot{\theta}_1 \end{bmatrix}, \tag{3.64}$$

and

$$\dot{\boldsymbol{\omega}}_1^1 = \begin{bmatrix} 0 \\ 0 \\ \ddot{\theta}_1 \end{bmatrix}. \tag{3.65}$$

Determining the linear acceleration of the link origin uses Equation (2.81) but some consideration must be given to the type of joint (the A-pair is essentially a combination of a P-pair and an R-pair with coupled motion). For this analysis the origin of the link frame, as shown in Figure 3.21, lies on the axis of rotation ($r_{0,1}^1 = 0$) and thus the revolute joint component of the linear acceleration is identically zero, if the origin was away from the axis of rotation the revolute joint component would need to be added to the translation component. This becomes relevant as more links and joints are added. The prismatic joint component of the linear acceleration is established with Equation (2.81) using the variables $\dot{d}_1$ and $\ddot{d}_1$ written as functions of $\theta, \dot{\theta}, \ddot{\theta}$. Using the equation for the distance between the fixed base and moving platform of the A-pair, Equation (2.29), these values are

$$\begin{aligned} d_1 &= \rho \sin\left(\frac{\theta}{2}\right), \\ \dot{d}_1 &= \frac{\rho}{2}\dot{\theta}\cos\left(\frac{\theta}{2}\right), \\ \ddot{d}_1 &= -\frac{\rho}{4}\dot{\theta}_1^2 \sin\left(\frac{\theta}{2}\right) + \frac{\rho}{2}\ddot{\theta}\cos\left(\frac{\theta}{2}\right), \end{aligned} \tag{3.66}$$

yielding

$$\ddot{\mathbf{p}}_1^1 = \begin{bmatrix} 0 \\ 0 \\ g_0 - \frac{\rho}{4}\dot{\theta}^2 \sin\left(\frac{\theta}{2}\right) + \frac{\rho}{2}\ddot{\theta}\cos\left(\frac{\theta}{2}\right) \end{bmatrix}. \tag{3.67}$$

The forward recursion is completed by determining the linear acceleration of the centre of gravity of Link 1 using Equation (2.82), however since the Link 1 origin and centre of gravity are coincident $\ddot{\mathbf{p}}^1_{C_1} = \ddot{\mathbf{p}}^1_1$.

In this analysis no external forces are being applied at the EE, hence $\boldsymbol{f}^2_2 = \boldsymbol{\mu}^2_2 = \begin{bmatrix} 0 & 0 & 0 \end{bmatrix}^T$. The backward recursion is carried out to find the forces and moments required to cause the accelerations. The forces exerted by Link 1 on the base are obtained with Equation (2.84):

$$\mathbf{f}^1_1 = \begin{bmatrix} 0 \\ 0 \\ m_{link}g_0 - \dfrac{m_{link}\rho}{4}\dot{\theta}^2_1 \sin\left(\dfrac{\theta_1}{2}\right) + \dfrac{m_{link}\rho}{2}\ddot{\theta}_1 \cos\left(\dfrac{\theta_1}{2}\right) \end{bmatrix}. \tag{3.68}$$

The moments are computed with Equation (2.85):

$$\boldsymbol{\mu}^1_1 = \begin{bmatrix} 0 \\ 0 \\ I_{zz}\ddot{\theta}_1 \end{bmatrix}. \tag{3.69}$$

Determining the joint torques requires the examination of two components: the linear and the rotational motions. The joint torque from the rotational motion, τ_{r_1}, comes directly from the equation for the torque of a revolute joint (Equation (2.86)) giving

$$\tau_{r_1} = I_{zz}\ddot{\theta}_1. \tag{3.70}$$

From the prismatic joint part of Equation (2.86), τ_{l_1} is actually not a torque at all, but a force along the joint axis:

$$\tau_{l_1} = m_{link}g_0 - \frac{m_{link}\rho}{4}\dot{\theta}^2_1 \sin\left(\frac{\theta_1}{2}\right) + \frac{m_{link}\rho}{2}\ddot{\theta}_1 \cos\left(\frac{\theta_1}{2}\right). \tag{3.71}$$

The Jacobian matrix is used to map this to the required joint torque, *i.e.* $\mathbf{J}^{(\ell_1)T}_T \tau_{l_1}$, giving

the total required joint torque:

$$\begin{aligned}\tau_1 = &\quad \tau_{r_1} + \mathbf{J}_T^{(\ell_1)T}\tau_{l_1} \\ = &\quad \left(\frac{m_{link}\rho^2}{8}\left(1+\cos\left(\theta\right)\right) + I_{zz}\right)\ddot{\theta} - \frac{m_{link}\rho^2}{16}\sin\left(\theta\right)\dot{\theta}^2 + \frac{m_{link}\rho g_0}{2}\cos\left(\frac{\theta}{2}\right).\end{aligned} \tag{3.72}$$

The joint torque obtained by the Newton-Euler formulation is identical to that obtained by the Lagrange formulation: *c.f.* Equations (3.63) and (3.72). Though these results are unsurprising, it is important to verify the equations before performing further analysis on the single A-pair and longer A-chains. It is important to note that friction has not been included in either the Lagrange or Newton-Euler formulation of the dynamic model.

3.7.3 Introduction of Leg Inertial Effects on a Single A-Pair Using the Lagrange Formulation

The Lagrange formulation is well suited to modelling the effects of the legs on the dynamic equations of motion. The kinetic and potential energy of each leg are functions of the generalized coordinate θ and they can easily be included in the Lagrangian and thus the dynamic equations of motion. The symmetry of the A-pair means that the kinetic energy effects of only one leg needs to be examined and then multiplied by six to account for all legs. The potential energy of each individual leg depends on the orientation of the A-pair. For a vertical joint (the gravity vector is parallel to joint axis) all legs have the same potential energy, in other orientations the potential energy is determined using the combined CG of the six legs (a point on the joint axis equidistant from the fixed base and moving platform).

The dynamics of parallel platforms, such as the Gough-Stewart platform, are well studied using different formulations such as the Newton-Euler formulation [96–98], the Lagrange formulation [99, 100], and the principle of virtual work [101–104]. In most of these works the full dynamic model requires that the CG, linear velocity, and angular velocity of each leg (each of which has two parts as the length of the legs change because they are prismatic joints) be determined as a function of the joint parameters and rates. The A-pair is much simpler in that each leg is of fixed length and the leg position and velocity are simple

functions of the joint position and rate.

The following sections show how the kinetic and potential energy of the legs are obtained in terms of the generalized coordinate and the influence of the legs is added to the results of Section 3.7.1 to increase the fidelity of the dynamic model.

Kinetic Energy of the Legs

The kinetic energy of the leg has two components: the linear motion of the leg CG and the angular motion about the leg anchor point on the fixed base. The leg is modelled as a slender rod and thus the kinetic energy from any rotation about the centre axis of the leg is considered to be negligible.

Figure 3.2 along with Equations (3.19) and (3.20) show that the position vector of the fixed base anchor point of Leg 1, B_1, in Σ_0 is ${}^0\mathbf{b}_1 = \begin{bmatrix} 0 & \frac{\rho\sqrt{2}}{2} & 0 \end{bmatrix}^T$ (noting that Equation (3.4) is used to express the anchor point position in terms of ρ as opposed to the length of the sides of the triangles, a) and the position of the moving platform anchor point for Leg 1, P_1, in Σ_1 is ${}^1\mathbf{p}_1 = \begin{bmatrix} 0 & -\frac{\rho\sqrt{2}}{4} & 0 \end{bmatrix}^T$. Recall that a point on the moving platform projects onto a circle in the $\hat{x}_0$-$\hat{y}_0$ plane as θ varies, while the $\hat{z}_0$ position is described by Equation (2.29). The position vector of P_1 in Σ_0 is ${}^0\mathbf{p}_1 = \begin{bmatrix} \frac{\rho\sqrt{2}}{4}\sin\theta & -\frac{\rho\sqrt{2}}{4}\cos\theta & \frac{\rho\sqrt{2}}{2}\sin\left(\frac{\theta}{2}\right) \end{bmatrix}^T$. The vector along the leg from B_1 to P_1, ${}^0\mathbf{r}_{P_1/B_1}$, is

$$ {}^0\mathbf{r}_{P_1/B_1} = {}^0\mathbf{p}_1 - {}^0\mathbf{b}_1 = \begin{bmatrix} \frac{\rho\sqrt{2}}{4}\sin\theta \\ -\frac{\rho\sqrt{2}}{4}(2+\cos\theta) \\ \rho\sin\left(\frac{\theta}{2}\right) \end{bmatrix}, \tag{3.73} $$

and the position vector of the CG of Leg 1, ${}^0\mathbf{p}_{leg}$, is

$$ {}^0\mathbf{p}_{leg} = {}^0\mathbf{b}_1 + \frac{1}{2}{}^0\mathbf{r}_{P_1/B_1} = \begin{bmatrix} \frac{\rho\sqrt{2}}{8}\sin\theta \\ \frac{\rho\sqrt{2}}{8}(2-\cos\theta) \\ \frac{\rho}{2}\sin\left(\frac{\theta}{2}\right) \end{bmatrix}. \tag{3.74} $$

The linear component Jacobian for the CG of the leg comes from $\frac{\partial \mathbf{p}_{leg}}{\partial \theta}$ and is

$$\mathbf{J}_P^{(leg)}(\theta) = \begin{bmatrix} \frac{\rho\sqrt{2}}{8}\cos\theta \\ \frac{\rho\sqrt{2}}{8}\sin\theta \\ \frac{\rho}{4}\cos\left(\frac{\theta}{2}\right) \end{bmatrix}, \tag{3.75}$$

and the linear velocity of the leg CG is ${}^0\dot{\mathbf{p}}_{leg} = \mathbf{J}_P^{(leg)}(\theta)\dot{\theta}$. The linear component of the kinetic energy of Leg 1 with mass m_{leg}, utilizing the trigonometric identity in Equation (3.59), is

$$\begin{aligned} T_{P_{leg}} &= \tfrac{1}{2} m_{leg} {}^0\dot{\mathbf{p}}_{leg}^T {}^0\dot{\mathbf{p}}_{leg} \\ &= \tfrac{1}{2} m_{leg} \mathbf{J}_P^{(leg)T} \mathbf{J}_P^{(leg)} \dot{\theta}^2 \\ &= \tfrac{\rho^2 m_{leg}}{64} \left(2 + \cos\left(\theta\right)\right) \dot{\theta}^2. \end{aligned} \tag{3.76}$$

The angular component of the kinetic energy requires the determination of the angular velocity of the leg. The velocity of P_1 with respect to B_1, ${}^0\mathbf{v}_{P_1/B_1} = {}^0\dot{\mathbf{r}}_{P_1/B_1}$ is the time rate of change of ${}^0\mathbf{r}_{P_1/B_1}$ where the only variable that is a function of time is θ. Therefore

$${}^0\mathbf{v}_{P_1/B_1} = \begin{bmatrix} \frac{\rho\sqrt{2}}{4}\cos\theta \\ \frac{\rho\sqrt{2}}{4}\sin\theta \\ \frac{\rho}{2}\cos\left(\frac{\theta}{2}\right) \end{bmatrix} \dot{\theta}. \tag{3.77}$$

A reference coordinate system for the leg is established with its origin at B_1 such that $\hat{z}_{leg}$ points along the leg from B_1 towards P_1, $\hat{y}_{leg}$ is parallel to ${}^0\mathbf{v}_{P_1/B_1}$ and $\hat{x}_{leg}$ completes the right hand system, as illustrated in Figure 3.22. Since the leg is represented as a slender rod and there is no rotation about $\hat{y}_{leg}$ (it is parallel to the velocity vector), only the magnitude of the angular velocity of the leg about $\hat{x}_{leg}$, $\omega_{x_{leg}}$, is of concern. The value of $\omega_{x_{leg}}$ is obtained by dividing the magnitude of the velocity of P_1 with respect to B_1 by the distance from B_1 to P_1, giving

$$\omega_{x_{leg}} = \frac{||{}^0\mathbf{v}_{P_1/B_1}||}{||{}^0\mathbf{r}_{P_1/B_1}||} = \frac{1}{3}\sqrt{2 + \cos\left(\theta\right)}\dot{\theta}. \tag{3.78}$$

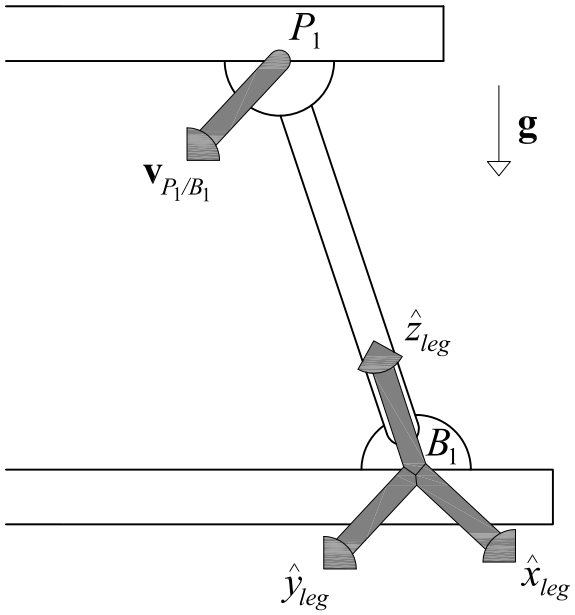

Figure 3.22: The leg coordinate system is affixed such that the origin is at B_1, the $\hat{z}_{leg}$ axis points along the leg towards P_1, the $\hat{y}_{leg}$ axis is parallel to $\mathbf{v}_{P_1/B_1}$ and the $\hat{x}_{leg}$ axis completes the right hand coordinate system.

The inertia tensor for the slender rod representing the leg in the leg reference frame is

$$\mathbf{I}_{leg}^{(leg)} = \begin{bmatrix} \frac{\rho\sqrt{2}}{4} m_{leg} & 0 & 0 \\ 0 & \frac{\rho\sqrt{2}}{4} m_{leg} & 0 \\ 0 & 0 & 0 \end{bmatrix}. \tag{3.79}$$

The angular kinetic energy of Leg 1 is

$$T_{O_{leg}} = \frac{1}{2}\omega_{x_{leg}}^2 I_{xx_{leg}} = \frac{\rho\sqrt{2}}{72} m_{leg} \left(2 + \cos\left(\theta\right)\right) \dot{\theta}^2. \tag{3.80}$$

The summation of Equations (3.76) and (3.80) represents the total kinetic energy of each A-pair leg. Each of the six legs of the A-pair has the same kinetic energy at any given time, thus the total kinetic energy of all of the legs is six times the value of the single leg, giving

$$T_0 = 6T_{O_{leg}}. \tag{3.81}$$

Potential Energy of the Legs

The potential energy of Leg 1 from Equation (2.69) is $\mathcal{U}_{leg} = m_{leg}\mathbf{g}_0^T\mathbf{p}_{leg}$, and the gravity term of the dynamic equations from Equation (2.72) is

$$\begin{aligned} g_{leg} &= \frac{\partial \mathcal{U}}{\partial \theta} \\ &= -m_{leg}\mathbf{g}_0^T\mathbf{J}_P^{(leg)} \\ &= \frac{\rho g}{4} m_{leg} \cos\left(\frac{\theta}{2}\right). \end{aligned} \tag{3.82}$$

Equation (3.82) assumes that $\mathbf{g}_0$ is parallel to the joint axis. In situations where the A-pair is not vertical the component of gravity vector that is parallel to the joint axis is used. The angle between the axis of a joint, say Joint i, and the gravity vector is a function of all of the joints preceding Joint i in the chain, *i.e.* Joints $1, 2, \ldots, i-1$.

Influence of Legs On the Dynamic Equations

The impact of all of the legs on the dynamic equations of motion is found by multiplying each leg term by six. The inertial term for the six legs, $\mathbf{B}_{legs}(\theta)$, is obtained from Equations (3.76) and (3.80):

$$\mathbf{B}_{legs}(\theta) = \frac{\rho m_{leg}\sqrt{2}}{192}\left(9\rho\sqrt{2} + 8\sqrt{3}\right)(2 + \cos(\theta)), \tag{3.83}$$

and the $\mathbf{C}_{legs}(\dot{\theta}, \theta)$ term comes from Equation (2.74) to give

$$\mathbf{C}_{legs}(\dot{\theta}, \theta) = \frac{\rho m_{leg}\sqrt{2}}{384}\left(9\rho\sqrt{2} + 8\sqrt{3}\right)\sin(\theta)\,\dot{\theta}. \tag{3.84}$$

The gravitational term for all six legs, $\mathbf{g}_{legs}(\theta)$, is six times Equation (3.82):

$$\mathbf{g}_{legs}(\theta) = \frac{3\rho m_{leg} g}{2}\cos\left(\frac{\theta}{2}\right). \tag{3.85}$$

The dynamic equations of motion of the single A-pair with the mass effects of the legs

included is

$$\tau = \left(\mathbf{B}_{link}(\theta) + \mathbf{B}_{legs}(\theta)\right)\ddot{\theta} + \left(\mathbf{C}_{link}(\dot{\theta},\theta) + \mathbf{C}_{legs}(\dot{\theta},\theta)\right)\dot{\theta} + \left(\mathbf{g}_{link}(\theta) + \mathbf{g}_{legs}(\theta)\right). \quad (3.86)$$

In general the leg masses are much smaller than the link masses and the $\mathbf{B}_{legs}(\theta)$ and $\mathbf{C}_{legs}(\dot{\theta},\theta)$ terms have much larger denominators than the corresponding terms for the link and therefore a smaller impact on the torque requirements. In the absence of friction the potential energy term for the legs has a small denominator and a larger impact than the kinetic energy terms, however the overall influence depends on the ratio of the link mass to the mass of the legs. When the difference between the masses is small the leg effects will be more pronounced and should be included. The choice to include or exclude leg effects depends on the application and desired dynamic model fidelity. When additional terms are introduced such as motor inertias, friction and external applied loads the impact of the leg effects on model fidelity is diminished further. Section 3.8.6 presents a numeric example exploring the magnitude of the leg effects for the prototype manipulator.

3.7.4 Obtaining the Dynamic Equations of Motion of a 4A-Chain

In this section the Lagrange formulation, detailed in Section 2.7.1, is used to obtain the dynamic equations of motion of a 4A-chain. The dynamic equations of motion for a general 4A-chain are difficult to express in closed form because the equations become very large, even in the early steps of the algorithm. In this section the algorithm for obtaining the dynamic equations of motion is outlined using the DH-parameters defined in Table 3.6 that were used for demonstrating how to obtain the Jacobian matrix of a 4A-chain in Section 3.6.2. Even when examining this particular configuration the equations become difficult to portray in any useful manner and thus the algorithm is discussed while showing only partial results. In Section 3.8 the dynamics of a specific 4A-chain are explored.

The Lagrange formulation requires that a Jacobian matrix be assembled for each Link i in the chain. Each link Jacobian has two components, the first mapping the joint rates to

the linear component of the link CG velocity is of the form

$$\mathbf{J}_P^{(Link_i)} = \left[\begin{array}{cccccc} \boldsymbol{\jmath}_{P_1}^{(Link_i)} & \cdots & \boldsymbol{\jmath}_{P_i}^{(Link_i)} & 0 & \cdots & 0 \end{array} \right], \tag{3.87}$$

and the second component, used to map the joint rates to the angular velocity of the Link CG, is of the form

$$\mathbf{J}_O^{(Link_i)} = \left[\begin{array}{cccccc} \boldsymbol{\jmath}_{O_1}^{(Link_i)} & \cdots & \boldsymbol{\jmath}_{O_i}^{(Link_i)} & 0 & \cdots & 0 \end{array} \right]. \tag{3.88}$$

For a prismatic joint, the Jacobian columns are

$$\boldsymbol{\jmath}_{P_j}^{(Link_i)} = \hat{\mathbf{z}}_{j-1}, \qquad \boldsymbol{\jmath}_{O_j}^{(Link_i)} = \mathbf{0}. \tag{3.89}$$

Whereas for revolute joints they are

$$\boldsymbol{\jmath}_{P_j}^{(Link_i)} = \hat{\mathbf{z}}_{j-1} \times ({}^0\mathbf{p}_{Link_i} - {}^0\mathbf{p}_{j-1}), \qquad \boldsymbol{\jmath}_{O_j}^{(Link_i)} = \hat{\mathbf{z}}_{j-1}. \tag{3.90}$$

In the case of an A-pair the column vectors are a combination of the two.

In what follows the Jacobian for Link 1 is derived, while those of the remaining links are simply reported.

Link 1

The centre of gravity of Link 1 is known with respect to Σ_1 as

$${}^1\mathbf{p}_1 = \left[\begin{array}{c} p_{x,Link_1} \\ p_{y,Link_1} \\ p_{z,Link_1} \end{array} \right]. \tag{3.91}$$

Using ${}^0\mathbf{T}_1$ from Equation (3.37) the position of the CG of Link 1 with respect to Σ_0 is

$$ {}^0\mathbf{p}_1 = {}^0\mathbf{T}_1 \, {}^1\mathbf{p}_1 = \begin{bmatrix} c_1 p_{x,Link_1} + s_1 p_{z,Link_1} \\ s_1 p_{x,Link_1} - c_1 p_{z,Link_1} \\ d_1 + \rho s\frac{\theta_1}{2} + p_{y,Link_1} \end{bmatrix}. \tag{3.92} $$

The component of the Jacobian accounting for the linear velocity of the CG of Link 1 due to the rotation of Joint 1 is found using Equation (3.90) (noting that $\hat{\mathbf{z}}_0$ is given in Equation (3.43) and ${}^0\mathbf{p}_0 = \mathbf{0}$):

$$ \boldsymbol{\jmath}_{P_1 r}^{(Link_1)} = {}^0\hat{\mathbf{z}}_0 \times ({}^0\mathbf{p}_{Link_1} - {}^0\mathbf{p}_0) = \begin{bmatrix} -s_1 p_{x,Link_1} + c_1 p_{z,Link_1} \\ c_1 p_{x,Link_1} + s_1 p_{z,Link_1} \\ 0 \end{bmatrix}. \tag{3.93} $$

The component of the Jacobian accounting for the linear velocity of the CG of Link 1 due to the translation of Joint 1 is found using Equation (3.89):

$$ \boldsymbol{\jmath}_{P_1 t}^{(Link_1)} = \frac{\rho}{2} c\frac{\theta_1}{2} \hat{\mathbf{z}}_0 = \begin{bmatrix} 0 \\ 0 \\ \frac{\rho}{2} c\frac{\theta_1}{2} \end{bmatrix}. \tag{3.94} $$

The linear velocity components are summed and the full linear velocity Jacobian for Link 1 is

$$ \mathbf{J}_P^{(Link_1)} = \begin{bmatrix} -s_1 p_{x,Link_1} + c_1 p_{z,Link_1} & 0 & 0 & 0 \\ c_1 p_{x,Link_1} + s_1 p_{z,Link_1} & 0 & 0 & 0 \\ \frac{\rho}{2} c\frac{\theta_1}{2} & 0 & 0 & 0 \end{bmatrix}. \tag{3.95} $$

The component of the Jacobian accounting for the angular velocity of the CG of Link 1

due to the rotation of Joint 1 is found using Equation (3.90):

$$\boldsymbol{\mathcal{J}}_{O_1}^{(Link_1)} = \hat{\mathbf{z}}_0 = \begin{bmatrix} 0 \\ 0 \\ 1 \end{bmatrix}. \tag{3.96}$$

The complete angular velocity Jacobian for Link 1 is:

$$\mathbf{J}_{O}^{(Link_1)} = \begin{bmatrix} 0 & 0 & 0 & 0 \\ 0 & 0 & 0 & 0 \\ 1 & 0 & 0 & 0 \end{bmatrix}. \tag{3.97}$$

Link 2

The CG of Link 2 is known with respect to Σ_2 as

$${}^2\mathbf{p}_2 = \begin{bmatrix} p_{x,Link_2} \\ p_{y,Link_2} \\ p_{z,Link_2} \end{bmatrix}. \tag{3.98}$$

Using ${}^0\mathbf{T}_2$ from Equation (3.39) the position of the CG of Link 2 with respect to Σ_0 is

$${}^0\mathbf{p}_2 = {}^0\mathbf{T}_2^2\mathbf{p}_2 = \begin{bmatrix} \rho\, s_1 s\frac{\theta_2}{2} + a_2\, c_1 s_2 - \rho\, s_1 + c_1 s_2 p_{x,Link_2} - c_1 c_2 p_{y,Link_2} - s_1 p_{z,Link_2} \\ -\rho\, c_1 s\frac{\theta_2}{2} + a_2\, s_1 s_2 + \rho\, c_1 + s_1 s_2 p_{x,Link_2} - s_1 c_2 p_{y,Link_2} + c_1 p_{z,Link_2} \\ \rho\, s\frac{\theta_1}{2} + d_1 - a_2\, c_2 - 1\, c_2 p_{x,Link_2} - 1\, s_2 p_{y,Link_2} \end{bmatrix}. \tag{3.99}$$

Using the same methods as for Link 1, the components of the Jacobian for the CG of Link 2 due to the motion of Joint 1 are

$$\boldsymbol{\mathcal{J}}_{P_1 r}^{(Link_2)} = \begin{bmatrix} \rho\, c_1 s\frac{\theta_2}{2} - a_2\, s_1 s_2 - \rho\, c_1 - s_1 s_2 p_{x,Link_2} + s_1 c_2 p_{y,Link_2} - c_1 p_{z,Link_2} \\ \rho\, s_1 s\frac{\theta_2}{2} + a_2\, c_1 s_2 - \rho\, s_1 + c_1 s_2 p_{x,Link_2} - c_1 c_2 p_{y,Link_2} - s_1 p_{z,Link_2} \\ 0 \end{bmatrix}, \tag{3.100}$$

$$\boldsymbol{\jmath}_{P_1\,t}^{(Link_2)} = \begin{bmatrix} 0 \\ 0 \\ \frac{\rho}{2} c\frac{\theta_1}{2} \end{bmatrix}, \tag{3.101}$$

and

$$\boldsymbol{\jmath}_{O_1}^{(Link_2)} = \begin{bmatrix} 0 \\ 0 \\ 1 \end{bmatrix}. \tag{3.102}$$

The components of the Jacobian of the CG of Link 2 due to the actuation of Joint 2 are

$$\boldsymbol{\jmath}_{P_2\,r}^{(Link_2)} = \begin{bmatrix} -c_1\left(-a_2\,c_2 - 1\,c_2 p_{x,Link_2} - 1\,s_2 p_{y,Link_2}\right) \\ -s_1\left(-a_2\,c_2 - 1\,c_2 p_{x,Link_2} - 1\,s_2 p_{y,Link_2}\right) \\ a_2\,s_2 + s_2 p_{x,Link_2} - c_2 p_{y,Link_2} \end{bmatrix}, \tag{3.103}$$

$$\boldsymbol{\jmath}_{P_2\,t}^{(Link_2)} = \begin{bmatrix} \frac{\rho}{2}\,s_1 c\frac{\theta_2}{2} \\ -\frac{\rho}{2}\,c_1 c\frac{\theta_2}{2} \\ 0 \end{bmatrix}, \tag{3.104}$$

and

$$\boldsymbol{\jmath}_{O_2}^{(Link_2)} = \begin{bmatrix} s_1 \\ -c_1 \\ 0 \end{bmatrix}. \tag{3.105}$$

The full linear and angular velocity Jacobian matrices for Link 2 are

$$\mathbf{J}_P^{(Link_2)} = \begin{bmatrix} \boldsymbol{\jmath}_{P_1\,r}^{(Link_2)} + \boldsymbol{\jmath}_{P_1\,t}^{(Link_2)} & \boldsymbol{\jmath}_{P_2\,r}^{(Link_2)} + \boldsymbol{\jmath}_{P_2\,t}^{(Link_2)} & 0 & 0 \end{bmatrix} \tag{3.106}$$

and

$$\mathbf{J}_O^{(Link_2)} = \begin{bmatrix} \boldsymbol{\jmath}_{O_1}^{(Link_2)} & \boldsymbol{\jmath}_{O_2}^{(Link_2)} & 0 & 0 \end{bmatrix}, \tag{3.107}$$

respectively.

Link 3

The Jacobian matrix components for Link 3 are found using the same methods as for the previous links. For the CG of Link 3 due to the actuation of Joint 1:

$$\boldsymbol{\jmath}_{P_1\,r}^{(Link_3)}=\begin{bmatrix}\rho\,c_1 s\frac{\theta_2}{2}-a_2\,s_1 s_2-\rho\,c_1 s\frac{\theta_3}{2}+s_1 c_{2-3}p_{x,Link_3}+c_1 p_{y,Link_3}+s_1 s_{2-3}p_{z,Link_3}\\ \rho\,s_1 s\frac{\theta_2}{2}+a_2\,c_1 s_2-\rho\,s_1 s\frac{\theta_3}{2}-c_1 c_{2-3}p_{x,Link_3}+s_1 p_{y,Link_3}-c_1 s_{2-3}p_{z,Link_3}\\ 0\end{bmatrix}, \quad (3.108)$$

$$\boldsymbol{\jmath}_{P_1\,t}^{(Link_3)}=\begin{bmatrix}0\\0\\\frac{\rho}{2}c\frac{\theta_1}{2}\end{bmatrix}, \quad (3.109)$$

and

$$\boldsymbol{\jmath}_{O_1}^{(Link_3)}=\begin{bmatrix}0\\0\\1\end{bmatrix}. \quad (3.110)$$

For the CG of Link 3 due to the actuation of Joint 2:

$$\boldsymbol{\jmath}_{P_2\,r}^{(Link_3)}=\begin{bmatrix}-c_1\left(-a_2\,c_2-s_{2-3}p_{x,Link_3}+c_{2-3}p_{z,Link_3}\right)\\ -s_1\left(-a_2\,c_2-s_{2-3}p_{x,Link_3}+c_{2-3}p_{z,Link_3}\right)\\ a_2\,s_2-c_{2-3}p_{x,Link_3}-s_{2-3}p_{z,Link_3}\end{bmatrix}, \quad (3.111)$$

$$\boldsymbol{\jmath}_{P_2\,t}^{(Link_3)}=\begin{bmatrix}\frac{\rho}{2}\,s_1 c\frac{\theta_2}{2}\\ -\frac{\rho}{2}\,c_1 c\frac{\theta_2}{2}\\ 0\end{bmatrix}, \quad (3.112)$$

and

$$\boldsymbol{\jmath}_{O_2}^{(Link_3)} = \begin{bmatrix} s_1 \\ -c_1 \\ 0 \end{bmatrix}. \tag{3.113}$$

For the CG of Link 3 due to the actuation of Joint 3:

$$\boldsymbol{\jmath}_{P_3\,r}^{(Link_3)} = \begin{bmatrix} c_1\left(-s_{2-3}p_{x,Link_3} + c_{2-3}p_{z,Link_3}\right) \\ s_1\left(-s_{2-3}p_{x,Link_3} + c_{2-3}p_{z,Link_3}\right) \\ c_{2-3}p_{x,Link_3} + s_{2-3}p_{z,Link_3} \end{bmatrix}, \tag{3.114}$$

$$\boldsymbol{\jmath}_{P_3\,t}^{(Link_3)} = \begin{bmatrix} -\frac{\rho}{2}\, s_1 c\frac{\theta_2}{2} \\ \frac{\rho}{2}\, c_1 c\frac{\theta_2}{2} \\ 0 \end{bmatrix}, \tag{3.115}$$

and

$$\boldsymbol{\jmath}_{O_3}^{(Link_3)} = \begin{bmatrix} -s_1 \\ c_1 \\ 0 \end{bmatrix}. \tag{3.116}$$

The full linear and angular velocity Jacobian matrices for Link 3 are

$$\mathbf{J}_P^{(Link_3)} = \begin{bmatrix} \boldsymbol{\jmath}_{P_1\,r}^{(Link_3)} + \boldsymbol{\jmath}_{P_1\,t}^{(Link_3)} & \boldsymbol{\jmath}_{P_2\,r}^{(Link_3)} + \boldsymbol{\jmath}_{P_2\,t}^{(Link_3)} & \boldsymbol{\jmath}_{P_3\,r}^{(Link_3)} + \boldsymbol{\jmath}_{P_3\,t}^{(Link_3)} & 0 \end{bmatrix} \tag{3.117}$$

and

$$\mathbf{J}_O^{(Link_3)} = \begin{bmatrix} \boldsymbol{\jmath}_{O_1}^{(Link_3)} & \boldsymbol{\jmath}_{O_2}^{(Link_3)} & \boldsymbol{\jmath}_{O_3}^{(Link_3)} & 0 \end{bmatrix}, \tag{3.118}$$

respectively.

Link 4

Using the same approach, the Jacobian for the CG of Link 4 due to Joint 1 is

$$\boldsymbol{\jmath}_{P_1\,r}^{(Link_4)} = \begin{bmatrix} \rho\, c_1 s\frac{\theta_2}{2} - a_2\, s_1 s_2 - \rho\, c_1 s\frac{\theta_3}{2} + \rho\, s_1 s_{2-3} s\frac{\theta_4}{2} + d_4\, s_1 s_{2-3} \\ \quad -(-s_1 c_{2-3} c_4 - c_1 s_4)\, p_{x,Link_4} - (s_1 c_{2-3} s_4 - c_1 c_4)\, p_{y,Link_4} \\ \quad +s_1 s_{2-3} p_{z,Link_4} \\ \rho\, s_1 s\frac{\theta_2}{2} + a_2\, c_1 s_2 - \rho\, s_1 s\frac{\theta_3}{2} - \rho\, c_1 s_{2-3} s\frac{\theta_4}{2} - d_4\, c_1 s_{2-3} \\ \quad +(-c_1 c_{2-3} c_4 + s_1 s_4)\, p_{x,Link_4} + (c_1 c_{2-3} s_4 + s_1 c_4)\, p_{y,Link_4} \\ \quad -c_1 s_{2-3} p_{z,Link_4} \\ 0 \end{bmatrix}, \tag{3.119}$$

$$\boldsymbol{\jmath}_{P_1\,t}^{(Link_4)} = \begin{bmatrix} 0 \\ 0 \\ \frac{\rho}{2} c\frac{\theta_1}{2} \end{bmatrix}, \tag{3.120}$$

and

$$\boldsymbol{\jmath}_{O_1}^{(Link_4)} = \begin{bmatrix} 0 \\ 0 \\ 1 \end{bmatrix}. \tag{3.121}$$

For the CG of Link 4 due to Joint 2:

$$\boldsymbol{\jmath}_{P_2\,r}^{(Link_4)} = \begin{bmatrix} -c_1 \Big(-a_2\, c_2 + \rho\, c_{2-3} s\frac{\theta_4}{2} + d_4\, c_{2-3} - s_{2-3} c_4 p_{x,Link_4} \\ \qquad\qquad +s_{2-3} s_4 p_{y,Link_4} + c_{2-3} p_{z,Link_4}\Big) \\ -s_1 \Big(-a_2\, c_2 + \rho\, c_{2-3} s\frac{\theta_4}{2} + d_4\, c_{2-3} - s_{2-3} c_4 p_{x,Link_4} \\ \qquad\qquad +s_{2-3} s_4 p_{y,Link_4} + c_{2-3} p_{z,Link_4}\Big) \\ a_2\, s_2 - \rho\, s_{2-3} s\frac{\theta_4}{2} - d_4\, s_{2-3} - p_{x,Link_4} c_{2-3} c_4 \\ \qquad\qquad +p_{y,Link_4} c_{2-3} s_4 - s_{2-3} p_{z,Link_4} \end{bmatrix}, \tag{3.122}$$

$$\boldsymbol{\jmath}_{P_2\,t}^{(Link_4)} = \begin{bmatrix} \frac{\rho}{2}\, s_1 c\frac{\theta_2}{2} \\ -\frac{\rho}{2}\, c_1 c\frac{\theta_2}{2} \\ 0 \end{bmatrix}, \tag{3.123}$$

and

$$\boldsymbol{\jmath}_{O_2}^{(Link_4)} = \begin{bmatrix} s_1 \\ -c_1 \\ 0 \end{bmatrix}. \tag{3.124}$$

For the CG of Link 4 due to Joint 3:

$$\boldsymbol{\jmath}_{P_3\,r}^{(Link_4)} = \begin{bmatrix} c_1\left(\rho\, c_{2-3} s\frac{\theta_4}{2} + d_4\, c_{2-3} - s_{2-3}c_4 p_{x,Link_4} + s_{2-3}s_4 p_{y,Link_4} + c_{2-3}p_{z,Link_4}\right) \\ s_1\left(\rho\, c_{2-3} s\frac{\theta_4}{2} + d_4\, c_{2-3} - s_{2-3}c_4 p_{x,Link_4} + s_{2-3}s_4 p_{y,Link_4} + c_{2-3}p_{z,Link_4}\right) \\ \rho\, s_{2-3} s\frac{\theta_4}{2} + d_4\, s_{2-3} + p_{x,Link_4} c_{2-3}c_4 - p_{y,Link_4} c_{2-3}s_4 + s_{2-3}p_{z,Link_4} \end{bmatrix}, \tag{3.125}$$

$$\boldsymbol{\jmath}_{P_3\,t}^{(Link_4)} = \begin{bmatrix} -\frac{\rho}{2}\, s_1 c\frac{\theta_2}{2} \\ \frac{\rho}{2}\, c_1 c\frac{\theta_2}{2} \\ 0 \end{bmatrix}, \tag{3.126}$$

and

$$\boldsymbol{\jmath}_{O_3}^{(Link_4)} = \begin{bmatrix} -s_1 \\ c_1 \\ 0 \end{bmatrix}. \tag{3.127}$$

For the CG of Link 4 due to Joint 4:

$$\boldsymbol{\jmath}_{P_4\,r}^{(Link_4)} = \begin{bmatrix} s_1 c_4 p_{x,Link_4} - s_1 s_4 p_{y,Link_4} + c_{2-3} p_{x,Link_4} c_1 s_4 + c_{2-3} p_{y,Link_4} c_1 c_4 \\ -p_{x,Link_4} c_1 c_4 + c_{2-3} p_{x,Link_4} s_1 s_4 + p_{y,Link_4} c_1 s_4 + c_{2-3} p_{y,Link_4} s_1 c_4 \\ s_{2-3} p_{x,Link_4} s_4 + s_{2-3} p_{y,Link_4} c_4 \end{bmatrix}, \tag{3.128}$$

$$\boldsymbol{\jmath}_{P_4\,t}^{(Link_4)} = \begin{bmatrix} -\frac{\rho}{2}\, c\frac{\theta_4}{2} c_1 s_{2-3} \\ -\frac{\rho}{2}\, c\frac{\theta_4}{2} s_1 s_{2-3} \\ \frac{\rho}{2}\, c\frac{\theta_4}{2} c_{2-3} \end{bmatrix}, \tag{3.129}$$

and

$$\boldsymbol{\jmath}_{O_4}^{(Link_4)} = \begin{bmatrix} -c_1 s_{2-3} \\ -s_1 s_{2-3} \\ c_{2-3} \end{bmatrix}. \tag{3.130}$$

The full linear and angular velocity Jacobian matrices for Link 4 are

$$\mathbf{J}_P^{(Link_4)} = \begin{bmatrix} \boldsymbol{\jmath}_{P_{1\,r}}^{(Link_4)} + \boldsymbol{\jmath}_{P_{1\,t}}^{(Link_4)} & \boldsymbol{\jmath}_{P_{2\,r}}^{(Link_4)} + \boldsymbol{\jmath}_{P_{2\,t}}^{(Link_4)} & \boldsymbol{\jmath}_{P_{3\,r}}^{(Link_4)} + \boldsymbol{\jmath}_{P_{3\,t}}^{(Link_4)} & \boldsymbol{\jmath}_{P_{4\,r}}^{(Link_4)} + \boldsymbol{\jmath}_{P_{4\,t}}^{(Link_4)} \end{bmatrix} \tag{3.131}$$

and

$$\mathbf{J}_O^{(Link_4)} = \begin{bmatrix} \boldsymbol{\jmath}_{O_1}^{(Link_4)} & \boldsymbol{\jmath}_{O_2}^{(Link_4)} & \boldsymbol{\jmath}_{O_3}^{(Link_4)} & \boldsymbol{\jmath}_{O_4}^{(Link_4)} \end{bmatrix}, \tag{3.132}$$

respectively.

The link Jacobian matrices, mapping the joint rates to the linear and angular velocity of the CG of each link in the chain are required to build the inertia matrix for the system. Once the coupling of translation and rotation of each A-pair is accounted for in the link Jacobian matrices the inertial matrices, $\mathbf{B}_i(\boldsymbol{\theta})$, and the centrifugal and Coriolis term matrices, $\mathbf{C}(\boldsymbol{\theta}, \dot{\boldsymbol{\theta}})$, are obtained using the methods reported in Section 2.7.1.

3.7.5 Assembling the Inertia Matrix for a 4A-Chain

The $n \times n$ inertia matrices, $\mathbf{B}_i(\boldsymbol{\theta})$, $i = 1, \ldots, 4$, are computed with Equation (2.68). Since the kinetic energy of the legs of the A-pair have been deemed negligible in Section 3.7.3 they do not impact the kinetic energy terms. For the 4A-chain ($n = 4$) the inertia matrix is

$$\mathbf{B}(\boldsymbol{\theta}) = \mathbf{B}_1(\boldsymbol{\theta}) + \mathbf{B}_2(\boldsymbol{\theta}) + \mathbf{B}_3(\boldsymbol{\theta}) + \mathbf{B}_4(\boldsymbol{\theta}). \tag{3.133}$$

While the general matrix $\mathbf{B}(\boldsymbol{\theta})$ is too large to show here, it can be obtained symbolically using a computer algebraic system, or numerically for a specific manipulator and orientation.

3.7.6 Building the Centrifugal and Coriolis Matrix for the 4A-Chain

The elements of the $n \times n$ matrices containing the centrifugal and coriolis terms, $\mathbf{C}_i(\boldsymbol{\theta}, \dot{\boldsymbol{\theta}})$, $i = 1, \ldots, 4$, are found using Equation (2.74). Like the $\mathbf{B}(\boldsymbol{\theta})$ matrix the general $\mathbf{C}(\boldsymbol{\theta}, \dot{\boldsymbol{\theta}})$ matrix for the 4A-chain is too large to show here, but can be obtained for specific manipulators and configurations, as is discussed in Section 3.8.

3.7.7 Potential Energy Effects of the 4A-Chain

The potential energy effects are examined in two components: the links and the legs. The effects of the links are obtained using the method outlined in Section 2.7.1, while the six legs of each joint are grouped together to determine the leg potential energy effects. This inclusion of the leg effects is unique to A-chains and incorporates the analysis of the dynamic effects of the legs of a single A-pair (Section 3.7.3) into the dynamic analysis of longer A-chains. The potential energy effects are represented in the dynamic equations of motion by the $n \times 1$ vector $\mathbf{g}(\boldsymbol{\theta})$. Each element g_i represents the moment generated at Joint i by gravity for the current configuration.

Potential Energy Effects of the Links

The link potential energy effects are obtained using Equation (2.72), with the mass of each Link i represented by m_{Link_i}, and the CG of each with respect to Σ_i by

$\begin{bmatrix} p_{xLink_i} & p_{yLink_i} & p_{zLink_i} \end{bmatrix}^T$. The resulting gravity terms for the prototype 4A-chain are

$$\begin{aligned}
g_1^{(Links)} &= \tfrac{m_{Link_1}\rho g}{2} c\tfrac{\theta_1}{2} + \tfrac{m_{Link_2}\rho g}{2} c\tfrac{\theta_1}{2} + \tfrac{m_{Link_3}\rho g}{2} c\tfrac{\theta_1}{2} + \tfrac{m_{Link_4}\rho g}{2} c\tfrac{\theta_1}{2}, \\
g_2^{(Links)} &= (a_2 s_2 + s_2 p_{xLink_2} - c_2 p_{yLink_2})\, m_{Link_2} g + (a_2 s_2 - c_{2-3} p_{xLink_3} \\
&\quad - s_{2-3} p_{zLink_3})\, m_{Link_3} g + \Big(a_2 s_2 - \rho\, s_{2-3} s\tfrac{\theta_4}{2} - d_4 s_{2-3} - p_{xLink_4} c_{2-3} c_4 \\
&\quad + p_{yLink_4} c_{2-3} s_4 - s_{2-3} p_{zLink_4}\Big)\, m_{Link_4} g, \\
g_3^{(Links)} &= (c_{2-3} p_{xLink_3} + s_{2-3} p_{zLink3})\, m_{Link_3} g + \Big(\rho\, s_{2-3} s\tfrac{\theta_4}{2} + d_4 s_{2-3} + p_{xLink_4} c_{2-3} c_4 \\
&\quad - p_{yLink_4} c_{2-3} s_4 + s_{2-3} p_{zLink_4}\Big)\, m_{Link_4} g, \\
g_4^{(Links)} &= \Big(s_{2-3} p_{xLink_4} s_4 + s_{2-3} p_{yLink_4} c_4 + 1/2\, \rho\, c\tfrac{\theta_4}{2} c_{2-3}\Big)\, m_{Link_4} g.
\end{aligned} \tag{3.134}$$

These link gravity terms represent the moment induced at each joint due to the mass of the links in the chain. Joint 1 has an induced moment, even though the gravity vector is parallel to the rotation axis, because the coupling of translation and rotation in A-pairs means that when a force is applied parallel to the axis of rotation a torque is induced about the joint axis. This is not true in R-pairs and is one of the major differences in the dynamics between the two types of kinematic pairs.

Potential Energy Effects of the Legs

The legs of each joint move relative to the joint's base and platform based on the position of joint. In Section 3.7.3 it was shown that for the purposes of determining the potential energy influence of the legs in each joint the mass of the six legs can be considered as a lumped point mass on the joint axis equidistant from the fixed base and moving platform anchor point planes. Once the position of the point mass is known the leg potential energy effects for each joint can be determined using Equation (2.72), and this method is used for some of the joints, however it is possible to determine some of the leg potential energy terms by analysis of the manipulator geometry. The total moment induced at each Joint i by the legs of Joint i, Joint $i+1$, ..., Joint n is the sum of the moment contributions from each joint's leg point mass.

For Joint 1 the joint axis is always vertical, as was the case with the link potential energy

in Equation (3.134), so the induced moment on Joint 1 by the mass of the Joint i leg point masses, m_{Legs_i}, is

$$g_1^{(Legs_1)} = \frac{m_{Legs_1}\rho g}{4} c\frac{\theta_1}{2}, \tag{3.135}$$

where the effect is half of what it was for that of the potential energy of the links because the leg CG translates half the distance of the links for the same joint rotation. The legs of Joints 2, 3, and 4 move in the same way that Links 2, 3, and 4 move as Joint 1 is actuated (see Equation (3.134)), thus

$$g_1^{(Legs_i)} = \frac{m_{Legs_i}\rho g}{2} c\frac{\theta_1}{2}, \tag{3.136}$$

for $i = 2, 3, 4$. In this dissertation, each of the A-pairs in the 4A-chain are identical so the legs in all of the joints posses the same mass properties. The total moment induced in Joint 1 by the mass of all of the legs in all of the joints, $g_1^{(Legs)}$:

$$g_1^{(Legs)} = g_1^{(Legs_1)} + g_1^{(Legs_2)} + g_1^{(Legs_3)} + g_1^{(Legs_4)} = \frac{7m_{Legs_i}\rho g}{4} c\frac{\theta_1}{2}. \tag{3.137}$$

The axis of Joint 2 is at all times horizontal and the point mass representing the legs of Joint 2 is always on the joint axis and thus there is no change in potential energy as Joint 2 is actuated and no moment is induced on the joint. The legs of Joints 3 and 4 are cantilevered from Joint 2 and do induce a moment. Since the axis of Joint 3 is always horizontal the potential energy of the point mass representing the legs of Joint 3 does not change as it is actuated and the distance from the axis of Joint 2 to the axis of Joint 3 (as well as its leg point mass) is constant. The Joint 3 leg point mass is a distance a_2 (the length of Link 2) from the Joint 2 axis, thus the moment induced on Joint 2 by the legs of Joint 3 is

$$g_2^{(Legs_3)} = m_{Legs_3} g a_2 s_2. \tag{3.138}$$

The impact of the Joint 4 legs on the moment induced at Joint 2 is more difficult to determine. A method similar to determining the the gravitation effects of the links works

well. The position of the leg point mass of Joint 4 with respect to Σ_3, ${}^3\mathbf{p}_{Legs_4}$, is

$$ {}^3\mathbf{p}_{Legs_4} = \begin{pmatrix} 0 \\ 0 \\ d_4 + \frac{\rho}{2} s\frac{\theta_4}{2} \end{pmatrix}, \tag{3.139} $$

which is transformed to the base frame using ${}^0\mathbf{p}_{Legs_4} = {}^0\mathbf{T}_3^{30}\mathbf{p}_{Legs_4}$. The linear velocity of the Joint 4 leg point mass due to the rotation of Joint 2 is

$$ \begin{aligned} \boldsymbol{\jmath}_{P_2 r}^{(Legs_4)} &= {}^0\hat{\mathbf{z}}_1 \times ({}^0\mathbf{p}_{Legs_4} - {}^0\mathbf{p}_1) \\ &= \begin{bmatrix} -c_1\left(-c_2a_2 + c_{2-3}\left(d_4 + \frac{\rho}{2}s\frac{\theta_4}{2}\right)\right) \\ -s_1\left(-c_2a_2 + c_{2-3}\left(d_4 + \frac{\rho}{2}s\frac{\theta_4}{2}\right)\right) \\ s_2a_2 - s_{2-3}d_4 - \frac{\rho}{2}s_{2-3}s\frac{\theta_4}{2} \end{bmatrix}. \end{aligned} \tag{3.140} $$

The linear velocity component of the Joint 4 legs due to the translation of Joint 2 does not influence the potential energy terms because the axis of Joint 2 is horizontal and translation in a horizontal plane does not change the potential energy. The moment induced in Joint 2 by the legs of Joint 4 is found using Equation (2.72):

$$ g_2^{(Legs_4)} = \frac{m_{Legs_4}g}{2}\left(s_2a_2 - s_{2-3}d_4 - \frac{\rho}{2}s_{2-3}s\frac{\theta_4}{2}\right). \tag{3.141} $$

The total moment induced at Joint 2 by all of the joint legs is

$$ g_2^{(Legs)} = g_2^{(Legs_3)} + g_2^{(Legs_4)}. \tag{3.142} $$

The moment induced at Joint 3 is not influenced by the legs of Joint 3 because the joint axis is at all times horizontal. The legs of Joint 4 do impart a moment at Joint 3 which is obtained by a method similar to the obtaining the influence of the Joint 4 legs on Joint 2. The result is

$$ g_3^{(Legs)} = g_3^{(Legs_4)} = \frac{m_{Legs_4}g}{2}s_{2-3}\left(d_4 + \frac{\rho}{2}s\frac{\theta_4}{2}\right). \tag{3.143} $$

The moment induced in Joint 4 by its own legs is found using the point mass representing the six legs that travels on the joint axis, z_3. The induced moment in Joint 4 by its own legs is

$$g_4^{(Legs)} = g_4^{(Legs_4)} = \frac{m_{Legs_4} g \rho}{4} c_{2-3} c\frac{\theta_4}{2}. \tag{3.144}$$

Total Potential Energy Effects

The total potential energy effects, considering both the link and leg influences on the moments induced at the joints, are obtained by

$$\mathbf{g} = \mathbf{g}^{(Links)} + \mathbf{g}^{(Legs)}. \tag{3.145}$$

The elements of $\mathbf{g}$ represent the moment induced by gravity on the respective joints. The vector $\mathbf{g}$ is used along with the inertia matrix and the centrifugal and coriolis matrix to assemble the dynamic equations of motion for the prototype 4A-chain.

3.7.8 Dynamic Equations of Motion for a 4A-Chain

Combining the kinetic and potential energy terms together, as per Section 2.7.1, yields the dynamic equations of motion for the 4A-chain. The inverse dynamics can be written as

$$\boldsymbol{\tau} = \mathbf{B}(\boldsymbol{\theta})\ddot{\boldsymbol{\theta}} + \mathbf{C}(\dot{\boldsymbol{\theta}}, \boldsymbol{\theta})\dot{\boldsymbol{\theta}} + (\mathbf{g}^{(Links)} + \mathbf{g}^{(Legs)}) + \mathbf{J}^T(\boldsymbol{\theta})\mathbf{h}_e, \tag{3.146}$$

where $\boldsymbol{\tau}$ is the vector of joint torques, and the $\mathbf{J}^T(\boldsymbol{\theta})\mathbf{h}_e$ term represents the joint torque induced by forces and moments applied by the EE on the surrounding environment. This work has not considered friction and external loading when deriving the dynamic equations of motion, however if the effects of friction are included in the model, the dynamic equations become

$$\boldsymbol{\tau} = \mathbf{B}(\boldsymbol{\theta})\ddot{\boldsymbol{\theta}} + \mathbf{C}(\dot{\boldsymbol{\theta}}, \boldsymbol{\theta})\dot{\boldsymbol{\theta}} + (\mathbf{g}^{(Links)} + \mathbf{g}^{(Legs)}) + \mathbf{F}_v\dot{\boldsymbol{\theta}} + \mathbf{F}_s \mathrm{sgn}(\dot{\boldsymbol{\theta}}) + \mathbf{J}^T(\boldsymbol{\theta})\mathbf{h}_e, \tag{3.147}$$

where the terms $\mathbf{F}_v\dot{\boldsymbol{\theta}}$ and $\mathbf{F}_s\text{sgn}(\dot{\boldsymbol{\theta}})$ are basic representations of the viscous and static friction models.

The dynamic equations of motion for general 4A-chains, and even for the chain described by the DH-parameters in Table 3.6 are too extensive to present here, as is the case with the study of the dynamics of most serial kinematic chains constructed using other types of kinematic pairs. This section outlines the method to follow to obtain the dynamic equations for 4A-chains, or A-chains of any length. In most cases the dynamic equations of motion will not be written out but utilized by software for simulation or control of serial A-chains. A numeric example of a 4A-chain is explored in Section 3.8 to illustrate the application of the techniques developed in this section.

3.8 Numeric Example

It is useful to examine a specific numeric example to illustrate the application of the theoretical techniques and to initiate comparisons between A-chains and geometrically similar R-chains. In this section the kinematics and dynamics of the prototype 4A-chain, introduced in Section 3.3, are examined. The prototype 4A-chain is shown in Figure 3.7. The kinematics of the prototype 4A-chain are examined through the definition of the DH-parameters, obtaining the direct kinematic equations in matrix form, approximating the reachable workspace, and application of the inverse kinematics algorithm. Also examined are the dynamics of a single A-pair and the dynamics of the prototype 4A-chain including the derivation of its Jacobian matrix, application of the Lagrange formulation to obtain the direct and inverse dynamics models, and the development of a rudimentary dynamic model of the manipulator for simulation.

3.8.1 Geometric Constant and DH-Parameters

The determination of the geometric constant ρ is covered in Section 3.1.2. The A-pairs of the prototype 4A-chain are all constructed using legs that are $l = 6.000$ in long. Using this value and rearranging Equation (3.3) the length of the sides of the fixed base and moving

Joint/Link	a_i	d_i	α_i	θ_{f_i}
1	0.000 in	7.343 in	90.000°	0.000°
2	12.000 in	$-\rho \approx -5.657$ in	180.000°	−90.000°
3	0.000 in	$-\rho \approx -5.657$ in	−90.000°	90.000°
4	0.000 in	8.000 in	0.000°	0.000°

Table 3.7: DH-parameters for the prototype manipulator.

platform anchor point triangles are $2l/\sqrt{3} \approx 6.928$ in and by Equation (3.4) the value of ρ is $4\sqrt{2} \approx 5.657$ in. This corresponds to the distance between the fixed base and moving platform of the A-pairs when $\theta = 180°$.

The assignment of DH-parameters to A-chains is discussed in Sections 2.5.4 and 3.1.1. The corresponding DH-parameters of the 4A-chain prototype are listed in Table 3.7. These values are based on the geometry of the first four joints and links of the Thermo CRS A465 manipulator. The values assigned to d_2 and d_3 in the 4A-chain are to account for the translation that is coupled to the rotation of the respective joints. The values of θ_{f_2} and θ_{f_3} are selected such that when $\theta_i = 180°$ the manipulator is fully extended along the $\mathbf{z}_0$ axis.

3.8.2 Direct Kinematics

The direct kinematics equations are derived via the method presented in Sections 2.5.5 and Section 3.1.3. With four joints $i = 4$ Equation (2.19) becomes

$$ {}^0\mathbf{T}_4 = \mathbf{M}_1\mathbf{G}_1\mathbf{M}_2\mathbf{G}_2\mathbf{M}_3\mathbf{G}_3\mathbf{M}_4\mathbf{G}_4, \tag{3.148} $$

where the $\mathbf{M}_i$ and $\mathbf{G}_i$ are defined in Equations (3.5) and (2.20), respectively.

The transformation matrix ${}^0\mathbf{T}_4$ was already constructed in Equation (3.35) as part of the process of obtaining the Jacobian matrix for a 4A-chain with the same symbolic DH-parameters in Section 3.6.2. The matrix ${}^0\mathbf{T}_4$ is the matrix representation of the direct kinematics equations.

3.8.3 Reachable Workspace

The reachable workspace of the prototype 4A-chain is obtained using the new algorithm described in Section 3.4. The reachable workspace is shown in Figure 3.23 and cross sections

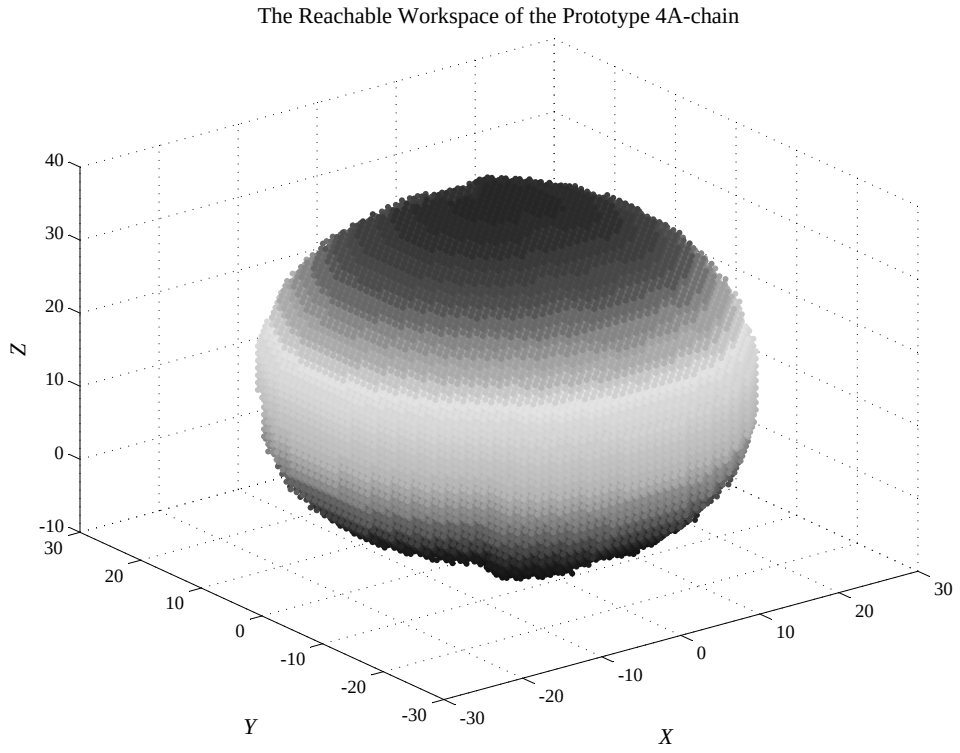

Figure 3.23: Isometric view of the reachable workspace of the prototype 4A-chain.

of the workspace are shown in Figure 3.24. When pixels are 0.5 in $\times$ 0.5 in $\times$ 0.5 in the EE reaches $487,640$ pixels, meaning the workspace is approximately $60,955$ in^3. If the pixels are 1 in $\times$ 1 in $\times$ 1 in then $60,416$ pixels are reached. The resolution of the ambient workspace affects precision (smaller pixels mean better resolution) however it becomes difficult to plot when there are more pixels. For this workspace the joint limits are set as $60^\circ \leq \theta_i \leq 300^\circ$ and self collisions have been ignored. The reachable workspace resembles a deformed sphere with a hollow core.

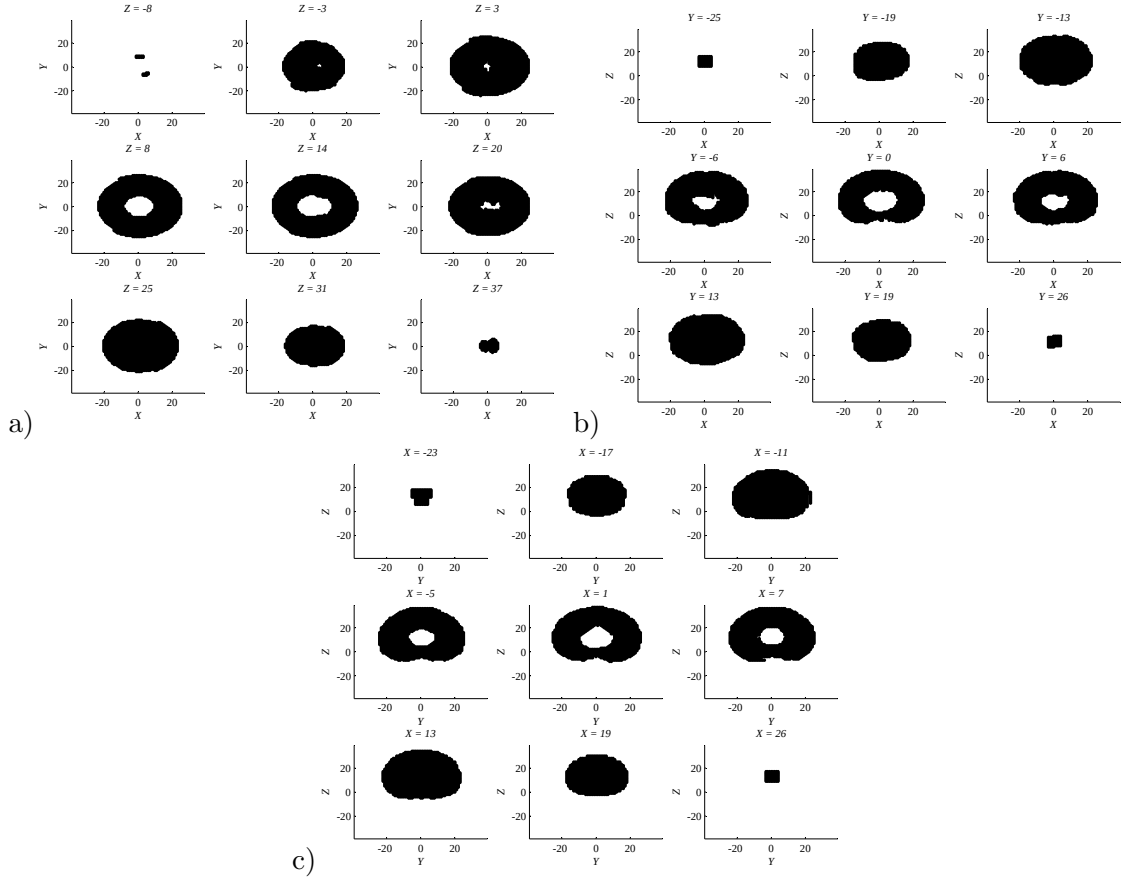

Figure 3.24: Cross sections of the reachable workspace along a) the Z-axis, b) the Y-axis and c) the X-axis.

3.8.4 Inverse Kinematics

The inverse kinematics algorithm for 4A-chains is presented in Section 2.5.6. Novel to this dissertation is the use of the revised 2A-chain constraint varieties obtained in Section 3.1.4. In this section the inverse kinematics algorithm is applied to the prototype 4A-manipulator to obtain the joint variables that place the EE in a desired target pose, Σ_{target}.

Target Pose

To ensure that Σ_{target} is obtainable by the prototype 4A-chain a set of four random joint values is used to obtain the target pose. These joint variable values are not used by the

algorithm but do allow for confirmation of the results. The following randomly generated (within the joint limits) joint variables are used:

$$\begin{aligned} \theta_1 &= 84.100^\circ, \\ \theta_2 &= 224.200^\circ, \\ \theta_3 &= 106.800^\circ, \\ \theta_4 &= 237.000^\circ. \end{aligned} \tag{3.149}$$

Using these values the target pose, obtained using the results of the direct kinematics, is

$$\Sigma_{target} = {}^0\mathbf{T}_4 = \begin{bmatrix} 1.000 & 0.000 & 0.000 & 0.000 \\ -1.345 & -0.860 & -0.502 & -0.0911 \\ -19.850 & -0.163 & 0.440 & -0.883 \\ 13.760 & 0.484 & -0.744 & -0.4604 \end{bmatrix}. \tag{3.150}$$

2A-Chain Constraint Varieties

The inverse kinematics algorithm begins by theoretically breaking the 4A-chain into two 2A-chains. The base 2A-chain contains Joints and Links 1 and 2, and the EE 2A-chain contains Joints and Links 3 and 4.

The base reference frame of the base 2A-chain, Σ_{0L}, is coincident with the base of the 4A-chain, *i.e* $\Sigma_{0L} = \Sigma_0$. The constraint variety of the base 2A-chain is therefore represented

by the intersection of the five polynomials of Equation (3.11). After substitution of the DH-parameters of Table 3.7 the polynomials become

$$
\begin{aligned}
&1 : x_0y_0 + x_1y_1 + x_2y_2 + x_3y_3 = 0,\\
&2 : {x_0}^2 - {x_1}^2 - {x_2}^2 + {x_3}^2 = 0,\\
&3 : -12\,x_0x_1 + 2\,x_0y_0 - 12\,x_2x_3 + 2\,x_3y_3 = 0,\\
&4 : -x_3y_0\left(13 - 4\sqrt{2}\right) + x_1y_2\left(13 - 4\sqrt{2}\right) - x_2y_1\left(13 - 4\sqrt{2}\right) + x_0y_3\left(13 - 4\sqrt{2}\right)\\
&\quad -8\,x_0x_1 + 8\,x_2x_3 + 1/2\,{x_1}^2\left(13 - 4\sqrt{2}\right)^2 + 1/2\,{x_2}^2\left(13 - 4\sqrt{2}\right)^2 - 12\,x_2y_3\\
&\quad +12\,x_3y_2 - 8\,x_1x_3 + 12\,x_0y_1 - 12\,x_1y_0 + 8\,x_0x_2 - 12\,x_0x_2\left(13 - 4\sqrt{2}\right)\\
&\quad +4\,x_2y_1\sqrt{2} + 4\,x_0y_3\sqrt{2} - 4\,x_1y_2\sqrt{2} + 12\,x_1x_3\left(13 - 4\sqrt{2}\right) - 4\,x_3y_0\sqrt{2} + 72\,{x_1}^2\\
&\quad +72\,{x_2}^2 + {y_0}^2 + {y_1}^2 + {y_2}^2 + {y_3}^2 = 0,\\
&5 : 2\,x_0x_3y_0 - 12\,x_2{x_3}^2 - 2\,{x_0}^2y_3 + 2\,{x_2}^2y_3 - 12\,x_0x_1x_3 + 2\,{x_1}^2y_3 = 0.
\end{aligned}
\tag{3.151}
$$

Obtaining the constraint variety EE 2A-chain in terms of Σ_0 requires some manipulation of the polynomials in Equation (3.16). The EE 2A-chain constraint variety was obtained with respect to $\Sigma_{0R} = \Sigma_4$. In order to represent the constraint variety with respect to Σ_0 a transformation in the base frame from Σ_0 to Σ_{target} is required. Section 2.1.8 discusses the effect of transformations in Euclidean space on points in the kinematic image space. Using Equations (2.14) and (2.15) the Study parameters of ${}^0\mathbf{T}_4$ are obtained. These Study parameters are substituted into Equation (2.17) to obtain the matrix $\mathbf{T}_b({}^0\mathbf{T}_4)$. The Study parameters are transformed by

$$\mathbf{x}' = \mathbf{T}_b({}^0\mathbf{T}_4)\mathbf{x}, \tag{3.152}$$

where

$$
\begin{aligned}
\mathbf{x} &= \begin{bmatrix} x_0 & x_1 & x_2 & x_3 & y_0 & y_1 & y_2 & y_3 \end{bmatrix}^T,\\
\mathbf{x}' &= \begin{bmatrix} x'_0 & x'_1 & x'_2 & x'_3 & y'_0 & y'_1 & y'_2 & y'_3 \end{bmatrix}^T,
\end{aligned}
$$

The values of $\mathbf{x}'$ are substituted for the corresponding $\mathbf{x}$ terms in the constraint variety polynomials of Equation (3.16). The resulting set of five polynomials that intersect to give

the constraint variety of the EE 2A-chain with respect to Σ_0 are

$$
\begin{aligned}
&1 : x_0y_0 + x_1y_1 + x_2y_2 + x_3y_3 = 0,\\
&2 : -0.26068\,{x_2}^2 + x_2x_3 + 0.26068\,{x_3}^2 + 0.26068\,{x_0}^2 - 1.0\,x_0x_1 + 0.10322\,x_0x_2\\
&\quad -0.26068\,{x_1}^2 + 0.10322\,x_1x_3 = 0,\\
&3 : 3.9150\,x_0x_1 + 44.490\,x_0x_2 + 44.490\,x_1x_3 - 3.9150\,x_2x_3 + 0.64926\,{x_2}^2 + 0.19045\,x_2y_0\\
&\quad +1.1276\,x_2y_2 + 1.8452\,x_2y_3 - 0.64926\,{x_3}^2 + 0.19045\,x_3y_1 + 1.8452\,x_3y_2 + 3.0516\,x_3y_3\\
&\quad -0.64926\,{x_0}^2 + 3.0516\,x_0y_0 - 1.8452\,x_0y_1 + 0.19045\,x_0y_2 + 0.64926\,{x_1}^2 - 1.8452\,x_1y_0\\
&\quad +1.1276\,x_1y_1 + 0.19045\,x_1y_3 = 0,\\
&4 : 59.046\,x_1x_2 + 1393.2\,{x_0}^2 + 569.51\,{x_1}^2 + 8.3585\,{y_3}^2 + 8.3585\,{y_2}^2 + 8.3585\,{y_0}^2 +\\
&\quad 8.3585\,{y_1}^2 + 106.85\,x_2y_0 - 106.85\,x_3y_1 - 106.85\,x_0y_2 + 106.85\,x_1y_3 + 1387.1\,{x_3}^2\\
&\quad +731.71\,x_0x_1 + 563.42\,{x_2}^2 - 36.420\,x_0x_2 + 25.150\,x_1x_3 - 5.1470\,x_0y_1 + 5.1470\,x_1y_0\\
&\quad -5.1470\,x_2y_3 + 5.1470\,x_3y_2 - 193.10\,x_3y_0 - 98.539\,x_2y_1 + 193.10\,x_0y_3 + 98.539\,x_1y_2\\
&\quad -731.71\,x_2x_3 + 59.046\,x_0x_3 = 0,\\
&5 : 2.2709\,x_1x_2y_3 + 1.4969\,x_0x_2y_3 - 0.79836\,x_0x_3y_3 - 1.2112\,x_1x_3y_3 + 1.0574\,x_2x_3y_3\\
&\quad +46.679\,x_0x_1x_2 + 38.612\,x_0x_2x_3 + 9.0867\,x_1x_2x_3 + 2.5653\,x_0x_1y_0 - 0.30551\,x_1x_2y_0\\
&\quad -0.73099\,x_0x_2y_0 - 0.078081\,x_1x_3y_0 - 5.2734\,x_2x_3y_0 + 4.4867\,x_0x_1y_1 - 0.88349\,x_1x_2y_1\\
&\quad -1.4490\,x_0x_2y_1 + 0.59614\,x_0x_3y_1 + 0.076804\,x_1x_3y_1 - 8.8079\,x_2x_3y_1 + 2.3655\,x_0x_1y_2\\
&\quad -2.3260\,x_0x_2y_2 - 3.6645\,x_1x_2y_2 + 1.9952\,x_1x_3y_2 + 1.2588\,x_0x_3y_2 - 0.83971\,x_2x_3y_2\\
&\quad -1.7103\,x_0x_1y_3 + 0.053195\,{x_2}^2y_3 - 0.25231\,{x_1}^2y_3 + 125.33\,x_2{x_3}^2 + 0.48101\,{x_0}^2y_3\\
&\quad -87.846\,x_0x_1x_3 + 0.28190\,x_0x_3y_0 + 9.9322\,{x_0}^3 + 0.75533\,{x_1}^3 - 1.8686\,{x_2}^3 + 32.091\,{x_3}^3\\
&\quad -37.847\,{x_0}^2x_1 - 5.3242\,x_0{x_1}^2 + 37.483\,{x_0}^2x_2 + 3.7624\,x_0{x_2}^2 - 1.8686\,{x_1}^2x_2\\
&\quad +0.75533\,x_1{x_2}^2 + 32.091\,{x_0}^2x_3 + 9.9322\,x_0{x_3}^2 + 0.76432\,x_1{x_3}^2 - 2.1606\,{x_0}^2y_0\\
&\quad -0.85350\,{x_1}^2y_0 + 1.4174\,{x_2}^2y_0 - 1.3623\,{x_3}^2y_0 - 3.6169\,{x_0}^2y_1 - 1.3540\,{x_1}^2y_1\\
&\quad +2.3105\,{x_2}^2y_1 - 2.3581\,{x_3}^2y_1 - 0.42220\,{x_0}^2y_2 + 0.55704\,{x_1}^2y_2 - 0.32645\,{x_2}^2y_2\\
&\quad -1.0183\,{x_3}^2y_2 + 0.76291\,{x_3}^2y_3 - 25.336\,{x_2}^2x_3 + 21.343\,{x_1}^2x_3 = 0.
\end{aligned}
\tag{3.153}
$$

Intersecting the Constraint Varieties

Recalling Section 2.5.6 the inverse kinematics problem is solved by intersecting the constraint varieties of the base and EE 2A-chains to determine all possible poses where $\Sigma_L = \Sigma_R$. When the 2A-chain EE frames are coincident the two frames are represented by identical sets of Study parameters (after the homogeneous Study parameters are normalized). The set(s) of Study parameters that satisfy this condition are obtained by intersecting the polynomials that represent the base and EE 2A-chains.

Examining the polynomials of Equations (3.151) and (3.153) reveals that both sets contain the Study quadric and therefore there are nine equations in the eight unknown homogeneous Study parameters. The homogeneity of the Study parameters means that they can be normalized by dividing all of the parameters by x_0 and the system becomes nine equations and seven unknowns. To solve this over determined system of equations seven of the polynomials will be used to determine the set(s) of Study parameters that satisfy the system and the results will be substituted into the remaining two polynomials to ensure that the full system is satisfied. In this case the seven equations used are Polynomials 1, 2, 3, and 4 from the base 2A-chain constraint variety in Equation (3.151) and Polynomials 2, 3, and 4 from the EE 2A-chain constraint variety in Equation (3.153).

Solving the system of equations numerically using Maple 16 yields two sets of Study parameters:

$$X_1 = \begin{bmatrix} x_0 \\ x_1 \\ x_2 \\ x_3 \\ y_0 \\ y_1 \\ y_2 \\ y_3 \end{bmatrix} = \begin{bmatrix} 1.000 \\ 0.362 \\ -1.043 \\ -0.457 \\ -0.525 \\ -11.590 \\ 0.863 \\ -12.030 \end{bmatrix}, \quad X_2 = \begin{bmatrix} x_0 \\ x_1 \\ x_2 \\ x_3 \\ y_0 \\ y_1 \\ y_2 \\ y_3 \end{bmatrix} = \begin{bmatrix} 1.000 \\ 0.422 \\ -1.049 \\ -0.527 \\ -3.270 \\ -6.590 \\ 2.925 \\ -17.300 \end{bmatrix}. \tag{3.154}$$

Both sets of Study parameters, X_1 and X_2, also satisfy the remaining equations, the fifth polynomial in each of Equation (3.151) and (3.153). This means that both sets are solutions to the system of polynomials and describe the intersection of the base and EE 2A-chain constraint varieties. The sets of Study parameters describe the pose of the coincident frames Σ_L and Σ_R and to obtain the corresponding joint variables the 2A-chain inverse kinematics problem must be solved for both the base and EE 2A-chains.

Obtaining the Joint variables

The two sets of Study parameters resulting from the constraint variety intersection are now used to find the corresponding joint variables. The two sets, X_1 and X_2, are examined separately, starting with X_1.

To obtain the joint variables of Joints 1 and 2 the transformation matrix describing Σ_L with respect to Σ_0, ${}^0\mathbf{T}_L$, in terms of the joint variables u_1 and u_2 is obtained by

$$ {}^0\mathbf{T}_L = \mathbf{M}_1\mathbf{G}_1\mathbf{M}_2\mathbf{G}_2. \tag{3.155} $$

The Study parameters of ${}^0\mathbf{T}_L$ in terms of u_1 and u_2 are obtained by Equations (2.14) and (2.15). The resulting parametric equations for the eight Study parameters are normalized by dividing all of the Study parameters by the equation for x_0. The normalized equations are now set equal to the Study parameters of X_1, resulting in an over determined system of seven equations in terms of the two unknown joint variables. Solving two of the equations yields several possible solutions. In this example solving the equations x_2 and x_3 yielded eight pairs of solutions for u_1 and u_2. Each pair is tested in the remaining five equations and the only pair found to satisfy all of the equations is

$$ u_1 = 0.384, \quad u_2 = 1.485. \tag{3.156} $$

The joint variables u_3 and u_4 are obtained by a similar method, but only after some manipulation to account for Σ_{target} being away from the origin. The transformation matrix

corresponding to the Study parameters of X_1, ${}^0\mathbf{T}_R$ is found by Equation (2.11) to be

$$ {}^0\mathbf{T}_R = \begin{bmatrix} 1.000 & 0.000 & 0.000 & 0.000 \\ -1.272 & -0.072 & 0.074 & -0.995 \\ -8.280 & -0.694 & 0.713 & 0.103 \\ 19.730 & 0.717 & 0.698 & 0.000 \end{bmatrix}. \tag{3.157} $$

The transformation matrix describing the pose of Σ_{target} with respect to Σ_R, ${}^R\mathbf{T}_{target}$, is found using Equation (2.37) and is

$$ {}^R\mathbf{T}_{target} = \begin{bmatrix} 1.000 & 0.000 & 0.000 & 0.000 \\ 3.747 & 0.522 & -0.803 & 0.289 \\ -12.420 & 0.157 & -0.242 & -0.957 \\ -1.116 & 0.839 & 0.545 & 0.000 \end{bmatrix}. \tag{3.158} $$

The normalized Study parameters of ${}^R\mathbf{T}_{target}$, found using Equations (2.14) and (2.15), are

$$ \begin{bmatrix} x_0 \\ x_1 \\ x_2 \\ x_3 \\ y_0 \\ y_1 \\ y_2 \\ y_3 \end{bmatrix} = \begin{bmatrix} 1.000 \\ 1.174 \\ -0.430 \\ 0.751 \\ 4.450 \\ 3.027 \\ 8.271 \\ -5.928 \end{bmatrix}. \tag{3.159} $$

The transformation matrix ${}^R\mathbf{T}_{target}$ in terms of the unknown joint variables u_3 and u_4 is obtained by

$$ {}^R\mathbf{T}_{target} = \mathbf{M}_3\mathbf{G}_3\mathbf{M}_4\mathbf{G}_4, \tag{3.160} $$

and the Study parameters describing the transformation ${}^{R}\mathbf{T}_{target}$ in terms of u_3 and u_4 are found using Equations (2.14) and (2.15) and normalized. By equating the parametric form Study parameters in terms of the two joint variables with the corresponding Study parameters of Equation (3.159) a system of seven equations in terms of the two unknown joint variables is obtained. This over-determined system is solved in the same manner as was used to find u_1 and u_2 and the joint variables for Joints 3 and 4 are found to be

$$u_1 = 0.503, \quad u_2 = 1.681. \tag{3.161}$$

Recalling that when the constraint variety of the 2A-chains were constructed in Section 3.1.4 tangent of the half-angle substitution (Section 2.11.1) was used to eliminate trigonometric functions, thus $\phi_i = 2\tan^{-1}(u_i)$ and

$$\begin{aligned} \phi_1 &= 42.053^\circ, \\ \phi_2 &= 112.101^\circ, \\ \phi_3 &= 53.395^\circ, \\ \phi_4 &= 118.498^\circ. \end{aligned} \tag{3.162}$$

Also recall that $\theta_{v_i} = 2\phi_i$ was used to eliminate fractions, therefore the joint variables resulting from the inverse kinematics algorithm are

$$\begin{aligned} \theta_{v_1} &= 84.107^\circ, \\ \theta_{v_1} &= 224.203^\circ, \\ \theta_{v_1} &= 106.791^\circ, \\ \theta_{v_1} &= 236.997^\circ, \end{aligned} \tag{3.163}$$

which are the same as the starting joint variables of Equation (3.149). The first set of Study parameters provided the intended solution to the inverse kinematics problem, the second solution must also be examined.

The set of Study parameters X_2 from Equation (3.154) are examined in the same way as X_1. When solving the over determined system of seven equations for the joint variables u_1

and u_2 no solution is obtained. In Section 2.3.1 it was noted that the implicit representation of the constraint variety may be larger than the actual constraint variety, which could potentially lead to spurious results. In this case the results of the intersection yielded one solution that is in the true constraint variety (X_1) and one that is not (X_2). This illustrates the importance of confirming that the results of the algorithm provide the correct solution to the problem. In this case there is one real solution to the inverse kinematics problem, though it is possible that this is not the general case. A 4R-chain, in general, may posses multiple solutions to the inverse kinematics problem [9] depending on the manipulator configuration. Further research is required to determine the number of solutions for the general 4A-chain.

3.8.5 Jacobian Matrix

The Jacobian matrix of the 4A-chain was derived in Section 3.6.2 using the prototype manipulator DH-parameters. The 6×4 Jacobian is assembled in Equation (3.54) completed for the prototype manipulator by substituting the DH-parameters in Table 3.7. The Jacobian is not repeated here as its structure is the same as that presented in Section 3.6.2.

3.8.6 Dynamics of a Single A-Pair

Examining the dynamics of a single A-pair both with and without the leg mass effects illustrates the influence the legs have on the overall dynamic equations of motion. The mass properties for this example are derived from the first joint in the prototype serial A-chain. The mass of the single link, m_{link}, is the mass of the A-pair moving platform and the various components attached to it. The moving platform is approximated as a 10.000 in by 8.000 in plate weighing 4.135 lb and the CG of the plate lies on the joint axis. The moment of inertia about the joint axis is $I_{zz} = \frac{m_{l_1}}{12}(10^2 + 8^2)$ lb-in^2. Each of the six legs is a 6.000 *in* long slender rod weighing 0.115 lb. The acceleration due to gravity is $g = 386.088$ in/s^2.

The A-pair is examined in two orientations, the first vertical, where the joint axis is parallel to the gravity vector and the potential energy terms dominate the dynamic equations and the second horizontal, where the joint axis is perpendicular to the gravity vector and the kinetic energy terms dominate. Friction is not included in this analysis. All simulations

were run using MATLAB Simulink software. The assigned joint trajectory ($\theta(t)$, $\dot{\theta}(t)$, and $\ddot{\theta}(t)$) rotated the A-pair from a stationary $\theta = 60^\circ$ to a stationary $\theta = 300^\circ$ in ten seconds. The different dynamic models are compared using the total work done to follow the assigned trajectory.

In the vertical orientation the effects of gravity on the A-pair motion are most evident. The four different versions of the dynamic model compared are: massless legs, leg mass included as part of the link (lumped mass), leg effects fully accounted for (with legs), and considering only the leg potential energy terms (PE only). Equation (3.86) is used to obtain the dynamic equations and determine the torque required to follow the given trajectory. The appropriate mass values and the resulting total torque required to follow the desired trajectory are provided in Table 3.8. The torque time histories of the various models following the desired trajectory are provided in Figure 3.25(a).

Table 3.8: Masses and total work done for the different dynamic models of the single A-pair in the vertical and horizontal orientations to follow the 10 s joint trajectory.

			Total Work	
Model	$m_{link}g$	$m_{leg}g$	Vertical	Horizontal
Massless Legs	4.135 lb	0.000 lb	28.520 in-lb	0.090 in-lb
Lumped Mass	4.825 lb	0.000 lb	33.279 in-lb	0.105 in-lb
With Legs	4.135 lb	0.115 lb	30.894 in-lb	0.092 in-lb
PE Only	4.135 lb	0.115 lb	30.892 in-lb	N/A

When the A-pair axis is horizontal the gravity effects are removed and, since friction is ignored, the inertial effects of the link and legs dominate the dynamic equations. Three versions of the dynamic model, massless legs, lumped mass, and with legs are compared in Table 3.8. The torque time histories of the various models following the desired trajectory are provided in Figure 3.25(b).

To further examine the kinetic effects the trajectory is repeated at a faster rate. The joint trajectory now rotates the A-pair from stationary $\theta = 60^\circ$ to a stationary $\theta = 300^\circ$ in one second. The average joint velocity is now $240^\circ/s$ as opposed to $24^\circ/s$ for the previous simulations. The increased rates are intended to highlight the mass effects on the dynamics of the system. Table 3.9 shows the total work required for the various models to follow

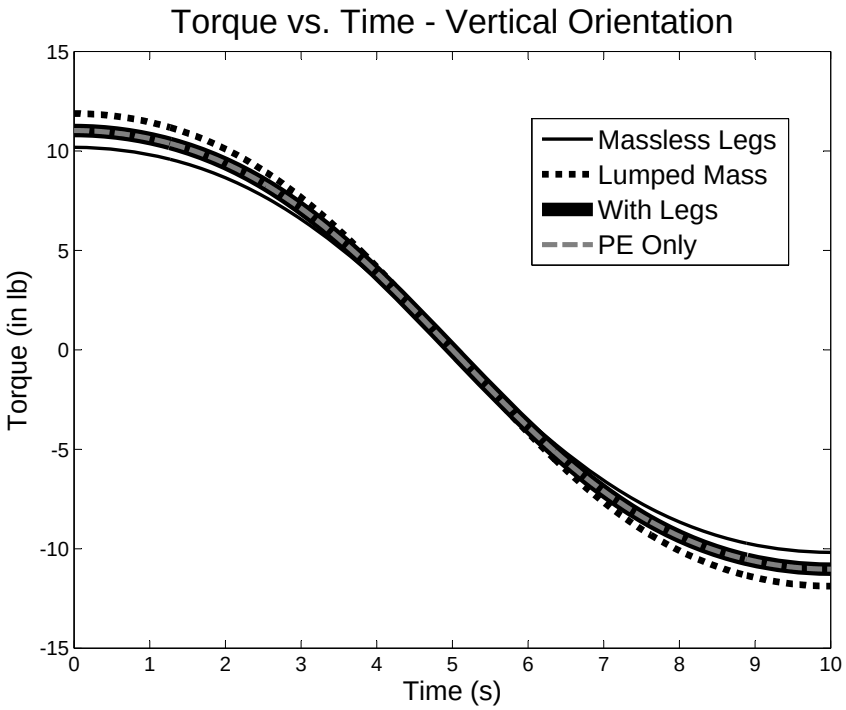

(a) Vertical orientation.

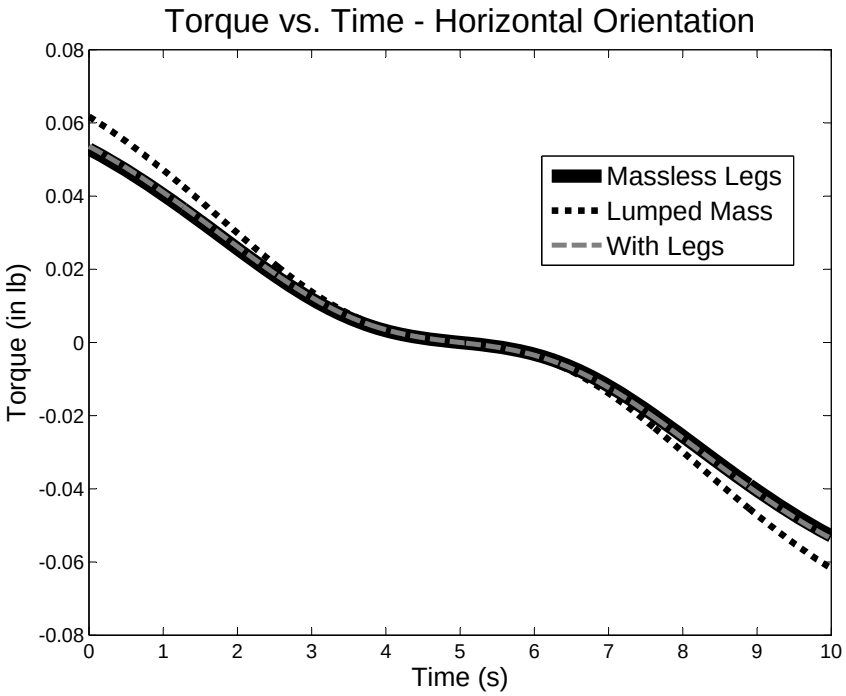

(b) Horizontal orientation.

Figure 3.25: Torque vs. time plots for the various models of an A-pair following a 10 s joint trajectory.

Table 3.9: Masses and total work done for the different dynamic models of the single A-pair in the vertical and horizontal orientations to follow the 1 s joint trajectory.

			Total Work	
Model	$m_{link}g$	$m_{leg}g$	Vertical	Horizontal
Massless Legs	4.135 lb	0.000 lb	44.999 in-lb	12.456 in-lb
Lumped Mass	4.825 lb	0.000 lb	52.508 in-lb	14.535 in-lb
With Legs	4.135 lb	0.115 lb	47.955 in-lb	12.632 in-lb
PE Only	4.135 lb	0.115 lb	47.772 in-lb	N/A

the defined joint trajectory and Figures 3.26 (a) and (b) show the torque time histories to follow the trajectory for the vertical and horizontal trajectories, respectively.

The two different orientations of the A-pair considered illustrate the impact of the inertial effects of the legs on the potential energy terms (vertical) and kinetic energy terms (horizontal). Analysis of the results provides some insight as to how to account for the leg effects in longer chains. The decision as to include leg effects or not and which model to use depends on the desired fidelity and the relative masses of the links and legs.

When the A-pair axis is vertical the potential energy effects of the link and legs dominate the dynamic equations (with friction ignored) and the kinetic energy effects are essentially negligible. For the masses used in the numerical example the total work done for the massless legs model is 7.7% less than that of the full leg model which is in turn 7.2% less than the lumped mass model for the 10 s simulation (6.2% and 8.7% for the 1 s simulation). If the difference between the link and leg mass is increased these percent differences decrease. For example if the link mass increases to 8.000 lb there is a 4% difference in total work done between the full leg and lumped mass models for the 10 s simulation. While the reason for the underestimation of the magnitude of the required torque by the massless legs model is obvious (the leg mass has been completely ignored) the difference between the lumped mass and full leg models results from the difference in the change in potential energy of the link versus the leg. As the trajectory is followed the difference in height of the link CG from the minimum to the maximum is 2.829 in while the CG of the legs varies by only 1.414 in. In the lumped mass model the change of potential energy for the leg mass is twice the actual value. The combined potential energy of the six legs can be determined by a

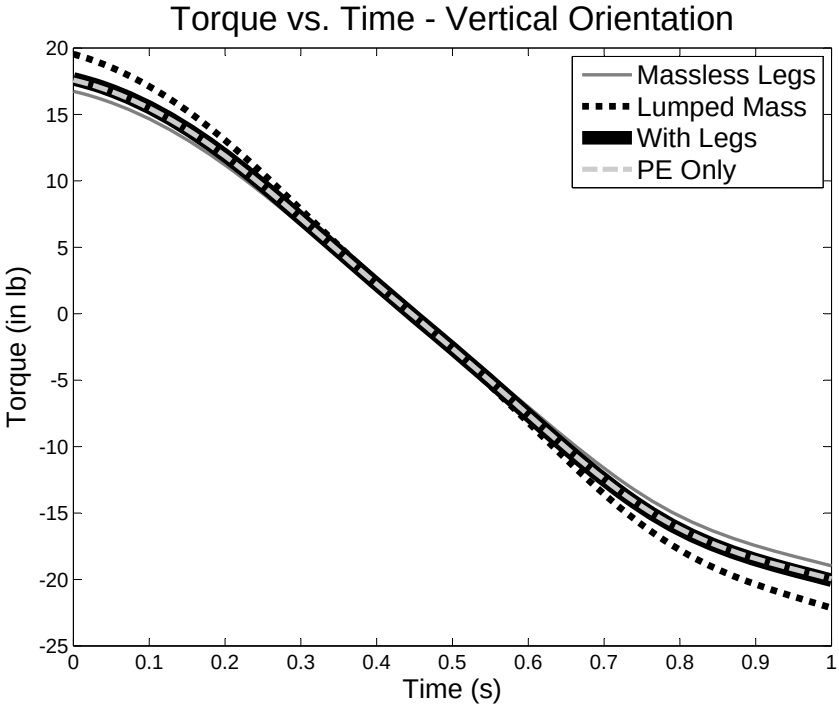

(a) Vertical orientation.

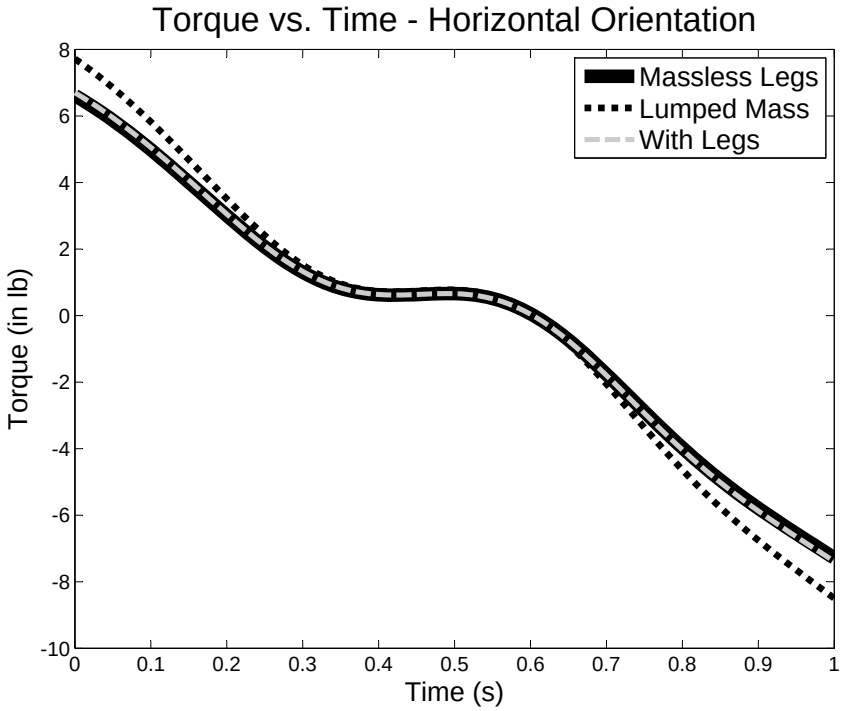

(b) Horizontal orientation.

Figure 3.26: Torque vs. time plots for the various models of an A-pair following a 1 s joint trajectory.

point mass equal to the total mass of the six legs on the joint axis equidistant to the fixed base and moving platform planes. Using this CG model allows for the determination of the leg potential energy when the A-pair joint axis is tilted away from vertical.

In the horizontal orientation the potential energy terms go to zero and only the kinetic energy terms are evident. The lumped mass model overestimates the total work by 14.3% for the 10 s simulation (15.1% for the 1 s simulation) while the massless leg model underestimates the total work by only 2.1% for the 10 s simulation (1.4% for the 1 s simulation). This suggests that for the masses used in this example the kinetic energy effects of the legs may be considered to be negligible.

The results of this numerical example suggests that little fidelity is lost if the leg kinetic energy terms are ignored, however the leg potential energy terms are important.

3.8.7 Dynamics of a 4A-Chain

The dynamic equations of motion for the prototype 4A-chain are derived in Section 3.7.4. This section focuses on the application of these equations to build a `Simulink` model of the prototype 4A-chain that can be used to determine the joint torques required to follow a given trajectory in the joint space or the trajectory of the EE for given joint torque time histories.

Mass Properties of the 4A-Chain

The mass properties of the prototype 4A-chain links were obtained using `Pro/Engineer` solid models. The aluminum was assumed to be a density of 0.100 lb/in^3 [105]. The mass properties of the links of the prototype 4A-chain are provide in Table 3.10. The CG and inertial tensor of Link i is given with respect to Σ_i. Each of the legs in the A-pairs is represented as a slender rod with a weight of 0.115 lb.

Assembling the Dynamic Equations for a 4A-chain

The derivation of the dynamic equations using the Lagrange method is covered in general in Section 2.7.1 and with regards to the prototype 4A-chain in Section 3.7.4. The inertia

Link	Vol. (in^3)	Weight (lb)	CG (in)	${}^i\mathbf{I}_{Link_i}$ ($lb-in^2$)
1	105.062	10.506	$\begin{bmatrix} -6.585\times10^{-5} \\ -4.062 \\ -1.636 \end{bmatrix}$	$\begin{bmatrix} 3684.737 & -6.562\times10^{-2} & 0.000 \\ -6.562\times10^{-2} & 1565.909 & -315.626 \\ 0.000 & -315.626 & 3765.518 \end{bmatrix}$
2	70.676	7.068	$\begin{bmatrix} -6.409 \\ 0.000 \\ -2.807 \end{bmatrix}$	$\begin{bmatrix} 1060.898 & 0.000 & -985.056 \\ 0.000 & 5801.630 & 0.000 \\ -98.506 & 0.000 & 5316.994 \end{bmatrix}$
3	79.967	7.997	$\begin{bmatrix} 0.000 \\ -1.419 \\ 3.562 \end{bmatrix}$	$\begin{bmatrix} 2229.924 & 0.000 & 0.000 \\ 0.000 & 2174.462 & 226.346 \\ 0.000 & 226.346 & 851.930 \end{bmatrix}$
4	28.511	2.851	$\begin{bmatrix} 0.000 \\ -3.140\times10^{-4} \\ -1.268 \end{bmatrix}$	$\begin{bmatrix} 248.954 & 0.000 & 0.000 \\ 0.000 & 248.962 & -3.071\times10^{-2} \\ 0.000 & -3.071\times10^{-2} & 130.650 \end{bmatrix}$

Table 3.10: Mass properties for the links of the prototype 4A-chain.

matrix, $\mathbf{B}(\boldsymbol{\theta})$, the matrix containing the centrifugal and coriolis terms, $\mathbf{C}(\boldsymbol{\theta}, \dot{\boldsymbol{\theta}})$, and the vector containing the potential energy terms $\mathbf{g}(\boldsymbol{\theta})$ are required to assemble the dynamic equations.

Using the link CG positions from Table 3.10 the link Jacobians are found using the equations of Section 3.7.4. The linear velocity components of the Jacobians, $\mathbf{J}_P^{Link_1}$, $\mathbf{J}_P^{Link_2}$, $\mathbf{J}_P^{Link_3}$, and $\mathbf{J}_P^{Link_4}$, are found by Equations (3.95), (3.106), (3.117), and (3.131), respectively. The angular velocity Jacobians, $\mathbf{J}_O^{Link_1}$, $\mathbf{J}_O^{Link_2}$, $\mathbf{J}_O^{Link_3}$, and $\mathbf{J}_O^{Link_4}$ are found by Equations (3.97), (3.107), (3.118), and (3.132), respectively. The inertial matrix, $\mathbf{B}_i(\boldsymbol{\theta})$, of each link is found using Equation (2.68) with the motor masses and inertial properties ignored at this time, thus

$$\mathbf{B}_i(\boldsymbol{\theta}) = m_{Link_i}\mathbf{J}_P^{(Link_i)T}\mathbf{J}_P^{(Link_i)} + \mathbf{J}_O^{(Link_i)T}\mathbf{R}_i^i\mathbf{I}_{Link_i}\mathbf{R}_i^T\mathbf{J}_O^{(Link_i)}, \tag{3.164}$$

where the link mass and inertial properties are obtained from Table 3.10. The full inertial matrix, $\mathbf{B}(\boldsymbol{\theta})$, is found by

$$\mathbf{B}(\boldsymbol{\theta}) = \mathbf{B}_1(\boldsymbol{\theta}) + \mathbf{B}_2(\boldsymbol{\theta}) + \mathbf{B}_3(\boldsymbol{\theta}) + \mathbf{B}_4(\boldsymbol{\theta}). \tag{3.165}$$

The resulting inertial matrix is too large to express explicitly. The $\mathbf{B}(\boldsymbol{\theta})$ matrix was obtained using `Maple` and converted to `MATLAB` format for use in `Simulink`.

The centrifugal and Coriolis terms of the $\mathbf{C}(\boldsymbol{\theta}, \dot{\boldsymbol{\theta}})$ matrix are obtained by Equation (2.74). Constructed using the elements of $\mathbf{B}(\boldsymbol{\theta})$, the $\mathbf{C}(\boldsymbol{\theta}, \dot{\boldsymbol{\theta}})$ is again to large to express here but was obtained using `Maple` and converted to `MATLAB` format for use in `Simulink`.

The potential energy effects of the links and legs are derived in Section 3.7.7. The potential energy terms for the four links are derived in Equation (3.134), describing the moment induced at each joint by the mass of each link, as a function of the joint angles $\boldsymbol{\theta}$. The moment induced on each joint due to the legs of each A-pair are given by Equations (3.137), (3.142), (3.143), and (3.144) for Joint 1, 2, 3, and 4, respectively. The total potential energy effects are assembled in Equation (3.145), resulting in the 4×1 vector $\mathbf{g}$ whose elements describe the moment induced at each joint by the potential energy in the system.

The inverse dynamic equations, describing the torque, $\boldsymbol{\tau}$, is provided in Equation (3.146). In this work friction and other dissipative effects are not included and it is assumed that the EE is free, exerting no forces or moments on the environment, thus the inverse dynamic equations can be written as

$$\boldsymbol{\tau} = \mathbf{B}(\boldsymbol{\theta})\ddot{\boldsymbol{\theta}} + \mathbf{C}(\dot{\boldsymbol{\theta}}, \boldsymbol{\theta})\dot{\boldsymbol{\theta}} + \mathbf{g}. \tag{3.166}$$

Simulation and Results

A simple feedback controller is built using the dynamic results for the prototype 4A-chain using the method discussed in Section 2.10. The elements of the dynamic equations, $\mathbf{B}(\dot{\boldsymbol{\theta}})$, $\mathbf{C}(\boldsymbol{\theta}, \dot{\boldsymbol{\theta}})$, and $\mathbf{G}(\boldsymbol{\theta})$ for the prototype 4A-manipulator are used to construct a `Simulink` model in the form of the block diagram in Figure 2.18.

To illustrate the application of the inverse dynamic equations a simple set of joint trajectories based on the capabilities of the Thermo CRS A645 robot arm. Table 3.11 shows the joint specifications of the A645 Thermo CRS. Only the first four joints are of concern when comparing to the prototype 4A-chain and the acceleration and maximum

Joint	Range	Max. Speed	Default Accel.	Cont. Stall Torque Rating
1	$\pm 175°$	$180°/s$	$720°/s^2$	$350 \text{ in} - \text{lb}$
2	$\pm 90°$	$180°/s$	$720°/s^2$	$350 \text{ in} - \text{lb}$
3	$\pm 110°$	$180°/s$	$720°/s^2$	$350 \text{ in} - \text{lb}$
4	$\pm 180°$	$171°/s$	$1430°/s^2$	$61 \text{ in} - \text{lb}$
5	$\pm 105°$	$173°/s$	$1430°/s^2$	$61 \text{ in} - \text{lb}$
6	$\pm 171°$	$171°/s$	$1430°/s^2$	$22 \text{ in} - \text{lb}$

Table 3.11: Joint specifications for the A645 Thermo CRS [95].

speed values are used to determine the torque required to actuate the prototype 4A-chain to similar specifications. The maximum range of motion of the A-pairs ($180° \pm 120°$) is used as opposed to the joint limits of the A645 Thermo CRS.

The joint trajectories are based on starting at rest at one joint extreme, accelerating the joint at the default acceleration to the maximum speed, holding the maximum speed and decelerating to rest at the other joint extreme. Figure 3.27 shows the shape of the

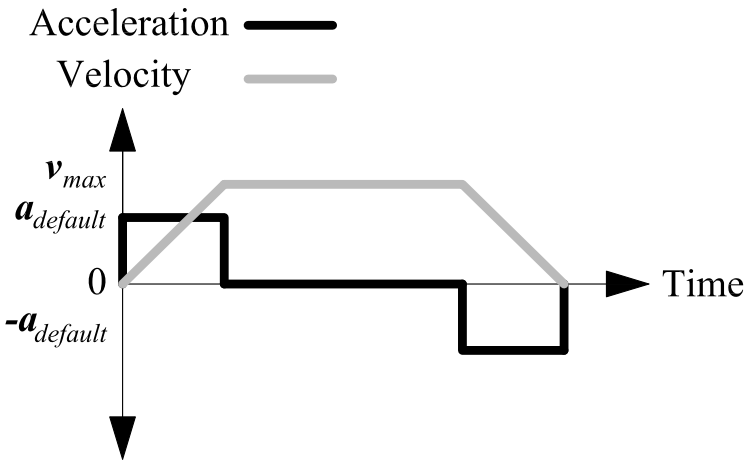

Figure 3.27: Approximations of the acceleration and velocity profiles for each joint in the 4A-chain.

acceleration and velocity time histories for such motion. Using the kinematic equations of motion the times for acceleration changes can be determined. For Joints 1, 2, and 3 starting at $\theta = 60°$ the joints accelerate at $720°/s^2$ from time $t = 0$ s to $t = 0.25$ s, hold at a constant $180°/s$ (acceleration is $0°/s^2$) until $t = 1.33$ s and accelerate at $-720°/s^2$ to rest at $300°$ at $t = 1.58$ s. Similarly, Joint 4 starts at $\theta = 60°$, accelerates at $1430°/s^2$ from time $t = 0$ s to

$t = 0.12$ s, holds at a constant 171°/s (acceleration is 0°/s^2) until $t = 1.4$ s and accelerates at -1430°/s^2 to rest at 300° at $t = 1.52$ s.

The time history of the four joint torques obtained by the `Simulink` model are as shown in Figure (3.28). The joint requiring the most torque is Joint 2. This is because there is a

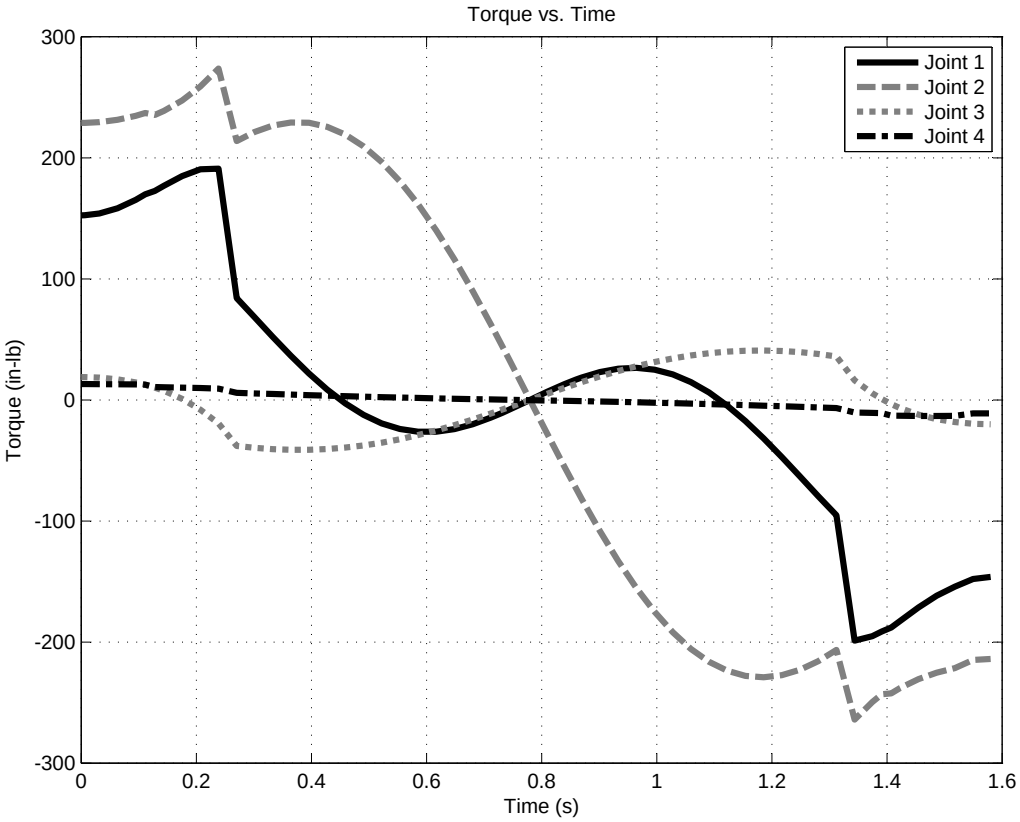

Figure 3.28: Plot of Simulink results for torque vs. time for the four joints of the prototype 4A-chain to follow the prescribed joint trajectories.

large mass (three links and two joints) cantilevered off of the joint with a long moment arm. The torque required for Joint 2 to follow the trajectory approaches a maximum of 300 in-lb (34 N-m). This is on par with the continuous stall torque rating listed in Table 3.11. The discontinuities in the torque time histories (between 0.2 s and 0.4 s, and between 1.2 s and 1.4 s) correspond to the instances in the joint trajectories where there is a step in the acceleration.

The sinusoidal shape of the torque time histories for Joints 2 and 3 is unsurprising and

is similar to what would be obtained for an R-chain. The axes of these two joints are always perpendicular to the gravity vector, supporting a cantilevered load. Interestingly, the torque time history of Joint 1 also follows a distinct sinusoidal path. The axes of Joint 1 is at all times parallel to the gravity vector. A motor driving an R-pair in such an orientation would require an almost constant torque to drive the joint at a constant velocity while the A-pair requires additional torque to raise and lower the mass of all of links parallel to the joint axis as the joint rotates. As the joint rotates from $\theta_1 = 60^\circ$ to $\theta_1 = 180^\circ$ the torque is required to lift the mass of the manipulator and from $\theta_1 = 180^\circ$ to $\theta_1 = 300^\circ$ a torque in the opposite direction is required to resist the mass of the manipulator as it is lowered.

This basic model of the prototype 4A-chain is presented to illustrate the implementation of the dynamic equations of motion. It can be used as a first step towards sizing motors for the prototype manipulator. A higher fidelity model will include motor and transmission mass effects, friction and damping effects, external loading, *etc.*

Chapter 4

Concluding Remarks

The main contribution of this dissertation was the characterisation of the kinematics and dynamics of A-pairs and A-chains. The analysis of the reachable workspace of serial A-chains was also initiated with the introduction of a novel algorithm for approximating the reachable workspaces of serial manipulators. Much of the presented material applies to general nA-chains though emphasis has been placed on 4A-chains to correspond with the design of a prototype 4A-manipulator. The work presented represents the first full kinematic and dynamic analysis of A-chains, major tools that will be required in the further study of chains constructed using this novel kinematic pair. The resulting formulations of the kinematic and dynamic equations can be utilised for manipulator design, the development of control schemes, manipulator simulation and the comparison of A-pairs and A-chains with R-pairs and R-chains. This research represents a significant advancement in the study of A-pairs and A-chains.

The position level kinematics of A-chains have been generalised. To do this, the A-chain DH-parameters which unambiguously describe the kinematic geometry of the A-chain have been revised to apply to general A-chains. This required that the joint angle θ be represented by the sum of two components, one fixed, θ_f and one variable, θ_v. The geometric constant ρ is also determined to provide for the general description of the A-pair. The derivation of the direct kinematic equations has been revised to account for these changes. The equations describing the constraint varieties of 2A-chains have been revised to account for the changes in the DH-parameters. As well, a new method for obtaining the implicit representation of

the constraint varieties has been employed. The resulting sets of equations that describe the constraint varieties are employed in the inverse kinematics algorithm for 4A-chains.

The joint limits of the new kinematic pair have been determined based on self-collisions between the legs of the A-pair, allowing for the determination of the maximum reachable workspace of nA-chains. Legs with a radius of zero were used to determine that the maximum range of motion is 240° or $60° < \theta_v < 300°$. Cylinder collision detection was used to determine the joint limits when the thickness of the legs is considered. A novel algorithm for approximating the reachable workspace of serial manipulators was introduced that significantly reduces the time required to determine the workspace relative to existing methods, while producing comparable results. The new reachable workspace algorithm was applied to find the reachable workspaces of A-chains possessing 1, 2, and 4 joints.

The derivation of the Jacobian matrix for a single A-pair and nA-chains was described providing for velocity level kinematics and static force analysis. The method is based on existing techniques but their application to A-pairs is unique because of the sinusoidal coupling of translation and rotation. The Jacobian of a 4A-chain was derived to illustrate the method of obtaining Jacobian matrices for longer A-chains and the technique is applicable to general nA-chains.

The dynamic equation of motion of a single A-pair was obtained using both the Lagrange and Newton-Euler formulations concurrently. As expected, the two methods provided identical results. The Lagrange formulation was also used to determine the influence of the mass properties of the A-pair legs on the dynamics of the single A-pair. The decision whether to include the leg mass effects in the dynamic model or not depends on factors such as the desired model fidelity and the relative mass of the legs and the other links in the chain. Results for the prototype manipulator suggest that the kinetic energy effects of the legs can be considered negligible, but the potential energy effects of the legs should be included as a point mass on the axis of rotation of the A-pair. The dynamic equations of motion for a specific configuration of a 4A-chain were obtained to illustrate the method of obtaining the equations for longer chains and incorporating the leg potential energy effects. Though only a 4A-chain was examined in this dissertation, the method applies to general nA-chains.

A numeric example based on a prototype 4A-chain was presented to illustrate the application of the techniques developed in this dissertation.

4.1 Future Research

The kinematic and dynamic analysis presented in this dissertation lays the foundation for future study in the area of A-pairs and A-chains. One area that should be pursued is the comparison of A-pairs and A-chains with R-pairs and R-chains. This is an important topic in that it will show the benefits and disadvantage of A-pairs when compared to the more traditional R-pair. The following is a list of suggestions for future study with regards to the comparison of A-pairs and R-pairs.

- The A-pair was initially proposed to take advantage of the stiffness inherent to parallel manipulators. While the self-motions of the A-pair lead to a well-defined one DOF motion about and along the axis of rotation the joint maintains the stiffness of a parallel manipulator in all other directions. A characterisation of this stiffness needs to be made and compared to the traditional R-pair. Literature on the topic has proven to be difficult to find so it is likely that future research will need to develop performance indices for joint stiffness and examine different designs of revolute joints and A-pair joints.

- Comparisons of the reachable workspaces of A-chains and R-chains should be explored in more depth. In this dissertation the chains are compared based on the amount of the R-chain reachable workspace that can be recreated by the A-chain. Other comparisons can be made with regards to workspace volume, the volume index performance index (relationship between workspace volume and manipulator length), the shape of the workspace, or other performance indices.

- A full comparison of the Jacobian matrices of similar A-chains and R-chains, especially a singularity analysis may show some important differences between the two types of kinematic chains. The A-chain singularities demonstrated in this dissertation do not

constitute a full singularity analysis but intend only to illustrate some basic singularities. The coupled translation and rotation of the A-pair may lead to instances where the R-chain possesses singularities but the the A-chain does not, or vice versa. The singularities of wrist partitioned 6R-chains are well studied [106], however A-chains do not function in the same manner as wrist partitioned manipulators, so a full analysis would be useful.

- A full comparison of the dynamic equations of motion would provide insight into the differences between A-chains and R-chains with regards to torque requirements to follow given trajectories. One interesting characteristic of the A-pair is that when the joint axis is vertical the coupled motion means that the rotation causes the attached links to raise or lower. This means that for part of the rotation the joint must lift the entire mass of the links, while at other times the mass of the link aids in the rotation of the joint. Further study is required to determine if this characteristic can be used as an advantage.

In addition to the comparison of A-chains and R-chains there are many topics in the study of A-pairs that lend themselves to future research. The following is a non-exhaustive list of topics in the study of A-pairs that should be explored in the future.

- Expand the number of joints from four to six and examine the dexterity of such a manipulator. The coupled translation and rotation will greatly influence the dexterous workspace.

- Examine other configurations of A-chains. It may be the case that mimicking an existing R-chain does not result in the optimal configuration for an A-chain.

- Adapt the algorithm for the inverse kinematics of 6R-chains to 6A-chains using the new method for obtaining 2A-chain constraint varieties.

- Use the dynamic model to size and select a motor and transmission for the prototype manipulator.

- Increase the fidelity of the dynamic model by including a friction model.
- Use the dynamic model to build a more detailed controller for the prototype manipulator.

In addition to the study of A-pairs and A-chains this dissertation introduced a new algorithm for quickly obtaining the reachable workspace of A-chains. Though the algorithm has proven to be effective more study is needed to optimize the algorithm and investigate how well it approximates the actual workspace. The new algorithm has applications beyond the study of A-chains as it can be applied to open serial chains constructed using any joint type.

References

[1] J. D. Robinson, "Direct and inverse kinematics of a new class of parallel-serial hybrid manipulator," Master's thesis, Carleton University, Canada, January 2008.

[2] X. Kong and C. M. Gosselin, "Type synthesis of 3t1r 4-dof parallel manipulators based on screw theory," *IEEE Transactions On Robotics and Automation*, vol. 20, no. 2, pp. 181–190, 2004.

[3] P.-L. Richard, C. M. Gosselin, and X. Kong, "Kinematic analysis and prototyping of a partially decoupled 4-dof 3t1r parallel manipulator," *Journal of Mechanical Design*, vol. 129, no. 6, pp. 611–617, 2007.

[4] R. Descartes, *La Géométrie*. Paris: A. Hermann, Librairie Scientifique, 1886.

[5] D. M. Y. Sommerville, *Analytic Geometry of Three Dimensions*. London: Cambridge University Press, 1934.

[6] D. Gans, *Transformations and Geometries*. New York: Apple-Century-Crofts, 1969.

[7] M. Pfurner, *Analysis of Spatial Serial Manipulators Using Kinematic Mapping*. PhD thesis, University of Innsbruck, Austria, October 2006.

[8] M. J. D. Hayes, P. J. Zsomber-Murray, and C. Chen, "Unified kinematic analysis of general planar parallel manipulators," *ASME Journal of Mechanical Design*, vol. 126, no. 5, pp. 866–874, 2004.

[9] J. J. Craig, *Introduction to Robotics Mechanics and Control*. Upper Saddle River, New Jersey: Pearson Prentice Hall, 2005.

[10] M. J. D. Hayes, *Kinematics of General Planar Stewart-Gough Platforms*. PhD thesis, McGill University, Montreal, Canada, September 1999.

[11] L. Euler, "Formulae generales pro translatione quacunque corporum rigidorum (general formulas for the translation of arbitrary rigid bodies)," *Novi Commentarii academiae scientiarum Petropolitanae*, vol. 20, no. E478.

[12] O. Bottema and B. Roth, *Theoretical Kinematics*. New York: North-Holland Publishing Company, 1979.

[13] H. Goldstein, *Classical Mechanics*. Reading, MA: Addison-Wesley, 1980.

[14] K. Brunnthaler, *Synthesis of 4R Linkages Using Kinematic Mapping*. PhD thesis, University of Innsbruck, Austria, 2007.

[15] W. R. Hamilton, "On quaternions," in *Proceedings of the Royal Irish Academy*, pp. 1–16, 1847.

[16] J. B. Kuipers, *Quaternions and Rotation Sequences: A Primer with Applications to Orbits, Aerospace and Virtual Reality*. Princeton, New Jersey: Princeton University Press, 2002.

[17] O. Rodrigues, "De l'attraction des sphéroïdes," *Correspondence sur l'École Impriale Polytechnique*.

[18] J. Angeles, "Rational kinematics," *Springer Tracts in Natural Philosophy*.

[19] J. Angeles, *Fundamental of Robotic Mechanical Systems: Theory, Methods, and Algorithms*. New York: Springer, 1997.

[20] E. Study, *Geometrie der Dynamen*. Leipzig, Germany: B.G. Teubner, 1903.

[21] A. Cayley, "Sur quelques propriétés des déterminants gauches," *Journal für die reine und angewandte Mathematik*, vol. 32, pp. 119–123, 1846.

[22] B. Siciliano, L. Sciavicco, L. Villani, and G. Oriolo, *Robotics Modelling, Planning and Control*. London: Springer-Verlag London Limited, 1995.

[23] KUKA Robot Group, "KUKA industrial robots." http://www.kuka-robotics.com.

[24] J. P. Merlet, *Parallel Manipulators*. New York: Springer, 2006.

[25] G. Carbone and M. Ceccarelli, "A stiffness analysis for a hybrid parallel-serial manipulator," *Robotica*, vol. 22, pp. 567–576, 2004.

[26] CAE, "Cae simulation products and services." http://www.cae.com.

[27] M. L. Husty, "An algorithm for solving the direct kinematics of general Stewart-Gough platforms," *Mechanism and Machine Theory*, vol. 31, no. 4, pp. 365–380, 1996.

[28] X. Z. Zheng, H. Z. Bin, and Y. G. Luo, "Kinematic analysis of a hybrid serial-parallel manipulator," *International Journal of Advanced Manufacturing Technology*, vol. 23, pp. 925–930, 2004.

[29] L. Romdhane, "Design and analysis of a hybrid serial-parallel manipulator," *Machine and Mechanism Theory*, vol. 34, pp. 1037–1055, 1999.

[30] M. Zhao, T. Gui, G. Chao, Q. Li, and D. Tan, "Development of a redundant robot manipulator based on three DOF parallel platforms," in *Proceedings of the 1995 IEEE International conference on Robotics and Automation*, (Nagoya, Japan), pp. 221–226, May 1995.

[31] O. Ibrahim and W. Khalil, "Inverse dynamic modeling of serial-parallel hybrid robots," in *Proceedings of the 2006 IEEE/RSJ International Intelligent Robots and Systems*, (Beijing, China), pp. 2156–2161, October 2006.

[32] J. Denavit and R. S. Hartenberg, "A kinematic notation for lower-pair mechanisms based on matrices," *Journal of Applied Mechanics*, vol. 77, pp. 215–221, 1955.

[33] J. E. Shigley and J. J. Uicker, *Theory of Machines and Mechanisms*. New York: McGraw-Hill, Inc., 1995.

[34] M. L. Husty, M. Pfurner, and H.-P. Schröcker, "A new and efficient algorithm for the inverse kinematics of a general serial 6R manipulator," *Mechanism and Machine Theory*, vol. 42, no. 1, pp. 66–81, 2007.

[35] M. L. Husty, M. Pfurner, H.-P. Schröcker, and K. Brunnthaler, "Algebraic methods in mechanism analysis and synthesis," *Robotica*, vol. 25, pp. 661–675, 2007.

[36] N. Chen and G. A. Parker, "Inverse kinematics solution to a calibrated PUMA 560 industrial robot," *Control Engineering Practice*, vol. 2, no. 2, pp. 239–245, 1994.

[37] J. Lloyd and V. Hayward, "Kinematics of common industrial robots," *Robotics and Autonomous Systems*, vol. 4, no. 2, pp. 169–191, 1988.

[38] R. Manseur and K. L. Doty, "Structural kinematics of 6-revolute-axis robot manipulators," *Mechanism and Machine Theory*, vol. 31, no. 5, pp. 647–657, 1996.

[39] A. Pashkevich, "Real-time inverse kinematics for robots with offset and reduced wrist," *Control Engineering Practice*, vol. 5, no. 10, pp. 1143–1450, 1997.

[40] F. Chapelle and P. Bidaud, "A closed form for inverse kinematics approximation of general 6R manipulators using genetic programming," in *Proceedings of the 2001 IEEE International Conference on Robotics and Automation*, (Seoul, Korea), pp. 3364–3369, May 2001.

[41] D. Pieper, *The Kinematics of Manipulators Under Computer Control*. PhD thesis, Stanford University, 1968.

[42] B. Roth, J. Rastegar, and V. Scheinmann, "On the design of computer controlled manipulators," in *First CISM-IFToMM Symposium*, (Cassino, Italy), May 1973.

[43] J. Duffy and C. Crane, "A displacement analysis of the general spatial 7-link, 7R mechanism," *Mechanism and Machine Theory*, vol. 15, pp. 153–169, 1980.

[44] L. W. Tsai and A. Morgan, "Solving the kinematics of the most general six- and five-degree-of-freedom manipulators by continuation methods," *Transactions of ASME, Journal of Mechanisms, Transmissions and Automation in Design*, vol. 107, pp. 189–200, June 1985.

[45] E. J. F. Primrose, "On the input-output equation of the general 7R-mechanism," *Mechanism and Machine Theory*, vol. 21, pp. 509–510, 1986.

[46] H. Y. Lee and C. G. Liang, "Displacement analysis of the spatial 7-link 6R-P linkage," *Machine and Mechanism Theory*, vol. 22, pp. 1–11, 1987.

[47] H. Y. Lee and C. G. Liang, "Displacement analysis of the general 7-link 7R mechanism," *Machine and Mechanism Theory*, vol. 23, pp. 219–226, 1988.

[48] M. Raghavan and B. Roth, "Kinematic analysis of the 6R manipulator of general geometry," in *Proceedings of the 5th International Symposium on Robotics Research*, (Tokyo, Japan), 1990.

[49] D. Manocha and J. F. Canny, "Real time inverse kinematics for general 6R manipulators," in *Proceedings of the IEEE International Conference on Robotics and Automation*, (Nice, France), pp. 383–389, May 1992.

[50] D. Kohli and M. Osvatic, "Inverse kinematics of the general 6R and 5R,P serial manipulators," *ASME Journal of Mechanical Design*, vol. 115, pp. 922–931, 1993.

[51] M. Ghazvini, *Computational Kinematics*, ch. Reducing the Inverse Kinematics of Manipulators to the Solution of a Generalized Eigenproblem, pp. 15–26. Kluwer Academic Publisher, 1993.

[52] M. Pfurner and M. L. Husty, "Implementation of a new and efficient algorithm for the inverse kinematics of serial chains," in *New Trends in Mechanism Science (Proceedings of EUCOMES10, The 3rd European Conference on Mechanism Science)*, (Cluj-Napoca, Romania), pp. 91–98, September 2010.

[53] M. L. Husty, M. Pfurner, and H.-P. Schröcker, "A new and efficient algorithm for the inverse kinematics of a general serial 6R manipulator," in *Proceedings of ASME 2005, 29th Mechanisms and Robotics Conference*, (Long Beach, California), September 2005.

[54] M. J. D. Hayes and R. G. Langlois, "Atlas: A novel kinematic architecture for six dof motion platforms," *Transactions of the Canadian Society for Mechanical Engineering*, vol. 29, no. 4, pp. 701–709, 2005.

[55] G. Castelli, E. Ottaviano, and M. Ceccarelli, "A fairly general algorithm to evaluate workspace characteristics of serial and parallel manipulators," *Mechanics Based Design of Structures and Machines*, vol. 36, pp. 14–33, 2008.

[56] T. W. Lee and D. H. C. Yang, "On the evaluation of manipulator workspace," *ASME Journal of Mechanical Design*, vol. 103, pp. 70–77, July 1981.

[57] H. Choset, K. Lynch, S. Hutchinson, G. Kantor, W. Burgard, L. Kavraki, and S. Thrun, *Principles of Robot Motion: Theory, Algorithms and Implementations*. Cambridge, Massachusetts: The MIT Press, 2005.

[58] B. Roth, "Performance evaluation of manipulators from a kinematic viewpoint," *National Bureau of Standards, Special Publication*, no. 459, pp. 39–68, 1975.

[59] A. Kumar and K. J. Waldron, "The dexterous workspace," *ASME Paper*, no. 80-DET-108, 1980.

[60] A. Kumar and K. J. Waldron, "The workspaces of a mechanical manipulator," *ASME Journal of Mechanical Design*, vol. 103, pp. 665–672, July 1981.

[61] D. C. H. Yang and T. W. Lee, "On the workspace of mechanical manipulators," *ASME Journal of Mechanisms, Transmissions, and Automation in Design*, vol. 105, no. 1, pp. 62–69, 1983.

[62] A. Gallant, R. Boudreau, and M. Gallant, "Dexterous workspace of a 3-prrr kinematically redundant planar parallel manipulator," *Transactions of the Canadian Society for Mechanical Engineering*, vol. 33, no. 4.

[63] A. Gallant, R. Boudreau, and M. Gallant, "Dexterous workspace of a n-prrr planar parallel manipulators," in *Proceedings of ASME International Design Engineering Technical Conferences*, (Montreal, Canada), August 2010.

[64] A. Gallant, R. Boudreau, and M. Gallant, "Dexterous workspace of n-rrrr and n-rrpr manipulators," in *Proceedings of The 2011 CCToMMM Symposium on Mechanisms, Machines and Mechatronics*, (Montreal, Quebec, Canada), June 2011.

[65] A. Gallant, R. Boudreau, and M. Gallant, "Geometric determination of the dexterous workspace of n-rrrr and n-rrpr manipulators," *Mechanism and Machine Theory*, 2012. To Appear.

[66] Y. C. Tsai and A. H. Soni, "An algorithm for the workspace of a general n-R robot," *ASME Journal of Mechanisms, Transmissions, and Automation in Design*, vol. 105, no. 1, pp. 52–57, 1983.

[67] A. Kumar and M. S. Patel, "Mapping the manipulator workspace using interactive computer graphics," *The International Journal of Robotics Research*, vol. 5, no. 2, pp. 122–130, 1986.

[68] M. Ceccarelli, "On the workspace of 3R robot arms," in *Proceedings of the Fifth IFToMM International Symposium on Theory and Practice of Mechanisms*, (Bucharest, Hungary), pp. 37–46, 1989.

[69] M. Ceccarelli, "A formulation for the workspace boundary of general n-revolute manipulators," *Mechanism and Machine Theory*, vol. 31, no. 5, pp. 637–646, 1996.

[70] J. D. Robinson, "Kinematic and dynamic analysis of a single algebraic screw pair." Internal Progress Report PHD-PR-06-V01, June 2010.

[71] D. R. Walter and M. L. Husty, "On implicitization of kinematic constraint equations," *Machine Design & Research*, vol. 26, pp. 218–226, 2010.

[72] M. T. Masouleh, D. R. Walter, M. L. Husty, and C. Gosselin, "Forward kinematic problem of the symmetric 5-dof parallel mechanisms (3t2r) using the linear implictization algorithm," in *Proceedings of the 13th World Congress in Mechanism and Machine Science*, (Guanajuato, Mexico), June 2011.

[73] D. R. Walter and M. L. Husty, "Kinematic analysis of the tsai-3upu parallel manipulator using algebraic methods.," in *Proceedings of the 13th World Congress in Mechanism and Machine Science*, (Guanajuato, Mexico), June 2011.

[74] M. T. Masouleh, C. Gosselin, M. L. Husty, and D. R. Walter, "Forward kinematic problem of 4-dof parallel mechanisms (3t1r) with identical limb structures acuated by revolute actuators using the linear implictization algorithm," in *Proceedings of the ASME Design Engineering Technical Conference*, (Washington, DC, USA), August 2011.

[75] M. T. Masouleh, C. Gosselin, M. L. Husty, and D. R. Walter, "Forward kinematic problem of 5-RPUR parallel mechanisms (3T2R) with identical limb structures," *Mechanism and Machine Theory*, vol. 46, no. 7, pp. 945–959, 2011.

[76] B. Bruchberger, *Ein Algorithmus zum Affinden der Basiselemente des Restklassenringes nach einem nulldimensionalen Polynomideal (An Algorithm for Finding the Basis Elements of the Residue Class Ring of a Zero Dimensional Polynomial Ideal)*. PhD thesis, University of Innsbruck, Austria, 1965.

[77] B. Bruchberger, "Ein algorithmisches kriterium für die lösbarkeit eines algebraischen gleichungssystems (an algorithmic criterion for the solvability of a system of algebraic equations)," *Aequationes Mathematicae*, vol. 4, no. 3, pp. 374–383, 1970.

[78] W. W. Adams and P. Loustaunau, *An Introduction to Gröbner Bases*. United States: American Mathematical Society, 1994.

[79] M. Griffis and J. Duffy, "Method and apparatus for controlling geometrically simple parallel mechanisms with distinctive connections." U.S. Patent Number: 5,179,525, Jan 1993.

[80] M. L. Husty and A. Karger, "Self-motions of Griffis-Duffy type parallel manipulators," in *Proceedings of ICRA '00 IEEE International conference on Robotics and Automation*, (San Francisco, CA, USA), pp. 7–12, April 2000.

[81] A. Karger and M. Husty, "Classification of all self-motions of the original Stewart-Gough platform," *Computer-Aided Design*, vol. 30, no. 3, pp. 2005–215, 2007.

[82] M. L. Husty and A. Karger, "Self motions of Stewart-Gough platforms, an overview," in *Proceedings of the workshop on fundamental issues and future research directions for parallel mechanisms and manipulators*, (Quebec City, Canada), pp. 131–141, October 2002.

[83] J. D. Robinson, "A new algorithm for obtaining the reachable workspace of a serial manipulator." Internal Progress Report, March 2010.

[84] J. D. Robinson and M. J. D. Hayes, "The kinematics of a-pair jointed serial linkages," in *Proceedings of The ASME 2010 International Design Engineering Technical Conferences, IDETC 2010*, (Montreal, Quebec, Canada), August 2010.

[85] L. Sciavicco and B. Siciliano, *Modeling and Control of Robot Manipulators*. New York: McGraw-Hill, Inc., 1996.

[86] J. M. Selig, *Geometric Fundamentals of Robotics*. New York: Springer, 2005.

[87] J. Plücker, "Über ein neues coordinatensystem," *Journal für die rein und angewandte Mathematik*, vol. 1, pp. 1–36, 1830.

[88] J. Plücker, "On a new geometry of space," *Philosophical Transactions of the Royal Society of London*, vol. 155, pp. 725–791, 1865.

[89] F. Klein, *Elementary Mathematics from an Advanced Standpoint: Geometry*. Mineola, New York: Dover Publishing, Inc., 2004.

[90] F. Pernkopf, *Workspace Analysis of Stewart-Gough Platforms*. PhD thesis, University of Innsbruck, September 2003.

[91] P. J. Zsombor-Murray, "Connecting skew lines - a line geometric approach," in *Proceedings of the 2002 American Society for Engineering Education Annual conference and Exposition: Vive L'ingenieur*, (Montreal, PQ, Canada), pp. 4355–4361, June 2002.

[92] J. S. Ketchel and P. M. Larochelle, "Line based collision detection of cylindrical rigid bodies," in *Proceedings of ASME 2004 Design Engineering Technical conferences and Computers and Information in Engineering conference*, (Salt Lake City, Utah, USA), September-October 2004.

[93] J. S. Ketchel and P. M. Larochelle, "Collision detection of cylindrical rigid bodies using line geometry," in *Proceedings of ASME 2005 International Design Engineering Technical conferences and Computers and Information in Engineering conference*, (Long Beach, California, USA), September 2005.

[94] J. S. Ketchel and P. M. Larochelle, "Collision detection of cylindrical rigid bodies for motion planning," in *Proceedings of the 2006 IEEE International conference on Robotics and Automation*, (Orlando, Florida, USA), pp. 1530–1535, May 2006.

[95] Thermo CRS, Ltd., *A465 Robot System User Guide, UMI-A465-400*, July 2002.

[96] W. Q. D. Do and D. C. H. Yang, "Inverse dynamic analysis and simulation of a platform type of robot," *Journal of Robotic Systems*, vol. 5, no. 53.

[97] P. Guglielmetti and R. Longchamp, "A closed form for inverse dynamics model of the delta parallel robot," in *Proceedings of the 1994 International Federation of Automatic Control Conference on Robot Control*, pp. 39–44, 1994.

[98] K. Y. Tsai and D. Kohli, "Modified newton-euler computational scheme for dynamic analysis and simulation of parallel manipulators with applications to configuration based on r-l actuators," in *Proceedings of the 1990 ASME Design Engineering Technical Conferences*, pp. 111–117, 1990.

[99] G. Lebret, K. Liu, and F. L. Lewis, "Dynamic analysis and control of a stewart platform manipulator," *Journal of Robotic Systems*, vol. 10, no. 5.

[100] H. Pang and M. Shahingpoor, "Inverse dynamics of a parallel manipulator," *Journal of Robotic Systems*, vol. 11, no. 8.

[101] L. W. Tsai, "Solving the inverse dynamics of a stewart-gough manipulator by the principle of virtual work," *Transactions of ASME, Journal of Mechanical Design*, vol. 122, pp. 3–9, March 2000.

[102] C. D. Zhang and S. M. Song, "An efficient method for inverse dynamics of manipulators based on the virtual work principle," *Journal of Robotic Systems*, vol. 10, no. 5, 1993.

[103] J. Wang and C. M. Gosselin, "Dynamic analysis of spatial four-degree-of-freedom parallel manipulators," in *Proceedings of the 1997 ASME Design Engineering Technical Conferences*, (Sacramento, CA), 1997. Paper No. DETC97/DAC3759.

[104] S. Staicu, "Dynamics of the 6-6 stewart parallel manipulator," *Robotics and Computer-Integrated Manufacturing*, vol. 27, pp. 212–220, 2011.

[105] J. E. Shigley and C. R. Mischke, *Mechanical Engineering Design*. New York: McGraw-Hill, Inc., 1989.

[106] M. J. D. Hayes, M. L. Husty, and P. J. Zsomber-Murray, "Singular configurations of wrist-partitioned 6R serial robots: a geometric perspective for users," *Transactions of the Canadian Society for Mechanical Engineering*, vol. 26, no. 1, pp. 41–55, 2002.

Appendix A

Prototype Manipulator Assembly Drawings

The figures on the following pages are the assembly drawings for the prototype 4A-chain. Figure A.1 shows the full 4A-chain, Figure A.2 shows the construction of the A-pair joints, and Figure A.3 provides the bill of materials.

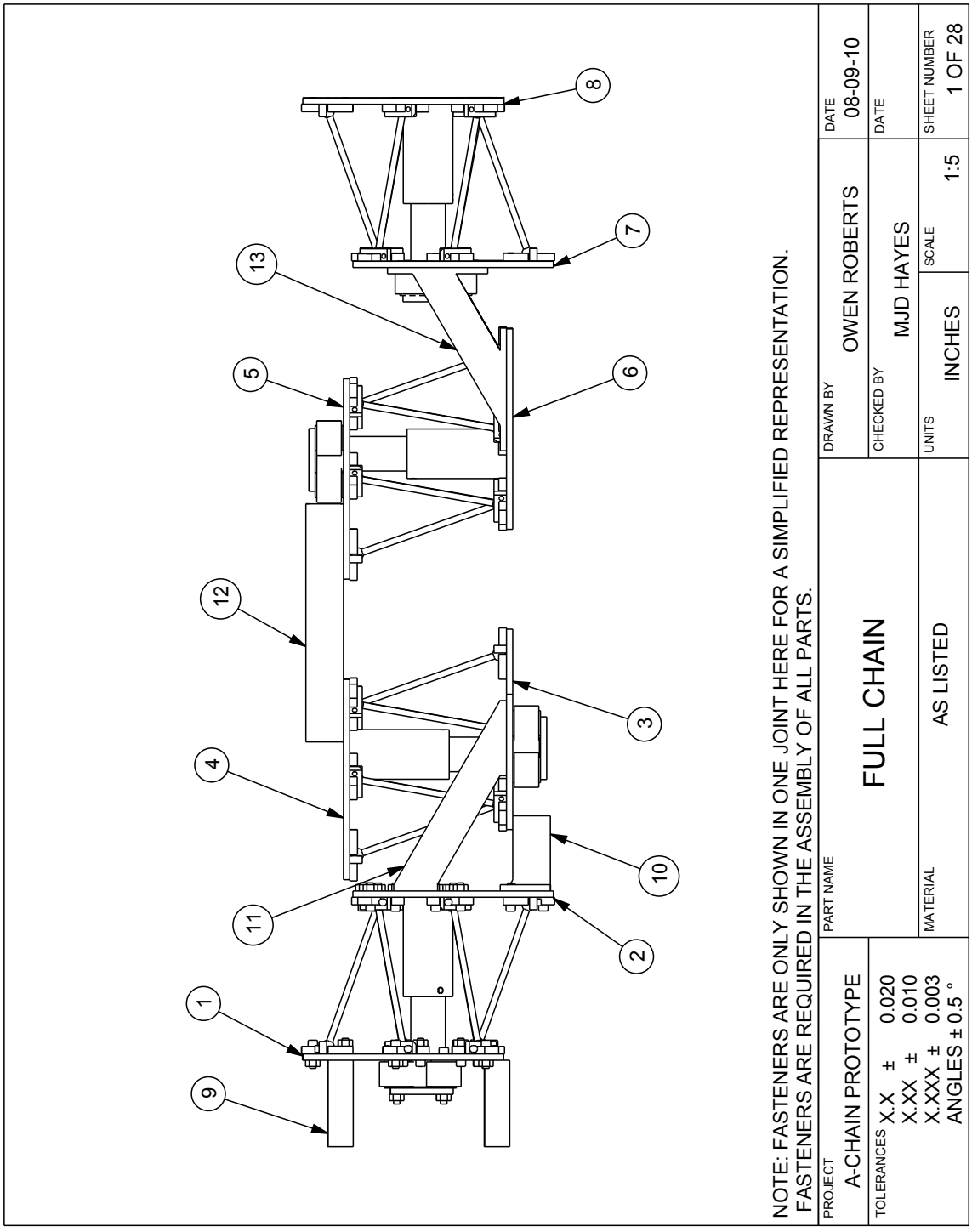

Figure A.1: Full assembly drawing of the prototype manipulator.

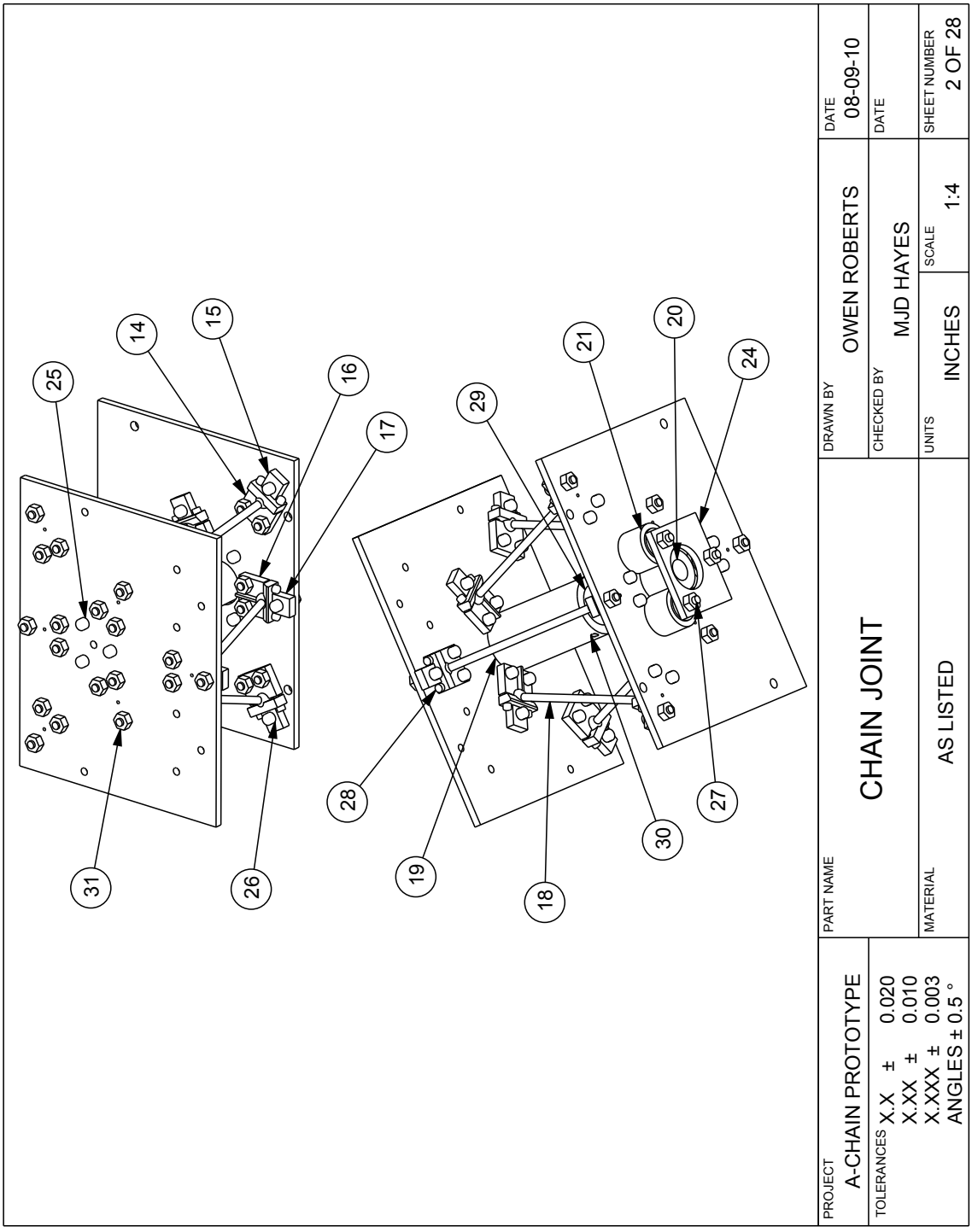

Figure A.2: Assembly drawing of joints of the prototype manipulator.

PROJECT A-CHAIN PROTOTYPE

BILL OF MATERIALS

ITEM	PART NAME	SHEET	QTY	ITEM	PART NAME	SHEET	QTY
1	PLATFORM JOINT 1-FIXED	5	1	18	LEG	17	24
2	PLATFORM JOINT 1-MOVING	6	1	19	GEAR ROD HOLDER	18	4
3	PLATFORM JOINT 2-FIXED	7	1	20	CENTRAL DRIVING GEAR	19	4
4	PLATFORM JOINT 2-MOVING	8	1	21	GEAR - SUPPORT	20	12
5	PLATFORM JOINT 3-FIXED	9	1	22	INNER BUSHING	21	12
6	PLATFORM JOINT 3-MOVING	10	1	23	OUTER BUSHING	22	12
7	PLATFORM JOINT 4-FIXED	11	1	24	GEAR GUIDE PLATE	23	4
8	PLATFORM JOINT 4-MOVING	12	1	25	SHCS 1/4-20 X 0.75	2	40
9	BASE POST	24	4	26	SHCS 1/4-20 X 0.875	2	144
10	CONNECTOR 1-2 UPRIGHT	10	2	27	SHCS 1/4-20 X 2.0	2	12
11	CONNECTOR 1-2 ANGLED	11	2	28	SHCS #8-32 X 0.625	2	96
12	CONNECTOR 2-3	12	2	29	SHCS 1/2-13 X 1.25	2	4
13	CONNECTOR 3-4	28	2	30	SET SCREW 1/4-28 X 0.37	2	4
14	APEX INNER BLOCK	13	24	31	NUT 1/4-20	2	196
15	APEX OUTER BLOCK	14	24	32	WASHER 0.25 ID X 1.0 OD	3	24
16	MIDPOINT INNER BLOCK	15	24	33	SHCS 5/16-18 X 1.0	2	4
17	MIDPOINT OUTER BLOCK	16	24				

Figure A.3: Bill of materials for the prototype manipulator.